Superlattices in van der Waals materials: a low-energy electron microscopy study

Jong, T.A. de

SUPERLATTICES IN VAN DER WAALS MATERIALS

A LOW-ENERGY ELECTRON MICROSCOPY STUDY

Proefschrift

ter verkrijging van
de graad van doctor aan de Universiteit Leiden,
op gezag van de rector magnificus prof. dr. ir. H. Bijl,
volgens het besluit van het college voor promoties
te verdedigen op donderdag 3 november 2022
klokke 15:00 uur

door

Tobias Arie DE JONG

geboren te Leiderdorp, Nederland
in 1992

Promotor: Prof. dr. ir. S.J. van der Molen
Co-promotor: Prof. dr. ir. R.M. Tromp

Promotiecommissie:

Prof. dr. C. Ropers	(Georg August Universität Göttingen)
Prof. dr. ir. H. Zandvliet	(Universiteit Twente)
Dr. S. Conesa-Boj	(Technische Universiteit Delft)
Prof. dr. J. Batenburg	
Prof. dr. J. van Ruitenbeek	
Prof. dr. J. Aarts	

Front & Back: An overview showing the wide variety of shapes of stacking domains occurring in graphene on silicon carbide (Chapter 7).
Printed by: Gildeprint – The Netherlands

The research for this thesis was conducted at the Leiden Institute of Physics, Leiden University. This work was financed by the Dutch Research Council (NWO) as part of the Frontiers of Nanoscience programme.

Casimir PhD Series, Delft-Leiden 2022-20

ISBN 978-90-8593-530-8

An electronic version of this dissertation is available at
https://scholarlypublications.universiteitleiden.nl/.

CONTENTS

Summary vii

Samenvatting xi

1 Introduction 1
- 1.1 Growing 2D materials . . . 3
- 1.2 Combining lattices: the Frenkel-Kontorova model . . . 4
- 1.3 Charge Density Waves . . . 6
- 1.4 Studying domains in van der Waals materials . . . 6
- 1.5 Content of this thesis . . . 7

2 Low Energy Electron Microscopy 11
- 2.1 Introduction . . . 12
- 2.2 Imaging . . . 12
- 2.3 Imaging modes . . . 15
- 2.4 LEEM and LEED spectroscopy . . . 16
  - 2.4.1 Further notes on experiments . . . 17

3 Quantitative analysis of spectroscopic LEEM data 19
- 3.1 Introduction . . . 20
- 3.2 Detector correction . . . 21
- 3.3 High dynamic range spectroscopy . . . 23
  - 3.3.1 Calibration . . . 24
  - 3.3.2 Active per-image optimization of MCP bias . . . 25
  - 3.3.3 Comparison of results . . . 26
- 3.4 Drift correction by image registration . . . 26
  - 3.4.1 Implementation details . . . 29
  - 3.4.2 Accuracy testing . . . 30
  - 3.4.3 Time complexity . . . 32
  - 3.4.4 Discussion . . . 32
- 3.5 Dimension reduction . . . 33
  - 3.5.1 Visualization . . . 35
  - 3.5.2 Clustering and automatic classification . . . 37
- 3.6 Conclusion . . . 38
- 3.7 Outlook: Drift correction improvements . . . 39
  - 3.7.1 GPUs for faster computation . . . 39
  - 3.7.2 Algorithmic speed improvements . . . 40
  - 3.7.3 Improvements to accuracy . . . 40

4 Intrinsic stacking domains in graphene on silicon carbide 49
4.1 Introduction . . . 50
4.2 Methods . . . 50
4.2.1 Sample fabrication . . . 50
4.2.2 Low-energy electron microscopy . . . 51
4.2.3 Computations . . . 51
4.3 Results . . . 52
4.3.1 Spectroscopy . . . 54
4.3.2 Domain morphology . . . 55
4.3.3 Influence on hydrogen de-intercalation . . . 57
4.4 Conclusion . . . 58

5 On stacking contrast of low energy electrons in multilayer graphene 63
5.1 Introduction . . . 64
5.1.1 Graphene on silicon carbide . . . 64
5.1.2 Twisted few-layer graphene . . . 65
5.1.3 Imaging domain boundaries . . . 66
5.2 Stacking contrast of bilayers in LEEM . . . 67
5.2.1 Unit cell averaging . . . 68
5.2.2 Twisted bilayer graphene results . . . 71
5.2.3 Comparison to strain domain boundaries in graphene on SiC . . . 72
5.3 Beyond bilayers . . . 76
5.3.1 2-on-2 graphene layers: phase contrast . . . 78
5.4 Moiré metrology . . . 79
5.5 Conclusion . . . 81
5.6 Outlook: possible computational improvements . . . 82

6 Imaging moiré deformation and dynamics in twisted bilayer graphene 87
6.1 Introduction . . . 88
6.2 Results . . . 88
6.2.1 Distortions & Strain . . . 90
6.2.2 Edge dislocations . . . 92
6.2.3 High temperature dynamics of the moiré lattice . . . 94
6.3 Conclusion . . . 95
6.4 Methods . . . 96
6.4.1 Sample fabrication . . . 96
6.4.2 LEEM . . . 96
6.4.3 Stitching . . . 97
6.4.4 Image analysis . . . 97
6.4.5 Reflectivity calculations . . . 97
6.4.6 Data & code availability . . . 98

7 Stacking domain morphology in epitaxial graphene 103
7.1 Qualitative description of sample features . . . 105
7.2 Stripe domains in epitaxial graphene . . . 108
7.2.1 GPA analysis of strain . . . 110
7.2.2 Discussion . . . 113

7.3 Symmetry breaking AA-sites (Spiral domain walls) . . . 115
7.4 Topological defects: Edge dislocations . . . 116
7.5 Conclusion . . . 118
7.6 Outlook . . . 118

8 Charge Density Waves in mixed polytype TaS_2 121
8.1 Introduction . . . 122
8.1.1 Transition metal dichalcogenides . . . 122
8.1.2 Polytypism . . . 122
8.1.3 Charge Density Waves . . . 123
8.1.4 Tantalum disulfide . . . 124
8.1.5 Towards 2D . . . 125
8.2 Sample preparation . . . 126
8.3 Pristine 1T-TaS_2 . . . 127
8.4 Mixed polytypes . . . 129
8.4.1 Spectra . . . 130
8.5 Charge Density Wave states . . . 132
8.5.1 In-plane CDW domains . . . 134
8.6 Discussion . . . 136
8.6.1 Comparison to low-temperature hidden state . . . 139
8.7 Conclusion . . . 139

9 Outlook 143
9.1 Device scale imaging . . . 144
9.2 Temperature-dependent measurements . . . 144
9.3 Technique combinations . . . 145
9.4 Computational opportunities . . . 145
9.4.1 Applications of adaptive GPA . . . 146
9.4.2 Computational denoising . . . 146
9.5 Concluding remarks . . . 146

A Geometric Phase Analysis 149
A.1 Deformations of a lattice . . . 149
A.2 Properties of the deformation . . . 150
A.3 Determination of the displacement field $\mathbf{u}(\mathbf{r})$ . . . 151
A.4 Additional notes on choice of reference vectors . . . 152
A.5 Adaptive GPA . . . 153
A.6 Decomposition of the displacement field.. . . . 154

B LEEM stitching 157
B.1 Considerations . . . 160
B.2 Parallelization . . . 160

C Additional data of the twisted bilayer graphene sample 161
C.1 Additional LEEM images/crops . . . 162
C.2 Additional figures on dynamics . . . 164
C.3 Additional dislocations . . . 165
C.4 AFM comparison . . . 168

C.5 Sample heating 169
D Additional TaS_2 figures **171**
Acknowledgements **177**
Curriculum Vitæ **179**
List of Publications **181**

SUMMARY

This thesis considers how lattices of different periodicities combine in two-dimensional materials. When adding two signals of different frequency, a modulation of the signal with the difference of the constituting frequencies occurs, commonly known as a beating pattern. The same effect can occur both in space and in time. In particular, the spatial variant occurs when combining two different two-dimensional lattices: an additional periodicity not present in the constituting lattices appears, with its spatial frequencies (inverses of the lattice periods) equal to the difference of the frequencies of the original lattices. If the difference in periods is small, the resulting pattern has a much larger periodicity, which is why they are sometimes called 'superlattices'. Such patterns are named 'moiré patterns', after a type of French textile consisting of two layers of fabric pressed together, yielding a watered pattern due to the interference of the two layers. Another common occurrence of this effect in daily life can be seen when two mesh fences overlap and one is slightly distorted by the perspective.

The same effect also occurs on the atomic scale when combining two-dimensional materials, also known as van der Waals materials. In such a combined system, the moiré periodicity can have surprising effects on the electronic properties of the combined materials. In this thesis, moiré patterns are studied in two different two-dimensional materials: graphene, the 2D form of carbon, and tantalum disulfide (denoted TaS_2). The latter is a transition metal dichalcogenide (TMD), a layered material that can be exfoliated to 2D just like graphite. This particular TMD is interesting because as a function of temperature it exhibits a variety of charge density wave (CDW) states.

Of all the many possible combinations of different two-dimensional materials, probably the most amazing example of new electronic properties occurs in the original 2D material, graphene, when combined with itself: When two graphene layers are combined at a specific 'magic' angle of about one degree, the resulting 'magic angle twisted bilayer graphene' (MABLG) turns out to become superconducting at low temperatures, an effect directly connected to a flat band in the band structure of the system and the moiré pattern that causes it.

In this thesis, I use Low-Energy Electron Microscopy (LEEM) to study moiré patterns in twisted bilayer graphene (TBG) and some other combinations of two-dimensional materials. LEEM has advantages in studying 2D materials compared to other imaging techniques. Unlike Transmission Electron Microscopy (TEM), it reflects electrons off the sample surface at low energies and is therefore inherently surface sensitive and much less prone to damaging the material itself. However, the electrons still penetrate the material to some depth and interact with the material in a way that depends on their precise landing energy. Due to the different interactions with different materials, there are variations in the amount of electrons reflected, causing so-called amplitude contrast between areas of different materials. As the reflectivity depends on the landing energy, the contrast can invert as a function of energy, where the 'darker' area (relative to another

area) at one landing energy becomes 'brighter' than the other area at another landing energy. This contrast mechanism enables for example counting the number of graphene layers on top of a substrate and imaging the local stacking of the first few layers of atoms and therefore any stacking domains forming between the layers.

Just like in any other modern microscopy technique, obtaining LEEM images is only part of the work. In so-called spectroscopy experiments, an image is taken for a range of different landing energies, to fully capture the energy-dependent reflectivity of the sample. To extract the most from such data, it is necessary to properly calibrate the data and correct for sample drift. The necessary techniques, which are applied throughout this thesis are described in Chapter 3. The calibration techniques are adopted from astronomy. First, a dark count image is subtracted from the data. Second, a flat field correction is applied by dividing out an evenly illuminated image to compensate for uneven detector gain. Furthermore, we describe a procedure to actively tune the (exponential) gain of the detector to obtain accurate reflectivity values over four orders of magnitude.

From TEM, we adopt a statistically averaged cross-correlation technique to register LEEM images of the same area. Here, the key components are to apply an edge-detection filter first to deal with contrast inversions and to compare all possible pairs of images to obtain sub-pixel accuracy. Finally, we highlight the use of Principal Component Analysis (PCA) to reduce the number of dimensions in the dataset and visualize the data in a few images and showcase that this corrected and reduced data is amenable to automatic clustering algorithms such as the k-means algorithm.

In Chapter 4, we use a specific imaging mode called Dark Field LEEM, which breaks rotational symmetry, to distinguish all the possible different stackings of bilayer and trilayer graphene. We show that in epitaxial graphene on silicon carbide stacking domains form from a moiré pattern between the graphene layer and the underlying buffer layer. We conclude that these stacking domains are intrinsic to (few-layer) epitaxial graphene on SiC, as the moiré pattern is due to the strain exerted on the buffer layer by the SiC substrate.

Furthermore, we show that these domains have implications for the process of hydrogen intercalation, which is used to create so-called quasi-free standing graphene. We conclude that the hydrogen, despite its small size, does not penetrate the pristine graphene. It only penetrates at pre-existing point defects in the graphene, and travels below the graphene, preferentially along the domain boundaries.

Extending on this, Chapter 5 explores how in few-layer graphene, the domain boundaries themselves can be directly imaged using LEEM and we compare the contrast mechanism in twisted bilayer graphene and in the strained graphene on SiC. We show that for large domains the contrast is a pure amplitude contrast caused by the local relative stacking of the layers. The measured reflectivity therefore matches well with computations of the reflectivity of such different stackings. For small domains on the other hand, a different contrast mechanism becomes dominant, namely phase contrast, where interference of the phase of the electron waves reflecting of neighboring areas creates contrast. The contribution of this contrast mechanism yields a higher visibility of the moiré pattern, in particular in thicker sandwiches such as twisted bilayer-on-bilayer graphene.

The imaging of the domain boundaries in this way is applied to twisted bilayer graphene (TBG) in Chapter 6 to characterize the spatial variations of the moiré pattern, which gov-

ern the electronic properties of such samples. Additionally, we show that LEEM can be used to measure temporal fluctuations of the moiré lattice in TBG. Although these fluctuations correspond to collective atomic movements of less than 70 pm, which is much smaller than the resolution of the LEEM, they can be imaged using a magnification factor due to the moiré pattern itself. The same magnification enables the imaging of edge dislocations in the atomic lattice.

In Chapter 7, the same imaging mechanism is applied to study the morphology of the stacking domains in several samples of high-quality graphene on SiC. The morphology of the stacking domains highlights that even in the most homogeneous of such samples, there is an intrinsic strain disorder, caused by a spontaneous symmetry breaking due to both atomic edge dislocations and the coexistence of striped and triangular domains. This can help explain the observation of varying electronic properties of the graphene in such samples and help further optimize the growth processes.

In Chapter 8, we change gears and use LEEM to study the combination of different lattices occurring in TaS_2. In this material, such superlattices are caused by two completely different aspects. First, the charge density wave (CDW) states cause an extra periodicity larger than the atomic lattice, where the precise periodicity depends on the temperature. Second, this TMD occurs in different polytypes, i.e. different internal arrangements of the atoms within the Van der Waals layers with slightly different lattice constants. After demonstrating that LEEM can be used to distinguish different stackings of mixes of such polytypes, we study the combination of the temperature dependent CDW lattice occurring in the 1T polytype of TaS_2 with the atomic lattice. We show that in mixed polytype samples, in-plane domains of the two possible orientations of the CDW lattice occur at room temperature at an angle which is not the same as the angle in bulk 1T-TaS_2. We find that the transition temperatures between the different CDW states depend on the precise local polytype stacking and that the angle of the CDW lattice seems linked with the size of the in-plane orientational domains. As the different CDW states have a strong influence on the conductivity, this would make mixed polytype TaS_2 interesting for sensor applications if a controlled way to engineer different polytype stackings could be found.

SAMENVATTING

SUPERROOSTERS IN VAN DER WAALS MATERIALEN:

EEN LAGE-ENERGIE-ELEKTRONMICROSCOPIE STUDIE

In dit proefschrift beschrijf ik hoe ik heb bestudeerd hoe roosters met verschillende periodes recombineren in twee-dimensionale materialen. Het combineren van twee signalen met verschillende frequenties geeft een modulatie in het resulterende signaal, met een frequentie die overeenkomt met het verschil van de frequenties van de originele signalen. Hetzelfde effect komt niet alleen in de tijdsdimensie, maar ook in ruimtelijke dimensies voor, bijvoorbeeld bij het combineren van twee verschillende tweedimensionale roosters: een extra periodiciteit verschijnt, met spatiële frequenties (de inverses van de roosterperiodes) gelijk aan de verschilfrequenties van de originele roosters. Wanneer de verschillen tussen de originele periodes klein zijn, heeft het resulterende patroon juist een zeer grote periode, waardoor je ze zou kunnen aanduiden als 'superroosters'. Deze patronen heten 'moirépatronen', vernoemd naar Franse weefsels die dit effect vertonen omdat ze bestaan uit twee tegen elkaar geplakte lagen stof. Een andere voorbeeld van moirépatronen in het dagelijks leven, is daar waar twee dezelfde hekken overlappen, waarbij één van de twee hekken licht wordt vervormd door het perspectief.

Hetzelfde effect komt ook voor op de atomaire schaal, wanneer twee twee-dimensionale materialen gecombineerd worden. In dit geval blijkt het effect een verbazende invloed uit te oefenen op de elektronische eigenschappen. In deze dissertatie worden moirépatronen in twee verschillende 2D-materialen, ook bekend als Van der Waals materialen, bestudeerd: in grafeen, de 2D-vorm van grafiet, en tantaaldisulfide (TaS_2). TaS_2 is één van de overgangsmetaal-dichalcogenides (TMD), gelaagde materialen die net zoals grafiet kunnen worden teruggebracht tot een 2D-vorm. Deze specifieke TMD is interessant, omdat het afhankelijk van de temperatuur diverse ladingsdichtheidsmodulatietoestanden (Engels: Charge Density Wave states, CDW) vertoont.

Het meest verbazingwekkende voorbeeld van nieuwe elektronische eigenschappen bij het recombineren van 2D-materialen komt waarschijnlijk op conto van het eerstontdekte 2D-materiaal, grafeen, zelf: als twee laagjes grafeen gestapeld worden met een zogeheten "magische" twisthoek tussen de twee lagen van ongeveer één graad, blijkt het resulterende materiaal (bij lage temperaturen) supergeleidend te zijn. Dit komt door een vlakke elektronenband in het systeem die ontstaat dankzij het moirépatroon.

In dit proefschrift gebruik ik lage-energie-elektronenmicroscopie (LEEM) om zulke moirépatronen te bestuderen in zowel getwist dubbellaags grafeen (TBG) als in een paar andere combinaties van 2D-materialen waarin ze voorkomen. Voor het bestuderen van 2D-materialen heeft LEEM een paar voordelen ten opzichte van andere microscopietechnieken. Zo worden, in tegenstelling tot in een transmissie-elektronenmicroscoop

(TEM), elektronen in een LEEM met een lage energie door het te bestuderen materiaal gereflecteerd. Door de relatief lage elektronenergie wordt het object veel minder snel beschadigd dan bij het gebruik van TEM. Doordat de elektronen reflecteren is de techniek bovendien vooral gevoelig voor de precieze eigenschappen van het oppervlak. Tijdens het reflectieproces gaan de elektronen nog wel een stukje het materiaal in en de precieze interactie met het materiaal (en dus welk deel van de elektronen gereflecteerd wordt) hangt af van de specifieke energie waarmee de elektronen het materiaal bereiken. Omdat elektronen verschillend reageren op verschillende materialen, varieert de hoeveelheid elektronen die verschillende materialen reflecteren. Hierdoor kunnen verschillende gebieden onderscheiden worden aan de hand van het resulterende amplitudecontrast. Aangezien de reflectiviteit afhangt van de landingsenergie van de elektronen, komt het voor dat het contrast omkeert voor verschillende waardes van de landingsenergie, zodat een bij de ene landingsenergie 'donkerder' gebied (ten opzichte van een ander gebied) bij een andere landingsenergie juist helderder kan zijn. Dit contrastmechanisme maakt het bijvoorbeeld mogelijk om het aantal laagjes grafeen op een substraat en bovendien de lokale relatieve stapeling van de eerste paar lagen atomen op het oppervlak te bepalen. Dit laatste zorgt er voor dat ook eventuele stapelingsdomeinen tussen de lagen in beeld gebracht kunnen worden.

Net als in elke andere moderne microscopietechniek is het vastleggen van de LEEM-afbeeldingen maar een deel van het werk. In zogenoemde spectroscopie-experimenten wordt een afbeelding gemaakt voor een reeks van verschillende waardes van de landingsenergie, om de energie-afhankelijke electronreflectiviteit van het te bestuderen object volledig te vast te leggen. Om zoveel mogelijk informatie uit zulke data te kunnen halen, is het nodig om de data te kalibreren en bewegingen van het oppervlak ten opzichte van de detector te corrigeren. De technieken die hiervoor in deze dissertatie gebruikt worden, worden beschreven in Hoofdstuk 3. Voor kalibratie passen we aangepaste technieken uit de sterrenkunde toe. Eerst wordt een onbelichte afbeelding van de data afgetrokken, waarna het resultaat gedeeld wordt door een vlak belichte afbeelding om te compenseren voor oneffenheden in de gevoeligheid van de detector. Ook beschrijven we hier een procedure om de gevoeligheid van de detector actief bij te stellen tijdens de meting, om zo een accurate reflectiviteit te kunnen meten over een dynamisch bereik van meer dan vier ordes van grootte.

Vanuit de TEM-wereld passen we een statistisch middelende kruiscorrelatietechniek toe om LEEM-afbeeldingen van eenzelfde gebied netjes over elkaar te leggen. Belangrijke aspecten voor de succesvolle toepassing hiervan zijn om eerst een rand-detectie filter te gebruiken om contrastomkeringen correct te behandelen en daarna alle mogelijke paren van afbeeldingen te vergelijken om sub-pixel precisie te bereiken. Tenslotte laten we zien dat hoofdcomponentenanalyse (Engels: Principal Component Analysis, PCA) toegepast kan worden om het aantal dimensies van de dataset te reduceren en de dataset te visualiseren in slechts een paar afbeeldingen. Ook laten we zien dat zo gecorrigeerde en gereduceerde data zich goed leent om automatische clusteralgoritmes zoals het Lloyd–Forgy algoritme (Engels: k-means algorithm) op toe te passen.

Vervolgens gebruiken we in Hoofdstuk 4 een specifieke opnamemodus van LEEM genaamd 'donkerveldmicroscopie'. Deze modus breekt de rotatiesymmetrie van de beeldvorming, opdat alle verschillende mogelijke stapelingen van dubbellaags en driedubbel-

laags grafeen onderscheiden kunnen worden. We laten zien dat in grafeen, gegroeid op siliciumcarbide, stapelingsdomeinen vormen uit het moirépatroon tussen de grafeenlaag en de onderliggende bufferlaag. We concluderen dat deze domeinen inherent zijn aan deze manier van grafeen groeien, aangezien het moirépatroon wordt veroorzaakt doordat de bufferlaag ietwat opgerekt wordt ten opzichte van de grafeenlaag door het onderliggende siliciumcarbide substraat.

We tonen aan dat deze domeinen invloed uitoefenen op het proces van waterstofintercalatie, wat gebruikt wordt om dit epitaxiale grafeen te converteren naar zogenoemd 'quasi-vrijstaand grafeen'. We concluderen dat het waterstof, ondanks zijn geringe grootte, niet door het pure grafeen heen kan. Het dringt alleen binnen bij reeds bestaande puntdefecten in het grafeen, waarna het onder het grafeen door beweegt, bij voorkeur langs de randen van de domeinen.

Hierop voortbordurend beschouwt Hoofdstuk 5 hoe de grenzen tussen stapelingsdomeinen in paarlaags grafeen direct afgebeeld kunnen worden met LEEM. We vergelijken het contrastmechanisme van getwist dubbellaags grafeen met dat van het opgerekte grafeen op siliciumcarbide. Voor grote domeinen wordt het contrast puur veroorzaakt door amplitudecontrast vanwege de lokale relatieve stapeling van de lagen in de domeingrens. Zodoende komt de gemeten reflectiviteit dan ook goed overeen met berekeningen van de reflectiviteit voor verschillende stapelingen. Voor kleinere domeinen daarentegen krijgt een ander contrastmechanisme de overhand, namelijk fasecontrast, waarbij een contrast veroorzaakt wordt door de interferentie van de fases van de elektrongolven die reflecteren van aangrenzende gebieden. De bijdrage van dit fasecontrast zorgt ervoor dat het moirépatroon beter zichtbaar is, in het bijzonder als het patroon zich in diepere lagen bevindt, zoals in dubbellaags-op-dubbellaags grafeen.

Het afbeelden van domeingrenzen op deze manier wordt in Hoofdstuk 6 toegepast op getwist dubbellaags grafeen om de spatiele vervormingen van het moirépatroon in praktische realisaties van dit materiaal te karakteriseren, aangezien deze de elektronische eigenschappen ervan bepalen. Bovendien laten we zien dat LEEM gebruikt kan worden om thermische fluctuaties van het moirépatroon te meten. Hoewel deze fluctuaties overeenkomen met collectieve atomaire bewegingen van minder dan 70 picometer, dat wil zeggen minder dan één atoomafstand en veel kleiner dan de resolutie van LEEM, is het mogelijk ze af te beelden door een extra vergrotingsfactor van het moirépatroon zelf. Deze vergrotingsfactor maakt het ook mogelijk om atomaire randdislocaties te detecteren.

Hetzelfde afbeeldingsmechanisme wordt in Hoofdstuk 7 toegepast om de vormen van de stapelingsdomeinen in diverse monsters van hoge kwaliteit grafeen op siliciumcarbide te bestuderen. De diverse morfologie van de stapelingsdomeinen in deze monsters verraadt de aanwezigheid van een intrinsieke oprekkingswanorde die zelfs in de meest homogene realisaties van dit materiaal tot nu toe bestaat. Deze wanorde wordt veroorzaakt door een spontane symmetriebreking die verband houdt met de simultane aanwezigheid van atomaire randdislocaties, driehoekige and langwerpige domeinen. Begrip over het bestaan van deze domeinen helpt de observatie van variërende elektronische eigenschappen van het grafeen in dit materiaal te verklaren en kan helpen om de groeiprocessen verder te optimaliseren.

In Hoofdstuk 8 wordt een heel ander soort combinatie van verschillende roosters

bestudeerd, die voorkomt in TaS_2. In dit materiaal komen superroosters voor door twee verschillende aspecten. Enerzijds vormen de ladingsdichtheidsmodulaties (Engels: CDW) voor een periodiciteit die groter is dan die van het atomaire rooster, waar bovendien het precieze CDW-rooster afhangt van de temperatuur. Anderzijds komt dit materiaal voor in verschillende polytypes, dat wil zeggen verschillende interne ordeningen van de atomen binnen de laagjes, met licht afwijkende roosterconstantes. We tonen aan dat LEEM-spectroscopie gebruikt kan worden om verschillende stapelingen van polytypes te onderscheiden. Vervolgens bestuderen we de CDW-toestand die voorkomt in het '1T'-polytype van TaS_2 in stapelingen met meerdere polytypes. In dat geval observeren we bij kamertemperatuur laterale domeinen van linksdraaiende en rechtsdraaiende CDWs, waar de hoek tussen de CDW en het atomaire rooster niet overeenkomt met die in bulk 1T-TaS_2. Bovendien meten we dat de transitietemperaturen tussen de verschillende CDW toestanden afhangen van de lokale stapeling van polytypes en dat de precieze hoek tussen de CDW en het atomaire rooster af lijkt te hangen van de grootte van de orientatiedomeinen. Aangezien de verschillende CDW-toestanden een sterke invloed hebben op de elektrische geleiding, suggereert dit dat TaS_2 met gemixte polytypes interessant kan zijn voor sensortoepassingen, mits er een gecontroleerde manier gevonden kan worden om verschillende polytype stapelingen te maken.

1

INTRODUCTION

1

Life in general and science in particular are most interesting at boundaries, on edges and at frontiers. Frontiers of human knowledge, where the unknown meets the known, but also boundaries between different systems. In condensed matter different types of such boundaries exist: between different phases of matter (e.g. a liquid–gas interface), between matter and vacuum (mostly studied by surface science), and between different condensed matter systems. The challenge in studying this last type of system has traditionally been to create an atomically clean interface between the two material systems, and has been served by the art of epitaxy: the deposition of layers of a material on the surface of a second system in an inert atmosphere. By ensuring the interface is atomically clean, it becomes possible to study the interaction between the two systems, how they bond and, of particular interest in this work, how their different lattices reconcile.

The boundary between two three-dimensional systems is a two-dimensional plane. As the dimensionality plays a large role in the description of electrons in materials, creating a truly two-dimensional electronic system has been a goal in experimental physics. An important early example are the gallium arsenide / aluminium gallium arsenide epitaxial interfaces, where a two-dimensional electron gas forms. Aside from physically interesting phenomena, e.g. the Hofstadter butterfly [1], this system also forms the basis of high-frequency field effect transistors.

The true start of the field now known as two-dimensional materials came in 2004, when Konstantin Novoselov and Andre Geim et al. realized the first two-dimensional material, showing that it was possible to thin down layered materials to a thickness of only a single atom using simple scotch tape [2]. As it turned out, the carbon atoms in graphite form layers that are strongly bonded by covalent bonds within a layer, but the layers are only held together by much weaker van der Waals forces (as visible in the schematic representation of graphite in Figure 1.1**a**). Therefore, tape sticks more strongly to the layers than the layers stick to each other, making it possible to peel layers of graphite from a crystal using tape. By sticking a new tape to the material on the tape, the peeled off layer can be split again, and again, until a single layer of carbon atoms in a hexagonal arrangement remains: graphene. This process to obtain atomically thin layers is called exfoliation.

The advent of exfoliation as a technique for the production of two-dimensional materials has started extended studies of atomically thin layers. Most notably, the electronic behavior changes as these materials become truly two-dimensional as no copies of the same electron orbital exist along the out-of-plane direction, leading to extraordinary properties.

After the original exfoliation of graphene, a larger assortment of materials has been added to the collection of so-called van der Waals materials. This includes the insulating material hexagonal boron nitride (hBN, Figure 1.1**b**), with the same structure as graphene, but consisting of alternating boron and nitrogen atoms, and the transition metal dichalcogenides (TMDs, Figure 1.1**c,d**), where the van der Waals layer consists of a layer of trigonally arranged transition metal atoms (molybdenum, tantalum, niobium, tungsten, etc.) sandwiched between two layers of chalcogens (sulfur, selenium or tellurium[1]). The set of all possible TMDs spans a wide range of properties: from semi-

[1] Aside from obvious reasons to not use these elements, polonium and livermorium tend to be too metallic in character to form TMDs [3]

conductor to metal, magnetic, and superconductor, often combining several properties depending on the temperature.

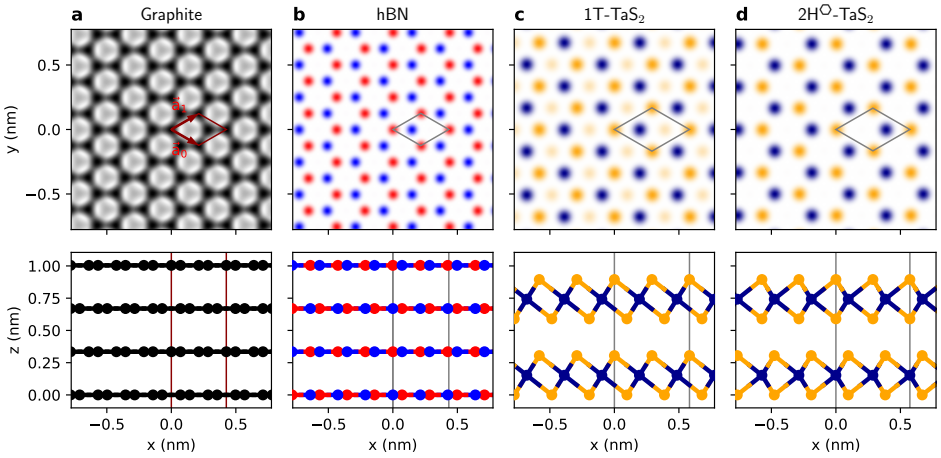

Figure 1.1: Van der Waals materials. *Top views and side views along the so-called arm chair direction of different van der Waals materials: graphite, the 'mother material' of graphene, its insulating sibling hexagonal boron nitride and the TMD TaS_2. In TMDs, different polytypes (layer arrangements) exist. Two of the stable polytypes for TaS_2 are shown: 1T and 2H⬡ (For more details about polytypes, see Section 8.1.2).*

In addition to the study of intrinsic properties of these 2D materials, exfoliation has led to a new way of studying matter–matter boundaries: by transferring subsequent van der Waals layers via exfoliation, so-called **heterostacks** of different layers with (areas of) an atomically clean interface between the subsequent layers can be created. In this way different electronic properties can be combined, used adjacent to each other, or even hybridized to create new properties.

The parameter space is enormous: in addition to the possibility to combine any pair of van der Waals materials, independent of the existence of conventional epitaxial growth procedures[2], the twist angle between subsequent layers enters the picture as a tunable parameter. This means that even interfaces between two layers of the *same* material can become interesting: a non-zero twist angle between the materials leads to a moiré pattern with its own larger geometry (the 'super' lattice), with significant influences on the electronic structure. Famously, this has led to the observation of superconductivity in twisted bilayer graphene (TBG), which forms a flat electronic band when the two layers are stacked at a 'magic' twist angle of approximately one degree [4, 5].

1.1 GROWING 2D MATERIALS

Maybe somewhat ironically, the interest in two-dimensional materials has also renewed the interest in traditional epitaxy: while exfoliation is an excellent platform to study 2D

[2] Although not all materials exfoliate to single layers with the same ease. There is no such thing as a free lunch.

materials, the process does not scale to industrial applications. Therefore, epitaxy, i.e. growing a 2D material on the surface of a 3D substrate, is pursued as a way to grow 2D materials on an industrial scale. Challenges in separating the 2D material from the substrate, in scalability and in homogeneity are the major factors complicating the delivery of applications of the promised 'miracle' material graphene in the past 18 years, despite significant efforts.

Chemical vapor deposition (CVD) can be used to grow bulk crystals of most van der Waals materials for exfoliation, but also to grow single layers on metallic substrates. Graphene growth on metals (most notably copper, iridium, and ruthenium) scales very well, but suffers from different rotational domains dominating the electronic properties. On the other hand, epitaxial graphene on silicon carbide, which is grown on the silicon face of SiC by thermal decomposition, has (almost) perfect rotational ordering, although it is harder to separate from its substrate and still exhibits varying electronic properties [6–10].

1.2 COMBINING LATTICES: THE FRENKEL-KONTOROVA MODEL

In general, when combining two different lattices, two things can happen. Either both lattices adapt a single shared lattice, the **commensurate** phase, or both lattices retain their own lattice, without significant distortion, known as the **incommensurate** phase. However, a boundary region between these two phases exists in the phase diagram, where lattices partially comply to each other and commensurate regions co-exist with domain boundaries in between, in which all relative lattice strain is contained. As such a (quasi-)periodic pattern of commensurate regions and domain boundaries can form with a periodicity that can be much larger than the underlying periodicities. This new, larger periodicity is called the '**superlattice**', and the resulting pattern is called a **moiré pattern**. The spatial frequency (i.e. the inverse of the lattice constant) of the superlattice is the difference of the spatial frequencies of the constituting lattices. Therefore, the smaller the difference between the lattice constants, the larger the periodicity of the superlattice.

Sometimes it is useful to distinguish higher-order commensurate phases from incommensurate phases. In case of a higher-order commensurate phase, the following holds for the lattice constant a_a and a_b of the two lattices:

$$na_a = ma_b$$

where n, m are (non-equal) integers. For larger integers n, m, the distinction from (partially) incommensurate becomes increasingly irrelevant, especially in the one-dimensional case.

Whether an incommensurate, commensurate, or mixed state occurs depends on the lattice mismatch, the interlayer interaction (Van der Waals forces) and the interaction within the layer (covalent bonds). This holds true in simple 1D models, in traditional epitaxy, and in van der Waals heterostacks.

The one-dimensional Frenkel-Kontorova (FK) model can be adapted to describe this phase transition between incommensurate and commensurate stacking. In its original, most simple form, the FK-model describes a chain of harmonically interacting particles

subject to a sinusoidal potential. To give an accurate description of the phase transition in a bilayer of one-dimensional atomic chains, two modifications have to be made. First, the sinusoidal potential is replaced by the interlayer potential caused by a second, fixed, strained atomic chain. Second, the harmonic interaction between atoms in the other chain is replaced by a suitably more accurate intralayer interaction [11]. Further extensions to two-dimensional interfaces exist, but to describe the full complexity of the phase diagram, it is necessary to incorporate the full complexity of the system: two lattice constants become two pairs of (2D) lattice *vectors*, and at least parts of the inter- and intralayer interaction functions become two-dimensional.

In the 2D case, the extra freedom given by the extra dimension means that higher-order commensurate structures become more relevant and more common, and they are sometimes known as 'reconstructions'. They are named after the size and orientation of the unit cell with respect to one lattice, e.g. the reconstruction of graphene on SiC(0001) is denoted $\left(6\sqrt{3}\times 6\sqrt{3}\right)R30°$, as a unit vector of the full unit cell is given by $\mathbf{a}' = 6\mathbf{a}_0 + 6\mathbf{a}_1$, which is 30° rotated with respect to the unit vectors $\mathbf{a}_0, \mathbf{a}_1$ of the SiC surface. Here, $|6\mathbf{a}_0 + 6\mathbf{a}_1| = 6\sqrt{3}\,|\mathbf{a}_0| \approx 13|\mathbf{b}_0|$ where $|\mathbf{b}_0| = 0.246\,\text{nm}$ is the lattice constant of graphene [12–14][3].

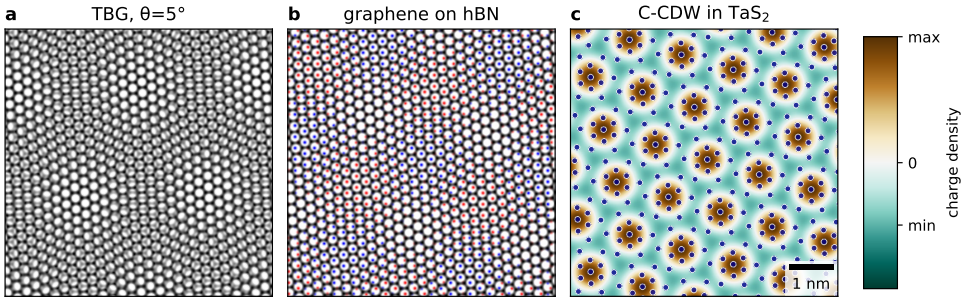

Figure 1.2: Diagrams of superlattices. a, *Twisted bilayer graphene (TBG) with a twist angle $\theta = 5°$.* ***b,*** *Graphene on hexagonal boron nitride with the same relative twist angle. As a result of the lattice mismatch, the moiré pattern is slightly smaller* ***c,*** *The commensurate charge density wave (C-CDW) and the corresponding star-of-David periodic lattice distortion of the tantalum atoms in TaS_2, where twelve atoms in the unit cell move slightly towards the charge density center on the thirteenth tantalum atom. The sulfur atoms are omitted for clarity. Scalebar applies to all panels.*

Even for the limited case of two hexagonal lattices with similar lattice constants (e.g. graphene-on-hBN, TBG or graphene on biaxially strained graphene), the influence of twist angle, lattice mismatch and a 2D interlayer interaction function mean that in addition to 'simple' hexagonal moiré patterns (as shown in Figure 1.2**a,b**), additional stripe phases and spiral domain wall phases can appear [15–19], which are studied in detail in Chapter 7.

[3] Typically one would claim strict equality (=) for the reconstruction, not ≈, but in Chapters 4 and 7 it will become clear that this is inaccurate.

1.3 CHARGE DENSITY WAVES

An additional way to combine two lattices in van der Waals materials is to combine the atomic lattice with the lattice of the **Charge Density Waves** (CDWs) occurring in some TMDs. CDWs are the multidimensional equivalent of the classical Peierls transition, where a new periodicity larger than the original atomic periodicity forms spontaneously. In TMDs, typical CDW periodicities include 3×3 and $\sqrt{13}\times\sqrt{13}$. In this case, the atomic positions over several unit cells and the associated electron density reorder to exchange electronic (band) energy with Coulomb energy of the atomic core positions, as illustrated in Figure 1.2**c**. The electronic energy is typically lowered by opening a band gap around the Fermi energy, lowering the energy of the states below the Fermi energy. This means the CDW forms only below a critical transition temperature, when the occupancy of the states above the Fermi energy is low enough to actually lower the total energy. It also means CDWs dramatically alter the electronic properties of a material, reducing the conductivity by orders of magnitude as the temperature decreases below the transition temperature.

A particularly complicated example which we will study in this thesis is 1T-TaS_2, where as the temperature increases, the CDW transitions from insulating commensurate (C-CDW, $\left(\sqrt{13}\times\sqrt{13}\right)R13.9°$, i.e. $\mathbf{a}_{\mathrm{CDW}} = 3\mathbf{a}_0 + \mathbf{a}_1$, the example illustrated in Figure 1.2**c**) to semiconducting nearly-commensurate (NC-CDW, $\left(\sqrt{13}\times\sqrt{13}\right)R10.9°$) to incommensurate (IC-CDW, $\left(\sqrt{13}\times\sqrt{13}\right)R0°$, i.e. $\mathbf{a}_{\mathrm{CDW}} = \sqrt{13}\mathbf{a}_0$), until it finally disappears.

However, the mechanism behind the Peierls transition does not translate to physical systems in more than one dimension. Although significant progress has been made in recent years to theoretically model and understand real CDW systems (e.g. Ref. [20]), the CDW states in bulk 1T-TaS_2, in particular the NC-CDW remain not fully understood. Additionally, in the context of 2D materials, the behavior of the CDW in the 2D limit of the material and the possibility to combine it with additional lattices in heterostacks open up new possibilities to modify the CDW behavior and therefore the electronic properties.

1.4 STUDYING DOMAINS IN VAN DER WAALS MATERIALS

The existence of different domains and the spatial variability of such domains turn out to be essential to explain the (variation of) electronic properties in heterostructures of van der Waals materials. In particular for van der Waals systems where the lattice mismatch is small, any small variation in the atomic lattice is magnified in the superlattice, which often determines the electronic properties. This means these materials, such as the aforementioned systems of superconducting 'magic' angle twisted bilayer graphene and NC-CDW 1T-TaS_2 and even epitaxial graphene on SiC, are extra sensitive to local variations, e.g. a small atomic strain in TBG can break the superconductivity [21]. The best way to study such variations and domains is to directly image them.

Traditionally [4], Scanning Tunneling Microscopy (STM) (and to a lesser extent Atomic Force Microscopy (AFM)) has been used extensively to study van der Waals materials, their growth and the existence of different (mostly rotational) domains. This technique is very well suited as it is intrinsically surface sensitive and can image the materials with atomic resolution. However, STM imaging is relatively slow. The atomically sharp tip

[4] Insofar 'traditionally' is applicable to a field that has existed for only 18 years

needed for STM experiments is fragile and can be easily destroyed by surface contaminations. The surface sensitivity of STM is however so extreme, that distinguishing what is happening in atomic layers beyond the top layer at the surface is hard, if not in most cases impossible. Another technique with atomic resolution, transmission electron microscopy (TEM), has also been used and has its own strengths, but it measures a projection of the sample along the direction of the electron beam. This necessitates extra effort and requirements to the sample to be able to separate the signal originating from the van der Waals material under study from the signal due to the substrate.

1.5 CONTENT OF THIS THESIS

In this thesis, we will use Low-Energy Electron Microscopy (LEEM) to study domains in van der Waals heterostructures. LEEM has advantages in studying 2D materials compared to other techniques. Unlike TEM, it reflects electrons off the sample surface at low energies and is therefore inherently surface sensitive and much less prone to damaging the material itself. However, the electrons still penetrate the material to some depth. This enables for example counting the number of graphene layers on top of a substrate and imaging the local stacking of the first few layers of atoms and therefore the stacking domains.

Chapter 2 briefly explains the operating principles and imaging modes of LEEM. However, obtaining the images is only part of the work. To extract the most from the data obtained with a LEEM, it is necessary to properly calibrate the data, correct for sample drift and visualize the resulting multi-dimensional datasets. This process is described in Chapter 3.

In Chapter 4, we use a specific imaging mode called Dark Field LEEM to distinguish the different stackings of bilayer and trilayer graphene. We show that stacking domains are intrinsic to (few-layer) epitaxial graphene on SiC due to the strain exerted by the SiC substrate. This has implications for the process of hydrogen intercalation, which is used to create so-called quasi-free standing graphene. We show that the hydrogen does not penetrate the graphene, except at pre-existing point defects in the graphene, and travels below the graphene, preferentially along the domain boundaries.

Extending on this, Chapter 5 explores how in few-layer graphene, the domain boundaries themselves can be directly imaged using LEEM and we compare the contrast mechanism in twisted bilayer graphene and in the strained graphene on SiC. The imaging of the domain boundaries is applied to twisted bilayer graphene in Chapter 6 to characterize the spatial variations of the moiré pattern, governing the electronic properties of such samples, as well as temporal fluctuations of the moiré lattice. Although these fluctuations correspond to atomic movements of less than 70 pm, which is much smaller than the resolution of the LEEM, they can be imaged using a magnification factor due to the moiré pattern itself. The same magnification enables the imaging of edge dislocations in the atomic lattice. In Chapter 7, the same imaging mechanism is applied to study the morphology of the stacking domains in several different graphene on SiC samples. The morphology of the stacking domains highlights that even in the most homogeneous of such samples, there is an intrinsic strain disorder, caused by a spontaneous symmetry breaking due to both atomic edge dislocations and the coexistence of striped and triangular domains.

In Chapter 8, we change gears and use LEEM to study the superlattices occurring in TaS_2. This TMD occurs in different polytypes, i.e different internal arrangements of the atoms within the van der Waals layers. After showing that LEEM can be used to distinguish different stackings of mixes of such polytypes, we study the interaction of the atomic lattice of TaS_2 with the temperature dependent Charge Density Waves occurring in the 1T polytype of TaS_2.

Finally, a short outlook on the implications of this research and future opportunities is given in Chapter 9.

REFERENCES

1. M. C. Geisler, J. H. Smet, V. Umansky, et al. Detection of a Landau Band-Coupling-Induced Rearrangement of the Hofstadter Butterfly. *Physical Review Letters* **92,** 256801. doi:10.1103/PhysRevLett.92.256801 (2004).
2. K. S. Novoselov, A. K. Geim, S. V. Morozov, et al. Electric Field Effect in Atomically Thin Carbon Films. *Science* **306,** 666–669. doi:10.1126/science.1102896 (2004).
3. M. Ates, E. Yılmaz & M. K. Tanaydın. In *Chalcogenide-Based Nanomaterials as Photocatalysts* (ed M. M. Khan) 307–337 (Elsevier, 2021). doi:10.1016/B978-0-12-820498-6.00014-7.
4. Y. Cao, V. Fatemi, S. Fang, et al. Unconventional superconductivity in magic-angle graphene superlattices. *Nature* **556,** 43–50. doi:10.1038/nature26160 (2018).
5. S. Lisi*, X. Lu*, T. Benschop*, T. A. de Jong*, et al. Observation of flat bands in twisted bilayer graphene. *Nature Physics* **17,** 189–193. doi:10.1038/s41567-020-01041-x (2021).
6. J. Kautz, J. Jobst, C. Sorger, et al. Low-Energy Electron Potentiometry: Contactless Imaging of Charge Transport on the Nanoscale. *Scientific Reports* **5,** 13604. doi:10.1038/srep13604 (2015).
7. S.-H. Ji, J. B. Hannon, R. M. Tromp, et al. Atomic-scale transport in epitaxial graphene. *Nature Materials* **11,** 114–119. doi:10.1038/nmat3170 (2012).
8. F. Kisslinger, C. Ott, C. Heide, et al. Linear magnetoresistance in mosaic-like bilayer graphene. *Nature Physics* **11,** 650–653. doi:10.1038/nphys3368 (2015).
9. M. K. Yakes, D. Gunlycke, J. L. Tedesco, et al. Conductance Anisotropy in Epitaxial Graphene Sheets Generated by Substrate Interactions. *Nano Letters* **10,** 1559–1562. doi:10.1021/nl9035302 (2010).
10. D. Momeni Pakdehi, J. Aprojanz, A. Sinterhauf, et al. Minimum Resistance Anisotropy of Epitaxial Graphene on SiC. *ACS Applied Materials & Interfaces* **10,** 6039–6045. doi:10.1021/acsami.7b18641 (2018).
11. A. M. Popov, I. V. Lebedeva, A. A. Knizhnik, Y. E. Lozovik & B. V. Potapkin. Commensurate–incommensurate phase transition in bilayer graphene. *Physical Review B* **84,** 045404. doi:10.1103/PhysRevB.84.045404 (2011).

12. C. Riedl, U. Starke, J. Bernhardt, M. Franke & K. Heinz. Structural properties of the graphene-SiC(0001) interface as a key for the preparation of homogeneous large-terrace graphene surfaces. *Physical Review B* **76,** 245406. doi:10.1103/PhysRevB.76.245406 (2007).

13. S. Kim, J. Ihm, H. J. Choi & Y.-W. Son. Origin of Anomalous Electronic Structures of Epitaxial Graphene on Silicon Carbide. *Physical Review Letters* **100,** 176802. doi:10.1103/PhysRevLett.100.176802 (2008).

14. F. Varchon, P. Mallet, J.-Y. Veuillen & L. Magaud. Ripples in epitaxial graphene on the Si-terminated SiC(0001) surface. *Physical Review B* **77,** 235412. doi:10.1103/PhysRevB.77.235412 (2008).

15. I. V. Lebedeva, A. V. Lebedev, A. M. Popov & A. A. Knizhnik. Dislocations in stacking and commensurate-incommensurate phase transition in bilayer graphene and hexagonal boron nitride. *Physical Review B* **93,** 235414. doi:10.1103/PhysRevB.93.235414 (2016).

16. S. Quan, L. He & Y. Ni. Tunable mosaic structures in van der Waals layered materials. *Physical Chemistry Chemical Physics* **20,** 25428–25436. doi:10.1039/C8CP04360D (2018).

17. J. Ravnik, I. Vaskivskyi, Y. Gerasimenko, et al. Strain-Induced Metastable Topological Networks in Laser-Fabricated TaS_2 Polytype Heterostructures for Nanoscale Devices. *ACS Applied Nano Materials* **2,** 3743–3751. doi:10.1021/acsanm.9b00644 (2019).

18. C. Gutiérrez, C.-J. Kim, L. Brown, et al. Imaging chiral symmetry breaking from Kekulé bond order in graphene. *Nature Physics* **12,** 950–958. doi:10.1038/nphys3776 (2016).

19. I. V. Lebedeva & A. M. Popov. Two Phases with Different Domain Wall Networks and a Reentrant Phase Transition in Bilayer Graphene under Strain. *Physical Review Letters* **124,** 116101. doi:10.1103/PhysRevLett.124.116101 (2020).

20. J. Henke, F. Flicker, J. Laverock & J. van Wezel. Charge order from structured coupling in VSe_2. *SciPost Physics* **9,** 056. doi:10.21468/SciPostPhys.9.4.056 (2020).

21. F. Mesple, A. Missaoui, T. Cea, et al. Heterostrain Determines Flat Bands in Magic-Angle Twisted Graphene Layers. *Physical Review Letters* **127,** 126405. doi:10.1103/PhysRevLett.127.126405 (2021).

2

Low Energy Electron Microscopy

The upside is: LEEM is sensitive to every tiny effect.
The downside is: LEEM is sensitive to each and every tiny effect.

2.1 INTRODUCTION

In this thesis, an Aberration Correcting Low Energy Electron Microscope (AC-LEEM) is used to image the structure of different Van der Waals materials. As the name suggests, LEEM uses electrons with low kinetic energy, typically just a few electronvolts.

Electrons are commonly used in microscopy instead of photons to obtain a resolution higher than the diffraction limit of (visible) light. Even at low kinetic energies the electron wavelength is much smaller than visible light photons and typically smaller than atomic distances in the sample.[1] Therefore, plane waves of electrons will diffract off the atomic lattice, forming multiple diffracted beams containing information about the atomic lattice itself.

Conventional electron microscopes, such as a Scanning Electron Microscope (SEM) or Transmission Electron Microscope (TEM), use a high energy electron beam and form an image with transmitted electrons, reflected electrons or secondary electrons, which are kicked out by the incoming beam. However, using high energy electrons has a significant downside: it generally damages the samples, significantly limiting the time that a sample can be imaged.

In contrast, most samples measured in LEEM can be imaged for hours or even days on end, without any significant damage to the sample. Furthermore, the low penetration depth of electrons at these low energies makes LEEM very surface-sensitive and the energy dependent reflectivity contains information about the three-dimensional atomic structure of the sample surface.

A LEEM setup is significantly different from what is used for TEM and SEM, and in some ways more similar to a conventional light microscope. To achieve the low interaction energies, the electrons in the microscope are, just like photons in a (conventional) light microscope, reflected off the sample surface. This reflection is enabled by an electric field which decelerates the electrons before the sample and reaccelerates them after reflection. Another aspect where LEEM is similar to a light microscope, is that the sample is illuminated by a broad beam (although of electrons instead of photons). Thus the image is created in one go, instead of built up pixel by pixel by scanning a beam as is done in SEM (and high resolution scanning TEM).

In this chapter, a brief introduction of the various principles of LEEM imaging used in this thesis is given. For the sake of brevity it does not cover all possibilities and details, but more elaborate explanations are available elsewhere [22–24].

The LEEM used in this work is the ESCHER LEEM at Leiden University. It is a SPECS P90 based system based on the aberration correcting design by R.M. Tromp [25–27].

2.2 IMAGING

To obtain a LEEM image in the ESCHER LEEM, electrons are first emitted from a cold field-emission gun, the electron source (at the top of Figure 2.1). To be able to form this beam and steer the electrons they are accelerated to a kinetic energy of 15 keV, as low energy electrons are too sensitive to changing stray fields (both electric and magnetic).

[1] However, LEEM can use energies so small that the electron wavelength is larger than atomic structures. The cross-over lies around 30 eV

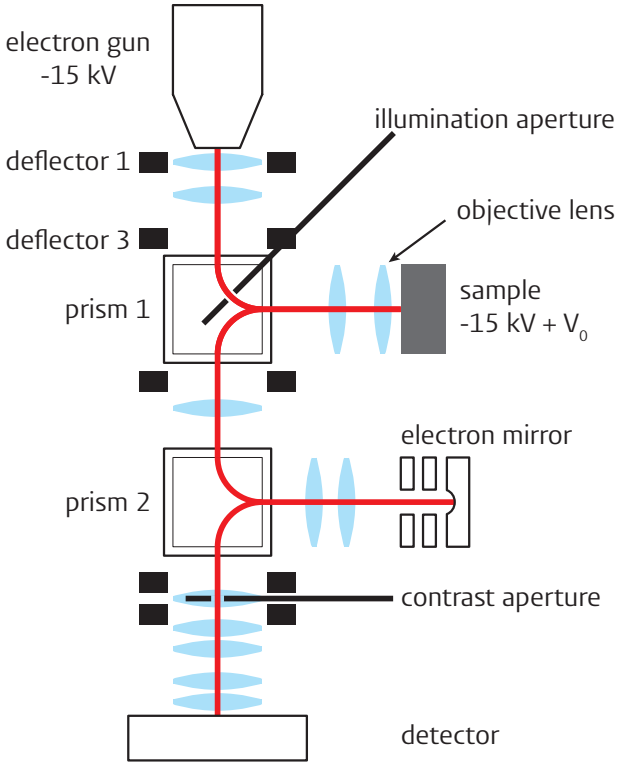

Figure 2.1: *Diagram of an aberration correcting LEEM as used throughout this work: the SPECS P90 based ESCHER LEEM at Leiden University with 90° deflecting prisms and an electron mirror for aberration correction. The path of the electron beam is indicated in red, the electron lenses in light blue and the most relevant deflectors with black rectangles.*

The electrons are shaped into a consistent beam using deflectors 1 and 3 and a pair of electron lenses[2].

To separate the incoming and reflected beams, the electrons, depicted in red, first go through a prism: a perpendicular magnetic field that bends the path of the electrons towards the sample due to the Lorentz force. The sample is mounted on a sample stage and is elevated to an electric potential of $-15\,\mathrm{kV} + V_0$. In this way, the electric field between the objective lens (which is at ground potential, just like the rest of the microscope) and the sample decelerates the electrons to a kinetic *landing energy* $E_0 := eV_0 + (\Phi_g - \Phi_s)$ before interacting with the sample. Here, $(\Phi_g - \Phi_s)$ is the difference in work function between the electron gun and the sample, such that the electrons interact with the sample itself for $E_0 > 0$. The landing energy E_0 can be changed by simply changing the potential offset V_0, i.e. the voltage applied to the sample.

The electrons form an illuminated area on the sample with a diameter of several micrometres. To align the sample with respect to the incoming electron beam and to access a larger area of the sample, it is mounted on a five axis movable sample stage that is moved using micro-actuators [28]. After interacting with the sample, the same electric field between sample and objective lens reaccelerates the electrons towards the prism.

[2] More deflectors are present in the LEEM (including deflector 2), but are not detailed here where they are not relevant to the working principles

Just like in a light microscope, the reflected (electron) waves now contain information about the sample in two complementary ways: in each *image plane* the intensity at a position corresponds to the reflectivity of the sample at the corresponding position and electrons emitted at all angles from this position are collected at the same position. Inversely, in each *diffraction plane* (or back-focal plane), the intensity at a position corresponds to the average reflectivity of the sample at a corresponding **angle**, with all electrons emitted under this angle at all illuminated positions of the sample collected at the same point. The coordinates in the diffraction plane are the in-plane momenta of the electrons as they leave the sample. Thus, the different diffracted beams are (spatially) separated as spots in diffraction planes (As visible in Figure 2.2**a**). As the electrons propagate through the microscope and get focused and refocused by the lenses, the beam alternately passes through several image and diffraction planes. It is worth noting that the image plane and diffraction plane exhibit *duality* properties in the full mathematical sense: applying the transformation from image to diffraction plane, (which corresponds to a Fourier transform) twice yields an image plane again (and vice versa) [3]. However, this (Fourier) transformation mixes intensity and phase information of a real space plane to both phase and intensity in a diffraction plane (and vice versa), while only intensities can be measured.

The aim of the rest of the microscope is to capture the relevant parts of this information using a detector. The prism directs the returning electrons down into the imaging column. In principle these electrons can now directly be used to create an image of either the image plane or the diffraction plane using an imaging electron detector. However, the resolution would be limited by the aberrations of the objective lens: it is impossible to design an aberration-free electron lens. Fortunately, it is possible to create an *electron mirror* with aberrations that can be tuned to cancel the worst, i.e. the leading orders, aberrations introduced by the objective lens. Therefore the electrons go through a second, identical prism (prism 2 in Figure 2.1) that directs them to the electron mirror. The mirror consists of three annular focusing electrodes (dioptric elements) and a solid spherical concave electrode (catoptric element) that controls the shape of the reflecting equipotential. This catadioptric mirror acts as a 1:1 transfer lens for both image and diffraction planes, with the incident and reflected images coinciding in the object plane, and the diffraction pattern located at the symmetry (i.e. reflection) plane. By tuning the relative potentials of the mirror electrodes, the aberrations of the mirror are set to cancel the aberration of the objective lens up to third order spherical aberration and second-rank chromatic aberration [24].

The reflected, and now aberration-corrected, electrons are once again deflected by prism 2 towards the projector. The projector consists of a set of deflectors and five lenses that create a magnified image on a pixelated detector generating a digital image.

The detector can switch easily between imaging the image plane and the diffraction plane, as the strength of the electron optical lenses in the projector (as for any electron-optical lens) can be changed quickly by changing the currents that determine the electromagnetic fields that form the lens. Imaging the diffraction plane is refered to as **Low-Energy Electron Diffraction** mode (LEED, or even VLEED, where V stands for 'Very', as the energies can be lower than in simpler, dedicated LEED instruments).

[3] See e.g. Ref. [22] for a nice visualization.

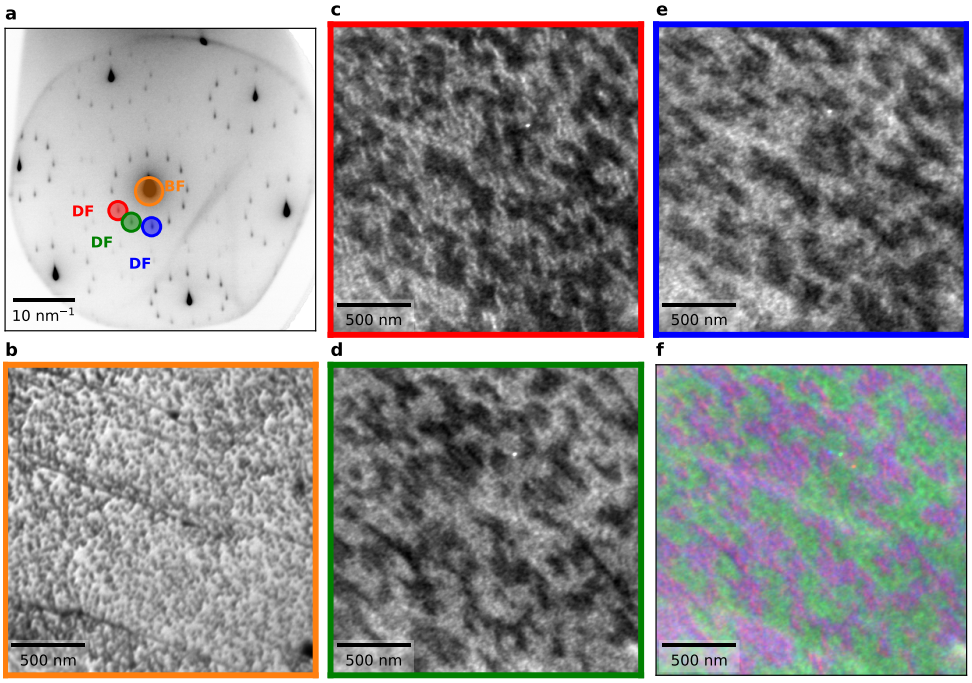

Figure 2.2: ***a,*** *Diffraction pattern of TaS_2, which has a twinned $\left(\sqrt{13}\times\sqrt{13}\right)R13.9°$ CDW reconstruction visible as extra spots (Explored in detail in Chapter 8). Aperture positions for Bright Field imaging and Dark Field imaging on 3 CDW spots are indicated with circles.* ***b,*** *Using a contrast aperture around the specular reflection spot yields a BF-LEEM image.* ***c,*** *Using a contrast aperture around any other spot (position indicated in* ***a****) yields a DF-LEEM image highlighting the areas where the (CDW) periodicity corresponding to the spot occurs on the sample.* ***d,e,*** *Using an aperture around different diffraction spots can yield an inequivalent DF-LEEM image.* ***f,*** *The (gray scale) DF-LEEM images in* ***c-e*** *can be combined into the color channels of a color image to create a composite dark field image. In this specific example, red and blue are equivalent, therefore the contrast in this case is mainly purple versus green.*

The aberration correction significantly increases the best achievable resolution in LEEM mode to a line resolution of lower than 6 nm (achieved on 2-on-2 Twisted bilayer graphene, see Figure 6.2), i.e. parallel lines with a spacing of less than 6 nm can be resolved. In terms of an often used 20%/80% criterion this corresponds to a resolution of about 1.2 nm. Despite this resolution improvement, the resolution is still not sufficient to directly image individual atoms using LEEM mode. In the next section, we explain how we instead rely on various imaging modes using LEEM and LEED modes in conjunction to extract information about the atomic lattice.

2.3 IMAGING MODES

To aid extracting specific information from the electron wavefront, several different imaging modes can be used, by restricting the electron beam with apertures that are mounted

at image planes and diffraction planes at several places in the microscope. The most important aperture is the *contrast aperture*, located in a diffraction plane in the projector, as indicated in Figure 2.1. Its name is derived from the fact that it fits in a diffraction plane and therefore can be used to select electrons leaving the sample within a specific range of angles to increase image contrast by blocking out all other electrons. This in particular includes non-elastically reflected electrons and secondary electrons, which leave the sample with a lower kinetic energy and are therefore deflected more strongly by the prisms.

If the contrast aperture is used to select the specularly (i.e. zeroth-order diffraction) reflected electrons, the resulting real space image is a **Bright Field** (BF-LEEM, Figure 2.2**b**) image. If the contrast aperture is used to select a diffracted beam, it is a **Dark Field** (DF-LEEM, Figure 2.2**c-e**) image. Such a Dark Field image has intensity only in positions on the sample that emit electrons under the specific angles selected by the position of the contrast aperture, e.g. positions on the sample that exhibit a periodicity of atoms that will emit a diffracted beam under that angle.

The second aperture relevant to this thesis is the *illumination aperture*. It slides into an image plane in the top half of prism 1, indicated in Figure 2.1. As the name suggests, it restricts the extent of the electron beam going towards the sample, limiting the area of the sample which is illuminated with electrons down to an area of a few hundred nanometre across. This enables **μLEED**, where a diffraction pattern can be obtained of a specific area of the sample. As the same area can be imaged in LEEM mode and this illuminated area is much smaller, this enables more detailed study of diffraction patterns than in a traditional LEED setup.

2.4 LEEM AND LEED SPECTROSCOPY

Both real space images and diffraction images can be obtained as a function of E_0 to obtain spectroscopic information. These spectroscopic datasets are traditionally labeled LEEM-I(V) and LEED-I(V) respectively, as the **I**ntensity is measured as a function of $\mathbf{V}_0$. (Not to be confused with a Current–Voltage measurement in transport physics!) However, for properly calibrated datasets (See Chapter 3), this is a bit of a misnomer, as the electron reflectivity as a function of E_0 is measured. In this thesis, such measurements are therefore referred to as spectroscopic LEEM and spectroscopic LEED data.

For spectroscopic LEEM data, consisting of real space images, spectra from different areas of the sample can be obtained by measuring the average intensity of such an area for each obtained image. For diffraction patterns, equivalently, spectra of intensity as a function of E_0 for different diffracted beams can be measured. Note again the duality between diffraction and real space: in BF/DF-LEEM spectroscopy the diffraction spot selection is done using the contrast aperture during the measurement and the sample area is selected during data analysis, while in μLEED spectroscopy the area is selected using the illumination aperture and the diffraction spot is selected during data analysis.

The addition of spectral information to images greatly enhances which information can be extracted from the sample [24, 29]. The energy dependent reflectivity is very sensitive to the atomic structure of the sample surface, enabling finger printing of different surface structures to distinguish them. By comparing measured spectra to calculations of the low energy electron reflectivity for different atomic structures, identification of

precise atomic structures is possible. Note that the inverse, *directly* deducing or calculating the atomic structure from LEED spectra is impossible, so to extract a precise atomic structure, the positions of the atoms have to be iteratively refined, calculating reflectivity from every configuration until an optimum is achieved.

The computational techniques were originally developed for traditional LEED, which uses slightly higher landing energies. They were therefore optimized by using a simplified model, making such calculations inaccurate for $E_0 \lesssim 80$ eV. Increasingly, it has become possible to calculate low energy electron reflectivity even for the very low energies occuring in LEEM by using ab-initio scattering calculations, essentially solving the full electron wave propagation problem, but computationally more expensive. Relevant for this thesis, it was for example shown that it is possible to count the number of Van der waals layers on a substrate [30, 31]. In this thesis, we will extend upon the possibilities to extract the relative positions of atoms in the Van der Waals layers by comparing to ab-initio calculations performed by Eugene Krasovskii.

2.4.1 FURTHER NOTES ON EXPERIMENTS

Both spectroscopic measurement methods, LEEM and (V)LEED, can obtain a spectrum of a specific diffraction spot as a function of energy. In practice, whether a dataset comparing different areas on the sample or a dataset with multiple diffraction spots of the same area is needed determines whether a dataset is measured in LEEM or in LEED mode. It is however worth noting that the obtained spectra are not fully equivalent. The selection of an area in an image or diffraction pattern during data analysis can be more precise, as it is not restricted by the physical size of apertures. A further subtle difference is that if the intensity is low compared to other areas or diffracted beams on the detector, the measured contrast can be limited by the dynamic range of the detector, even in high dynamic range imaging mode as detailed in Chapter 3.

All LEEM images and spectroscopic LEEM data in this thesis use a contrast aperture and are therefore either BF-LEEM or DF-LEEM data.

Beyond varying E_0, other parameters can be varied as well, for example the sample position in a μLEED measurement for so-called *scanning* μLEED [32, 33], or the in-plane momentum for Angular Resolved Reflective Electron Spectroscopy [34]. These combined techniques play however no significant role in this thesis.

The next chapter will focus on extracting spectra from the raw data, the necessary steps before we can use such data for material science.

REFERENCES

22. J. Kautz. *Low-energy electron microscopy on two-dimensional systems : growth, potentiometry and band structure mapping* PhD thesis (Leiden University, 2015). https://hdl.handle.net/1887/32852.

23. T. A. de Jong. *Stacking domains in bilayer Van der Waals materials* MSc thesis (Leiden University, 2017). https://hdl.handle.net/1887/52790.

24. R. Tromp. In *Springer Handbook of Microscopy* (eds P. W. Hawkes & J. C. H. Spence) 565–604 (Springer International Publishing, Cham, 2019). doi:10.1007/978-3-030-00069-1_11.

25. R. Tromp, J. Hannon, A. Ellis, et al. A new aberration-corrected, energy-filtered LEEM/PEEM instrument. I. Principles and design. *Ultramicroscopy* **110,** 852–861. doi:10.1016/j.ultramic.2010.03.005 (2010).

26. S. Schramm, J. Kautz, A. Berghaus, et al. Low-energy electron microscopy and spectroscopy with ESCHER: Status and prospects. *IBM Journal of Research and Development* **55,** 1–1. doi:10.1147/JRD.2011.2150691 (2011).

27. R. M. Tromp, J. B. Hannon, W. Wan, A. Berghaus & O. Schaff. A new aberration-corrected, energy-filtered LEEM/PEEM instrument II. Operation and results. *Ultramicroscopy* **127,** 25–39. doi:10.1016/j.ultramic.2012.07.016 (2013).

28. A. W. Ellis & R. M. Tromp. A versatile ultra high vacuum sample stage with six degrees of freedom. *Review of Scientific Instruments* **84,** 075112. doi:10.1063/1.4813739 (2013).

29. J. I. Flege & E. E. Krasovskii. Intensity-voltage low-energy electron microscopy for functional materials characterization. *Physica Status Solidi - Rapid Research Letters* **8,** 463–477. doi:10.1002/pssr.201409102 (2014).

30. H. Hibino, H. Kageshima, F. Maeda, et al. Microscopic thickness determination of thin graphite films formed on SiC from quantized oscillation in reflectivity of low-energy electrons. *Physical Review B* **77,** 075413. doi:10.1103/PhysRevB.77.075413 (2008).

31. T. A. de Jong, J. Jobst, H. Yoo, et al. Measuring the Local Twist Angle and Layer Arrangement in Van der Waals Heterostructures. *physica status solidi (b)* **255,** 1800191. doi:10.1002/pssb.201800191 (2018).

32. K. L. W. Lau, K. M. Yu, D. Luo, R. S. Ruoff & M. S. Altman. High throughput scanning μLEED imaging of surface structural heterogeneity: Defective graphene on Cu(111). *Ultramicroscopy* **200,** 67–72. doi:10.1016/j.ultramic.2019.02.015 (2019).

33. V. A. E. C. Janssen. *Electronic Properties of (Pseudo-) Two-Dimensional Materials* PhD thesis (2020). doi:10.4233/UUID:0C9F992C-7390-4D8F-AA6D-D89F0E7866A0.

34. J. Jobst, A. J. H. van der Torren, E. E. Krasovskii, et al. Quantifying electronic band interactions in van der Waals materials using angle-resolved reflected-electron spectroscopy. *Nature Communications* **7,** 13621. doi:10.1038/ncomms13621 (2016).

3

QUANTITATIVE ANALYSIS OF SPECTROSCOPIC LEEM DATA

By aiming for better microscopy pictures,
new science will typically follow.

For many complex materials systems, low-energy electron microscopy (LEEM) offers detailed insights into morphology and crystallography by naturally combining real-space and reciprocal-space information. Its unique strength, however, is that all measurements can easily be performed energy-dependently. Consequently, one should treat LEEM measurements as multi-dimensional, spectroscopic datasets rather than as images to fully harvest this potential. Here we describe a measurement and data analysis approach to obtain such quantitative spectroscopic LEEM datasets with high lateral resolution. The employed detector correction and adjustment techniques enable measurement of true reflectivity values over four orders of magnitudes of intensity. Moreover, we show a drift correction algorithm, tailored for LEEM datasets with inverting contrast, that yields sub-pixel accuracy without special computational demands. Finally, we apply dimension reduction techniques to summarize the key spectroscopic features of datasets with hundreds of images into two single images that can easily be presented and interpreted intuitively. We use cluster analysis to automatically identify different materials within the field of view and to calculate average spectra per material. We demonstrate these methods by analyzing bright-field and dark-field datasets of few-layer graphene grown on silicon carbide and provide a high-performance Python implementation.

Parts of this chapter have been published as T. A. de Jong, D. N. L. Kok, A. J. H. van der Torren, H. Schopmans, R. M. Tromp, S. J. Van der Molen and J. Jobst, Ultramicroscopy **213** 112913 (2020) [35].

3.1 INTRODUCTION

In this Chapter, we describe the methodology developed to optimize the extraction of information out of LEEM data. LEEM has proven to be a versatile tool, due to its damage-free, real-time imaging capabilities and its combination of electron diffraction with spectroscopic, and real-space information. This enables more advanced LEEM-based techniques such as dark-field imaging, where electrons from a single diffracted beam are used to create a real-space image, revealing spatial information on the atomic lattice of the sample [36, 37].

Aside from usage as an imaging tool, LEEM is frequently used as a tool for quantitative analysis of physical properties of a wide range of materials. Multi-dimensional datasets can be created by recording LEEM images as a function of one or more parameters such as interaction energy E_0, angle of incidence, or temperature [29, 38]. Using this, a wide range of properties can be studied, for example, layer interaction, electron bands [34], layer stacking [37], catalysis [39], plasmons [40], and surface corrugation [41].

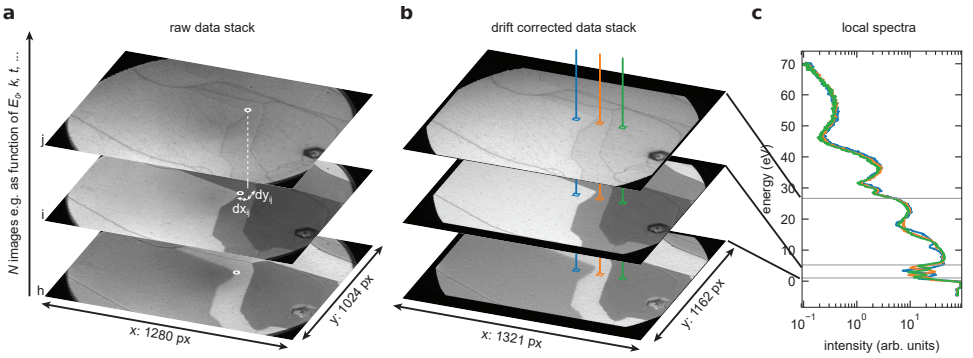

Figure 3.1: ***a,*** *A stack of raw LEEM images where images are shifted with respect to each other due to experimental drift.* ***b,*** *Drift correction aligns features in the detector-corrected images to compensate for this drift.* ***c,*** *Spectra corresponding to pixels indicated in (b).*

However, to unlock the true potential of quantitative analysis of multi-dimensional LEEM data, post-processing of images and combination with meta-data is needed. In particular, it is necessary to correct for detector artifacts and image drift and to convert image intensity to physical quantities.

To this end, we here present a modular data acquisition and analysis pipeline for multi-dimensional LEEM data, combining techniques well established in other fields such as general astronomy or transmission electron microscopy (TEM), that yields high resolution spectroscopic datasets and visualizations thereof. In particular, starting with the raw data (shown in Figure 3.1**a**), we correct for detector artifacts using flat field and dark current correction. Combining these corrections on the images with active feedback on detector gain enables High Dynamic Range (HDR) spectroscopy, which makes it possible to measure spectra over four orders of magnitude of intensity. Subsequently, we demonstrate that compensation of detector artifacts also enables drift correction with sub-pixel accurate image registration, yielding a fully corrected data stack (Figure 3.1**b**).

This creates a true pixel-by-pixel spectroscopic dataset, as shown in Figure 3.1**c**, i.e. every pixel contains a reflectivity spectrum of the corresponding position on the sample. Finally, we explore the potential for more advanced computational data analysis. We show that by using relatively simple dimension reduction techniques and clustering, these datasets can be intuitively analyzed and visualized, enabling semi-automatic identification of areas with different spectra. The implementation of the methodology presented here, is programmed in Python and published as open source at Ref. [42].

To demonstrate these features and quantify the accuracy, we apply the drift correction algorithm to artificial data and then apply the full pipeline to a real dataset.The sample of the dataset is few-layer graphene grown by thermal decomposition of silicon carbide (SiC) [43], followed by hydrogen intercalation to decouple the graphene from the SiC substrate [44, 45]. [1] Bright Field LEEM spectra can be used to distinguish the resulting mixture of bilayer, trilayer and thicker graphene, as interlayer states cause distinct minima in the reflectivity spectra [30, 46]. In addition, the growth process causes strain-induced stacking domains, which can be distinguished using Dark Field LEEM spectra [37, 47]. The sample dataset consists of bright-field and dark-field LEEM images of the same area for a range of landing energies (sometimes referred to as LEEM-I(V)). The dark-field dataset uses a first order diffraction spot and tilted illumination such that the incident beam has the opposite angle to the normal as the diffracted beam, as described in more detail in Chapter 4. The data is available as open data [48] and is interpreted and investigated in detail in Chapter 4.

3.2 DETECTOR CORRECTION

No physical detector system is perfect, i.e. each detector system introduces systematic errors and noise. Knowledge of the sources of these imperfections enables the correction of most of them. The ESCHER LEEM has the classical detector layout: A chevron microchannel plate array (MCP, manufactured by Hamamatsu) for electron multiplication, a phosphor screen to convert electrons to photons and a CCD camera (a PCO sensicam SVGA) to record images of the phosphor screen.

The CCD introduces artifacts in the form of added dark counts and a non-uniform gain [49–52]. Furthermore, the MCP gain is also spatially non-uniform, for example due to overexposure damaging of the MCP, resulting in locally reduced gain. Therefore we describe the measured intensity I_{CCD} on the CCD as the following combination of the previously named detector artifacts and the 'true' signal I_{in}:

$$I_{\mathrm{CCD}}(x,y) = DC(x,y) + I_{\mathrm{in}}(x,y) \cdot G(x,y) \tag{3.1}$$

Where $DC(x,y)$ is the intensity caused by dark current and $G(x,y)$ is the position-dependent and as-of-yet unknown gain factor comprising *all* modifications to the gain due to the complete detector system comprised of the MCP, phosphor screen and CCD camera together.

To compensate for these detector artifacts, we employ techniques well-established in astronomy (and other fields using CCD cameras) to effectively invert the relation in

[1] We thank Christian Ott and Heiko Weber for the fabrication of the graphene on SiC samples

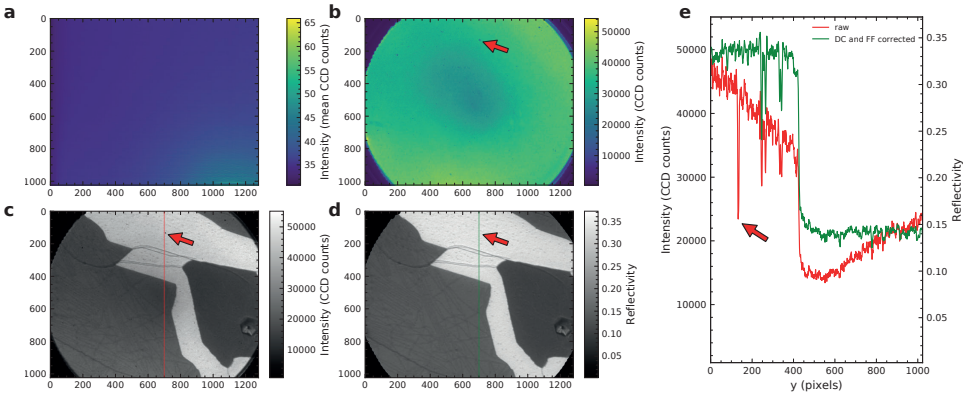

Figure 3.2: a, *Dark Count image taken on ESCHER averaged over* 19×16 *images with* 250 ms *exposure time.* ***b,*** *Flat field image with visible edges of the round microchannel plate and damaged areas (arrow).* ***c,*** *Uncorrected bright-field LEEM image from the sample dataset. The field of view corresponds to* 3.5 µm. ***d,*** *Dark count and flat field corrected version of the image in (c).* ***e,*** *Line cut through the raw image (c) and the corrected image (d) shown in red and green, respectively. Note that the dip due to MCP damage at* $y = 140$ *(arrow) is removed and the profiles for similar areas are flattened.*

Eq. (3.1), to extract $I_{\text{in}}(x, y)$ without the deleterious effects of background dark counts $DC(x, y)$ and local gain variations $G(x, y)$.

First, the dark current of the CCD is compensated by pixel-wise subtracting a non-illuminated *dark count* image, i.e. an image with the same exposure time as used for the measurement, but no electron illumination at all. A pixel-wise average of a set of such dark count images is shown in Figure 3.2**a**. The dark current arises from thermal excitations in the sensor and varies over time with an approximately Gaussian distribution. The mean of this distribution is dependent on the pixel, i.e. the x, y location, for example visible in Figure 3.2**a** as a slight increase in the lower right corner. To suppress the thermal fluctuations in the template dark current image, it is desirable to average over several dark count images to prevent the introduction of systematic errors. We assume that the per-pixel dark currents are identically distributed with a variance $\text{Var}_{\text{therm}}$ except for a spatial variance $\text{Var}_{\text{spatial}}$ of the mean. This is mathematically equivalent to assuming the dark current fluctuates around its mean with both spatially dependent (but fixed in time) noise and time-dependent thermal noise. By averaging multiple dark images, we reduce the thermal variance but not the spatial variance. The remaining variance is given by:

$$\begin{aligned}\text{Var}_{\text{tot}}(n) &= \text{Var}_{\text{therm}}(n) + \text{Var}_{\text{spatial}} \\ &= \frac{1}{n}\text{Var}_{\text{therm}}(1) + \text{Var}_{\text{spatial}}\end{aligned}$$

Where $\text{Var}(n)$ is used to denote the variance of n pixel-wise averaged images. By determining $\text{Var}_{\text{tot}}(n)$ and $\text{Var}_{\text{tot}}(1)$ experimentally we can isolate the thermal noise on a

single image:

$$\mathrm{Var}_{\mathrm{therm}}(1) = \left[\mathrm{Var}_{\mathrm{tot}}(1) - \mathrm{Var}_{\mathrm{tot}}(n)\right] \cdot \frac{n}{n-1} \tag{3.2}$$

For the ESCHER system with its Peltier-cooled camera, we find:

$$\mathrm{Var}_{\mathrm{therm}}(16 \times 250\,\mathrm{ms\ image}) = 114.3.$$

Therefore, by taking $n = 120$, a set of 120×16 images (a total exposure time of 8 minutes) is sufficient to suppress the systematic errors to values smaller than the discretization error. We find that the dark count image does not significantly change over time, and therefore remeasuring dark count images is seldomly needed.

Second, to compensate for spatial gain variations, which are mostly due to the MCP, a (conventional) *flat field* correction is performed, dividing the full dark count-corrected dataset by an evenly illuminated image [53]. In LEEM, when the potential of the sample corresponds to a higher potential electron energy than the kinetic energy of the electrons of the beam, all incoming electrons turn around before they reach the sample. In this situation the electron landing energy is negative and the sample behaves as a mirror. Imaging at a landing energy of $E_0 \approx -20\,\mathrm{eV}$ yields an almost perfect flat field image as approximation of $G(x, y)$ in Eq. (3.1). A relatively large value for the negative energy is taken to prevent artifacts from local in-plane electric field components, e.g. due to work function or height differences in the sample [54–56]. For the ESCHER system, it is necessary to take flat field images within hours of the measurement, as the MCP wears over time and the gun emission profile and system alignment change on relatively short timescales [57]. Furthermore, taking a flat field image at the same precise alignment as the measurement is preferred for two reasons. First, barring absolutely perfect alignment of the system as well as a perfectly uniform emission from the electron gun, the beam intensity is not spatially uniform. As illumination inhomogeneities are dependent on the precise settings of the lenses, these will also be compensated for if the flat field is recorded in the exact same configuration. Second, for proper normalization of the data, as explained in Section 3.3, the same magnification (projector settings) is needed.

An alternative to this mirror mode flat fielding is to average over a sufficiently large set of images of different positions on the sample and use the resulting average as a flat field image. In most cases however, mirror mode flat fielding is preferred over such ensemble-average flat fielding since for the latter many images of different locations are required. Even when such a set is already available, it is hard to rule out any systematic (statistical) errors. Lastly ensemble-average cannot provide proper normalization of the data to convert to true reflectivity.

3.3 HIGH DYNAMIC RANGE SPECTROSCOPY

In LEEM and LEED, large variations occur in the amplitude of the signal, both within individual images and from image to image. For example, in quantitative LEED, features of interest are often orders of magnitude less bright than primary Bragg peaks. This necessitates a detector system with a large dynamic range. The CCD-camera of the ESCHER setup has a bit depth of 12 bits and a possibility to accumulate 16 images in hardware, yielding an effective bit depth of 16 bits for singular images.

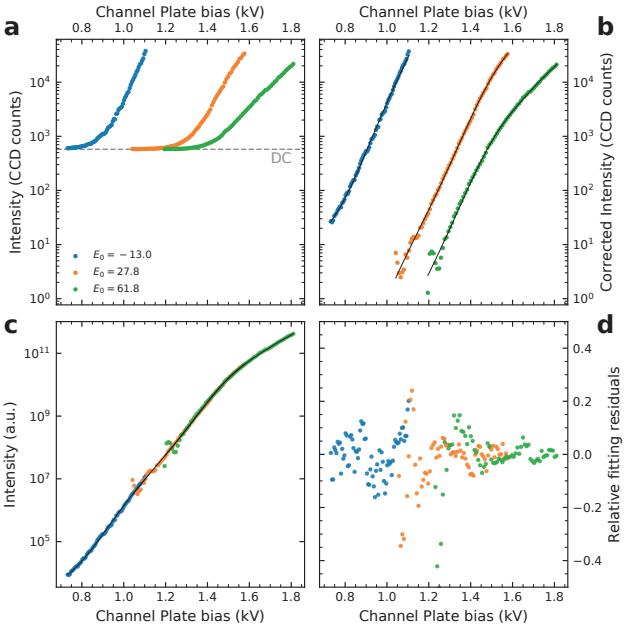

Figure 3.3: a, *Calibration curves as measured with* $16 \times 250\,\mathrm{ms}$ *exposure time per image measured on graphene on SiC.* ***b,*** *Calibration curves corrected for dark count.* ***c,*** *Calibration curves with matched intensity and normalized by joint curve fit of Eq. (3.3) and resulting best fit (black line).* ***d,*** *Residuals of the joint fit in (c).*

For most materials, the reflected intensity $I(E_0)$ changes over orders of magnitude as a function of E_0. Starting in mirror mode with unity reflectivity, the reflected intensity tends to decrease orders of magnitude for $E_0 \lesssim 100\,\mathrm{eV}$. To obtain spectra with such a large dynamic range, the dynamic range offered by the bit depth of the CCD alone is not sufficient.

However, the gain G of the MCP, i.e. the ratio of outgoing electrons to incoming electrons, can be tuned by the voltage V_{MCP} applied over the MCP. This gain scales approximately exponential in V_{MCP} (over a reasonable range, see next section), enabling image formation of approximately constant intensity on the CCD, for a wide range of incident electron intensities. We use this property to develop a scheme to further increase the dynamic range in which $G(V_{\mathrm{MCP}})$ is adjusted by setting a new MCP bias for each new image, i.e. increasing the gain for images where the reflected intensity is low. Measuring V_{MCP} for each recorded image and calibrating $G(V_{\mathrm{MCP}})$ makes it possible to employ the full dynamic range of the CCD-camera for all landing energies, without losing the information of the absolute magnitude of the measured intensities, thus extending the range of spectroscopy without significant decrease in signal-to-noise ratio.

3.3.1 CALIBRATION

Hamamatsu Photonics K.K., the manufacturer of the microchannel plate in the ESCHER setup, specifies an exponential gain as function of voltage for a part of the range of possible biases [58]. To extend the useful range beyond this limit and thus enable the use of the full bias range up to the maximal 1800 V, the gain versus bias curve was calibrated as follows:

1. First, in mirror mode, V_{MCP} is adjusted such that the maximum intensity in the image corresponds to the full intensity on the CCD, staying just below intensities damaging the MCP.

2. While decreasing V_{MCP}, images are acquired for evenly spaced bias values. The intensities of these images form the dataset for calibration of the low bias part.

3. Returning V_{MCP} to the previous maximum value, E_0 is increased until the intensity of the image is so low that it is barely distinguishable from the dark count.

4. Again V_{MCP} is turned up until the maximum image intensity corresponds to the maximum CCD intensity.

5. Steps 2. to 4. are repeated until a dataset is acquired starting at maximum MCP bias V_{MCP}. The resulting average intensity curves are shown in Figure 3.3**a**.

6. These datasets are then corrected for dark count as discussed above, resulting in the average intensity curves shown in Figure 3.3**b**. Comparing to the uncorrected curves, the increase in accuracy for low intensity values, crucial for accurate calibration, is very apparent. Averaging over a sufficiently large area ensures sufficient reduction of other noise sources such as MCP noise.

7. A joint fit of Eq. (3.3), allowing for a different amplitude A_i for each curve, is performed to the corrected data to obtain a general expression for MCP gain G as a function of V_{MCP}. The fit is performed using least squares on the logarithm of the original data with no additional weights, to ensure a good fit over the large range of orders of magnitude. The fitted curve is then normalized to a convenient value, e.g. $G(1\,\mathrm{kV}) = 1$. This normalization can be freely chosen, as G will be applied equally to datasets and flat field images, yielding absolute reflectivity as resulting data.

A first choice for a fitting function would be a simple exponential, but this would not account for any deviation from perfect exponential gain, visible as deviations from a straight line in Figure 3.3**b**. For the ESCHER setup we therefore choose to add correction terms of odd power in the exponent:

$$G(V_{\mathrm{MCP}}) = A_i \exp\left(\sum_{k=0}^{8} c_k {V_{\mathrm{MCP}}}^{2k+1}\right) \tag{3.3}$$

Only odd powers were used to accurately capture the visible trends in the data. For the ESCHER setup correction terms up to order V_{MCP}^{17} ($k < 9$) turned out to give a satisfactory good approximation, as illustrated by the residuals in Figure 3.3**d**.

3.3.2 ACTIVE PER-IMAGE OPTIMIZATION OF MCP BIAS

The resulting curve with calibration coefficients is then used to actively tune the MCP bias during spectroscopic measurements: A desired range is defined for the maximum intensity on the camera, corresponding to a maximum safe electron intensity on the MCP to prevent damage on the one hand, and a minimum desired intensity of the image on the CCD on the other hand. Whenever the maximum intensity of an image falls

outside this range, the MCP gain $G(V_{\mathrm{MCP}})$ will be adjusted such that the intensity of the next image again falls in the center of this range. Assuming the intensity changes continuously, this method ensures the use of the full intensity range of the camera for each image, while protecting the MCP against damage.

Additionally, after the measurements, the calibration curve is used to calculate the real, relative intensity from the image intensity and the recorded V_{MCP}. By dividing this intensity by the intensity of the flat field image (taken in mirror mode and corrected for dark current and the MCP bias), we calculate a (floating point) conversion factor to true *reflectivity* values for each image. These ratios are added to the metadata of every image. By applying this conversion as a final step after any analysis of the data, errors due to discretization of highly amplified, and therefore low true intensity, images are minimized. Note that this procedure makes the conversion to true reflectivity possible even for datasets with no mirror mode in the dataset itself, such as dark field measurements.

3.3.3 COMPARISON OF RESULTS

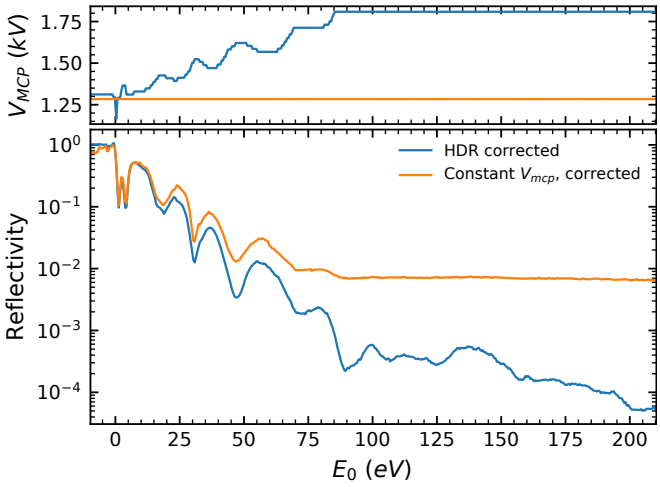

Figure 3.4: *Regular spectroscopic reflectivity curve (orange) of bilayer graphene on SiC, corrected for dark count and flat field, but with a single setting of V_{MCP} (top panel). The HDR measurement of the same area with active MCP bias tuning (blue) can resolve details down to lower intensity.*

Spectroscopic LEEM-I(V) curves on bilayer graphene on silicon carbide are measured both with constant MCP bias and with adaptive MCP bias as described above. A comparison between the resulting curves is shown in Figure 3.4. While the regular, constant MCP, curve starts to lose detail around $E_0 = 50\,\mathrm{eV}$, i.e. after a factor of 100 decrease in signal, the adaptive measurement captures intensity variations in the spectrum almost 4 orders of magnitude lower than the initial intensity. We thus call the adaptive method high dynamic range (HDR) imaging.

3.4 DRIFT CORRECTION BY IMAGE REGISTRATION

In LEEM imaging, the position of the image on the detector tends to shift during measurement as shown in Figure 3.1**a**. This prevents per-location interpretation of the data, both for spectroscopic measurements and measurements with varying temperature. Al-

though the shift can be minimized by precise alignment of the system, we find that a significant shift always remains, especially in tilted illumination experiments such as DF-LEEM or angle-resolved reflected-electron spectroscopy (ARRES) [37, 38, 56], which makes the compensation of this image drift necessary.

This problem has been studied in depth in the field of image registration, motivated by wide-ranging applications such as stabilization of conventional video, combination of satellite imagery and medical imaging [59–61]. Techniques generally rely on defining a measure of similarity between a template and other images, either by some form of cross correlation, or by identifying specific matching features in both. The image is then deformed by a fixed set of transformations (either affine, i.e. purely shifts and rotations or non-rigid, i.e. additional deformation), until the match between the features in the images and the features in the template is maximal. For LEEM data, the measurement drift is almost completely described by in-plane shifts, significantly reducing the space of expected transformations. A common approach in this case is to use the (two-dimensional) cross-correlation as a measure of similarity between two shifted images and to find the maximum for all images compared to a template, as the location of maximum of the cross-correlation corresponds directly to the shift between the image and the used template.

The cross correlation of two $n \times n$ pixels images $I_1(x,y)$ and $I_2(x,y)$ is defined as follows:

$$\mathscr{C}(I_1, I_2)(x,y) = \frac{1}{n^2} \sum_{x'=0}^{n-1} \sum_{y'=0}^{n-1} I_1(x',y') I_2(x+x', y+y') \tag{3.4}$$

where the coordinates can be wrapped around, i.e. all spatial coordinates are modulo n. Furthermore, we can relate this to the convolution operation (denoted as $\circ$):

$$\begin{aligned} \mathscr{C}(I_1, I_2)(x,y) &= \frac{1}{n^2} \sum_{x'=0}^{n-1} \sum_{y'=0}^{n-1} I_1(x',y') I_2(x-(-x'), y-(-y')) \\ &=: \big(I_1(x',y') \circ I_2(-x',-y')\big)(x,y) \end{aligned} \tag{3.5}$$

Using this, the cross correlation can be expressed in terms of (two-dimensional) Fourier transforms $\mathscr{F}$:

$$\mathscr{C}(I_1, I_2) = I_1(x',y') \circ I_2(-x',-y') = \mathscr{F}^{-1}\left(\mathscr{F}(I_1) \cdot \overline{\mathscr{F}(I_2)}\right) \tag{3.6}$$

Where $\overline{\mathscr{F}(I_2)}$ denotes the complex conjugate of the Fourier transform of I_2. This makes the cross-correlation extra suitable as a measure of similarity, since it can be computed efficiently using the two-dimensional Fast Fourier Transform (FFT). Determining the local maximum of the cross-correlation yields the integer shift for which the two input images are most similar, with the height of the maximum an indication of the quality of the match. To further increase accuracy, several variants, such as gradient cross-correlation and phase-shift cross-correlation, have been shown to achieve sub-pixel accuracy for pairs of images [59, 62–64].

For LEEM data however, the straightforward cross-correlation approach is often hindered by the physics underlying the electron spectra, resulting in contrast changes (cf. Figure 3.5**a,b**) and even inversions for different values of E_0. The problem can be slightly

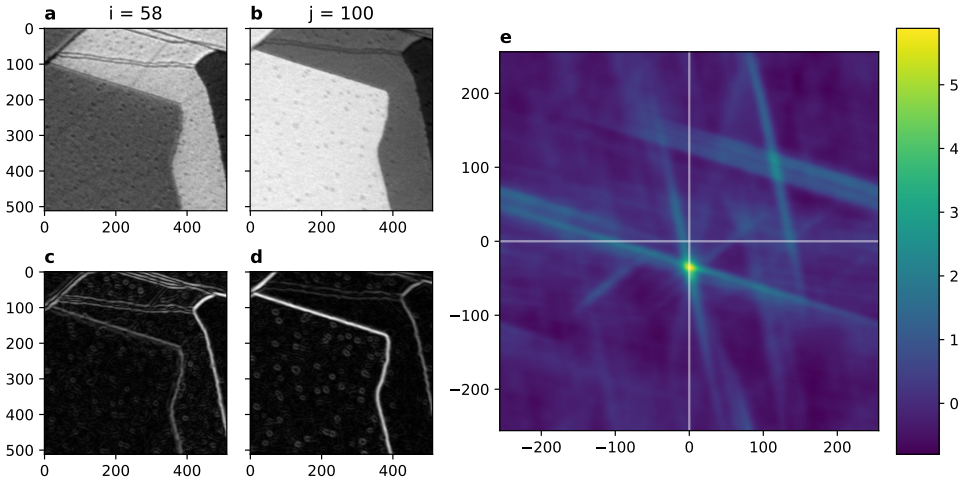

Figure 3.5: a,b, *Two bright-field LEEM images of few-layer graphene obtained at different E_0.* ***c,d,*** *Their Gaussian and Sobel-filtered versions with a Gaussian standard deviation of 3 pixels highlights the edges and erases the contrast inversion.* ***e,*** *The cross-correlation of the filtered images exhibits a clear maximum. Its position compared to zero (white lines) corresponds to the relative shift of the images.*

alleviated by using multiple templates, but in general this approach is unsatisfactory. Instead we present another approach here: We first apply digital filters and then compare each image to all other images, similar to the algorithm by Schaffer et al. for energy filtered transmission electron microscopy [65, 66]. It then uses a statistical average of the found integer shifts between all pairs of images to achieve sub-pixel accuracy.

We analyze the accuracy of this algorithm using an artificial test dataset and show that the accompanying Python implementation [42] is fast enough to process stacks of hundreds of images in mere minutes by performing benchmarks on a real dataset, followed by a discussion of the algorithm and results.

The algorithm consists of the following steps:

1. Select an area of each of the (detector-corrected) N images, suitably sized for FFTs (i.e. preferably $2^n \times 2^n$ pixels).

2. Apply Gaussian smoothing with standard deviation of σ pixels to reduce Poissonian noise in the images.

3. Apply a (magnitude) Sobel filter to highlight edges only, as shown in Figure 3.5**c** and **d**. As such, images with inverted contrast (cf. Figure 3.5**a,b**) become similar to each other.

4. Using Eq. (3.6), compute the cross-correlation, as shown in Figure 3.5**e**. Do this for all pairs (i, j) of images.

5. Compute the location $(DX, DY)_{ij}$ and value W_{ij} of the maximum of the cross-correlation for all image pairs (i, j). DX_{ij} and DY_{ij} form the anti-symmetric matrices of found relative shifts in either direction, while W_{ij} is a symmetric matrix of weights of the found matches, as shown in Figure 3.6.

6. Normalize the maximum values W_{ij} to be used as weights in step 8: $\overline{W}_{ij} = \frac{W_{ij}}{\sqrt{W_{ii} \cdot W_{jj}}}$.

7. Pick a threshold W_{min} to remove any false positive matches between images. A threshold of $W_{\text{min}} = 0.15$, based on DX, DY and W_{ij}, is shown in Figure 3.6 as gray shading. Set $\overline{W}_{ij} = 0$ for all $\overline{W}_{ij} < W_{\text{min}}$.

8. To reduce the N^2 relative shifts DX to a length N vector of horizontal shifts dx, minimize the errors $\left(dx_i - dx_j - DX_{ij}\right)\overline{W}_{ij}^4$ (using least squares). Do the same with DY to obtain the vertical shift vector dy.

9. Apply these found shifts dx and dy to the original detector corrected images, interpolating (either bi-linearly or via Fourier) for non-integer shifts.

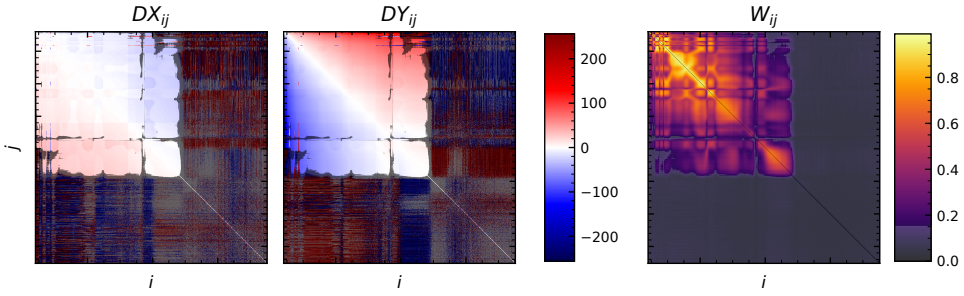

Figure 3.6: *Calculated shift matrices DX and DY and weight matrix $\overline{W}_{ij}$ for the bright-field dataset. Matches of a weight below $W_{\text{min}} = 0.15$ (shaded in gray) are mostly false positives. Consequently, they are set to zero weight in the algorithm.*

3.4.1 IMPLEMENTATION DETAILS

The implementation makes extensive use of `dask` [67, 68]. This open source library, developed and maintained by Anaconda Inc., in particular its `Array` submodule, enables easy parallelization of array operations in common `numpy` syntax. It allows the lazy definition of computational operations on data, forming a task graph describing the computations to be performed. Delaying actual computation until explicitly called for enables `dask` to easily parallelize and stream computations, efficiently using all cores of a single computer. It should even allow to easily scale up to compute clusters.

The implementation uses of `dask` in combination with `scikit-image` code for blocked filtering of images [69].

The complete set of correlations is written in `dask` via the FFT functions and the multiplication in Fourier space. This, via `dask`'s task graph, allows every forward FFT to be

computed only once for each image, as opposed to the N times for the naive implementation.

The optimization step uses `scipy` code, in particular the `least-squares` routine in the `optimization` module in combination with an explicit `scipy.sparse` Jacobian. [69–72]. We found that the use of an explicit Jacobian significantly reduced computation time and memory use for larger optimizations.

For easy interfacing with the user, `jupyter-notebook` and `ipython-widgets` are used [73]. For the dimension reduction using principal component analysis and clustering described in Section 3.5, `dask-ml` and `scikit-learn` are applied [74].

3.4.2 ACCURACY TESTING

To validate and benchmark the accuracy of the drift correction algorithm beyond visual inspection of resulting drift corrected datasets, an artificial test dataset with known shifts was created. This enables exact comparison of results to a 'true' drift.

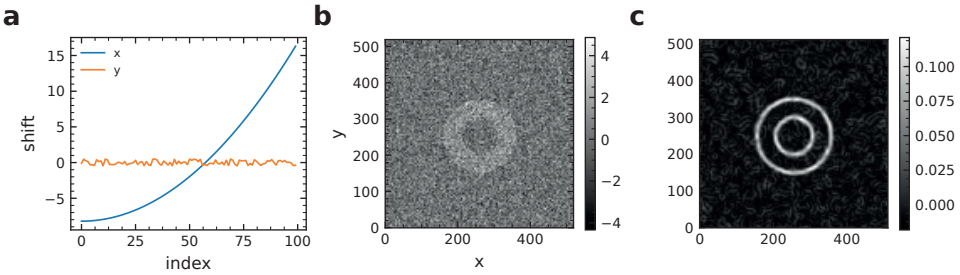

Figure 3.7: a, *Image shifts in x and y used for the synthetic dataset.* ***b,*** *Image 0 of the synthetic dataset with Gaussian noise with standard deviation of $A = 1.0$.* ***c,*** *Gaussian- and Sobel-filtered version of (b), with a Gaussian filter width of 5 pixels, highlighting edges.*

The test dataset, as shown in Fig. 3.7, consists of $N = 100$ copies of an annulus of intensity 1.0 on a background of 0.0. The dataset is shifted over a parabolic shift in the x-direction and random shifts uniformly chosen from the interval $[-0.5, 0.5]$ pixels in the y direction (see Figure 3.7**a**). Finally pixel-wise Gaussian (pseudo-) random noise is added to all images. The standard deviation A of the added random noise is then varied to simulate images with different signal-to-noise ratios (SNR).

BENCHMARK METHODOLOGY

Benchmarks were run on a desktop PC with an Intel `i7-7700K` running at 4.20 GHz with 32 GB of RAM and Windows 10 x64 installed. The full stack of images was read from separate `TIFF` files on a Toshiba XG5 NVMe SSD for each run during the filter and cross correlation phase and written to a uncompressed `zarr` archive on the same SSD during the shift and write phase.

The benchmark was run in a Jupyter notebook, with an installation of the Anaconda environment of Python 3.6 with at least the following packages installed:

```
numpy=1.16.3, matplotlib=3.0.3, dask=1.2.0, distributed=1.27.1,
scikit-image=0.15.0, scipy=1.2.1, jupyterlab, scikit-learn=0.20.3,
dask-ml=0.12.0, xarray=0.12.0, h5py=2.9.0, mkl=2019.3, mkl_fft=1.0.12,
numba=0.43.1, zarr=2.2.0
```

Note: Accuracy benchmarks were performed with images of 512×512 pixels, the time benchmarks in the next session on subimages of 256 × 256 pixels.

RESULTS

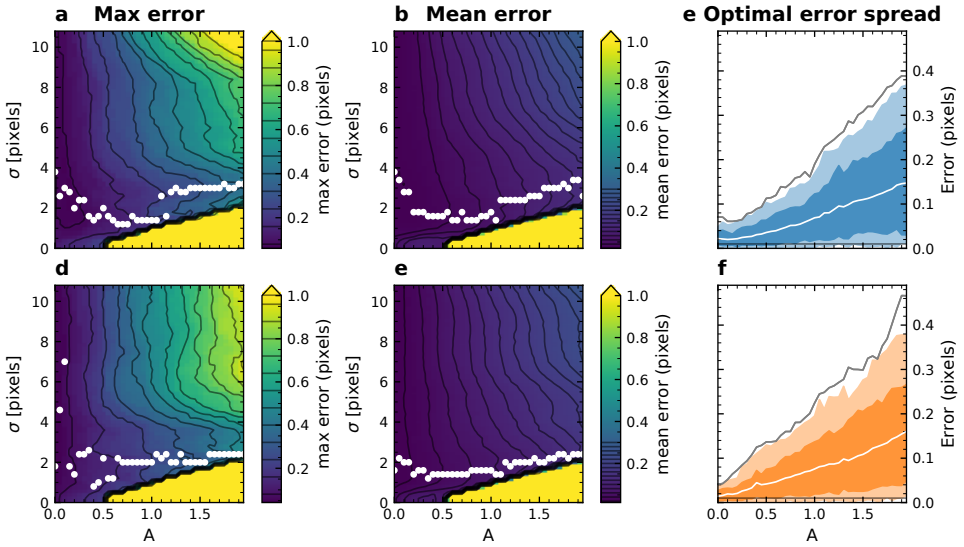

Figure 3.8: ***a,b,*** *Maximum and mean error in dx shift as calculated by the algorithm for different values of noise amplitude A and smoothing parameter σ. The optimal value of the Gaussian smoothing σ as a function of added noise amplitude A is drawn in white. Black contour lines are added as a guide to the eye.* ***c,*** *Spread of the error for the optimal values of σ for varying A. Dark and light bands are respectively 1 and 2 standard deviations, maximum error is indicated as gray line.* ***d,e,f,*** *Same for the y direction.*

The resulting maximum error in the found shift compared to the original, 'true' shift, as well as the resulting mean error for different values of A and σ is shown in Figure 3.8, separately for the x and y directions. These results verify that, at least for synthetic datasets, the algorithm achieves sub-pixel accuracy, with the mean absolute error in pixels of about 0.1 times the relative noise amplitude A for the optimal value of smoothing σ, and the maximum absolute error just reaching 0.5 pixel for the extreme value of $A = 2$. As expected, the error is strictly increasing for decreasing SNR, i.e. increasing A. After an initial cutoff, visible in saturated yellow in Figure 3.8, the accuracy of the algorithm is also generally decreasing for increasing smoothing width σ. However, after this initial cutoff, there is a comfortably large range of σ where the algorithm performs well.

The choice of smoothing parameter σ has significant influence on the analysis of real data, as is visible in Fig. 3.6: for high E_0, the noise level is so high that no feasible matches

were found for the used value of smoothing σ. Increasing σ alleviates this, but reduces the match quality for images with low noise level.

We found that most features visible in the high-σ, high-A regime of Figure 3.8**b,d** are dependent on the initialization of the random generator for the added pixel-wise noise and are thus not significant.

3.4.3 TIME COMPLEXITY

To benchmark the computational complexity of the algorithm, it was applied to subsequently larger parts of the real dataset, while measuring the computation times for the least squares optimization (step 8 above) and the shifting and writing of images (step 9) separately.

The results show calculating the cross-correlations takes the most time, as it scales almost perfectly quadratically in the number of images N, as shown in Fig. 3.9. The shifting and writing of images scales linearly and is not significant for larger datasets. The total time therefore scales nearly perfectly quadratically, with a dataset of 500 images drift corrected in less than 7 minutes of computation time. As such, LEEM spectroscopy datasets can be comfortably and regularly drift corrected on a desktop PC.

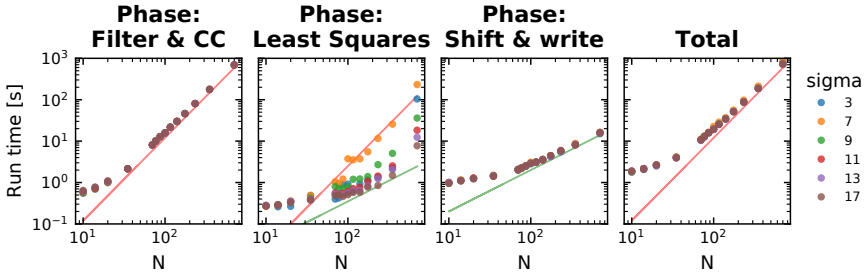

Figure 3.9: *Run times of different phases of the drift correction algorithm on* 256×256 *pixel images. Linear (green) and quadratic (red) slopes are added as a guide to the eye, illustrating that the cross correlations scales quadratically in the number of images N, while the shifting and saving of images itself is linear.*

3.4.4 DISCUSSION

We elaborate here on the choices made in the algorithm. The use of the magnitude Sobel filter has multiple benefits, similar to using the gradient cross-correlation: Contrast inversions between areas with different spectroscopic properties nonetheless result in similar images (cf. Figure 3.5**c,d**). In addition, the constant zero background reduces errors due to wrap-around effects due to performing the calculation in the Fourier domain.

The exponent 4 for the weighing matrix W_{ij} in the least squares minimization step 8 was empirically found to give the best results for real datasets.

As already noted by Schaffer et al., the use of cross-correlation between multiple image pairs and combining the returned integer shift values enables sub-pixel accuracy. The maximum theoretical accuracy is $\frac{1}{N}$ pixels, but is reduced for images where false positive matches are thresholded out.

Alternative methods of obtaining sub-pixel accuracy in determining shifts include a combination of upscaling and matrix-multiplication discrete cosine transforms [63] and a rather elegant interpolation of the phase cross-correlation method proposed by Foroosh et al. [59]. However our current method is less complex and combines robustness against global drift with handling of changing contrasts, which is crucial for spectroscopic LEEM data. Although the sub-pixel precise phase correlation method seems a straightforward extension of regular cross correlation, it is less suitable for datasets with changing noise levels and not suitable for false positive detection by normalization, both properties we found essential to handle spectroscopic LEEM data.

Fourier interpolation for non-integer shifts, corresponding to Whittaker-Shannon interpolation, is optimal when the image resolution is limited by the optical transfer function of the intstrument, instead of pixel sampling-limited [75]. In this case, almost always true for LEEM measurements, the imaginary part is zero up to floating point precision and can be discarded. If however the resolution is limited by the detector, e.g. at very low magnifications, bi-linear interpolation is the better choice.

Contrary to Schaffer et al., we found smaller values of Gaussian smoothing width σ yield the best results, with larger values yielding artificial shifts around contrast inversions for real datasets and generally performing worse for the synthetic dataset, as visible in Fig. 3.8.

Schaffer et al. found their approach at the time (2004) not computationally feasible for large amounts of images but, as shown in the previous section, the current implementation is able to drift correct a stack of several hundreds of images comfortably on a single desktop computer. We want to emphasize that the use of `Python` gives flexibility and makes it easy to adapt the code. For instance, increasing performance even more lies within reach by performing the FFT cross-correlations and maximum search on one or more graphical processing units using one of several libraries or by using a cluster running a `dask` scheduler. Further speedup would be possible by pruning which pairs of images are to be cross-correlated. An avenue not explored here, but used in the image stitching described in Appendix B, is the use of pyramid methods to create a multi-step routine where firstly a fast estimate of the shift is computed on a smoothened and reduced-size image before using consecutively larger images to refine the estimate [76, 77].

Beyond drift correction, the same method presented here can also be applied to create precisely stitched overview images of areas much larger than the electron beam spot size. Although, as no contrast inversions or large feature differences are expected for the matching areas, the added value of using a gradient filter is nullified. Additionally the number of images that can be matched to the same template is limited, forcing a low upper bound on the sub-pixel accuracy of the optimization part of the algorithm. Instead, we found that an algorithm based on more regular phase-shift cross-correlation is sufficient for sub-pixel accurate stitching (See Appendix B).

3.5 DIMENSION REDUCTION

The sub-pixel accuracy drift correction now makes it possible to reinterpret a LEEM-I(V) dataset as a truly per-pixel set of spectroscopic curves, opening up possibilities for further data analysis. For a dataset of N images, each such curve (cf. Fig. 3.1) can be seen

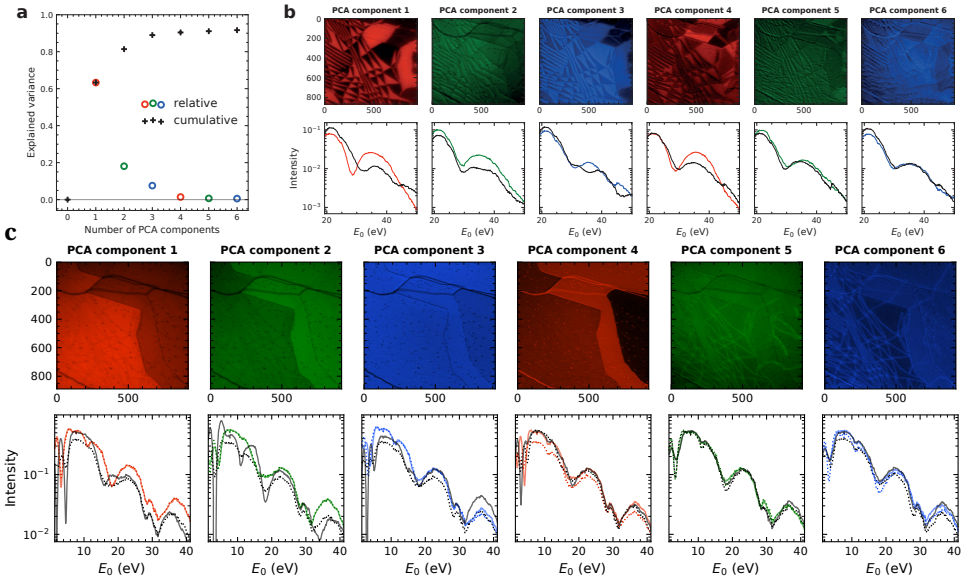

Figure 3.10: a, *Scree plot indicating the retained variance per PCA component for the Dark Field dataset.* ***b,*** *Images of the first six PCA components for the Dark Field sample dataset and the spectra corresponding to the maximum and minimum of the respective components occurring in the dataset.* ***c,*** *Images of the first six PCA components for the Bright Field sample data set and the spectra corresponding to the maximum and minimum of this component occurring in the dataset (dashed) and the spectrum corresponding to the corresponding eigen-spectrum itself.*

as a vector in a N-dimensional vector space of the mathematically possible spectra. Even for moderate datasets of a few hundred images this is a huge vector space. In almost all cases however, the physical behavior of the data can be described with a model with far fewer degrees of freedom, i.e. the vector space of physically possible spectra has a much lower number of dimensions. Therefore, it should be possible to summarize all significant behavior in a much smaller dataset, which can be analyzed (and visualized) much more easily.

Here, we use Principal Component Analysis (PCA), a linear technique based on singular value decomposition (SVD), often used for dimension reduction in data science fields [78–80]. The randomized iterative variant of PCA allows for efficient computation of the largest variance components without performing the full SVD decomposition [81]. This technique therefore projects the spectroscopic data to a lower dimensional subspace, in such a way that maximal data variance is retained. It does so in a computationally efficient way, making it well suited for, and popular in, data science. Before applying PCA, we crop the dataset to remove any areas that lie outside of the detector for any image inside the used range of E_0. Additionally, each image is scaled to zero mean and unit variance, to not let brighter images contribute more strongly to the analysis as they have larger variance. A lot of other choices for standardization of the data are possible, most of them with useful results, but for the scope of this paper we adhere to this standard

choice.

After performing PCA, the lower dimensional subspace or PCA-space, is now spanned by orthogonal 'eigen-spectra', referred to as PCA components. Since the projection map onto this subspace retains most of the variance in the dataset, it is possible to build an approximate reconstruction of the full physical spectra from the reduced PCA spectra.

Although the aim is dimension reduction, the number of PCA dimensions should be chosen large enough, such that the mathematical PCA-space contains all physical behaviour up to a certain noise level [82]. A so-called scree plot, displaying the captured variance, aids to pick the right number of dimensions. For the sample dataset of dark-field images of $N = 300$ energies, a scree plot is shown in Figure 3.10**a**. In general, for spectroscopic LEEM datasets, we find that reducing down to 6 dimensions is often enough to capture more than 90% of all variance.

The dataset can be projected onto a single PCA component by taking the per-pixel inner product with the corresponding 'eigen-spectrum'. This yields images visualizing the variance retained by the respective components, as shown in the top half of Figure 3.10**b** and **c,** for all 6 PCA components of the dark field and bright field data respectively. Below each image, the spectra corresponding to the pixels with the minimum and maximum value of this projection are shown in black and color, respectively.

3.5.1 VISUALIZATION

Reducing a spectrum from hundreds of dimensions to a few opens up new opportunities for data visualization. In particular, it allows for the visualization of nearly all of the variation in spectra of an entire dataset in only two images, as shown in Fig. 3.11. Here, the values of the six principal components (cf. Fig. 3.10), are displayed as the RGB color channels of two pictures per dataset. To lift the degeneracy in the possibilities of the sign of the PCA components (a PCA eigen-spectrum with the opposite signs retains as much variance), we change the signs such that the a positive projection onto the PCA component corresponds to having the higher average relative brightness in the images. This way, areas that are bright in the majority of the original images also appear bright in the visualization. To compensate for the human eyes' preference for green, a scaling of colors as proposed by Kovesi is applied [83]. It is given by the following matrix:

$$\begin{pmatrix} R' \\ G' \\ B' \end{pmatrix} = \begin{pmatrix} 0.90 & 0.17 & 0.00 \\ 0.00 & 0.50 & 0.00 \\ 0.10 & 0.33 & 1.00 \end{pmatrix} \begin{pmatrix} R \\ G \\ B \end{pmatrix}$$

The results are striking. All the sample features are directly visible in Fig. 3.11: In the bright field dataset, bilayer and thicker graphene are clearly separated in orange and green, respectively in the first three PCA components (Figure 3.11**a**). Moreover, SiC step edges, domain walls and point-like defects are clearly visible. The next three PCA components (Figure 3.11**b**) highlight the difference between bilayer (green), trilayer (orange) and four-layer graphene (dark green) and in addition separates step edges (orange), domain boundaries (turquoise) and the defects in different colors. Furthermore, two types of domain boundaries can be observed in the four-layer area that are hard to tell apart in conventional LEEM images (See also Section 5.3). The light green and dark ones are presumably domain boundaries in the top-most and lower layers, respectively.

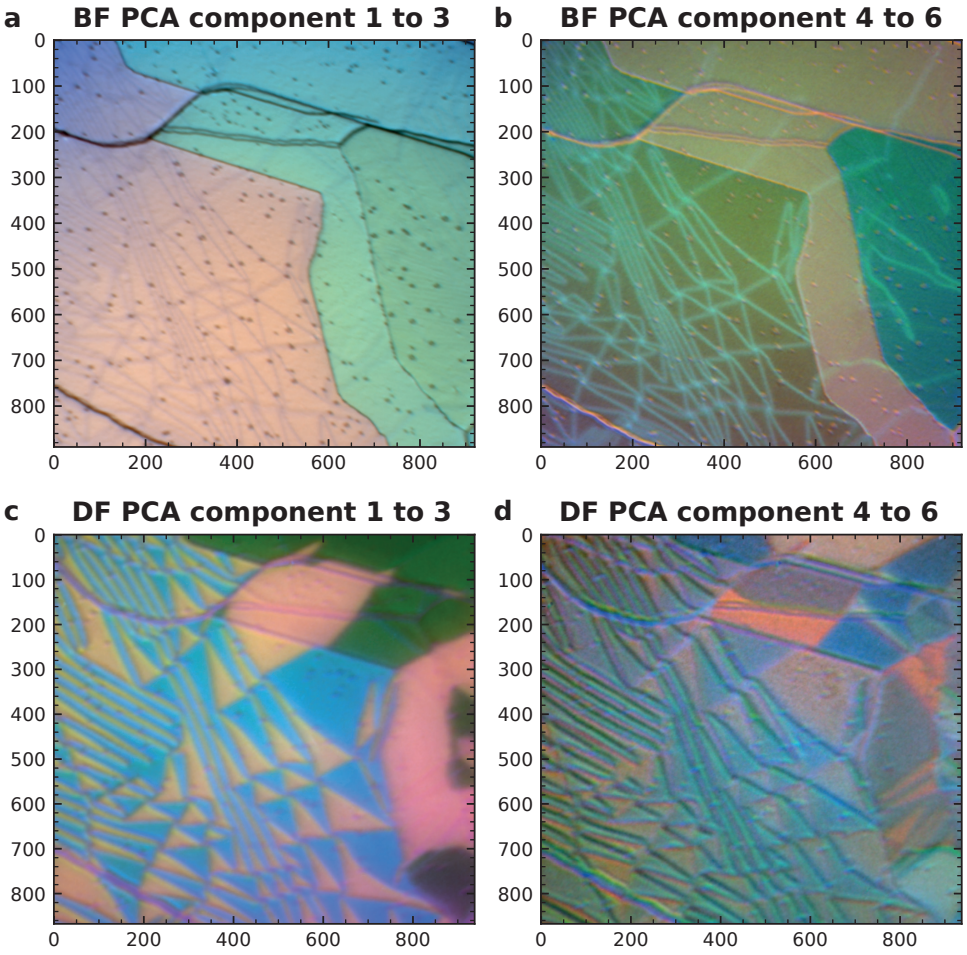

Figure 3.11: *The first six PCA components can be used to summarize a spectroscopic LEEM measurement in two RGB pictures.* ***a,b,*** *Visualization of a spectroscopic bright-field LEEM measurement of quasi-freestanding few-layer graphene on SiC. Different layer counts, stacking boundaries of two types and point defects are distinguishable.* ***c,d,*** *Visualization of a spectroscopic dark-field LEEM measurement of the same area. All six different possible stacking orders for up to trilayer graphene are easily distinguishable.*

This visualization using the first three PCA components of the dark field dataset (Figure 3.11**c**) clearly separates the different stacking orders in bilayer (AB in orange and AC in blue) and trilayer graphene. The PCA components 4 to 6 (Figure 3.11**d**) highlights the different stacking orders in trilayer and four-layer areas (different shades of orange and blue) and display an interference effect causing double lines at one type of (corresponding to one direction of) domain edge. This clear visualization is particularly remarkable

as the dark-field dataset presents a worst case scenario due to its extreme off-axis alignment (see Chapter 4 for full details), which causes strong image drift and relative shifts of features.

3.5.2 CLUSTERING AND AUTOMATIC CLASSIFICATION

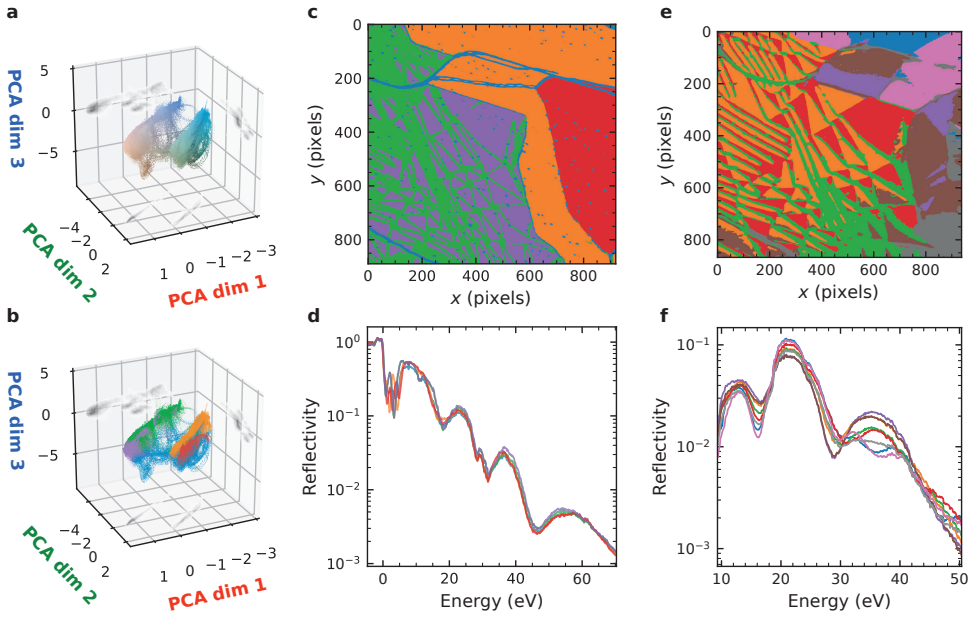

Figure 3.12: ***a,*** *Bright-field dataset visualized as point cloud in the space of the first three PCA components. The points are colored according to the mapping in Fig. 3.11(a) and are projected onto the planes in gray scale.* ***b,*** *Point cloud as in subfigure (a), but colored according to the computed clustering.* ***c,*** *Indication of the cluster labels in the real-space image.* ***d,*** *Mean bright-field spectroscopy curves for each cluster, automatically recovering layer count and domain walls.* ***e,f,*** *Same as subfigures (c,d) for the dark-field dataset reveals all stacking orders present as well as two sets of edge-case curves. Cf. Figure 4.2.*

In addition to the visualization possibilities explored in the previous section, the dimension reduction by PCA lowers the complexity of the data enough to enable the use of other, more quantitative data analysis techniques. In particular, reduction to less than ten dimensions is enough to perform unsupervised classification or clustering on the entire dataset. Here, we show that a relatively simple clustering algorithm, the classical k-means, also known as Lloyd's algorithm [84], applied to the PCA reduced dataset, can already be used to distinguish the relevant, different areas. The structure of the bright field dataset is visualized in terms of the first three PCA components in Figure 3.12**a**, both as a point cloud with colors corresponding to Figure 3.11**a** and as density projections (gray scale) on the three planes. The resulting classification from the application of k-means to the six PCA components is visualized in the same way in Figure 3.12**b**, where the color of the points now corresponds to the assigned labels. These same label

colors are shown in real space in Figure 3.12**c**. In the real space visualization it is clear that the different layer counts are separated (bilayer, trilayer and four-layer as purple, orange and red, respectively) from a class with the point defects and step edges (blue) and a class containing the domain boundaries in the bilayer (green). The cluster labels can now be used to calculate spectra of each area, e.g. all trilayer pixels without the defects. For this, we take the mean over all pixels belonging to one cluster for each energy in the full N-dimensional dataset. This can be done even for energies outside the range used for the initial clustering as well as for energies where we only have partial data due to drift. The resulting spectra for the clustering in Figure 3.12**c** are plotted in Figure 3.12**d**.

The same clustering method is applied only to the first 4 PCA components of the dark-field dataset since component 5 and 6 show virtually no distinguishing features and corresponds to very little variance (cf. Figure 3.10**a,b**). The resulting real space labeling of the clusters and the spectra are shown in Fig. 3.12**e** and **f**, respectively. Here, although not perfect, the clustering algorithm manages to mostly separate the different possible stacking orders (red and orange for the bilayer and purple, brown, pink and blue for the trilayer). The green and gray areas correspond to areas where clear classification as a stacking order is not possible due to phase contrast and non-uniform illumination artefacts due to the tilted illumination.

Thanks to the proper calibration and mutual registration of the data, this relatively simple algorithm classifies the areas in the dark-field data set with only minor errors (e.g. the incorrect assignment of brown trilayer spectrum in the lower left), *without* any input of the positions of each spectrum in the image or any input about the expected differences between spectra. We anticipate that this classification using unsupervised machine learning will be useful for identifying unknown spectra in new datasets. In Chapter 8 for example, it is applied to distinguish the different spectra found on TaS_2 samples.

3.6 CONCLUSION

We have shown that treating (energy-dependent) LEEM measurements as multi-dimensional datasets rather than as collection of images, opens rich opportunities for detailed and quantitative insights into complex material systems that go well beyond morphological and crystallographic characterization.

Three key steps are necessary to convert a stack of raw LEEM images into spectroscopic dataset with a greatly increased body of quantitative information. First, we compensate for common detector artefacts such as camera dark count and non-uniform detector gain, which is crucial to quantitatively interpret LEEM images. Second, by calibrating the channel plate gain and adjusting it during spectroscopic measurements, we can not only extend the dynamic range of the dataset by two orders of magnitude, but also convert image intensity into absolute reflectivity or electron intensity (provided the beam current is accurately measured). Third, we describe a drift-correction algorithm that is tailored for spectroscopic LEEM datasets where contrast inversions make many other approaches infeasible. It relies on digital filtering and cross-correlation of every image to all other images and, without requiring large computation times, yields sub-pixel accuracy. It thus produces spectral LEEM data with high spatial resolution, i.e., true pixel-wise spectra.

This suite of techniques is already in regular use to obtain data from the ESCHER system in Leiden [25–27, 31, 34, 37]. In addition, the resulting spectral datasets enable more sophisticated data classification and visualization methods that rely on the spectrum (I(V)-curve) in every pixel. We demonstrate how we can use dimension reduction on the spectra to automatically compose images from only the six strongest spectroscopic features (PCA components). This approach produces rich color images that capture most of the features of the dataset and can thus give an intuitive view on complex material systems. Furthermore, we show that a relatively simple cluster analysis on those data sets of reduced dimensionality yields a quantitative representation of this information. Different materials within a field of view are automatically identified and statistical information such as the mean spectra and their spread per material can be extracted.

Treating LEEM measurements as multidimensional datasets as presented here will further strengthen the role of LEEM as a quantitative spectroscopic tool rather than as a pure imaging instrument, thus deepening its impact in the research and discovery of novel material systems. Furthermore, the presented techniques can be applied to related spectroscopic imaging techniques, such as energy-filtered PEEM [85] or even adapted for use in scanning probe techniques such as scanning tunneling spectroscopy [79, 86]. To facilitate the use of the approaches discussed here, the test data as well as Python code is available online [42, 48].

3.7 OUTLOOK: DRIFT CORRECTION IMPROVEMENTS

This is an addendum to the drift correction algorithm and the image stitching algorithm as described in this chapter and in Appendix B. The implementations of both are published in Ref. [42].

The drift correction as presented in this chapter can straightforwardly be extended in several ways, to increase computation speed or accuracy or to adopt to different datasets. I will list some ideas to do so here. Some of these are borrowed from the work done for stitching of images, others have been planned for a long time, but were never prioritized enough for time to be available to implement them.

3.7.1 GPUS FOR FASTER COMPUTATION

Graphical Processing Units (GPUs) are very efficient at massively parallel computation in general, and image handling specifically. Therefore moving computation from the CPU to one or more GPUs can be a way to increase performance by orders of magnitude if the workload allows. However, traditionally programming for GPUs has been more involved, as it relied on specific extensions of general purpose programming languages to allow computation on GPU. With this came a lot of specific programming paradigms to accommodate the significantly different architecture of GPUs (compared to CPUs) and the moving of data from main memory to the GPU memory and back.

However, the software stack has been significantly maturing, even for more high-level languages such as Python, in particular for NVIDIA GPUs. This has led to Python being adopted as the language of choice for the quickly emerging field of data science, greatly enhancing the ecosystem by the sheer number of programmers working in it. Therefore it would now be relatively straightforward to implement a GPU-accelerated

version of the drift correction by utilizing `cupy` [87] to handle array computations where `numpy` is used now. Massive work has been done to push the API of `cupy` towards higher compatibility with `numpy` and `scipy`, meaning that for (almost) all used functions, drop-in `cupy` replacements exist. Experience from rewriting some core `pyGPA` [88] routines to use `cupy` confirms that significant gains in speed can be achieved without much (programming) effort. Furthermore, it should work transparently with `dask`.

3.7.2 ALGORITHMIC SPEED IMPROVEMENTS

The core of the statistical drift correction algorithm is the $\mathcal{O}(N^2)$ comparison of every pair of images. While this enables subpixel accuracy, it is a major Achilles heel in computation speed and scalability. Not only does this mean a quadratic increase in computations for more images, it also prevents early release from memory of computed Fast Fourier Transforms (FFTs) of images, as any block of images is needed in combination with every other block of images. By drawing a parallel to the stitching algorithm, two solutions to this present itself:

- For larger smoothing filters, images can be scaled down, significantly reducing memory load and needed computation for the FFTs.
- Instead of comparing all pairs of images, we can compare each image only to k 'nearest' neighbors, with $k \ll N$, resulting in a $\mathcal{O}(N \times k)$ algorithm, now linear in N. The natural 'distance' to determine the nearest neighbors is now not the stage coordinates, but whichever other (set of) parameters is changed, e.g. landing energy. Even just the time at which the images were taken, comparing images taken after each other would yield a reasonable 'distance' to use. A non-optimized version of this linear variant has been implemented in the repository [42].

It is even possible to combine the two approaches in a two-pass algorithm, to create a faster algorithm without losing too much accuracy. This can work, because the 'quality' of a match between two images, depends on the overlap between them. A first, linear pass, will be used to generate an initial estimate of the absolute shift vectors. The subsequent, quadratic pass can now be done on crops based on the first pass, allowing for smaller crops to be used, decreasing memory and computational load. For a 4 times smaller crop in each direction (a reasonable value) this would save a factor $4^2 = 16$ on memory use and a factor $4\log(4)$ on computation, with improved cache locality expected to provide further speed gains.

As an alternative for this two-pass algorithm, a mixed strategy could be considered, optimizing for matrices of relative shifts containing both k nearest neighbors and the quadratic, farther out combinations for every l-th image (striding through the full dataset), corresponding to a $\mathcal{O}\left(N \times k + \frac{N^2}{l^2}\right)$ algorithm.

3.7.3 IMPROVEMENTS TO ACCURACY

For any pair of images, there is an optimal (Gaussian) smoothing width σ to suppress the noise, depending on the signal-to-noise ratio (SNR). In spectroscopic LEEM imaging, the SNR strongly depends on the intensity of the image, and therefore on the landing energy, resulting in a widely varying SNR within a single spectroscopic dataset. In the currently

described algorithm, a fixed σ is manually picked for the entire dataset and any matches between images with insufficient match quality, determined by the also manually set w_{min}, are discarded.

This can be improved upon in several ways, as discussed below.

AUTOMATIC DETERMINATION OF w_{MIN}

The most straightforward way is to borrow once again from the stitching algorithm, and to determine w_{min} automatically as the *maximum value* for which the number of connected components of the graph of all valid matches is still equal to 1, i.e. such that all images can still be related to all the other images. An alternative, likely superior method is described and implemented by Savitzky et al. in Ref. [66]. They force all relative shifts to be consistent and drop any relative shifts that cause inconsistency in the optimization.

ADAPTIVE SMOOTHING

Two more elaborate ways to improve upon this involving an adaptive value for σ could be explored.

The first uses *image pyramids* to find the lowest value for σ for each match pair for which a sufficiently high w weight can be achieved. Image pyramids are a common way of dealing with high resolution images [76]. The pyramid is formed by multiple versions of the image, with each layer being a smoothed and down-scaled version of the layer below. By moving down the pyramid, more detail is obtained, at the cost of a larger image size. Starting at the top of the pyramid for each image, we have a high σ, low-resolution version of the image, for which the cross-correlations can be computed cheaply, with a high likelihood of a sufficient match between the images. Moving down the pyramid, the match can be updated to a higher precision version, until $w_{ij} < w_{\text{min}}$, or until a larger than expected jump in the relative shift vector is detected. This algorithm is more involved than the original algorithm, but allows for optimal σ value selection for each match, ultimately increasing the information fed into the optimization and improving the result, without just adding σ as another full dimension to the computation.

SIGNAL-TO-NOISE DETERMINATION

The second way to select an optimal value of σ per image pair is based on the following. The smoothing is applied to suppress (amplification of) the noise in the image, which causes spurious peaks in the cross-correlation. For a higher SNR, a larger σ value is needed to average over enough pixels to suppress the noise to a level that the cross-correlation yields the correct result. Therefore, if the SNR of an image is approximately known, it would be possible to estimate the optimal value of σ to use on it.

The SNR can be determined by comparing two, subsequently taken, *nominally equal* images by computing the normalized weight $\bar{w}$ from the cross-correlations (equivalent to what is used in the drift correction algorithm). A higher $\bar{w}$ corresponds to more similar images and therefore less random noise.

Although taking twice as many images might sound like a high cost at first glance, in practice the cost is relatively low, as the images can be combined to a longer exposure image by averaging and treated as a single image afterwards. This combination could already be applied during imaging, and as an extension of that, one could adaptively

average images until a sufficient SNR is achieved before moving on to the next parameter value in the measurement.

However, we can circumvent the need for extra images entirely by an approximation under the sufficient sampling assumption, i.e. in the case that subsequent images in the dataset are sufficiently close together in parameter space to sample all behavior as a function of the varied parameter (e.g. E_0). This assumption should be satisfied in almost any sensible experiment, so it is a reasonable one to make. In this case, we can replace the nominally equal image from the preceeding description by the next best option: a neighboring image in parameter space, which should only be marginally different. An even more sophisticated option would be to take an average of two neighboring images from opposing sides, although proper normalization of image intensities would be needed in that case.

REGULARIZATION OF POSITIONS

A final, relatively easy to implement, possible improvement to the accuracy of the algorithm is the addition of a regularization term in the optimization step. By penalizing the second derivative of the position, prior information is added: generally, the image is not expected to suddenly jump between subsequent images[2], for example, in the case of thermal drift, the mass of the stage and Newton's second law alone prevent sudden jumps of the sample stage, and therefore, of the image. This would also provide a better solution in the (undesired) case of multiple connected components in the matrix of used relative shifts, preventing the large jumps occurring without any regularization.

REFERENCES

25. R. Tromp, J. Hannon, A. Ellis, et al. A new aberration-corrected, energy-filtered LEEM/PEEM instrument. I. Principles and design. *Ultramicroscopy* **110,** 852–861. doi:10.1016/j.ultramic.2010.03.005 (2010).

26. S. Schramm, J. Kautz, A. Berghaus, et al. Low-energy electron microscopy and spectroscopy with ESCHER: Status and prospects. *IBM Journal of Research and Development* **55,** 1–1. doi:10.1147/JRD.2011.2150691 (2011).

27. R. M. Tromp, J. B. Hannon, W. Wan, A. Berghaus & O. Schaff. A new aberration-corrected, energy-filtered LEEM/PEEM instrument II. Operation and results. *Ultramicroscopy* **127,** 25–39. doi:10.1016/j.ultramic.2012.07.016 (2013).

29. J. I. Flege & E. E. Krasovskii. Intensity-voltage low-energy electron microscopy for functional materials characterization. *Physica Status Solidi - Rapid Research Letters* **8,** 463–477. doi:10.1002/pssr.201409102 (2014).

30. H. Hibino, H. Kageshima, F. Maeda, et al. Microscopic thickness determination of thin graphite films formed on SiC from quantized oscillation in reflectivity of low-energy electrons. *Physical Review B* **77,** 075413. doi:10.1103/PhysRevB.77.075413 (2008).

[2] In some tilted Dark Field alignments, focus tracking of the objective lens can actually cause apparent jumps between images. In this case using regularization would not be the best choice.

31. T. A. de Jong, J. Jobst, H. Yoo, et al. Measuring the Local Twist Angle and Layer Arrangement in Van der Waals Heterostructures. *physica status solidi (b)* **255,** 1800191. doi:10.1002/pssb.201800191 (2018).

34. J. Jobst, A. J. H. van der Torren, E. E. Krasovskii, et al. Quantifying electronic band interactions in van der Waals materials using angle-resolved reflected-electron spectroscopy. *Nature Communications* **7,** 13621. doi:10.1038/ncomms13621 (2016).

35. T. A. de Jong, D. N. L. Kok, A. J. H. van der Torren, et al. Quantitative analysis of spectroscopic low energy electron microscopy data: High-dynamic range imaging, drift correction and cluster analysis. *Ultramicroscopy* **213,** 112913. doi:10.1016/j.ultramic.2019.112913 (2020).

36. E. Bauer, M. Mundschau, W. Swiech & W. Telieps. Surface studies by low-energy electron microscopy (LEEM) and conventional UV photoemission electron microscopy (PEEM). *Ultramicroscopy* **31,** 49–57. doi:10.1016/0304-3991(89)90033-8 (1989).

37. T. A. de Jong, E. E. Krasovskii, C. Ott, et al. Intrinsic stacking domains in graphene on silicon carbide: A pathway for intercalation. *Physical Review Materials* **2,** 104005. doi:10.1103/PhysRevMaterials.2.104005 (2018).

38. J. Jobst, J. Kautz, D. Geelen, R. M. Tromp & S. J. van der Molen. Nanoscale measurements of unoccupied band dispersion in few-layer graphene. *Nature Communications* **6,** 8926. doi:10.1038/ncomms9926 (2015).

39. A. Schmid, W. Święch, C. Rastomjee, et al. The chemistry of reaction-diffusion fronts investigated by microscopic LEED I–V fingerprinting. *Surface Science* **331-333,** 225–230. doi:10.1016/0039-6028(95)00128-x (1995).

40. B. Frank, P. Kahl, D. Podbiel, et al. Short-range surface plasmonics: Localized electron emission dynamics from a 60-nm spot on an atomically flat single-crystalline gold surface. *Science Advances* **3,** e1700721. doi:10.1126/sciadv.1700721 (2017).

41. A. Locatelli, K. R. Knox, D. Cvetko, et al. Corrugation in Exfoliated Graphene: An Electron Microscopy and Diffraction Study. *ACS Nano* **4,** 4879–4889. doi:10.1021/nn101116n (2010).

42. T. A. de Jong. *Quantitative Data Analysis for spectroscopic LEEM* version v0.2.0. 2021. doi:10.5281/zenodo.3539538.

43. J. Röhrl, E. Rotenberg, J. Jobst, et al. Towards wafer-size graphene layers by atmospheric pressure graphitization of silicon carbide. *Nature Materials* **8,** 203–207. doi:10.1038/nmat2382 (2009).

44. F. Speck, J. Jobst, F. Fromm, et al. The quasi-free-standing nature of graphene on H-saturated SiC(0001). *Applied Physics Letters* **99,** 122106. doi:10.1063/1.3643034 (2011).

45. C. Riedl, C. Coletti, T. Iwasaki, A. A. Zakharov & U. Starke. Quasi-Free-Standing Epitaxial Graphene on SiC Obtained by Hydrogen Intercalation. *Physical Review Letters* **103,** 246804. doi:10.1103/PhysRevLett.103.246804 (2009).

46. R. M. Feenstra, N. Srivastava, Q. Gao, et al. Low-energy electron reflectivity from graphene. *Physical Review B* **87,** 041406. doi:10.1103/PhysRevB.87.041406 (2013).

47. H. Hibino, S. Mizuno, H. Kageshima, M. Nagase & H. Yamaguchi. Stacking domains of epitaxial few-layer graphene on SiC(0001). *Physical Review B* **80,** 085406. doi:10.1103/PhysRevB.80.085406 (2009).

48. T. A. de Jong & J. Jobst. *Data underlying the paper: Quantitative analysis of spectroscopic Low Energy Electron Microscopy Data* 2019. doi:10.4121/uuid:7f672638-66f6-4ec3-a16c-34181cc45202.

49. R. van Gastel, I. Sikharulidze, S. Schramm, et al. Medipix 2 detector applied to low energy electron microscopy. *Ultramicroscopy* **110,** 33–35. doi:10.1016/J.ULTRAMIC.2009.09.002 (2009).

50. R. Widenhorn, M. M. Blouke, A. Weber, A. Rest & E. Bodegom. *Temperature dependence of dark current in a CCD* in *Sensors and Camera Systems for Scientific, Industrial, and Digital Photography Applications III* (eds M. M. Blouke, J. Canosa & N. Sampat) **4669** (SPIE, 2002), 193–201. doi:10.1117/12.463446.

51. R. Widenhorn, J. C. Dunlap & E. Bodegom. Exposure Time Dependence of Dark Current in CCD Imagers. *IEEE Transactions on Electron Devices* **57,** 581–587. doi:10.1109/TED.2009.2038649 (2010).

52. R. Widenhorn, L. Mündermann, A. Rest & E. Bodegom. Meyer-Neldel rule for dark current in charge-coupled devices. *Journal of Applied Physics* **89,** 8179–8182. doi:10.1063/1.1372365 (2001).

53. J. A. Seibert, J. M. Boone & K. K. Lindfors. *Flat-field correction technique for digital detectors* in *Medical Imaging 1998: Physics of Medical Imaging* (eds J. T. Dobbins III & J. M. Boone) **3336** (SPIE, 1998), 348. doi:10.1117/12.317034.

54. R. Yu, S. Kennedy, D. Paganin & D. Jesson. Phase retrieval low energy electron microscopy. *Micron* **41,** 232–238. doi:10.1016/j.micron.2009.10.010 (2010).

55. S. M. Kennedy, C. X. Zheng, W. X. Tang, D. M. Paganin & D. E. Jesson. Laplacian image contrast in mirror electron microscopy. *Proceedings of the Royal Society A: Mathematical, Physical and Engineering Sciences* **466,** 2857–2874. doi:10.1098/rspa.2010.0093 (2010).

56. J. Jobst, L. M. Boers, C. Yin, et al. Quantifying work function differences using low-energy electron microscopy: The case of mixed-terminated strontium titanate. *Ultramicroscopy* **200,** 43–49. doi:10.1016/j.ultramic.2019.02.018 (2019).

57. S. M. Schramm, S. J. van der Molen & R. M. Tromp. Intrinsic Instability of Aberration-Corrected Electron Microscopes. *Physical Review Letters* **109,** 163901. doi:10.1103/PhysRevLett.109.163901 (2012).

58. *Catalog: MCP(MICROCHANNEL PLATE) AND MCP ASSEMBLY* Hamamatsu Photonics K.K., (), 1–2. https://www.hamamatsu.com/content/dam/hamamatsu-photonics/sites/documents/99_SALES_LIBRARY/etd/MCP_assembly_TMCP0003E.pdf.

59. H. Foroosh, J. Zerubia & M. Berthod. Extension of phase correlation to subpixel registration. *IEEE Transactions on Image Processing* **11,** 188–200. doi:10.1109/83.988953 (2002).

60. S. Klein, M. Staring, K. Murphy, M. Viergever & J. Pluim. elastix: A Toolbox for Intensity-Based Medical Image Registration. *IEEE Transactions on Medical Imaging* **29,** 196–205. doi:10.1109/TMI.2009.2035616 (2010).

61. D. Shamonin, E. E. Bron, B. P. Lelieveldt, et al. Fast parallel image registration on CPU and GPU for diagnostic classification of Alzheimer's disease. *Frontiers in Neuroinformatics* **7,** 50. doi:10.3389/fninf.2013.00050 (2013).

62. E. M. Ismaili Aalaoui & E. Ibn-Elhaj. Estimation of Subpixel Motion Using Bispectrum. *Research Letters in Signal Processing* **2008,** 1–5. doi:10.1155/2008/417915 (2008).

63. M. Guizar-Sicairos, S. T. Thurman & J. R. Fienup. Efficient subpixel image registration algorithms. *Optics Letters* **33,** 156. doi:10.1364/OL.33.000156 (2008).

64. G. Tzimiropoulos, V. Argyriou & T. Stathaki. Subpixel Registration With Gradient Correlation. *IEEE Transactions on Image Processing* **20,** 1761–1767. doi:10.1109/TIP.2010.2095867 (2011).

65. B. Schaffer, W. Grogger & G. Kothleitner. Automated spatial drift correction for EFTEM image series. *Ultramicroscopy* **102,** 27–36. doi:10.1016/j.ultramic.2004.08.003 (2004).

66. B. H. Savitzky, I. El Baggari, C. B. Clement, et al. Image registration of low signal-to-noise cryo-STEM data. *Ultramicroscopy* **191,** 56–65. doi:10.1016/j.ultramic.2018.04.008 (2018).

67. Dask Development Team. *Dask: Library for dynamic task scheduling* (2016). https://dask.org.

68. M. Rocklin. *Dask: Parallel Computation with Blocked algorithms and Task Scheduling* in *Proceedings of the 14th Python in Science Conference* (eds K. Huff & J. Bergstra) (2015), 126–132. doi:10.25080/Majora-7b98e3ed-013.

69. S. van der Walt, J. L. Schönberger, J. Nunez-Iglesias, et al. scikit-image: image processing in Python. *PeerJ* **2,** e453. doi:10.7717/peerj.453 (2014).

70. E. Jones, T. Oliphant, P. Peterson & E. Al. *SciPy: Open source scientific tools for Python, http://www.scipy.org* 2001. http://www.scipy.org.

71. M. A. Branch, T. F. Coleman & Y. Li. A Subspace, Interior, and Conjugate Gradient Method for Large-Scale Bound-Constrained Minimization Problems. *SIAM Journal on Scientific Computing* **21,** 1–23. doi:10.1137/S1064827595289108 (1999).

72. R. H. Byrd, R. B. Schnabel & G. A. Shultz. Approximate solution of the trust region problem by minimization over two-dimensional subspaces. *Mathematical Programming* **40-40,** 247–263. doi:10.1007/BF01580735 (1988).

73. F. Perez & B. E. Granger. IPython: A System for Interactive Scientific Computing. *Computing in Science & Engineering* **9,** 21–29. doi:10.1109/MCSE.2007.53 (2007).

74. F. Pedregosa, G. Varoquaux, A. Gramfort, et al. Scikit-learn: Machine Learning in Python. *Journal of machine learning research* **12,** 2825–2830. http://arxiv.org/abs/1201.0490 (2012).

75. D. P. Petersen & D. Middleton. Sampling and reconstruction of wave-number-limited functions in N-dimensional euclidean spaces. *Information and Control* **5,** 279–323. doi:10.1016/S0019-9958(62)90633-2 (1962).

76. E. H. Adelson, P. J. Burt, C. H. Anderson, J. M. Ogden & J. R. Bergen. Pyramid methods in image processing. *RCA engineer* **29,** 33–41 (1984).

77. P. Thevenaz, U. Ruttimann & M. Unser. A pyramid approach to subpixel registration based on intensity. *IEEE Transactions on Image Processing* **7,** 27–41. doi:10.1109/83.650848 (1998).

78. S. Wold, K. Esbensen & P. Geladi. Principal component analysis. *Chemometrics and Intelligent Laboratory Systems* **2,** 37–52. doi:10.1016/0169-7439(87)80084-9 (1987).

79. S. Jesse & S. V. Kalinin. Principal component and spatial correlation analysis of spectroscopic-imaging data in scanning probe microscopy. *Nanotechnology* **20,** 085714. doi:10.1088/0957-4484/20/8/085714 (2009).

80. H. Abdi & L. J. Williams. Principal component analysis. *Wiley Interdisciplinary Reviews: Computational Statistics* **2,** 433–459. doi:10.1002/wics.101 (2010).

81. N. Halko, P. G. Martinsson & J. A. Tropp. Finding Structure with Randomness: Probabilistic Algorithms for Constructing Approximate Matrix Decompositions. *SIAM Review* **53,** 217–288. doi:10.1137/090771806 (2011).

82. B. C. Geiger & G. Kubin. *Signal Enhancement as Minimization of Relevant Information Loss* in *SCC 2013; 9th International ITG Conference on Systems, Communication and Coding* (2013), 1–6.

83. P. Kovesi. Good Colour Maps: How to Design Them. *arXiv preprint.* http://arxiv.org/abs/1509.03700 (2015).

84. S. Lloyd. Least squares quantization in PCM. *IEEE Transactions on Information Theory* **28,** 129–137. doi:10.1109/TIT.1982.1056489 (1982).

85. O. Renault, N. Barrett, A. Bailly, et al. Energy-filtered XPEEM with NanoESCA using synchrotron and laboratory X-ray sources: Principles and first demonstrated results. *Surface Science* **601,** 4727–4732. doi:10.1016/j.susc.2007.05.061 (2007).

86. J. Yamanishi, S. Iwase, N. Ishida & D. Fujita. Multivariate analysis for scanning tunneling spectroscopy data. *Applied Surface Science* **428,** 186–190. doi:10.1016/J.APSUSC.2017.09.124 (2018).

87. R. Okuta, Y. Unno, D. Nishino, S. Hido & C. Loomis. *CuPy: A NumPy-Compatible Library for NVIDIA GPU Calculations* in *Proceedings of Workshop on Machine Learning Systems (LearningSys) in The Thirty-first Annual Conference on Neural Information Processing Systems (NIPS)* (2017), 7. http://learningsys.org/nips17/assets/papers/paper_16.pdf.

88. T. A. de Jong. *pyGPA* 2021. doi:10.5281/zenodo.5589555.

4

INTRINSIC STACKING DOMAINS IN GRAPHENE ON SILICON CARBIDE

Graphene on silicon carbide (SiC) bears great potential for future graphene electronic applications [89–93] because it is available on the wafer-scale [94–97] and its properties can be custom-tailored by inserting various atoms into the graphene/SiC interface [45, 98–103]. It remains unclear, however, how atoms can cross the impermeable graphene layer during this widely used intercalation process [45, 104, 105]. Here we demonstrate that, in contrast to the current consensus, graphene layers grown in argon atmosphere on SiC are not homogeneous, but instead composed of domains of different crystallographic stacking as they have been observed in other systems [47, 106, 107]. We show that these domains are intrinsically formed during growth and that dislocations between domains dominate the (de)intercalation dynamics. Tailoring these dislocation networks, e.g. through substrate engineering, will increase the control over the intercalation process and could open a playground for topological and correlated electron phenomena in two-dimensional superstructures [4, 108–112].

Parts of this chapter have been published as T. A. de Jong, E. E. Krasovskii, C. Ott, R. M. Tromp, S. J. van der Molen, and J. Jobst, Phys. Rev. Materials **2** 104005 (2018) [37].

4.1 INTRODUCTION

Graphene can routinely be produced on the wafer scale by thermal decomposition of silicon carbide (SiC) [94–97]. Due to the direct growth on SiC(0001) wafers, epitaxial graphene (EG) naturally forms on a wide band gap semiconductor, providing a doped or insulating substrate compatible with standard CMOS fabrication methods. Hence, EG is a contender for future graphene electronic applications such as power electronics [89, 92], high-speed transistors [90], quantum resistance standards [91] and terahertz detection [93]. In EG, the first hexagonal graphene layer resides on an electrically insulating monolayer of carbon atoms that are sp^3 bonded to silicon atoms of the SiC(0001) surface [94–96, 113]. The presence of this so-called buffer layer strongly affects the graphene on top, e.g. by pinning the Fermi level. Consequently, the graphene properties can be tuned via intercalation of atoms into the buffer layer/SiC interface. The intercalation of hydrogen is most widely used and results in the conversion of the buffer layer to a quasi-freestanding graphene (QFG) layer by cutting the silicon-carbon bonds and saturating silicon dangling bonds with hydrogen. This treatment reverses the graphene doping from n-type to p-type and improves the mobility [44, 45]. Intercalation of heavier atoms is used to further tailor the graphene properties, e.g. to form pn-junctions [98, 101], magnetic moments [102] or potentially superconducting [99] and topologically non-trivial states [100].

It has been realized that the quality of the grown graphene can be greatly improved by reducing the desorption rate of silicon atoms (which allows for a raised growth temperature), for example, by encapsulation of the SiC chip [96], or by growth in low-pressure silane environment [103, 114] or in ambient-pressure argon atmosphere [94, 95]. Graphene (EG and QFG) grown on SiC using these methods appears homogeneous with low defect concentration in most techniques [45, 94–97]. Together with the fact that layers span virtually unperturbed over SiC substrate steps [6, 7, 115], this has led to the consensus of perfectly crystalline graphene. On the other hand, two observations point to a less perfect sheet. First, the charge carrier mobility is generally low, even at cryogenic temperatures [44, 95]. Second, an ideal graphene sheet is impermeable even to hydrogen [104, 105], whereas a wide variety of atomic and molecular species has been intercalated into EG [45, 99–103]. Stacking domains as they have been observed in vacuum-grown graphene on SiC[47] and freestanding bilayer graphene [106, 107] could explain these contradictions. In this Chapter, we demonstrate that graphene grown on SiC in argon atmosphere is, in fact, less homogeneous than widely believed but is fractured into domains of different crystallographic stacking order. We use advanced low-energy electron microscopy (LEEM) methods and *ab initio* calculations to show that those domains are naturally formed during growth due to nucleation dynamics and built-in strain. Their presence is thus intrinsic to all graphene-on-SiC materials, including high-quality graphene grown in argon atmosphere.

4.2 METHODS

4.2.1 SAMPLE FABRICATION

Graphene growth is carried out on commercial 4H-SiC wafers (semi-insulating, nominally on axis, RCA cleaned) at ~1700 °C and 900 mbar Ar pressure for ~30 min as de-

scribed in Ref. [95]. To convert EG to bilayer QFG via hydrogen intercalation, the sample is placed in a carbon container and heated to 970 °C for 90 min at ambient hydrogen pressure as described in Ref. [44, 45]. Samples with small bilayer patches on large substrate terraces are achieved in a three-step process. First, SiC substrates are annealed at ~1700 °C and 900 mbar Ar pressure for 30 min in a SiC container to enable step bunching. Second, unwanted graphitic layers formed during this process are removed by annealing the sample at 800 °C in an oxygen flow for 30 min. Third, graphene growth is carried out as described above.

4.2.2 LOW-ENERGY ELECTRON MICROSCOPY

The LEEM measurements are performed using the aberration correcting ESCHER LEEM facility [26] which is based on a commercial SPECS P90 instrument and provides high-resolution imaging. Limitations on the angles of the incident and imaging beams make dark-field imaging in the canonical geometry, where the diffracted beam used for imaging leaves the sample along the optical axis, impossible. Instead, we use a tilted geometry where the incident angle is chosen such that the specular beam and the refracted beam used for imaging leave the sample under equal, but opposite, angles (illustrated in Fig. 4.1f,i). The tilted incidence yields an in-plane k-vector, which influences the reflectivity spectrum [34, 38]. This is taken into account in our calculations, but needs to be considered when comparing to other LEEM and LEED data. Microscopy is performed below 2×10^{-9} mbar and at 600 °C, to prevent the formation of hydrocarbon-based contaminants under the electron beam. Images are corrected for detector-induced artifacts by subtracting a dark count image and dividing by a gain image as described in the previous chapter before further analysis. Figure 4.4 is corrected for uneven illumination by dividing by the beam profile. Additionally, the minimum intensity in images shown is set to black and maximum intensity is set to white to ensure visibility of all details. In this chapter, all dark-field images and images showing domain walls are integrated for 4 s, all other images for 250 ms.

4.2.3 COMPUTATIONS

All calculations were performed with a full-potential linear augmented plane waves method based on a self-consistent crystal potential obtained within the local density approximation, as explained in Ref. [116]. The ab initio reflectivity spectra are obtained with the all-electron Bloch-wave-based scattering method described in Ref. [117]. The extension of this method to stand-alone two-dimensional films of finite thickness was introduced in Ref. [118]. Here, it is straightforwardly applied to the case of finite incidence angle to represent the experimental tilted geometry. An absorbing optical potential $V_i = 0.5\,\text{eV}$ was introduced to account for inelastic scattering: the imaginary potential $-iV_i$ is taken to be spatially constant over a finite slab (where the electron density is non-negligible) and to be zero in the two semi-infinite vacuum half-spaces. In addition, a Gaussian broadening of 1 eV is applied to account for experimental losses.

4.3 RESULTS

Figure 4.1**a,b** show bright-field LEEM images of two QFG samples with areas of different graphene thickness. Bright-field images are recorded using specularly reflected electrons that leave the sample perpendicular to the surface (see Figure 4.1**c**). The main contrast mechanism in this mode is the interaction of the imaging electrons with the thickness-dependent, unoccupied band structure of the material, which is used to un-

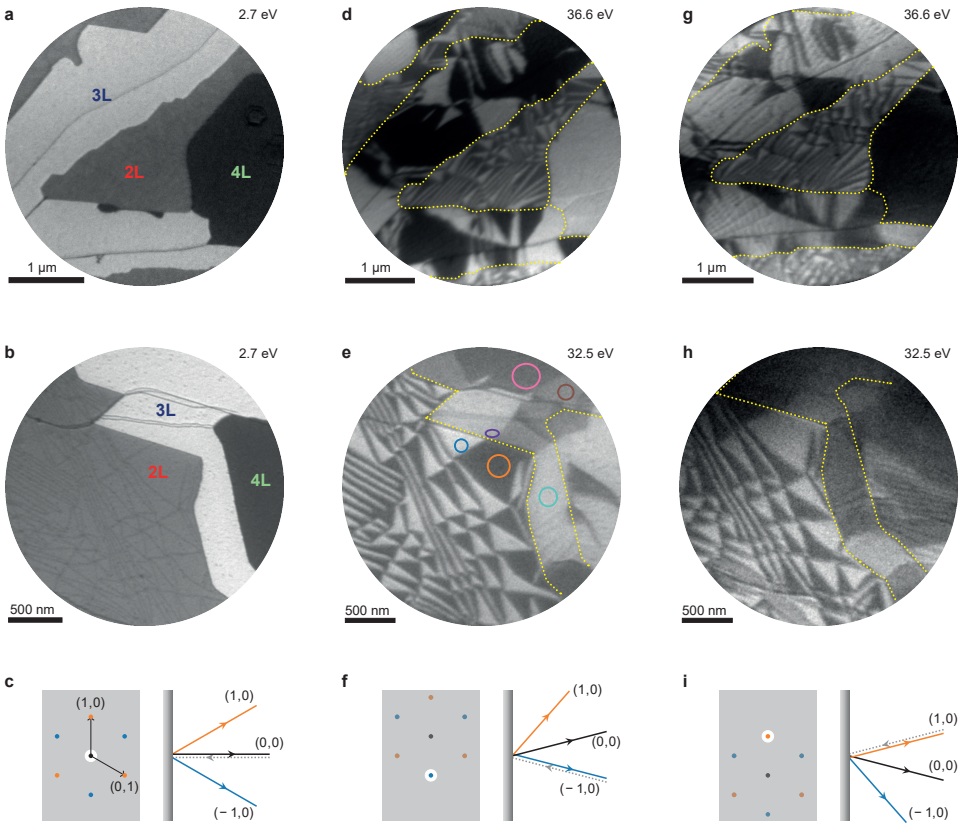

Figure 4.1: Graphene on SiC is composed of domains of different stacking order. a,b, *Bright-field LEEM micrographs of two samples of bilayer, trilayer and four-layer QFG.* ***c,*** *In bright-field geometry, images are recorded from specularly reflected electrons (black) by selecting the* (0,0) *diffraction spot using an aperture (gray rectangle) that blocks all diffracted beams (orange and blue).* ***d, e,*** *Dark-field images of the same area as in a,b. Domains of alternating contrast are clearly visible, indicating areas of different stacking order.* ***f,*** *Sketch of the tilted dark-field geometry selecting the* (−1,0) *spot as used for d,e.* ***g, h,*** *Dark-field images using the inequivalent* (1,0) *diffraction spot show inverted contrast compared to d,e.* ***i,*** *Measurement geometry used for g,h. See Methods for details on LEEM imaging modes. Yellow lines in* ***d-h*** *are guides to the eye indicating areas of constant layer number. Circles in e indicate areas from which the spectroscopy data in Fig. 4.2****c,d*** *is obtained.*

ambiguously determine the number of graphene layers [30, 38, 46]. Large, homogeneous areas of bilayer, trilayer and four-layer graphene can thus be distinguished in Figure 4.1**a,b**, supporting the notion of perfect crystallinity.

In stark opposition to this generally accepted view, the dark-field images in Figure 4.1**d,e** clearly reveal that all areas are actually fractured into domains of alternating contrast. The symmetry breaking introduced in dark-field imaging, where the image is formed from one diffracted beam only (cf. Figure 4.1**f**), leads to strong contrast between different stacking types of the graphene layers [47, 119]. In fact, the contrast between different domains inverts (Figure 4.1**d,e** versus **g,h**) when dark-field images are recorded from non-equivalent diffracted beams (cf. Fig. 4.1**f** and **i**).

At first glance, the observation of different stacking orders might seem surprising, as it is known that graphene layers grown on SiC(0001) are arranged in Bernal stacking [96]. However, two energetically equivalent versions of Bernal stacking (AB and AC) exist, and have been observed in other graphene systems [47, 106, 107, 120]. The AC stacking order can be thought of either as AB bilayer where the top layer is translated by one bond length, or alternatively, as a full AB bilayer rotated by 60 degrees (Fig. Figure 4.2**a,b**). Consequently, AB and AC stacking are indistinguishable in bright-field imaging. Subsequent layers can be added in either orientation, generating more complicated stacking orders for trilayer and beyond.

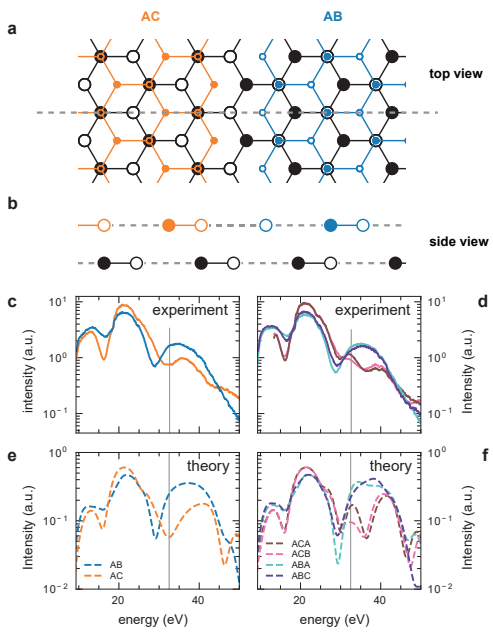

Figure 4.2: Low-energy electron reflectivity spectra reveal the local stacking order. ***a,*** *Sketched top view illustrating the difference between AC (orange) and AB (blue) stacking orders. Inequivalent atoms of the unit cell of the top layer (orange or blue) sit in the center of the hexagon of the bottom layer (black).* ***b,*** *Side view of the stacking along the dashed line in (a). Open and closed circles denote the inequivalent atoms of the graphene unit cell.* ***c,d,*** *Experimental dark-field reflectivity spectra recorded on different stacking domains on bilayer and trilayer graphene, respectively. The areas from which the spectra are recorded are indicated by circles in Fig. 4.1**e**.* ***e,f,*** *Theoretical dark-field spectra for AB and AC as well as ABA, ABC, ACA and ACB stacking orders obtained by* ab initio *calculations. A Gaussian broadening of* 1 eV *is applied to account for experimental losses. The vertical lines in **c** to **f** indicate the landing energy at which Figure 4.1**e,h** are recorded.*

4.3.1 SPECTROSCOPY

In order to identify the exact stacking in each area, we simulate bilayer and trilayer graphene slabs in different stacking orders and compare their reflectivity with measured low-energy electron reflectivity spectra. The latter are extracted from the intensity of an area in a series of spectroscopic LEEM images recorded at different electron landing energy (see Supplementary Movie 1 and 2 for such measurements of the area in Fig. 4.1**b** in bright-field and dark-field geometry, respectively)[1].

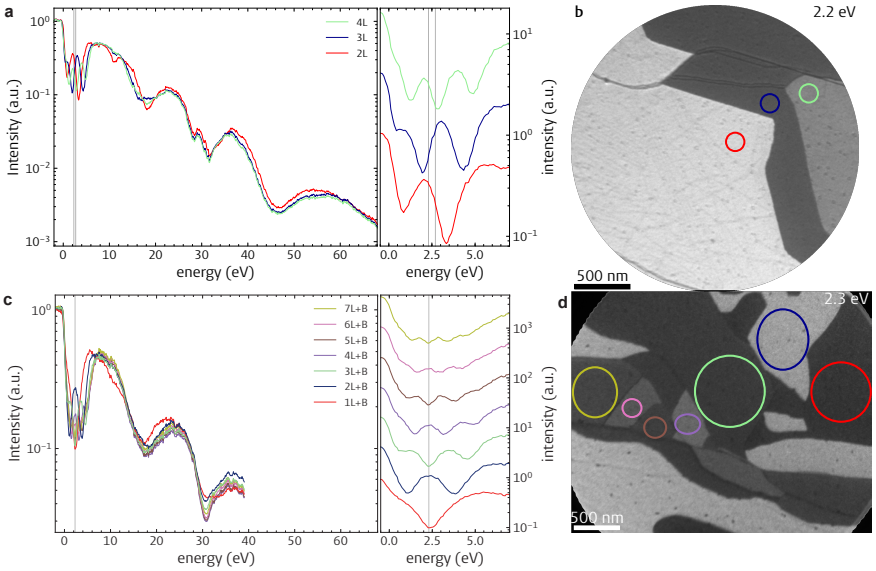

Figure 4.3: a, *Bright field intensity curves extracted from the data set of Supplementary Movie 1 (QFG). The minima used to determine graphene layer count are enlarged and offset for clarity on the right. Indicated with gray lines are the landing energies at which Supplementary Movie 3 and Figure 4.1**a,b** are taken.* ***b,*** *Same area as Figure 4.1**b**, but rendered at the energy of Supplementary Movie 3 and with the areas used for layer counting indicated.* ***c,*** *Bright field intensity curves of a non-intercalated EG sample with 1–7 layers. The minima used to determine graphene layer count are enlarged and offset for clarity on the right. Compared to QFG the minima are slightly shifted [46]. Indicated with gray line is the energy at which Supplementary Movie 3 is taken.* ***d,*** *Micrograph of EG sample with the areas used for layer counting in (c) indicated.*

While different domains show identical bright-field reflectivity (see Figure 4.3), dark-field spectra extracted from different bilayer domains (marked blue and orange in Fig. 4.2**c** and 4.1**e**) are clearly distinguishable. Moreover, four distinct reflectivity curves are observed for trilayer graphene (Fig. 4.2**d**). Figure 4.2**e,f** shows theoretical dark-field spectra, obtained by *ab initio* calculations (As described in Section 4.2.3), of different bilayer and trilayer stacking orders, respectively. The excellent agreement of theoretical and experimental data in Fig. 4.2**c,e** is clear evidence that the assignment of Bernal AB and AC

[1] Supplementary Movies of this chapter are available as Supplementary material to the original publication at http://link.aps.org/supplemental/10.1103/PhysRevMaterials.2.104005 [37]

stacking orders for different bilayer domains is correct. Moreover, the comparison of Fig. 4.2**d** and **f** shows that using these dark-field LEEM methods, we can distinguish the more complicated trilayer stacking orders: Bernal, ABA (cyan) and ACA (pink), versus rhombohedral ABC (purple) and ACB (brown). Due to the small electron penetration depth in LEEM, however, the spectra fall into two families (ABA and ABC vs. ACA and ACB) dominated by the stacking order of the top two layers.

4.3.2 DOMAIN MORPHOLOGY

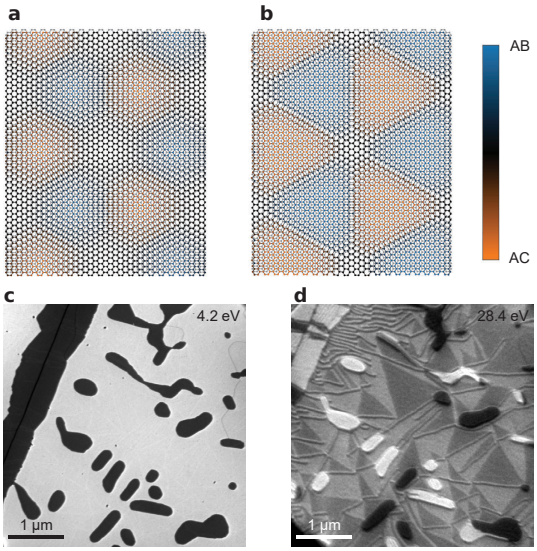

Figure 4.4: Stacking domains are caused by growth-induced strain and graphene nucleation dynamics. ***a,*** *Sketch of bilayer graphene where the top layer is uniformly strained causing a moiré pattern.* ***b,*** *Sketch of the energetically favored arrangement of AB and AC stacked domains with all strain concentrated into dislocation lines. The trigonal shape of the domains is clearly visible. The color denotes how close a local stacking order is to AB or AC stacking.* ***c,*** *A bright-field LEEM image of EG where growth was stopped shortly after bilayer starts to form.* ***d,*** *Dark-field LEEM of the same area reveals that the resulting islands, which emerged from individual nucleation sites, exhibit constant stacking order, i.e. they are either AB (bright) or AC (dark) stacked.*

In addition to their stacking orders, bilayer graphene and thicker areas differ in the morphology of the stacking domains (cf. Figure 4.1**d,e**), which indicates two distinct formation mechanisms. Most notably, bilayer domains are smaller, triangular and relatively regular. Similar morphologies have been observed in free-standing bilayer graphene, both etched from graphene-on-SiC [107] and transferred from copper [106, 121], where they were linked to strain between the layers introduced during sample growth or fabrication. While uniform strain causes a moiré reconstruction (Fig. 4.4**a**), it is often energetically favorable to form domains of commensurate, optimal Bernal stacking. In this case, all strain is concentrated into the domain walls, thus forming dislocation lines [106, 107], as sketched in Fig. 4.4**b**. Upon close examination of Fig. 4.1**b**, the network of these domain walls is visible as dark lines in our bright-field measurements. These lines correspond to the patterns observed by Speck et al. [103]. Such domain walls were predicted to host topological edge states [108, 109], which has also been experimentally confirmed recently [110, 120, 122].

The size of the triangular domains shrinks for increasing uniform strain, while anisotropic strain causes domains elongated perpendicular to the strain axis. The observed average domain diameter of ~100–200 nm coincides well with relaxation of the 0.2% lattice mismatch between buffer layer and first graphene layer [123]. We thus conclude that the tri-

angular domains in bilayer graphene result from strain thermally induced during growth and from the lattice mismatch with the SiC substrate and are intrinsic to the growth process. The presence of elongated triangular domains indicates non-uniform strain due to pinning to defects and substrate steps. (See Chapter 7 for a more extensive treatment of the relation between the domain sizes and the lattice strain).

The larger, irregularly shaped domains that dominate trilayer and four-layer areas (Figure 4.1**d,g**) can be explained by nucleation kinetics. To test this hypothesis, we study EG samples where the growth was stopped shortly after the nucleation of bilayer areas to prevent their coalescence. The resulting small bilayer islands on monolayer terraces are shown in bright-field and dark-field conditions in Figure 4.4**c** and **d**, respectively. We observe that bilayer areas with a diameter below ~300 nm form single domains of constant stacking order (either bright or dark in Fig. 4.4**d**) and that AB and AC stacked bilayer islands occur in roughly equal number. This indicates that new layers nucleate below existing ones in one of the two Bernal stacking orders randomly [95, 96, 113]. At the elevated growth temperature, domain walls in the existing layers can easily move to the edge of the new island where they annihilate. As islands of different stacking grow and coalesce, new domain walls are formed where they meet (cf. Fig. 4.2**a**). This opens the interesting possibility to engineer the dislocation network by patterning the SiC substrate before graphene growth.

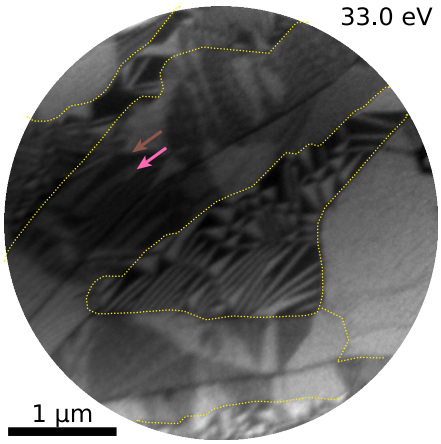

Figure 4.5: *Strain-induced triangular domains are also visible in the trilayer. They are formed between the two bottom-most layers and are, hence, only visible at certain energies. At 33 eV ABA stacked areas appear dark (e.g. marked by a brown arrow) and ABC domains bright (e.g. pink arrow). This assignment can be made from the dark-field reflectivity spectra shown in Figure 4.2**d**. The same area as in Figure 4.1**d,g** is shown with areas of different layer number outlined in yellow. The same dark-field alignment as in Figure 4.1**d–f** is used here.*

Notably, we observe strain-induced domains also in monolayer EG (Figure 4.4**d**) and between the bottom two layers in trilayer QFG (visible only for some energies, e.g. E_0 = 33 eV in Figure 4.5). The prevalence of these triangular domains in all EG and QFG samples between the two bottommost layers demonstrates that stacking domains are a direct consequence of the epitaxial graphene growth and consequently are a general feature of this material system. The resulting domain wall network explains the linear magnetoresistance observed in bilayer QFG [8] and might be an important culprit for the generally low mobility in EG and QFG [44].

4.3.3 INFLUENCE ON HYDROGEN DE-INTERCALATION

The presence of these strain-induced domains in EG as well as QFG raises the question of their role during (hydrogen) intercalation. Since the high hydrogen pressures necessary for intercalation are not compatible with in situ imaging, we investigate the inverse process. Figure 4.6**a,** shows a time series of bright-field LEEM images of the area shown in Figure 4.1**b** recorded at ~1000 °C (cf. Supplementary Movie 3). At this temperature, hydrogen slowly leaves the SiC–graphene interface [44, 45] and n-layer QFG is transformed back to $n-1$ layer (+ buffer layer) EG. The change in the reflectivity spectrum accompanied with this conversion (cf. Figure 4.3) yields strong contrast (e.g. dark in the bilayer in Figure 4.6**a**) and enables capture of the full deintercalation dynamics. Deintercalation starts at distinct point-like defect sites where hydrogen can escape and proceeds

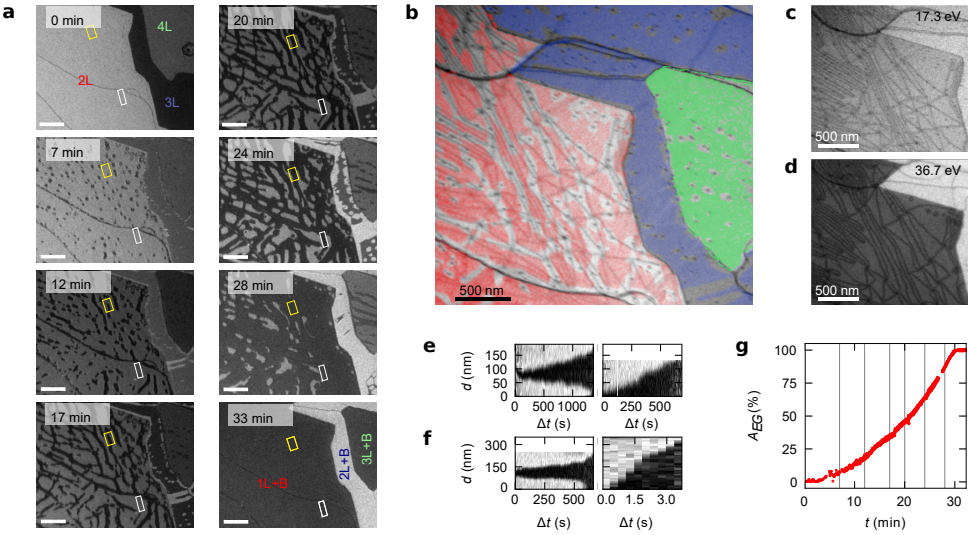

Figure 4.6: The hydrogen deintercalation dynamics is dominated by the graphene dislocation network. a, *Bright-field LEEM snapshots ($E = 2.2$ eV) of hydrogen deintercalation at ~1000 °C (the full time series is available as Supplementary Movie 3). Deintercalation starts in distinct points and deintercalated areas (dark in the bilayer region) grow in a strongly anisotropic fashion. Scale bars are 500 nm.* ***b,*** *Overlay of the deintercalation state at 15 min with a LEEM image showing the dislocation network (dark lines) beforehand. It reveals that deintercalation proceeds faster along dislocation lines. Areas shaded in color are still intercalated, while hydrogen is already removed in the uncolored areas.* ***c, d,*** *Bright-field images comparing the domain boundaries before and after deintercalation, respectively. While some dislocations move slightly, the overall features remain unchanged during the process.* ***a*** *to* ***d*** *show the same area as Fig. 4.1**b**.* ***e,*** *Slices along the time axis, perpendicular (left) and parallel (right) to the dislocation line marked yellow in* ***a****, illustrate the velocity of the deintercalation front.* ***f,*** *Same for the dislocation marked white in* ***a****. The movement of all deintercalation fronts is roughly linear in time and much faster parallel to dislocation lines than perpendicular.* ***g,*** *The fraction of deintercalated area A_{EG} extracted from the bilayer area in* ***a*** *grows non-linearly in time, indicating that the process is limited by the desorption of hydrogen at the boundary between intercalated and deintercalated areas.*

in a highly anisotropic fashion. An overlay of the half deintercalated state (15 min) with an image of the dislocations in the initial surface (Figure 4.6**b**) shows that deintercalation happens preferentially along dislocation lines. Although the dislocation lines are slightly mobile at higher temperatures (cf. Figure 4.6**c,d**) before and after deintercalation, respectively), their overall direction and density is preserved during the process. The local deintercalation dynamics reveal details of the underlying microscopic mechanism. Figure 4.6**e,f,** show that deintercalation fronts move roughly linearly in time both perpendicular and parallel to dislocation lines. The velocity of the deintercalation fronts however, is much larger parallel to dislocation lines (up to $v_{\parallel} = 95\,\mathrm{nm\,s^{-1}}$), than perpendicular to them ($v_{\perp} \approx 0.1\,\mathrm{nm\,s^{-1}}$). The linear movement rules out that deintercalation is limited by hydrogen diffusion, but indicates that hydrogen desorption at the deintercalation front is the limiting factor. The non-linear growth of the fraction of deintercalated area A_{EG} (Figure 4.6**g**) demonstrates that deintercalation is also not capped by the venting of hydrogen from the defects where deintercalation starts (7 min in Figure 4.6**a**). We conclude from these observations that the hydrogen desorption barrier is smaller within the domain walls than within the Bernal-stacked domains, possibly triggered by the higher lattice strain in the former. While $v_{\perp}$ is the same for all areas, $v_{\parallel}$ varies from $0.2\,\mathrm{nm\,s^{-1}}$ to $95\,\mathrm{nm\,s^{-1}}$ (marked yellow and white in Figure 4.6**a**, respectively), suggesting that the deintercalation process is strongly affected by the precise atomic details of the domain walls. These findings indicate that not only the deintercalation, but also the intercalation of hydrogen and other species, which all can not penetrate graphene, is dominated by the presence of stacking domains. Consequently, their manipulation, e.g. by patterning the substrate, will open a route towards improved intercalation and tailored QFG on the wafer-scale.

4.4 CONCLUSION

We conclude that graphene on SiC is a much richer material system than has been realized to this date. Specifically, we show that domains of AB and AC Bernal stacking orders are always present in this material, even for high quality argon-grown samples, and even though its layers appear perfectly crystalline to most methods. We deduce that these domains are formed between the two bottommost carbon layers (either graphene and buffer layer for EG or bilayer QFG) by strain relaxation. In addition, the nucleation of grains of different stacking order during growth causes larger domains in thicker layers. We show that dislocation lines between domains dominate hydrogen deintercalation dynamics, highlighting their importance for intercalation as well. By engineering these dislocation networks, we foresee wide implications for customized QFG for electronic applications. Moreover, the dislocation networks observed here could yield a wafer-scale platform for topological [108–110, 120, 122] and possibly strongly correlated electron phenomena [4, 111, 112] when tailored into periodic structures.

REFERENCES

4. Y. Cao, V. Fatemi, S. Fang, et al. Unconventional superconductivity in magic-angle graphene superlattices. *Nature* **556,** 43–50. doi:10.1038/nature26160 (2018).

6. J. Kautz, J. Jobst, C. Sorger, et al. Low-Energy Electron Potentiometry: Contactless Imaging of Charge Transport on the Nanoscale. *Scientific Reports* **5,** 13604. doi:10.1038/srep13604 (2015).

7. S.-H. Ji, J. B. Hannon, R. M. Tromp, et al. Atomic-scale transport in epitaxial graphene. *Nature Materials* **11,** 114–119. doi:10.1038/nmat3170 (2012).

8. F. Kisslinger, C. Ott, C. Heide, et al. Linear magnetoresistance in mosaic-like bilayer graphene. *Nature Physics* **11,** 650–653. doi:10.1038/nphys3368 (2015).

26. S. Schramm, J. Kautz, A. Berghaus, et al. Low-energy electron microscopy and spectroscopy with ESCHER: Status and prospects. *IBM Journal of Research and Development* **55,** 1–1. doi:10.1147/JRD.2011.2150691 (2011).

30. H. Hibino, H. Kageshima, F. Maeda, et al. Microscopic thickness determination of thin graphite films formed on SiC from quantized oscillation in reflectivity of low-energy electrons. *Physical Review B* **77,** 075413. doi:10.1103/PhysRevB.77.075413 (2008).

34. J. Jobst, A. J. H. van der Torren, E. E. Krasovskii, et al. Quantifying electronic band interactions in van der Waals materials using angle-resolved reflected-electron spectroscopy. *Nature Communications* **7,** 13621. doi:10.1038/ncomms13621 (2016).

37. T. A. de Jong, E. E. Krasovskii, C. Ott, et al. Intrinsic stacking domains in graphene on silicon carbide: A pathway for intercalation. *Physical Review Materials* **2,** 104005. doi:10.1103/PhysRevMaterials.2.104005 (2018).

38. J. Jobst, J. Kautz, D. Geelen, R. M. Tromp & S. J. van der Molen. Nanoscale measurements of unoccupied band dispersion in few-layer graphene. *Nature Communications* **6,** 8926. doi:10.1038/ncomms9926 (2015).

44. F. Speck, J. Jobst, F. Fromm, et al. The quasi-free-standing nature of graphene on H-saturated SiC(0001). *Applied Physics Letters* **99,** 122106. doi:10.1063/1.3643034 (2011).

45. C. Riedl, C. Coletti, T. Iwasaki, A. A. Zakharov & U. Starke. Quasi-Free-Standing Epitaxial Graphene on SiC Obtained by Hydrogen Intercalation. *Physical Review Letters* **103,** 246804. doi:10.1103/PhysRevLett.103.246804 (2009).

46. R. M. Feenstra, N. Srivastava, Q. Gao, et al. Low-energy electron reflectivity from graphene. *Physical Review B* **87,** 041406. doi:10.1103/PhysRevB.87.041406 (2013).

47. H. Hibino, S. Mizuno, H. Kageshima, M. Nagase & H. Yamaguchi. Stacking domains of epitaxial few-layer graphene on SiC(0001). *Physical Review B* **80,** 085406. doi:10.1103/PhysRevB.80.085406 (2009).

89. C. R. Eddy & D. K. Gaskill. Silicon Carbide as a Platform for Power Electronics. *Science* **324,** 1398–1400. doi:10.1126/science.1168704 (2009).

90. Y.-M. Lin, C. Dimitrakopoulos, K. A. Jenkins, et al. 100-GHz Transistors from Wafer-Scale Epitaxial Graphene. *Science* **327,** 662–662. doi:10.1126/science.1184289 (2010).

91. A. Tzalenchuk, S. Lara-Avila, A. Kalaboukhov, et al. Towards a quantum resistance standard based on epitaxial graphene. *Nature Nanotechnology* **5,** 186–189. doi:10.1038/nnano.2009.474 (2010).

92. S. Hertel, D. Waldmann, J. Jobst, et al. Tailoring the graphene/silicon carbide interface for monolithic wafer-scale electronics. *Nature Communications* **3,** 957. doi:10.1038/ncomms1955 (2012).

93. F. Bianco, D. Perenzoni, D. Convertino, et al. Terahertz detection by epitaxial-graphene field-effect-transistors on silicon carbide. *Applied Physics Letters* **107,** 131104. doi:10.1063/1.4932091 (2015).

94. C. Virojanadara, M. Syväjarvi, R. Yakimova, et al. Homogeneous large-area graphene layer growth on 6 H-SiC (0001). *Physical Review B* **78,** 245403. doi:10.1103/PhysRevB.78.245403 (2008).

95. K. V. Emtsev, A. Bostwick, K. Horn, et al. Towards wafer-size graphene layers by atmospheric pressure graphitization of silicon carbide. *Nature Materials* **8,** 203–207. doi:10.1038/nmat2382 (2009).

96. W. A. de Heer, C. Berger, M. Ruan, et al. Large area and structured epitaxial graphene produced by confinement controlled sublimation of silicon carbide. *Proceedings of the National Academy of Sciences* **108,** 16900–16905. doi:10.1073/pnas.1105113108 (2011).

97. Y.-M. Lin, A. Valdes-Garcia, S.-J. Han, et al. Wafer-Scale Graphene Integrated Circuit. *Science* **332,** 1294–1297. doi:10.1126/science.1204428 (2011).

98. K. V. Emtsev, A. A. Zakharov, C. Coletti, S. Forti & U. Starke. Ambipolar doping in quasifree epitaxial graphene on SiC(0001) controlled by Ge intercalation. *Physical Review B* **84,** 125423. doi:10.1103/PhysRevB.84.125423 (2011).

99. R. Nandkishore, L. S. Levitov & A. V. Chubukov. Chiral superconductivity from repulsive interactions in doped graphene. *Nature Physics* **8,** 158–163. doi:10.1038/nphys2208 (2012).

100. Y. Li, P. Tang, P. Chen, et al. Topological insulators in transition-metal intercalated graphene: The role of d electrons in significantly increasing the spin-orbit gap. *Physical Review B* **87,** 245127. doi:10.1103/PhysRevB.87.245127 (2013).

101. J. Baringhaus, A. Stöhr, S. Forti, U. Starke & C. Tegenkamp. Ballistic bipolar junctions in chemically gated graphene ribbons. *Scientific Reports* **5,** 9955. doi:10.1038/srep09955 (2015).

102. N. A. Anderson, M. Hupalo, D. Keavney, M. C. Tringides & D. Vaknin. Intercalated europium metal in epitaxial graphene on SiC. *Physical Review Materials* **1,** 054005. doi:10.1103/PhysRevMaterials.1.054005 (2017).

103. F. Speck, M. Ostler, S. Besendörfer, et al. Growth and Intercalation of Graphene on Silicon Carbide Studied by Low-Energy Electron Microscopy. *Annalen der Physik* **529,** 1700046. doi:10.1002/andp.201700046 (2017).

104. V. Berry. Impermeability of graphene and its applications. *Carbon* **62,** 1–10. doi:10.1016/j.carbon.2013.05.052 (2013).

105. S. Hu, M. Lozada-Hidalgo, F. C. Wang, et al. Proton transport through one-atom-thick crystals. *Nature* **516,** 227–230. doi:10.1038/nature14015 (2014).

106. J. S. Alden, A. W. Tsen, P. Y. Huang, et al. Strain solitons and topological defects in bilayer graphene. *Proceedings of the National Academy of Sciences* **110,** 11256–11260. doi:10.1073/pnas.1309394110 (2013).

107. B. Butz, C. Dolle, F. Niekiel, et al. Dislocations in bilayer graphene. *Nature* **505,** 533–537. doi:10.1038/nature12780 (2014).

108. I. Martin, Y. M. Blanter & A. F. Morpurgo. Topological Confinement in Bilayer Graphene. *Physical Review Letters* **100,** 036804. doi:10.1103/PhysRevLett.100.036804 (2008).

109. X. Li, F. Zhang, Q. Niu & A. H. MacDonald. Spontaneous layer-pseudospin domain walls in bilayer graphene. *Physical Review Letters* **113,** 116803. doi:10.1103/PhysRevLett.113.116803 (2014).

110. L. Ju, Z. Shi, N. Nair, et al. Topological valley transport at bilayer graphene domain walls. *Nature* **520,** 650–655. doi:10.1038/nature14364 (2015).

111. B. Hunt, J. D. Sanchez-Yamagishi, A. F. Young, et al. Massive Dirac Fermions and Hofstadter Butterfly in a van der Waals Heterostructure. *Science* **340,** 1427–1430. doi:10.1126/science.1237240 (2013).

112. Y. Cao, V. Fatemi, A. Demir, et al. Correlated insulator behaviour at half-filling in magic-angle graphene superlattices. *Nature* **556,** 80–84. doi:10.1038/nature26154 (2018).

113. S. Tanaka, K. Morita & H. Hibino. Anisotropic layer-by-layer growth of graphene on vicinal SiC(0001) surfaces. *Physical Review B* **81,** 041406. doi:10.1103/PhysRevB.81.041406 (2010).

114. R. M. Tromp & J. B. Hannon. Thermodynamics and Kinetics of Graphene Growth on SiC(0001). *Physical Review Letters* **102,** 106104. doi:10.1103/PhysRevLett.102.106104 (2009).

115. P. Lauffer, K. V. Emtsev, R. Graupner, et al. Atomic and electronic structure of few-layer graphene on SiC(0001) studied with scanning tunneling microscopy and spectroscopy. *Physical Review B* **77,** 155426. doi:10.1103/PhysRevB.77.155426 (2008).

116. E. E. Krasovskii, F. Starrost & W. Schattke. Augmented Fourier components method for constructing the crystal potential in self-consistent band-structure calculations. *Physical Review B* **59,** 10504–10511. doi:10.1103/PhysRevB.59.10504 (1999).

117. E. E. Krasovskii. Augmented-plane-wave approach to scattering of Bloch electrons by an interface. *Physical Review B* **70,** 245322. doi:10.1103/PhysRevB.70.245322 (2004).

118. V. U. Nazarov, E. E. Krasovskii & V. M. Silkin. Scattering resonances in two-dimensional crystals with application to graphene. *Phys. Rev. B* **87,** 041405. doi:10.1103/PhysRevB.87.041405 (4 2013).

119. D. A. Siegel, S. Y. Zhou, F. El Gabaly, et al. Three-fold diffraction symmetry in epitaxial graphene and the SiC substrate. *Physical Review B* **80,** 241407 (2009).

120. H. Yoo, R. Engelke, S. Carr, et al. Atomic and electronic reconstruction at the van der Waals interface in twisted bilayer graphene. *Nature Materials* **18,** 448–453. doi:10.1038/s41563-019-0346-z (2019).

121. L. Brown, R. Hovden, P. Huang, et al. Twinning and Twisting of Tri- and Bilayer Graphene. *Nano Letters* **12,** 1609–1615. doi:10.1021/nl204547v (2012).

122. L.-J. Yin, H. Jiang, J.-B. Qiao & L. He. Direct imaging of topological edge states at a bilayer graphene domain wall. *Nature Communications* **7,** 11760. doi:10.1038/ncomms11760 (2016).

123. T. Schumann, M. Dubslaff, M. H. Oliveira, et al. Effect of buffer layer coupling on the lattice parameter of epitaxial graphene on SiC(0001). *Physical Review B* **90,** 041403. doi:10.1103/PhysRevB.90.041403 (2014).

5

ON STACKING CONTRAST OF LOW ENERGY ELECTRONS IN MULTILAYER GRAPHENE

Parts of this chapter are under review as T. A. de Jong, X. Chen, E. E. Krasovskii, R. M. Tromp, J. Jobst & S. J. van der Molen, Low-Energy Electron Microscopy contrast of stacking boundaries: comparing twisted few-layer graphene and strained epitaxial graphene on silicon carbide [124]

5.1 INTRODUCTION

In the previous chapter we have shown that Dark Field LEEM can be used to image stacking domains in bilayer and trilayer graphene on SiC. Tilted DF-LEEM was used, as the rotational equivalency between AB and AC stacking means no contrast can be expected in Bright Field LEEM. However, the domain boundaries themselves can be imaged in BF-LEEM, as is already visible in for example Figure 4.6**c,d** and Figure 3.11**b**. In this chapter, we will explore the contrast mechanisms enabling this. To do so, the intensity of the domain boundaries needs to be separated from the domains themselves, which is non-trivial because the domain boundaries are a few pixels wide at most. Improving on the PCA-based method used in Section 3.5.2, we will here average over multiple unit cells to increase the resolution and signal-to-noise ratio and extract the contrast information as a function of E_0 we need. We will use this information to compare domain boundaries in graphene on SiC with the similar domain boundaries occurring in twisted bilayer graphene. First the material systems and precise type of domain boundaries occurring in them are discussed, before the averaging method and the results.

5.1.1 GRAPHENE ON SILICON CARBIDE

Graphene on silicon carbide (SiC(0001)) is grown by thermal decomposition. As silicon has a lower sublimation point than carbon, heating an atomically flat surface of SiC to 1200°C or higher, the silicon evaporates, while the carbon stays behind [12, 125]. Every three layers of carbon of the original SiC crystal form a single layer of hexagonal carbon [126]. Growing the graphene at higher temperatures or keeping it hot for longer causes more silicon to evaporate and extra layers to form between the buffer layer and the lowest graphene layer [127]. This growth is faster and less regular on the carbon face of the SiC than on the Si face, and here we will focus on growth on the Si face. To create more regular layers, a gas backpressure of silane [114] or, more commonly, argon of up to one bar can be supplied. This achieves more uniform growth at lower speeds and higher temperatures [95]. Additionally, extra carbon can be provided by depositing carbon in advance [10, 128].

There are several benefits in this growth method compared to the alternative, graphene growth on metals. The main advantage is that the growth is epitaxial, and therefore results in a single orientation of graphene, while for all metal growth procedures step edges, metal grains and multiple possible growth orientations will cause domains of varying orientation. Furthermore, SiC wafers integrate well in the semiconductor industry, making wafer-scale applications easier to implement.

However, the lattice constant of hexagonal carbon does not match the lattice constant of SiC. Thus a higher-order commensurate reconstruction, i.e. a moiré pattern is formed, denoted by $\left(6\sqrt{3}\times 6\sqrt{3}\right)R30°$ [12, 13].

The first layer of hexagonal carbon is covalently bonded to the SiC surface. This means this so-called buffer layer is insulating due to the lack of pure sp^2 hybridization and that it adheres perfectly to the higher-order commensurate reconstruction. All subsequent carbon layers are true graphene layers and thus only bonded to the lower layers by Van der Waals forces. Aside from the implications for the conduction, this also implies that the graphene layer on top of the buffer layer has much lower interlayer interaction energies than the buffer layer with respect to the SiC substrate. Therefore, any residual

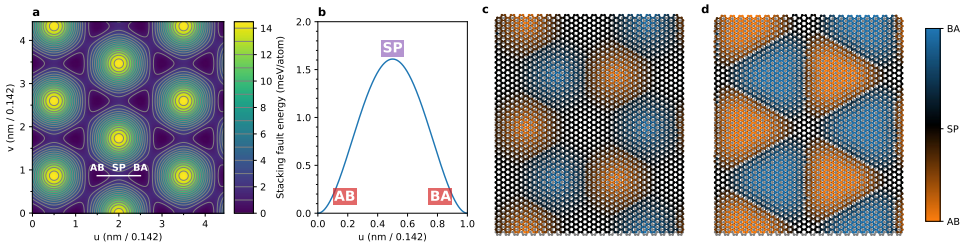

Figure 5.1: ***a,*** *Approximate interlayer stacking energy (in meV/atom) for bilayer graphene as a function of relative displacement in units of the graphene bond length $l_0 = 0.142\,nm$, as given in Ref. [19]. (cf. calculated energy in Ref. [11]). Note that the stacking energy for AA stacking relative to Bernal stacking (AB/BA) is around 9 times higher than the maximum occurring in a domain wall, which is labeled SP (for saddle point).* ***b,*** *Least energy cut through the energy landscape as indicated in* ***a****, from AB to BA stacking across the saddle point.* ***c,*** *Schematic of two unrelaxed hexagonal lattices with slightly different lattice constant.* ***d,*** *As Bernal stacking (AB/BA) is energetically favorable compared to other stackings, the bilayer will relax to form triangular Bernal stacked domains with all strain concentrated in the boundaries.*

lattice constant mismatch between graphene and the $\left(6\sqrt{3}\times 6\sqrt{3}\right)R30°$ reconstruction of the buffer layer can be resolved, especially at the high growth temperatures.

As the buffer layer is similar to a graphene layer, the interlayer stacking energy landscape should be similar to that of bilayer graphene, which is shown in Figure 5.1**a**. Here, the Bernal stackings (AB/BA)[1] are the energy minima. When one of the layers is shifted to form AA stacking, this corresponds to a maximum. For a small residual lattice mismatch, schematically shown in Figure 5.1**c**, the relative stacking and therefore the local interlayer stacking energy varies continuously as a function of position. When relaxing this structure, the interlayer stacking energy will be minimized at the cost of some stretching of the layer. Now, triangular domains form, where in each boundary the strain is concentrated (Figure 5.1**d**), and the stacking varies smoothly, going from one Bernal minimum to the other via the saddle point (SP) in the energy landscape (Figure 5.1**b**).

Indeed, in Chapter 4, we have shown that the residual lattice mismatch at the growth temperature causes such stacking domains between the (intercalated) buffer layer and the subsequent graphene layer [129, 130], with an influence on the (de-)intercalation process. The morphology and variety of the domains and the connection to strain and defects is explored in more depth in Chapter 7.

5.1.2 TWISTED FEW-LAYER GRAPHENE

In twisted few-layer graphene made by mechanical exfoliation, the lattice mismatch is not due to an intrinsic mismatch of the lattice constant of the graphene with respect to that of the substrate, but by artificially rotating the top layers by a twist angle θ with respect to the bottom layers.

[1] As stacking labels correspond to the sublattice labels, which can be freely permuted when labeling bilayers, AB, BC and CA are equivalent, as are AC, BA and CB. While technically one can argue that in the case of graphene on SiC the buffer layer is commensurate to the substrate and should therefore maintain the same label, for simplicity we will use AB and BA for the two different Bernal stackings in this chapter.

Here, a continuous transition from the commensurate case at $\theta = 0$ to the incommensurate case for twist angles larger than a critical angle occurs. This critical angle depends on the precise number of layers. Here, precise estimates of the critical angle vary, with estimates for the 1-on-1 layer case between about 1 and 2 degree [120, 129].[2] Below the critical angle, locally commensurate stacking domains form, with all strain concentrated in domain boundaries [129, 130]. However, these domain boundaries are qualitatively different for the twisted case compared to the biaxially strained case: while in the strained case the lattice mismatch or displacement compensated by the domain boundary is perpendicular to the so-called **tensile** domain boundary, in the twisted case this is parallel to the so-called **shear** domain boundary.

In the more general case of mixed twist and (uniaxial) strain, mixes between these two types also occur. Applying the two chain Frenkel-Kontorova model to bilayer graphene, Lebedeva and Popov found that the shear domain boundary has a slightly lower total energy cost per unit length than the tensile boundary [19]. They also calculated a width of 13.4 nm for the tensile domain wall and 8.6 nm for the shear domain wall. These values match experimental values of 11 nm and 6–7 nm measured using TEM [106, 131] to within the expected accuracy of their model.

Both in the twisted case and in the biaxially strained case, domain boundaries that occur at different azimuthal angles have to cross. In bilayer graphene, such a domain boundary crossing corresponds to AA-stacking, and is therefore called an AA-node.

Notably, in the twisted case, such domain boundary stackings are in some sense topologically protected: short of destroying the lattice by adding or removing atoms, they can only be destroyed by moving them all the way to the edge of the system. As they therefore exhibit particle-like properties, they are sometimes called **twistons** [132]. Similar properties hold in the strained case, and therefore we mint the term **strainons** for AA-nodes in graphene on SiC.

As AA stacking corresponds to a maximum in the stacking energy, domain boundary crossings have an extra energy cost. When that energy cost is higher than the cost of absorbing the strain to a commensurate stacking in one direction, a stripe phase occurs where the strain is concentrated in domain boundaries in only one direction [19].

5.1.3 IMAGING DOMAIN BOUNDARIES

There are several reasons to study domain boundaries in twisted and strained systems. A first reason is to accurately measure the atomic lattice mismatch of the constituting systems. A second reason is that the domain boundaries may have effects on physical properties of the system, as is the case for hydrogen (de-)intercalation of graphene on SiC (Chapter 4) and the existence of edge states along the domain boundary [108, 122, 133, 134]. A final reason, employed in Ref. [17] as well as in Chapters 6 and 7, is that the domain boundary patterns magnify the local relative differences of the lattices, enabling imaging of local strain and deformations. This includes local topological atomic defects, which are magnified in the domain boundary pattern, in particular edge dislocations. Thus, such defects can be made visible without imaging the atomic lattice directly.

[2] Notably, this critical angle and the first magic angle for bilayer graphene are very close. What is more, for additional layers, both angles increase.

In this chapter, we use Bright Field Low Energy Electron Microscopy (BF-LEEM) to characterize the contrast of domain boundaries in both twisted graphene systems and in the strained graphene on (buffer layer on) SiC and subsequently compare them [25, 27, 37, 135]. In Chapter 7, the domain boundaries are used to extract information about the influences that different growth procedures may have on the interlayer interaction and the local disorder this produces.

5.2 STACKING CONTRAST OF BILAYERS IN LEEM

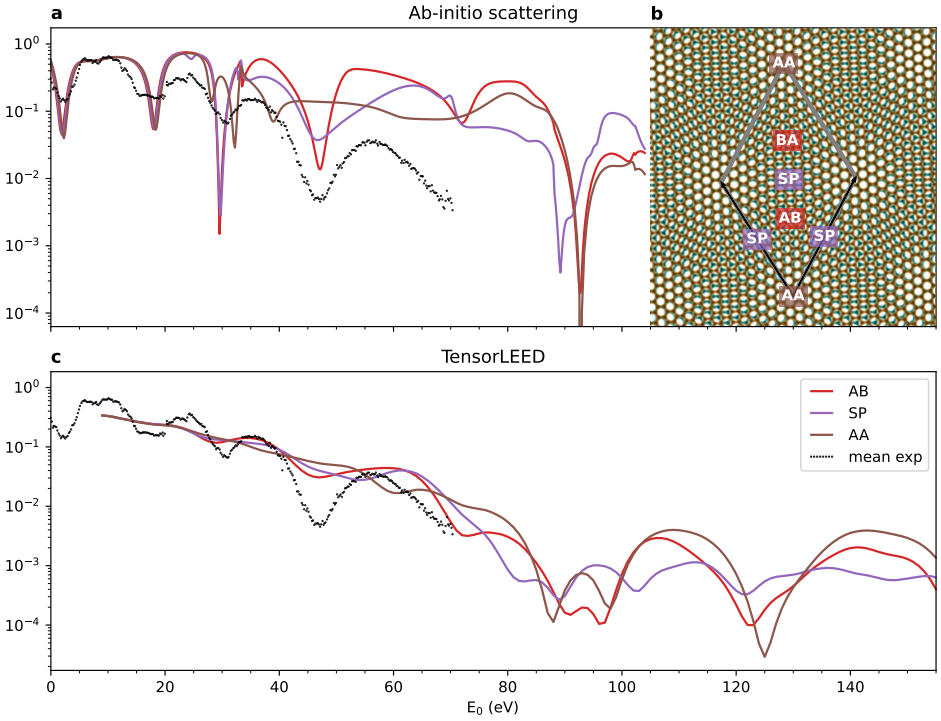

Figure 5.2: ***a,*** *Calculated electron reflectivity with the ab-initio Bloch-wave-based scattering method described in Ref. [136] for different bilayer graphene stackings as calculated by E.E. Krasovskii. The different relative shifts of the two graphene layers correspond to different positions within the unit cell. In black dots, the mean reflectivity of* $\theta \approx 0.18^\circ$ *TBG on hBN is overlayed for comparison.* ***b,*** *TBG unit cell schematic with positions where the different stackings occur labeled.* ***c,*** *Similar as a, but calculated using tensorLEED, from ref. [137].*

In Dark Field LEEM (DF-LEEM), the rotational equivalence between the two possible Bernal stackings, AB and BA, is broken, causing contrast between the domains themselves [37, 138]. In BF-LEEM, both Bernal stackings are fully equivalent by rotation and no contrast between them can be expected, but the domain boundaries themselves do cause contrast. To understand the domain boundary contrast observed with LEEM we

would like to compare measurements to theoretical calculations. Unfortunately, the super cells, both of twisted bilayer graphene at angles near the magic angle and of any reasonable lattice mismatch caused by strain, contain too many atoms to be amenable to reflectivity calculations using conventional methods. A simplifying assumption to tackle the problem would be that for large enough unit cells, the main contrast mechanism is due to stacking contrast, e.g. the different local stackings in the super cell having slightly different electron reflectivities as a function of landing energy, causing visible contrast to image the super cells. Here any lateral interaction between the different areas in the unit cell is ignored, which is equivalent to assuming pure amplitude contrast and no phase contrast [139].

To test this assumption, we compare experimentally observed contrast to ab-initio calculations from different sources: an ab-initio Bloch-wave-based scattering method computed by E.E. Krasovskii [135, 140] and traditional tensorLEED calculations as reported in Ref. [137]. Computed reflectivity curves from both methods are shown in Figure 5.2, together with an indication of where the different stackings occur in the unit cell of TBG.

Both calculations predict very little contrast between different stackings at landing energies lower than the appearance of the first order diffraction spots, i.e. $E_0 \lesssim 30\,\text{eV}$. The contrast increases for higher E_0. However, two things should be noted here. First, the so-called muffin tin approximation used in tensorLEED severely limits its accuracy at low energies. The ab-initio scattering method is much more accurate in this energy regime. Remarkably, the difference between the different stackings in the ab-initio scattering calculations seems to be limited to a small shift along energy, i.e. a slight work function difference. The second thing to note is that although high contrast is predicted for higher energies, in experimental practice, the measured contrast for higher energies is decreased by both inelastic losses, causing broadening of the measured spectra, and decreasing intensity, causing decreased signal-to-noise ratios. This means that a priori, it is not clear from these calculations what would be the optimal energy to measure such stacking contrast.

5.2.1 UNIT CELL AVERAGING

To further complicate comparison to experiment, the width of a single domain boundary is too small to accurately sample at a single position, making comparison to the calculated reflectivity of different stackings for different regions of interest impractical.[3]

Therefore, to optimally compare experiment and theory, we will try to average data over multiple unit cells of the moiré lattice. However, in general, strain and twist angle variation will cause deformation of the unit cell, which means we can not just project back into the unit cell by shifting pixels over integer multiples of the unit vectors. Instead, as illustrated in Figure 5.3, we should first correct the deformation due to strain and twist angle, which we can do by calculating the displacement field $\mathbf{u}(\mathbf{r})$ (green arrows in Figure 5.3**a**) using geometric phase analysis (See Appendix A), such that $\mathbf{r}' = \mathbf{r} + \mathbf{u}(\mathbf{r})$ with $\mathbf{r}'$ the corresponding position in the *undistorted* lattice. This can then be used to perform a Lawler-Fujita type distortion correction [135, 141–143], where an undistorted image is

[3] In fact, the domain boundaries might be too thin to observe at all in non-aberration corrected LEEM, as attempts using microscopes without aberration correction have so far been unsuccessful.

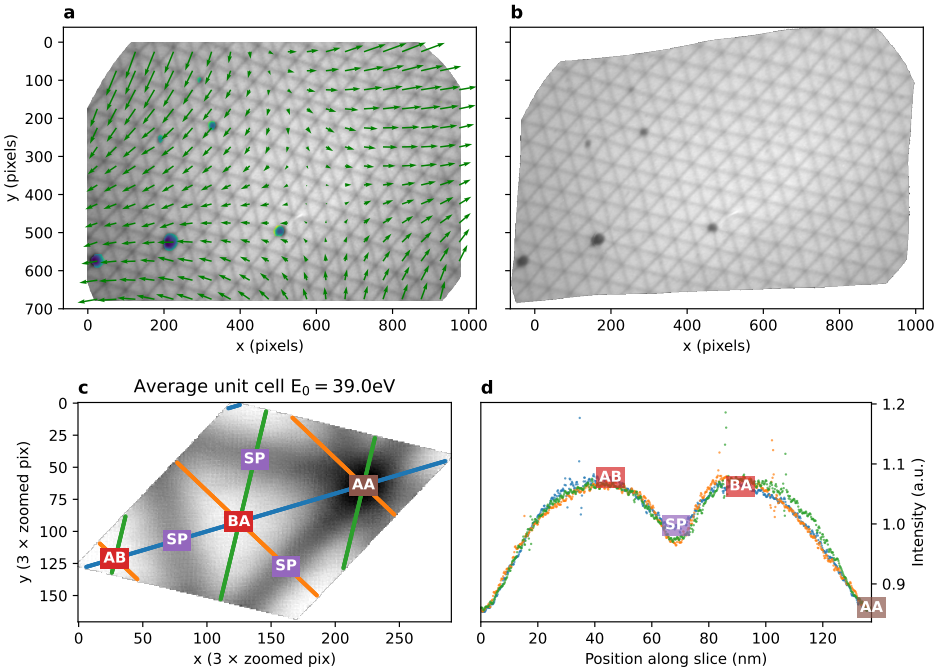

Figure 5.3: Unit cell averaging. ***a,*** *From a displacement field* $\mathbf{u}(\mathbf{r})$ *calculated using GPA (green arrows), we can compute a corrected regular lattice as shown in* ***b****. This regular lattice can be averaged by projecting into a single unit cell* ***c*** *by subtracting integer multiples of the lattice vectors.* ***d,*** *To visualize the unit cell as a function of energy, equivalent cuts in different directions along the unit cell can be made. Colors match the indicated slices in* ***c*** *and Figure 5.4. Spikes in the intensity are due to incorrect handling of the edges of the unit cell (See Section 5.6) and are filtered out in the results. The image used for illustration here is the* $\theta \approx 0.18°$ *TBG sample also used in Figure 5.4.*

sampled from positions $\mathbf{r}' + \mathbf{u}^{-1}(\mathbf{r}')$ by interpolation, where $\mathbf{u}^{-1}$ is determined by approximation or by numerical inversion. Of the resulting image, shown in Figure 5.3**b**, it is now possible to project all cells into a single unit cell (Figure 5.3**c**) by integer multiples of the unit vectors:

$$\mathbf{r}_p = \left(A^{-1}\mathbf{r}\right) \mod 1$$

Here, A is the matrix with the lattice vectors as columns, such that A^{-1} converts to coordinates in terms of the lattice vectors.

However, this two-step process would cause interpolation errors twice and is unsuited for upscaling of the unit cell to recover more detail. Fortunately, once $\mathbf{u}(\mathbf{r})$ is known, we can directly compute the precise (i.e. sub-pixel coordinates) position inside the unit cell for each pixel in the original image:

$$\mathbf{r}_p = \left(A^{-1}(\mathbf{r} + \mathbf{u}(\mathbf{r}))\right) \mod 1$$

Therefore we can directly combine all pixels of the original image (Figure 5.3**a**) into an average unit cell (**c**), scaling up and using a 'drizzle' like [144, 145] approach to minimize the smoothing caused by the recombination and we may even hope to recover some additional detail not apparent from the original images.[4]

The process described above allows us to compute a single average unit cell from an image with distortion, provided that the moiré contrast and signal-to-noise ratio are high enough. By doing this for all images in a spectroscopic LEEM dataset, we can obtain the average unit cell reflectivity as a function of E_0. However, the contrast of the moiré will be essentially zero for some energies, causing the extraction of the distortion field to fail. We also need to exclude areas with significant (dirt) artefacts. Furthermore, the area used for averaging should be limited to an area with approximately constant distortion, as the contrast may depend on the distortion. For example, domain boundaries have an approximately constant width, independent of unit cell size and distortion, which is thus distorted when projecting back different size unit cells to a single unit cell. Accommodating these complications, the unit cell averaging process we use is as follows:

0. Properly correct the dataset for detector artefacts and drift.
1. Compute $\mathbf{u}(\mathbf{r})$ with respect to an isotropic lattice for a value of E_0 where the contrast of the moiré is high enough. Preferably use an image consisting of the average over a few images around that energy to minimize noise.
2. Determine the high symmetry point (in practice the AA site) from the same image. This is used to take one-dimensional slices of the data later on.
3. Mask out any adsorbates and otherwise unwanted areas. In implementation, this is done by converting any such areas to NaNs and explicitly ignoring NaNs in the actual unit cell averaging.[5]
4. Use the same distortion field $\mathbf{u}(\mathbf{r})$ to compute an average unit cell for all landing energies.
5. Take appropriate slices through the unit cells that enumerate the theoretically computed stackings.
6. To cancel out disagreements between models and experimental data in the global intensity, divide these cuts by some reference stacking, in this case Bernal stacking. In the following, if this is not feasible due to remaining detector drift, we divide by the average spectrum instead. Finally, for comparison, we take the natural logarithm of the result.

The core unit cell averaging algorithm is written in Python and made available as part of `pyGPA` [88], and the Python code used to generate the figures in this Chapter is available at Ref. [146].

[4] The amount of detail within the unit cell that can be recovered in this way depends on the ratio between the pixel pitch and the width of the contrast transfer function (CTF) of the instrument. Therefore this technique might be applied with much more result to experiments where this ratio is large, such as large field-of-view STM, STEM, or AFM measurements.

[5] For simplicity, any area where data is missing for any value of E_0 due to detector drift is ignored, although this could in theory be used for the energies where data exists.

5.2.2 TWISTED BILAYER GRAPHENE RESULTS

The unit cell averaging procedure introduced in the previous section is applied to a dataset of twisted bilayer graphene (TBG), with a twist angle of $\theta \approx 0.18^\circ$ and a detector resolution in the original dataset of 1.36 nm/pixel (See Figure 5.3). The results are compared to the ab-initio theory in Figure 5.4. Although the experimental contrast is much lower, a remarkably good correspondence is achieved above 20 eV. This includes the contrast inversions, where domain boundaries and the AA site change from brighter than the Bernal (AB or BA) stacking (red) to darker (blue) and vice versa as a function of energy.

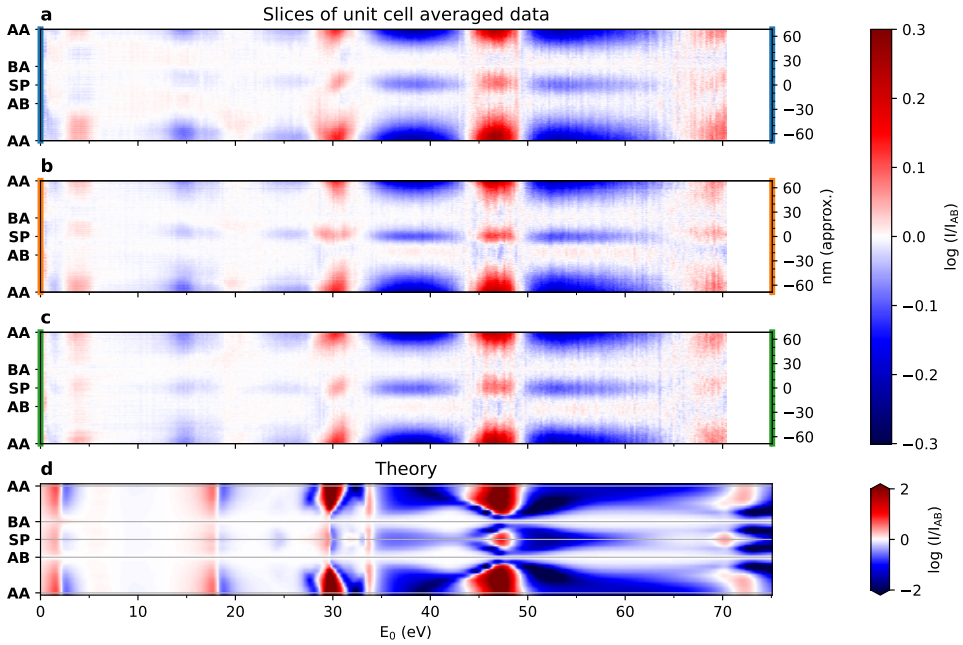

Figure 5.4: *Natural logarithm of the intensity of cuts through the averaged unit cells normalized with respect to the Bernal reflectivity in the three equivalent directions indicated with the same colors in Figure 5.3c (top three panels, corresponding to $\theta \approx 0.18^\circ$, detector resolution was 1.36 nm/pixel.) compared with (bottom panel) calculations of shifted equivalent stackings using the ab-initio theory, smoothed with a Gaussian with $\sigma = 0.2$ eV to account for experimental smoothing.*

Therefore, we conclude that at low twist angles, the moiré contrast is mainly caused by the different electron reflectivity of different local stackings and no significant phase contrast plays a role.

However, limitations of this approach in its current form are also immediately visible. Around contrast inversions, most prominently around 30 eV, it is clear from the asymmetric and different shapes in the three slices that the drift correction was not perfect, even relative to the large unit cell of this low twist angle. Note that the contrast inversions take place around the minima of the original spectra, where low intensity and energy spread of the electron source cause the most significant artefacts.

Notably, for lower energies, where ab-initio scattering mostly predicts a slight shift along E_0, experiment seems to indicate the inverse contrast, i.e. a shift in the opposite direction.

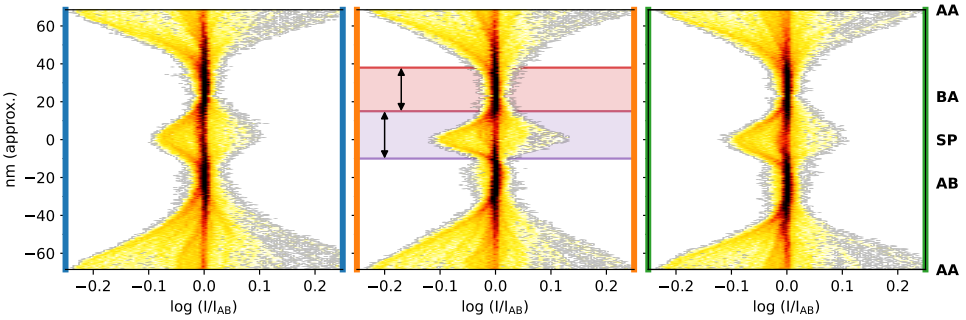

Figure 5.5: *2D-Histograms of the relative intensities (with respect to AB stacking) in Figure 5.4 for the different positions along the cuts, i.e. projected along E_0. Indicated in purple is the extracted domain boundary width, and in red the Bernal stacked area.*

Real space dimensions can also be extracted from these slices. The width around the indicated Bernal stacking in Figure 5.4 with approximately the same intensity is significantly larger than in the theoretical curves. This reaffirms that relaxation to Bernal stacking takes place, forming locally commensurate domains [120, 129] (which was also clear from the original data, such as in Figure 5.3**a,b**).

This broadening can be observed more clearly from the 2D-histogram of log-contrast values projected along E_0, as shown in Figure 5.5.

The width of the domain boundary is extracted from this, by measuring the length along the cut between AB and BA which has (significant) deviation from the Bernal stacking intensity for the full range of E_0, as indicated with the purple arrow in Figure 5.5. The observed width of about 25 nm is still much higher than the expected 7 nm, possibly by smearing during unit cell averaging, both intrinsic (thermal) broadening and electron optical broadening, and from imperfections of the extracted $\mathbf{u}(\mathbf{r})$.[6]

5.2.3 COMPARISON TO STRAIN DOMAIN BOUNDARIES IN GRAPHENE ON SIC

Next, we would like to compare the results on TBG from the previous section to the domain boundaries as observed in epitaxial graphene on silicon carbide. In the latter case, intrinsic stacking domains occur due to the lattice mismatch between the buffer layer and the graphene layers, as explored in Chapter 4 and 7. This means that in this system stacking contrast should occur due to tensile domain boundaries. This should hold both for hydrogen intercalated graphene on SiC, so-called quasi-freestanding bilayer graphene (QFBLG), and for epitaxial monolayer-on-buffer layer in the non-intercalated or de-intercalated material (EMLG). Indeed, domain boundaries in both systems cause contrast in BF-LEEM, as shown in Figure 5.6. Due to intrinsic disorder in this system

[6] Although the width along the slices in both other directions is larger, this is most probably due to the aforementioned remaining drift and therefore the minimum values can be assumed to be an upper bound.

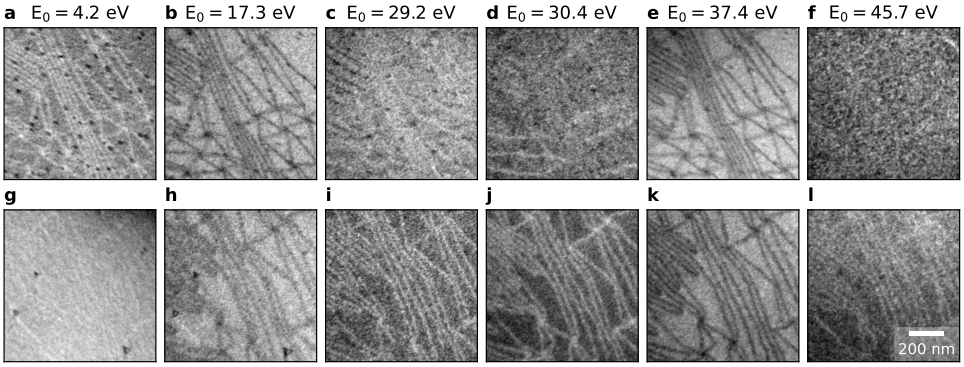

Figure 5.6: a-f, *Bright field stacking domain boundary contrast in quasi-freestanding bilayer graphene on SiC.* ***g-l,*** *The same for graphene on buffer layer on SiC (same area after hydrogen deintercalation). Both sets clearly show that depending on E_0, the domain boundaries can occur either bright or dark, although interestingly not at identical energies.*

however, no areas were imaged that are homogeneous enough to apply GPA to enable the same unit cell average analysis as applied in the previous section.

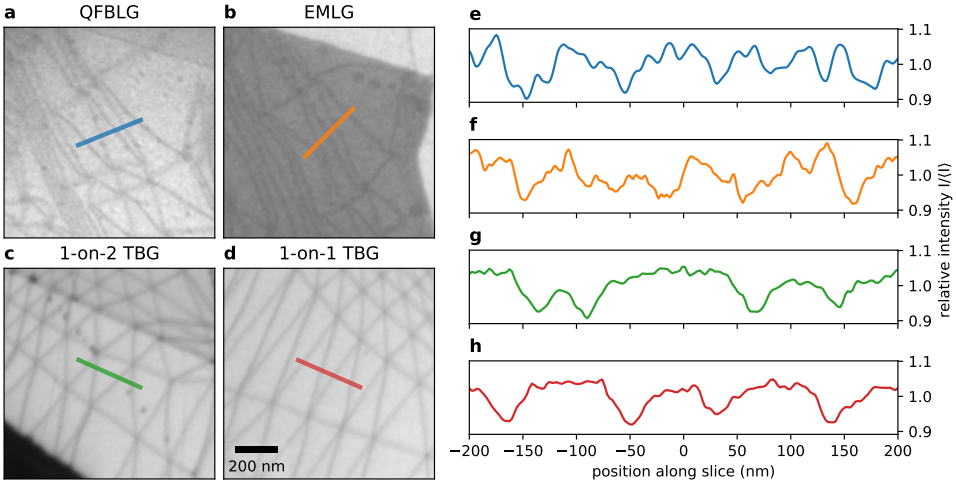

Figure 5.7: a-d, *Locations of the slices through stacking domain boundaries in several spectroscopic datasets. Scalebar applies to all panels and E_0 = 38 eV for all images and all images are individually optimized for contrast. The epitaxial graphene datasets have an original resolution of 2.2 nm/pixel, the TBG dataset a resolution of 3.7 nm/pixel.* ***e-h,*** *Normalized intensity along the slices indicated in respectively* ***a-d****.*

Nevertheless, we compare the contrast as a function of E_0 as observed in the epitaxial graphene samples to the twisted case by appropriate cross-sections through domain boundaries. The cross-sections, shown in Figure 5.7, were taken through multiple

domain boundaries, but without attempting to cross an AA site, as any remaining drift would invalidate such results.

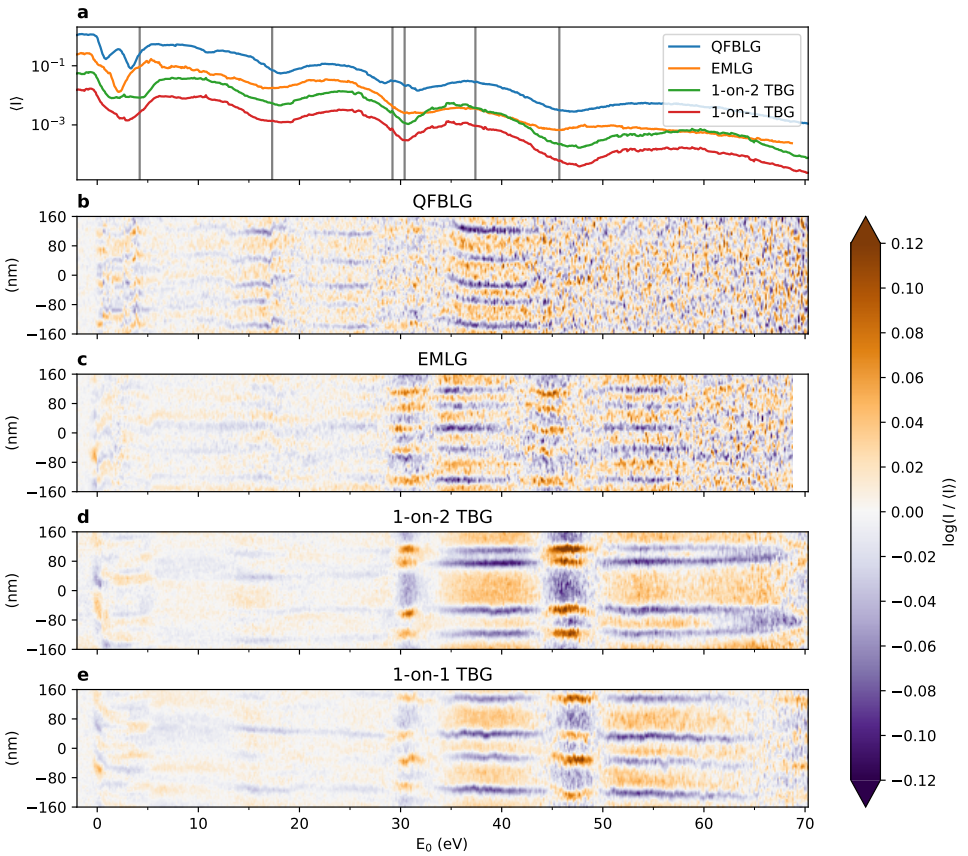

Figure 5.8: Comparison of domain boundaries with a single graphene top layer. ***a,*** *Average intensity along each slice* $\langle I \rangle$ *as a function of* E_0*, offset for clarity. Vertical lines indicate the images in Figure 5.6.* ***b-e,*** *Log-contrast, i.e. (natural) logarithm of the intensity relative to the slice average* $\langle I \rangle$ *as a function of* E_0*. The SiC slices (QFBLG and EMLG) are taken in the same area of Ref. [147], the TBG slices are taken from the data in Ref. [140]. Locations of the different slices are shown in Figure 5.7.*

The resulting energy-dependent average reflectivity $\langle I \rangle(E_0)$ along each slice is shown in Figure 5.8**a**, recovering the expected spectra for QFBLG, EMLG, bilayer graphene on hBN and trilayer graphene on hBN. The log-contrast $\log(I/\langle I \rangle)$ as a function E_0 along each slice is shown Figure 5.8**b-e**. Here, in addition to the regular flat field correction (as described in Chapter 3), a linear profile along the spatial direction is subtracted to compensate for remaining illumination inhomogeneity.

Contrast is remarkably similar for all systems shown, with dark (blue) domain boundaries for E_0 between 35 and 43 eV and contrast inversion above and below that, con-

sistent with the calculations, which show similar contrast inversions. For QFBLG and EMLG, the contrast washes out at higher E_0 (QFBLG above 45 eV, EMLG above 65 eV). However, this is an artefact most likely caused by insufficient integration time combined with incorrect focus tracking of the objective lens, causing the images to defocus at the high energies. Notably, the contrast below 30 eV is lower in EMLG than in the others, possibly due to the slightly different structure of the buffer layer compared to 'true' graphene layers in QFBLG and the TBG areas.

Some residual drift is present in the slices of each system, as the domain boundaries move collectively as a function of energy. Notably, some domain boundaries also move with respect to each other, e.g. the center two domain boundaries of 1-on-1 TBG around 39 eV. Such dynamics of the moiré pattern are in fact common and characterized more precisely in Chapter 6. By comparing the 1-on-1 TBG in Figure 5.8 to the unit cell averaged data in Figure 5.4, it becomes clear that the log-contrast for unit cell averaged data is about 1.5 times larger (0.2 peak-to-peak in Figure 5.8 versus 0.3 Bernal-to-peak in the unit cell averaged case).[7] Contrary to theory, all systems seem to consistently show at least some contrast for all energies lower than 30eV, although with varying strength and sign.

Domain boundaries in all four datasets are wider than the 6–11 nm predicted by simulations [19, 106], even when taking into account the non-perpendicular cuts. This suggests the data is again limited by electron optical reasons: either electron optical resolution of the measurements, or contribution of a phase component in addition to the pure amplitude component of the calculated stacking contrast to the image formation.

The 1-on-2 TBG data is remarkably similar to that of the other systems in this section, matching well to theory. The most evident difference in this system is the contrast between neighboring domains, which correspond to ABA and ABC stacking respectively, for example around 0, 10, 33 and 65 eV. This contrast between different Bernal and rhombohedral stackings will be explored in more detail in the next section.

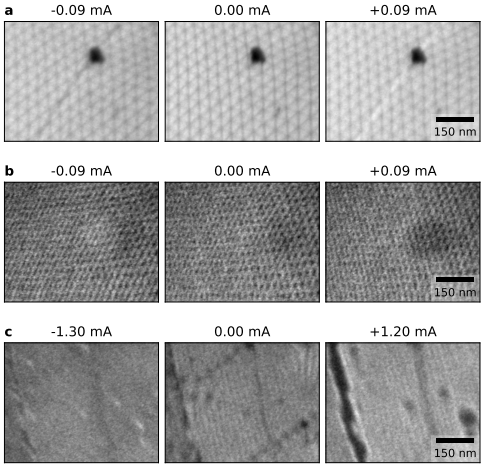

Figure 5.9: Defocus series. ***a,*** *Defocus series of TBG at $\theta \approx 0.18°$ at $E_0 = 36.5$ eV. The contrast of a diagonal line feature, presumably in the hBN substrate, inverts: from dark in underfocus to bright in overfocus.* ***b,*** *Defocus series of TBG at $\theta \approx 0.6°$ at $E_0 = 37.3$ eV. A round feature, presumably a bubble under the TBG, inverts contrast from bright in underfocus to dark in overfocus.* ***c,*** *Defocus series of graphene on SiC at $E_0 = 37.3$ eV. Several adsorbed carbohydrate residue particles change from bright in underfocus to dark in overfocus. Data taken on sample B as described in Chapter 7. Defocus is indicated above each panel in terms of objective lens excitation current relative to focus. Scalebars apply to all panels.*

[7] In terms of non-log contrast this corresponds to approximately a factor 1.2 peak-to-peak for the slices and 1.35 Bernal-to-peak for the unit cell averaged case.

Further evidence that the contrast in 1-on-1 TBG and graphene on SiC is pure amplitude contrast is given by the defocus series shown in Figure 5.9. If there would be a (strong) phase component to the contrast, this would invert as a function of defocus. Indeed, for all three defocus series, there are features present of which the contrast does invert as a function of defocus, but the domain boundaries do not show any signs of inverting contrast as a function of defocus in any of them. This confirms a pure amplitude contrast for domain boundaries both in TBG and in graphene on SiC.

5.3 BEYOND BILAYERS

While for bilayer graphene as explored in the previous sections, both possible Bernal stackings (AB / AC) are strictly equivalent as they are related by rotational symmetry (ignoring substrate effects), for trilayer and more layers, this equivalence is broken. In this section, the consequences of this for BF LEEM imaging of stacking domains multilayer (i.e. more than two layers) graphene are explored.

Bernal stacked trilayer graphene (ABA, occurring in natural graphite) has a distinct structure from rhombohedral graphene (ABC). The latter is hypothesized to possess interesting electronic properties, including flat bands [148–150] and a slightly different stacking energy [151, 152]. However, large areas of rhombohedral graphene turn out to be hard to create using standard stacking methods and even harder to stabilize, with samples typically showing a strong tendency to revert to Bernal stacking [120, 152].

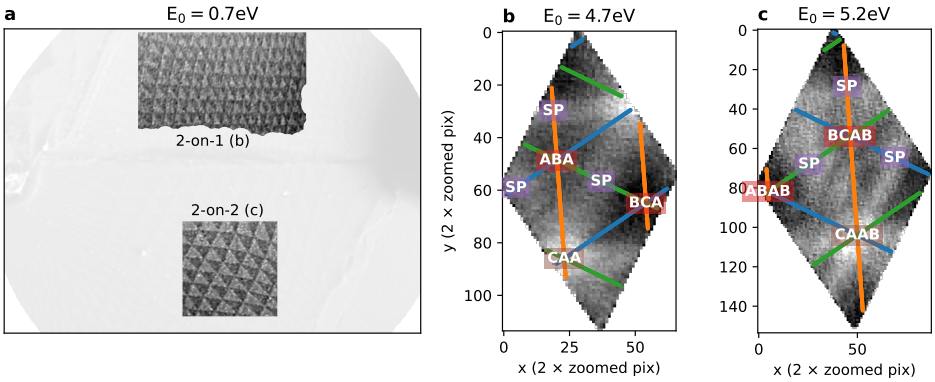

Figure 5.10: a, *BF LEEM image of an area of a TBG sample with both a 2-on-1 and a 2-on-2 area. The areas used for unit cell averaging are highlighted.* ***b,*** *Average unit cell for the 2-on-1 area at $E_0 = 4.7eV$ with the deduced stacking assignment indicated.* ***c,*** *Average unit cell for the 2-on-2 area at $E_0 = 5.2eV$ with the deduced stacking assignment indicated.*

Both minimally twisted multilayers and strained epitaxial graphene form a natural platform to study differences between different stackings, as areas of different stackings are inherently created in alternating patterns. Furthermore, they are topologically protected, since boundary nodes, which are as such sometimes referred to as 'twistons' in the twisted case, can only disappear by moving all the way to the edge of the sample. This behavior corresponds to full untwisting of the sample over relatively large length scales

for twisted samples. For the strainons in the strained epitaxial samples, the same holds, as the conservation is enforced by the binding to the substrate step edges and defects.

Aside from DF-LEEM, as described in Chapter 4 and used there to distinguish the different possible stackings in trilayer graphene on SiC, we will here explore the BF-LEEM characteristics of both domains and domain boundaries of different trilayer and quadlayer stackings.

As visible in Figure 5.8 (in the previous section), for 1-on-2, the domain boundaries yield very similar contrast to 1-on-1. This is expected, as the 'substrate' (an extra layer of graphene on hBN versus hBN in this case) has much less influence on the observed LEEM spectra than the top layers. However, some contrast between ABA and ABC stacking does appear when comparing to the bilayers, confirming the broken rotational symmetry.

Wildly different is the bright field contrast for samples where the twisted top layer consists of bilayer graphene, i.e. 2-on-1 and 2-on-2 TBG, as shown for $E_0 = 0.7$ eV in Figure 5.10**a**. Here, it is already clear that Bernal versus rhombohedral stacking dominates the contrast near mirror mode, visible as dark and bright triangles. These triangles are used to compute $\mathbf{u}(\mathbf{r})$ for unit cell averaging.

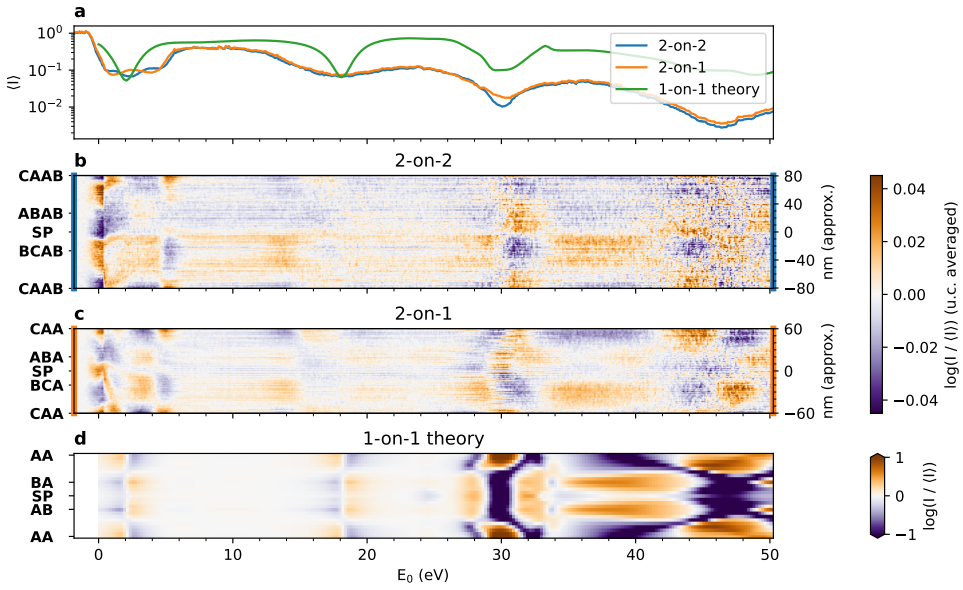

Figure 5.11: ***a,*** *Average intensity* $\langle I \rangle$ *as a function of* E_0 *for the areas indicated in Figure 5.10* ***a*** *and the average intensity for the computed theoretical reflectivities.* ***b,c,*** *Relative intensity of cuts through the averaged unit cells in the three directions indicated in Figure 5.10* ***b,c*** *for twisted bilayer-on-bilayer graphene. Data was taken at a magnification of 3.7 nm/pixel.* ***d,*** *Calculated relative intensity scaled by the average intensity for 1-on-1 bilayer.*

When looking at the resulting energy-dependent, unit cell averaged 2-on-1 and 2-on-2 data shown in Figure 5.11, the difference in contrast compared to the 1-on-X data in the previous section is clear. The overall contrast is much lower and the contrast between

ABA and ABC stacking dominates, although some (C)AA(B) and SP contrast is visible, for example around 5 eV.

5.3.1 2-ON-2 GRAPHENE LAYERS: PHASE CONTRAST

The results shown in the previous sections are fairly consistent with the calculations and therefore with pure amplitude contrast. However, something unexpected happens for 2-on-2 TBG data of a higher twist-angle, smaller unit cell area, such as in Figure 5.12.

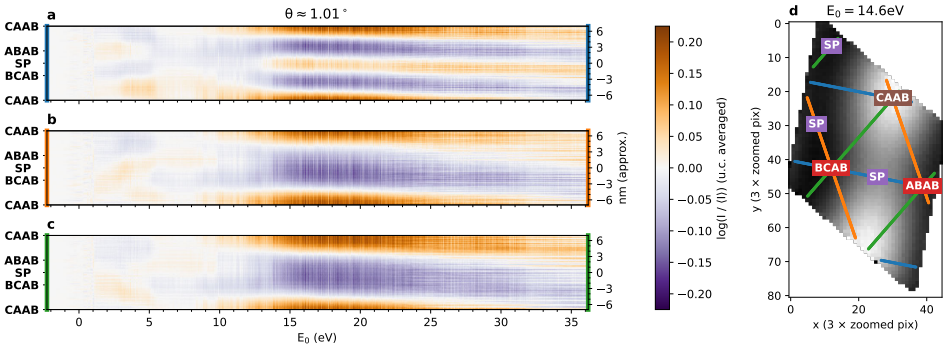

Figure 5.12: a-c, *Relative intensity of cuts through the averaged unit cells for twisted bilayer-on-bilayer graphene near the magic angle. Data was taken at a magnification of 0.9 nm/pixel. Note the difference in colorscale compared to Figures 5.11 and 5.13.* ***d,*** *Averaged unit cell with the cuts taken in* ***a-c*** *indicated.*

Although the size of this moiré is close to the resolution limit of the instrument, the contrast is very high and shows no inversions between ~ 10 eV and 36 eV. The observed contrast is the highest of all measurements presented in this work, peaking at $\frac{I_{\max}}{I_{\min}}\Big|_{E_0} \approx 1.5$ for a relatively wide region around $E_0 = 20$ eV.[8]

The stacking assignment as indicated in Figure 5.12**d** is speculative: it could as well be mainly caused by BCAB/ABAB contrast instead of the CAAB nodes yielding the main contribution to the contrast as was assumed there. The precise distinction seems impossible to make from this data due to the resolution limits of LEEM and the remaining astigmatism.

Nevertheless, the much higher contrast and lack of contrast inversion at this higher twist angle compared to the $\theta = 0.08$ data (shown for comparison for all three equivalent cuts in Figure 5.13), indicates phase contrast (where electrons reflecting off different parts of the unit cell interfere with each other) dominates for these higher twist angles in 2-on-2 TBG.

The proof of the pudding that the observed contrast for high twist angle 2-on-2 TBG is due to phase contrast would be a contrast inversion of the moiré pattern as a function of defocus. A defocus series is shown in Figure 5.14, but unfortunately the same small size of the moiré pattern that would enable phase contrast puts it right on the edge of

[8] $1.5 \approx \exp(0.42)$, i.e. the contrast of 1.5 corresponds to difference of 0.42 on the purple–orange color scales in the figures.

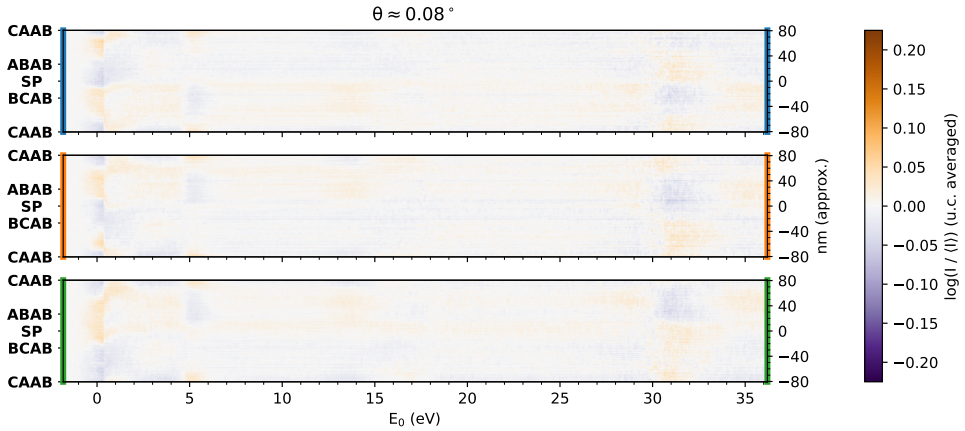

Figure 5.13: *Relative intensity of cuts through the averaged unit cells in the three directions indicated in Figure 5.10* ***c*** *for 2-on-2 TBG, with the colorscale matched to Figure 5.12 for comparison. Data was taken at a magnification of 3.7 nm/pixel.*

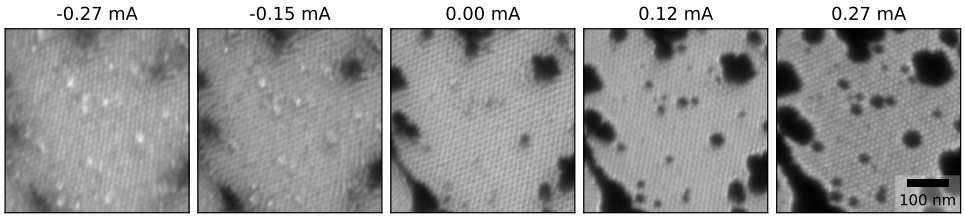

Figure 5.14: Defocus series of $\theta = 1.01°$ ***2-on-2 TBG.*** *Data taken at* $E_0 = 5.3$ *eV. Defocus relative to the center panel is expressed in mA excitation of the objective lens.*

the achievable resolution in the LEEM. Combined with the lack of clear reference points and some astigmatism makes it impossible to say for sure from this data if the contrast inverts or shifts or is completely stable. Although easily confused with remaining sample drift, it does however seem as if the contrast shifts around.

5.4 MOIRÉ METROLOGY

Beyond measuring the contrast of reflected low energy electrons of moiré patterns and determining the local twist angle, there is more that we can learn from imaging moiré patterns in such samples.

As described by Halbertal et al. for the case of 2-on-2 layer twisted graphene [151, 153], the shape of the domain boundaries can be directly related to any energy differences between different stackings and therefore can be used to *measure* (hence moiré *metrology*) these stacking energy differences.

In general, in a system with states of different energy that is in thermal equilibrium, the state with the lower energy will occur more often. The ratio between occupancy of the states is directly related to the energy difference by the Boltzmann factor. Although

the number of twistons in a twisted system, and therefore the number of alternating domains is conserved (ignoring edge cases), the size of the domains can change by movement of the domain boundaries.

However, the relative size of different stacking domains does not map directly to such a Boltzmann factor, as the energy cost per unit length of domain boundary has to be taken into account. What is more, this energy cost is dependent on the local angle between the domain boundary and the atomic lattice. Nevertheless, Halbertal et al. show that the generalized stacking fault energy (GSFE), the stacking energy as a function of relative displacement of lattices, can be directly related to the curvature κ of domain boundaries of the triangular domains, which they image using scanning near-field optical microscopy (SNOM). This methodology works for 2-on-2 TBG, but also for other materials.

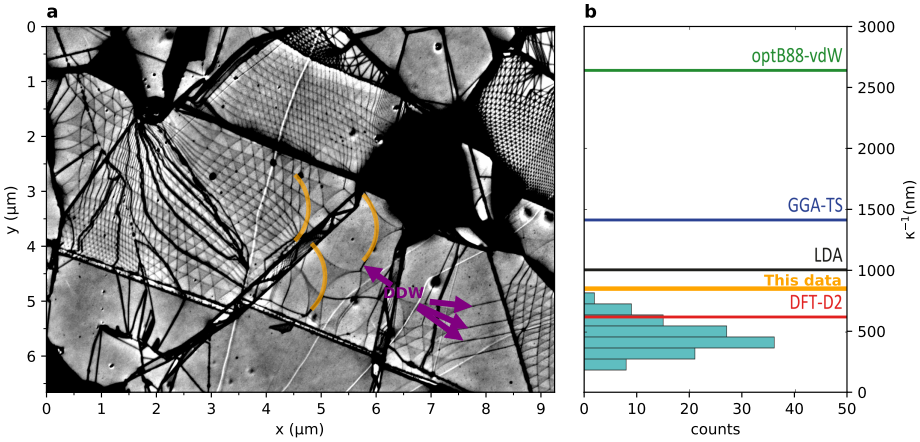

Figure 5.15: Moiré metrology. ***a,*** *BF-LEEM image of a 2-on-2 TBG area with very low twist angle (same device as ref. [135]). Domain boundaries in the 2-on-2 TBG areas are clearly visible, as is a slight contrast between ABAB and BCAB domains. In the very low twist angle areas, the curvature of the domain bounderies is very apparent. For three of them a matching orange arc with a curvature of* $\kappa^{-1} = 850$ *nm, is overlayed. Some double domain walls (DDW) are indicated with purple arrows.* ***b,*** *Measured curvatures using SNOM as a histogram with the predictions from different ab-initio calculation schemes indicated as lines, adapted from [151]. The curvature drawn in* ***a*** *is also indicated with an orange line.*

As shown in the preceding sections, LEEM can similarly image domains in diverse systems of heterostacks, providing another way to measure the shapes of these domain boundaries and therefore calibrate theoretical calculations of such stacking differences.

As calculations seem to suggest that both magnitude and direction of heterostrain influence the energy differences between different stackings, measuring larger areas of twisted heterostructures seems very worthwhile [152]. In such samples, varying strain can be characterized locally using GPA (as described in Ref. [21, 135, 151, 154]) and in conjunction the energy difference between the stackings can be determined by domain boundary curvature. This way, varying strain and energy difference can be connected

experimentally.

In Figure 5.15 a proof-of-concept of using LEEM to do such measurements is shown. Although the sample used only showed some areas of low enough twist angle to measure κ, it is already clear that we measure a value outside of the range of values that Halbertal et al. obtained as indicated by the histogram in Figure 5.15**b** and, interestingly, closer to theoretically predicted values using LDA, GGA-TS and optB88-vdW, but farther away from the one from DFT-D2 (for more details on the differences between these calculations, see the Methods section of Ref. [151]). Furthermore we observe double domain walls in the 2-on-2 TBG (for example the ones indicated with purple arrows in Figure 5.15), similar to observations by Halbertal et al., although we note that these did not occur in the 1-on-1 and 2-on-1 areas of the sample.

The possibilities for such measurements in a LEEM opens up a further research avenue: to explore the *dynamics* of the domain wall positions in such minimally twisted samples, similar to the work on higher twist angle data in Ref. [135]. By mapping the domain wall mobility as well as equilibrium curvatures as a function of temperature, it would be possible to not only explore the energy differences between the stackings, but also further characterize the stacking energy landscape.

5.5 CONCLUSION

In conclusion, we have shown that for large stacking domains in bilayer graphene, the local stacking in the domain walls and nodes is the primary BF-LEEM amplitude contrast mechanism for $E_0 \gtrsim 30$ eV. The contrasts observed in this energy range correspond very well to theoretical calculations, both for (low angle) 1-on-1 and 1-on-2 twisted bilayer graphene as well as for QFBLG and EMLG on silicon carbide, although the observed contrast is much lower due to the spatial resolution limitations of the experiment and thermal broadening.

Furthermore, we have applied similar methods to map the stacking contrast for 2-on-2 and 2-on-1 TBG. Here, for low angle data, the contrast is much lower, and mostly caused by contrast between the (meta-)stable Bernal and rhombohedral stackings, with domain boundaries only exhibiting minor contrast at some landing energies. Curiously, for $\theta \approx 1^\circ$, 2-on-2 TBG exhibits a much stronger contrast, stronger even than 1-on-1 TBG, suggesting that a phase contrast mechanism distinct from the local stacking contrast starts to become dominant.

The optimal landing energy range to image domain boundaries in a bilayer of graphene seems to be 30– 50 eV, where a strong amplitude contrast occurs and the intensity is still relatively high. For domain boundaries between deeper lying layers, the amplitude contrast at high values of E_0 is much lower, and the optimal energy to image the domains themselves is at very lower energies, 0 – 10 eV, where there is plenty of intensity and the work function difference causes relatively strong contrast. An exception holds for larger twist angles / smaller domains, where phase contrast is the dominant contrast mechanism causing strong contrast between 10 and 20 eV. We speculate that these trends are more generally applicable to stacking boundaries in Van der Waals heterostacks, beyond the graphene-graphene system alone: significant amplitude stacking contrast only for E_0 larger than the energy at which the first order diffraction spots appear, large deeper

lying domains most clearly imagable by slight work function differences and small domains dominated by phase contrast, especially for deeper lying stacking differences.

The contrast mechanisms as explored here are exploited to measure local strain and twist angle in TBG in Chapter 6 (Ref. [135]) and to explore relative strain and disorder in epitaxial graphene on SiC in Chapter 7.

Finally, we have shown the potential of using such contrast in twisted heterostacks to closely study the energy differences between different possible stackings.

5.6 OUTLOOK: POSSIBLE COMPUTATIONAL IMPROVEMENTS

Although several conclusions could be drawn from the unit cell averaged data in this chapter, it is also clear that there are still algorithmic limitations of the current implementation of the unit cell averaging, both in the unit cell averaging itself and in the adaptive Geometric Phase Analysis (GPA) used to obtain the displacement field $\mathbf{u}(\mathbf{r})$. As an outlook, I will here list several algorithmic improvements that could still be made to improve the data quality.

- Some residual drift plagues the unit cell cuts. Some of this is unavoidable in the current method, as due to different contrast mechanisms and height differences, the moiré pattern tends to move slightly different compared to larger features such as folds and adsorbates. It should however be possible to derive a final correction of the drift by minimizing asymmetry of the resulting cuts through the unit cell.

- Non-isotropic unit vectors for GPA can be used instead of the forced isotropic ones used now. This way, they would correspond to the average local deformation and limit distortion. Additionally, influences of the strain could be studied by comparing different direction cuts through the unit cell.

- GPA intrinsically introduces a convolution with a broadening kernel (in this work always Gaussian). In principle, this convolution can be deconvolved from the GPA result if the signal to noise ratio in the result is low enough. This increases the accuracy of the recovered $\mathbf{u}(\mathbf{r})$, especially in areas with gradients. However, due to SNR requirements and inherent inaccuracy of the unit cell averaging introduced by strongly changing unit cell sizes the improvement obtained using deconvolution might be limited.

- Deformation changes: We have seen the moiré lattice fluctuates. Therefore, instead of using a fixed $\mathbf{u}(\mathbf{r})$, compute $\mathbf{u}(\mathbf{r})$ for multiple different energies with high contrast and interpolate between those.

- Pixels on an edge of the unit cell are not treated perfectly, yielding severe edge effects. Therefore an overlap should be used to created a drizzled average slightly larger than the unit cell. To achieve the smallest such overlap, one should add pixels falling on the edge (i.e. for which the drop falls on at least one pixel with a coordinate outside the unit cell) to both sides of the unit cell to ensure coverage of these drizzle drops on both sides. An alternative would be to drizzle in fractional lattice vector coordinates instead of Cartesian coordinates, but this would yield more complicated computations and non-trivial drizzle drop shapes.

- The size and potentially also the shape of the drizzle drops can be optimized. The current choice for a 1-by-1 pixel square in the resulting averaged unit cell was easiest to implement, but probably not optimal.

REFERENCES

10. D. Momeni Pakdehi, J. Aprojanz, A. Sinterhauf, et al. Minimum Resistance Anisotropy of Epitaxial Graphene on SiC. *ACS Applied Materials & Interfaces* **10,** 6039–6045. doi:10.1021/acsami.7b18641 (2018).

11. A. M. Popov, I. V. Lebedeva, A. A. Knizhnik, Y. E. Lozovik & B. V. Potapkin. Commensurate–incommensurate phase transition in bilayer graphene. *Physical Review B* **84,** 045404. doi:10.1103/PhysRevB.84.045404 (2011).

12. C. Riedl, U. Starke, J. Bernhardt, M. Franke & K. Heinz. Structural properties of the graphene-SiC(0001) interface as a key for the preparation of homogeneous large-terrace graphene surfaces. *Physical Review B* **76,** 245406. doi:10.1103/PhysRevB.76.245406 (2007).

13. S. Kim, J. Ihm, H. J. Choi & Y.-W. Son. Origin of Anomalous Electronic Structures of Epitaxial Graphene on Silicon Carbide. *Physical Review Letters* **100,** 176802. doi:10.1103/PhysRevLett.100.176802 (2008).

17. J. Ravnik, I. Vaskivskyi, Y. Gerasimenko, et al. Strain-Induced Metastable Topological Networks in Laser-Fabricated TaS_2 Polytype Heterostructures for Nanoscale Devices. *ACS Applied Nano Materials* **2,** 3743–3751. doi:10.1021/acsanm.9b00644 (2019).

19. I. V. Lebedeva & A. M. Popov. Two Phases with Different Domain Wall Networks and a Reentrant Phase Transition in Bilayer Graphene under Strain. *Physical Review Letters* **124,** 116101. doi:10.1103/PhysRevLett.124.116101 (2020).

21. F. Mesple, A. Missaoui, T. Cea, et al. Heterostrain Determines Flat Bands in Magic-Angle Twisted Graphene Layers. *Physical Review Letters* **127,** 126405. doi:10.1103/PhysRevLett.127.126405 (2021).

25. R. Tromp, J. Hannon, A. Ellis, et al. A new aberration-corrected, energy-filtered LEEM/PEEM instrument. I. Principles and design. *Ultramicroscopy* **110,** 852–861. doi:10.1016/j.ultramic.2010.03.005 (2010).

27. R. M. Tromp, J. B. Hannon, W. Wan, A. Berghaus & O. Schaff. A new aberration-corrected, energy-filtered LEEM/PEEM instrument II. Operation and results. *Ultramicroscopy* **127,** 25–39. doi:10.1016/j.ultramic.2012.07.016 (2013).

37. T. A. de Jong, E. E. Krasovskii, C. Ott, et al. Intrinsic stacking domains in graphene on silicon carbide: A pathway for intercalation. *Physical Review Materials* **2,** 104005. doi:10.1103/PhysRevMaterials.2.104005 (2018).

88. T. A. de Jong. *pyGPA* 2021. doi:10.5281/zenodo.5589555.

95. K. V. Emtsev, A. Bostwick, K. Horn, et al. Towards wafer-size graphene layers by atmospheric pressure graphitization of silicon carbide. *Nature Materials* **8,** 203–207. doi:10.1038/nmat2382 (2009).

106. J. S. Alden, A. W. Tsen, P. Y. Huang, et al. Strain solitons and topological defects in bilayer graphene. *Proceedings of the National Academy of Sciences* **110,** 11256–11260. doi:10.1073/pnas.1309394110 (2013).

108. I. Martin, Y. M. Blanter & A. F. Morpurgo. Topological Confinement in Bilayer Graphene. *Physical Review Letters* **100,** 036804. doi:10.1103/PhysRevLett.100.036804 (2008).

114. R. M. Tromp & J. B. Hannon. Thermodynamics and Kinetics of Graphene Growth on SiC(0001). *Physical Review Letters* **102,** 106104. doi:10.1103/PhysRevLett.102.106104 (2009).

120. H. Yoo, R. Engelke, S. Carr, et al. Atomic and electronic reconstruction at the van der Waals interface in twisted bilayer graphene. *Nature Materials* **18,** 448–453. doi:10.1038/s41563-019-0346-z (2019).

122. L.-J. Yin, H. Jiang, J.-B. Qiao & L. He. Direct imaging of topological edge states at a bilayer graphene domain wall. *Nature Communications* **7,** 11760. doi:10.1038/ncomms11760 (2016).

124. T. A. de Jong, X. Chen, E. E. Krasovskii, et al. Low-Energy Electron Microscopy contrast of stacking boundaries: comparing twisted few-layer graphene and strained epitaxial graphene on silicon carbide. *under review.* https://arxiv.org/abs/2207.14616 (2022).

125. A. J. Van Bommel, J. E. Crombeen & A. Van Tooren. LEED and Auger electron observations of the SiC(0001) surface. *Surface Science* **48,** 463–472. doi:10.1016/0039-6028(75)90419-7 (1975).

126. J. B. Hannon, M. Copel & R. M. Tromp. Direct Measurement of the Growth Mode of Graphene on SiC(0001) and SiC (000 1 ¯). *Physical Review Letters* **107,** 166101. doi:10.1103/PhysRevLett.107.166101 (2011).

127. S. Tanaka, K. Morita & H. Hibino. Anisotropic layer-by-layer growth of graphene on vicinal SiC(0001) surfaces. *Physical Review B* **81,** 041406. doi:10.1103/PhysRevB.81.041406 (2010).

128. M. Kruskopf, D. M. Pakdehi, K. Pierz, et al. Comeback of epitaxial graphene for electronics: large-area growth of bilayer-free graphene on SiC. *2D Materials* **3,** 041002. doi:10.1088/2053-1583/3/4/041002 (2016).

129. S. Carr, D. Massatt, S. B. Torrisi, et al. Relaxation and domain formation in incommensurate two-dimensional heterostructures. *Physical Review B* **98,** 224102. doi:10.1103/PhysRevB.98.224102 (2018).

130. E. Annevelink, H. T. Johnson & E. Ertekin. Topologically derived dislocation theory for twist and stretch moiré superlattices in bilayer graphene. *Physical Review B* **102,** 184107. doi:10.1103/PhysRevB.102.184107 (2020).

131. J. Lin, W. Fang, W. Zhou, et al. AC/AB Stacking Boundaries in Bilayer Graphene. *Nano Letters* **13,** 3262–3268. doi:10.1021/nl4013979 (2013).

132. S. Turkel, J. Swann, Z. Zhu, et al. Twistons in a Sea of Magic. *arXiv:2109.12631 [cond-mat].* http://arxiv.org/abs/2109.12631 (2022) (2021).

133. S. Huang, K. Kim, D. K. Efimkin, et al. Topologically Protected Helical States in Minimally Twisted Bilayer Graphene. *Physical Review Letters* **121,** 037702. doi:10.1103/PhysRevLett.121.037702 (2018).

134. J. D. Verbakel, Q. Yao, K. Sotthewes & H. J. W. Zandvliet. Valley-protected one-dimensional states in small-angle twisted bilayer graphene. *Physical Review B* **103,** 165134. doi:10.1103/PhysRevB.103.165134 (2021).

135. T. A. de Jong, T. Benschop, X. Chen, et al. Imaging moiré deformation and dynamics in twisted bilayer graphene. *Nature Communications* **13,** 70. doi:10.1038/s41467-021-27646-1 (2022).

136. E. Krasovskii. Ab Initio Theory of Photoemission from Graphene. *Nanomaterials* **11,** 1212. doi:10.3390/nano11051212 (2021).

137. H. Hibino, S. Mizuno, H. Kageshima, M. Nagase & H. Yamaguchi. Stacking domains of epitaxial few-layer graphene on SiC(0001). *Physical Review B* **80,** 085406. doi:10.1103/PhysRevB.80.085406 (2009).

138. P. Schädlich, F. Speck, C. Bouhafs, et al. Stacking Relations and Substrate Interaction of Graphene on Copper Foil. *Advanced Materials Interfaces* **8,** 2002025. doi:10.1002/admi.202002025 (2021).

139. S. M. Schramm, A. B. Pang, M. S. Altman & R. M. Tromp. A Contrast Transfer Function approach for image calculations in standard and aberration-corrected LEEM and PEEM. *Ultramicroscopy* **115,** 88–108. doi:10.1016/j.ultramic.2011.11.005 (2012).

140. T. de Jong, T. Benschop, X. Chen, et al. *Data underlying the paper: Imaging moiré deformation and dynamics in twisted bilayer graphene.* (4TU.ResearchData, 2021). doi:10.4121/16843510.

141. T. Benschop*, T. A. de Jong*, P. Stepanov*, et al. Measuring local moiré lattice heterogeneity of twisted bilayer graphene. *Physical Review Research* **3,** 013153. doi:10.1103/PhysRevResearch.3.013153 (2021).

142. J. A. Slezak, J. Lee, M. Wang, et al. Imaging the impact on cuprate superconductivity of varying the interatomic distances within individual crystal unit cells. *Proceedings of the National Academy of Sciences* **105,** 3203–3208. doi:10.1073/pnas.0706795105 (2008).

143. M. J. Lawler, K. Fujita, J. Lee, et al. Intra-unit-cell electronic nematicity of the high-Tc copper-oxide pseudogap states. *Nature* **466,** 347–351. doi:10.1038/nature09169 (2010).

144. A. S. Fruchter & R. N. Hook. Drizzle: A Method for the Linear Reconstruction of Undersampled Images. *Publications of the Astronomical Society of the Pacific* **114,** 144–152. doi:10.1086/338393 (2002).

145. A.-J. Quist. *Superresolution in Low Energy Electron Microscopy using drizzle* BSc thesis (Leiden University, 2020). https://hdl.handle.net/1887/133077.

146. T. A. de Jong. *Graphene stacking domains code* 2022. https://github.com/TAdeJong/graphene-stacking-domains-code.

147. T. A. de Jong, J. Jobst & E. E. Krasovskii. *Data underlying the paper: Intrinsic stacking domains in graphene on silicon carbide: a pathway for intercalation* (4TU.ResearchData, 2018). doi:10.4121/uuid:a7ff07f4-0ac8-4778-bec9-636532cfcfc1.

148. D. Pierucci, T. Brumme, J.-C. Girard, et al. Atomic and electronic structure of trilayer graphene/SiC(0001): Evidence of Strong Dependence on Stacking Sequence and charge transfer. *Scientific Reports* **6,** 33487. doi:10.1038/srep33487 (2016).

149. H. Henck, J. Avila, Z. Ben Aziza, et al. Flat electronic bands in long sequences of rhombohedral-stacked graphene. *Physical Review B* **97,** 245421. doi:10.1103/PhysRevB.97.245421 (2018).

150. D. Marchenko, D. V. Evtushinsky, E. Golias, et al. Extremely flat band in bilayer graphene. *Science Advances* **4,** eaau0059. doi:10.1126/sciadv.aau0059 (2018).

151. D. Halbertal, N. R. Finney, S. S. Sunku, et al. Moiré metrology of energy landscapes in van der Waals heterostructures. *Nature Communications* **12,** 242. doi:10.1038/s41467-020-20428-1 (2021).

152. R. Guerrero-Avilés, M. Pelc, F. Geisenhof, T. Weitz & A. Ayuela. Relative Stability of Bernal and Rhombohedral Stackings in Trilayer Graphene under Distortions. *arXiv:2110.06590 [cond-mat].* http://arxiv.org/abs/2110.06590 (2022) (2021).

153. V. V. Enaldiev, V. Zólyomi, C. Yelgel, S. J. Magorrian & V. I. Fal'ko. Stacking Domains and Dislocation Networks in Marginally Twisted Bilayers of Transition Metal Dichalcogenides. *Physical Review Letters* **124,** 206101. doi:10.1103/PhysRevLett.124.206101 (2020).

154. D. Halbertal, S. Shabani, A. N. Passupathy & D. N. Basov. Extracting the Strain Matrix and Twist Angle from the Moiré Superlattice in van der Waals Heterostructures. *ACS Nano* **16,** 1471–1476. doi:10.1021/acsnano.1c09789 (2022).

6

IMAGING MOIRÉ DEFORMATION AND DYNAMICS IN TWISTED BILAYER GRAPHENE

In 'magic angle' twisted bilayer graphene (TBG) a flat band forms, yielding correlated insulator behavior and superconductivity. In general, the moiré structure in TBG varies spatially, influencing the overall conductance properties of devices. Hence, to understand the wide variety of phase diagrams observed, a detailed understanding of local variations is needed.

Here, we study spatial and temporal variations of the moiré pattern in TBG using aberration-corrected Low Energy Electron Microscopy (AC-LEEM). We find a smaller spatial variation than reported previously. Furthermore, we observe thermal fluctuations corresponding to collective atomic displacements over 70 pm on a timescale of seconds. Remarkably, no untwisting is found up to 600 °C.

We conclude that thermal annealing can be used to decrease local disorder. Finally, we observe edge dislocations in the underlying atomic lattice, the moiré structure acting as a magnifying glass. These topological defects are anticipated to exhibit unique local electronic properties.

Parts of this chapter have been published as T. A. de Jong, T. Benschop, X. Chen, E. E. Krasovskii, M. J. A. de Dood, R. M. Tromp, M. P. Allan and S. J. van der Molen, Nat. Commun. **13**, 70 (2022) [135].

6.1 INTRODUCTION

In twisted bilayer graphene (TBG) a moiré pattern forms that introduces a new length scale to the material. At the 'magic' twist angle $\theta_m \approx 1.1°$, this causes a flat band to form, yielding emergent properties such as correlated insulator behavior and superconductivity [4, 5, 155, 156]. In general, the moiré structure in TBG varies spatially, influencing the local electronic properties [157–161]. This has clear consequences for charge transport experiments, where a percolative average of the microscopic properties is measured. Local variation in twist angle and strain in TBG will directly influence the result of such experiments. In particular, to understand the wide variety observed in the phase diagrams and critical temperatures, a more detailed understanding of the local moiré variation is needed [162].

However, imaging such microscopic variations is non-trivial. A myriad of experimental techniques has been applied to the problem [106, 120, 151, 163–166], each only resolving part of the puzzle due to practical limitations (capping layer or device substrate, surface quality or measurement speed).

Here, we use aberration-corrected Low Energy Electron Microscopy (AC-LEEM) [25, 27], which measures an image of the reflection of a micron-sized beam of electrons at a landing energy E_0 (0–100 eV, referenced to the vacuum energy) in real space, in reciprocal space (diffraction), or combinations thereof. This allows us to perform large-scale, fast and non-destructive imaging of TBG, including device-scale moiré images and dynamics on timescales of seconds. Additionally, spectroscopic measurements, yielding information on the material's unoccupied bands can be done by varying E_0 [29, 34].

Using AC-LEEM to image moiré patterns enables high temperature imaging and has the benefit no suspended samples are required, like they are for TEM-based techniques. This means that sample geometries closely resembling device geometries can be imaged, including devices with leads. Even though not shown here, imaging the moiré pattern through a capping layer of hBN would be possible, although this would be limited to an very thin capping layer of at most a few atomic layers (where SEM-based techniques have demonstrated imaging through much thicker layers [166]).

At 500 °C, we observe thermal fluctuations of the moiré lattice, corresponding to collective atomic displacements of less than 70 pm on a time scale of seconds [167]. Despite previous concerns, no untwisting of the layers is found, even at temperatures as high as 600 °C [112, 168]. Finally, we report the existence of individual edge dislocations in the atomic and moiré lattice.

6.2 RESULTS

A schematic of a TBG sample as used in this work is shown in Figure 6.1**a**. In Figure 6.1**b**, LEEM spectra are shown, taken on several locations of such a TBG sample. These LEEM spectra are directly related to layer count, as described in Refs. [31, 34, 46, 169]; on the one hand via interlayer resonances in the 0–5 eV range, on the other hand via the gradual disappearance of a minimum at 8 eV. Here, more graphene layers (having a band gap at 8 eV) are progressively masking an hBN band underneath. This allows us to determine the local graphene layer count for each point on our sample. To visualize that, we choose three characteristic energies, i.e. $E_0 = 4$ eV (red), $E_0 = 8$ eV (green) and $E_0 = 17$ eV (blue)

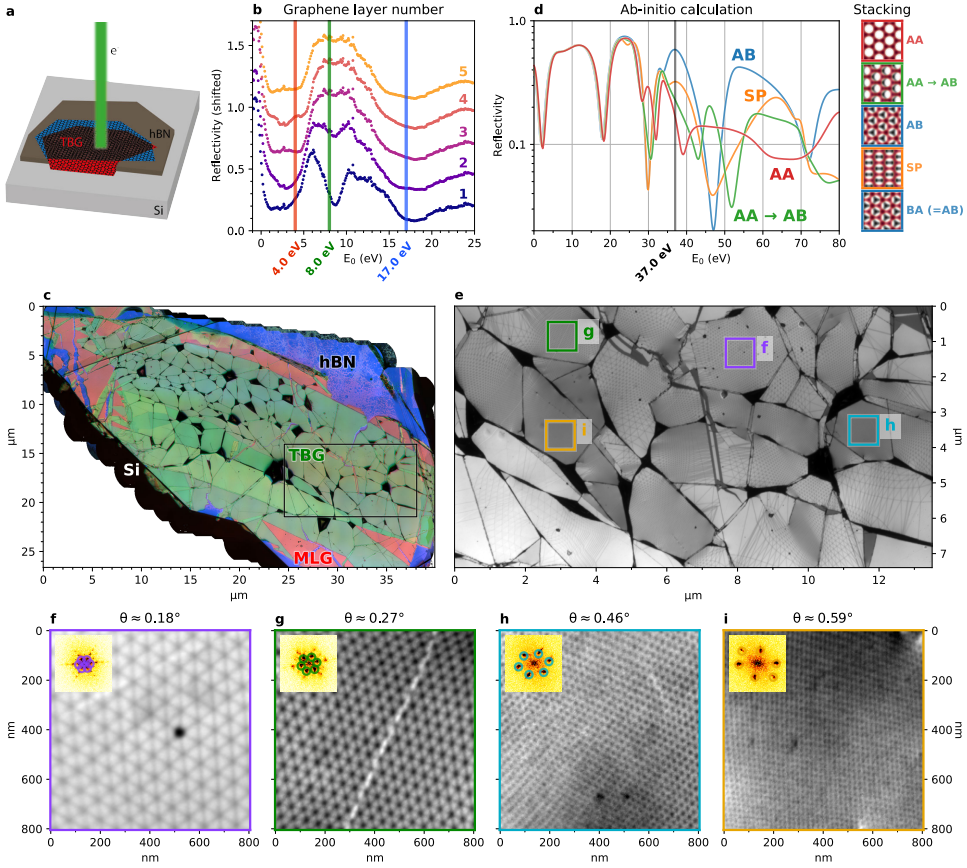

Figure 6.1: Device-scale imaging of TBG. ***a,*** *Schematic of the sample, with two twisted graphene flakes (TBG) on top of an hexagonal boron nitride (hBN) flake on a silicon (Si) substrate.* ***b,*** *Local spectra used to determine the graphene layer count. Vertical lines indicate the imaging energies used for panel c, number of graphene layers is indicated on the right.* ***c,*** *Stitched composite bright field overview of a sample using 4 eV, 8 eV and 17 eV as imaging energies in red, green and blue respectively (see main text for color interpretation). Visible defects include folds in black, tears, where the monolayer (red/pink, indicated as MLG) or even bare hBN (blue, purple) shines through, bubbles (bright) and some polymer residue in the lower and upper right (dark speckles). The black rectangle indicates the area shown in panel d.* ***d,*** *Ab-initio calculations of LEEM spectra of different relative stackings of bilayer graphene, 37 eV indicated.* ***e,*** *Stitched bright field overview of the same sample imaged at $E_0 = 37$ eV, for optimal stacking contrast, revealing the moiré patterns.* ***f-i,*** *Crops of different twist angles areas from* ***e,****. Insets show Fourier transforms and the detected moiré peaks, with the average twist angle θ extracted from those indicated. All data shown in the main text have been collected from the sample represented in panel* ***c****.*

(as indicated in Figure 6.1**b**), and combine stitched overviews at these energies into a single false-color image (Figure 6.1**c**). This overview confirms that the sample consists of large TBG areas (darker green in Figure 6.1**c**) surrounded by monolayer graphene (pink),

on an hBN flake (blue/purple) on silicon (black). Stripes of brighter green indicate areas of 2-on-2 graphene layers (lower stripe), 2-on-1 (upper stripe), and 1-on-2 (wedge on the lower right). The relatively homogeneous areas are themselves separated by folds, appearing as black lines. The folds locally combine in larger dark nodes (confirmed by AFM, See Figure C.8 in Appendix C). A few folds, however, have folded over and appear as lines of higher layer count. Hence, Figure 6.1**c** provides a remarkable overview of a larger-scale sample, with detailed local information.
Increasing E_0 beyond 25 eV, stacking boundaries and AA-sites become visible [37, 169]. This is consistent with ab-initio calculations of LEEM spectra for different relative stackings, as presented in Figure 6.1**d**. Therefore, imaging at $E_0 = 37$ eV (indicated in Figure 6.1**d**) yields a precise map of the moiré lattice over the full TBG area (see Figure 6.1**e**). We find that separate areas, between folds, exhibit different moiré periodicities and distortion [170]. This allows us to study different moiré structures on a single sample. Figure 6.1**f-i** shows full resolution crops of areas indicated in Figure 6.1**e**. The observed twist angles on this sample range from $< 0.1°$ to $0.7°$. For smaller angles, we observe local reconstruction towards Bernal stacking within the moiré lattice, consistent with literature [120, 165]. The best resolution was reached on another sample with a twist angle of $1.3°$ (See Figure 6.2).

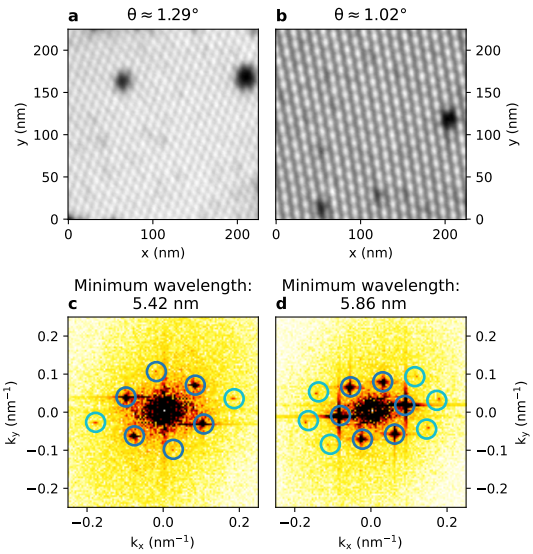

Figure 6.2: ***a,b,*** *Images of 2-on-2 layer twisted graphene at E_0 = 17.0 eV, with twist angles of respectively $\theta \approx 1.29°$ and $\theta \approx 1.02°$* ***c,d,*** *FFTs of the images in a and b respectively, with Bragg peaks corresponding to the moiré pattern indicated in blue. Higher order moiré peaks are also visible (indicated in cyan), corresponding to minimum detectable wavelengths of less than 6 nm.*

6.2.1 DISTORTIONS & STRAIN

The moiré patterns shows distortions, corresponding to local variations in twist angle and (interlayer) strain. Near folds, for instance, the strain increases resulting in strongly elongated triangles, for example in the lower right corner of Figure 6.1**d** [171]. Despite their relative homogeneity, the moiré areas in Figure 6.1**f-i** also show subtle distortions. As structural variations correlate directly with local electronic properties, we quantify

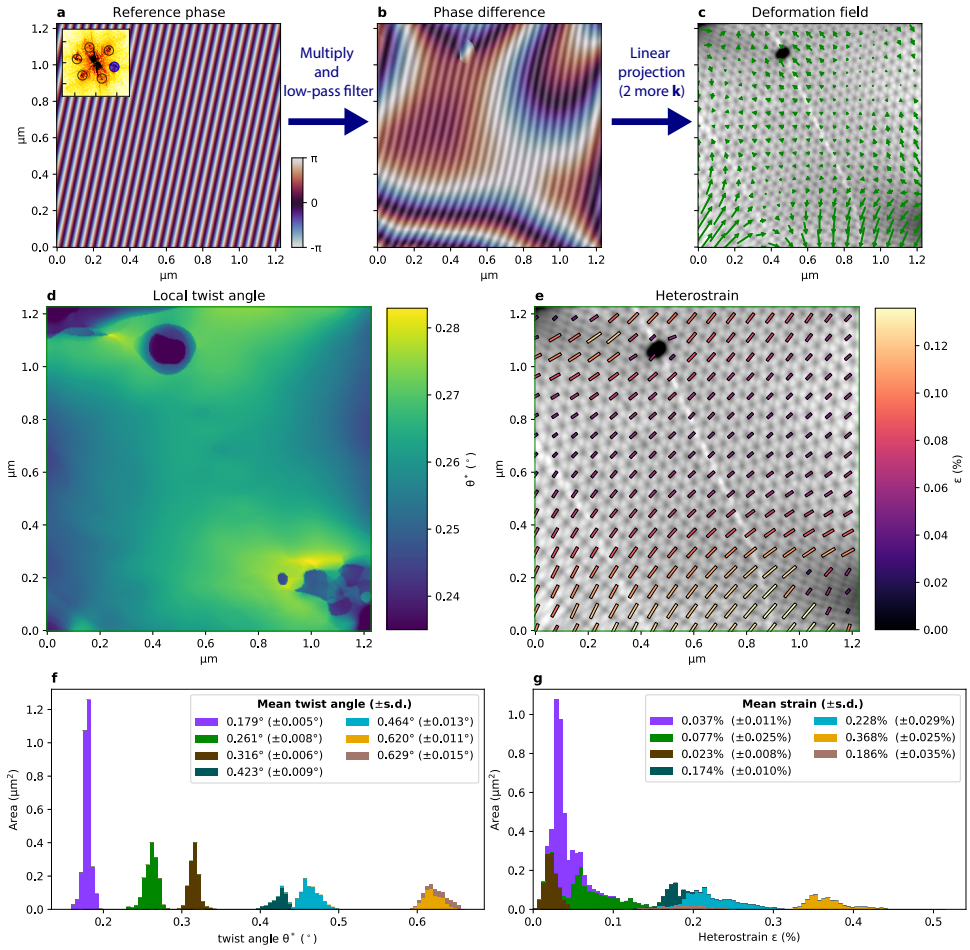

Figure 6.3: Distortion variation from Geometric Phase Analysis. a, *Reference phase corresponding to one k-vector used in GPA, as extracted from the Fourier transform of the corresponding image (inset, extracted k-vectors are indicated by black circles).* ***b,*** *Phase difference or GPA phase, obtained by multiplying with the original image and low-pass filtering. Overlayed is the corresponding extracted image wave in gray scale.* ***c,*** *The displacement field extracted from the GPA phase represented in panel b and those of 2 more k-vectors.* ***d,*** *Extracted local twist angle θ^*.* ***e,*** *Extracted local heterostrain. Length and color of bars indicates the magnitude ϵ of the heterostrain, direction is the direction of elongation of the atomic lattice.* ***f,g,*** *Distribution of θ^* & ϵ extracted from different areas on the sample. Bar colors correspond to colors in Figure 6.1**e**, with the remaining areas shown in Figure C.1 in Appendix C.*

them in detail [157, 158]. For this, we use adaptive geometric phase analysis (GPA), extending our earlier work on STM data of moiré patterns in TBG (see Appendix A) [88, 141, 143, 172, 173]. This method, illustrated in Figure 6.3**a-c**, yields the displacement field with respect to a perfect lattice, by multiplying the original image with complex ref-

erence waves followed by low-pass filtering to obtain the GPA phase differences, which are then converted to the displacement field. This field fully describes the distortion of the moiré lattice and allows us to extract key parameters such as the local twist angle $\theta^*(\mathbf{r})$ (see Figure 6.3**d**), and heterostrain magnitude $\epsilon(\mathbf{r})$ and direction (see Figure 6.3**e**), as described in Appendix A.6 [141, 174]. The distortions of the moiré pattern correspond directly to distortions of the atomic lattices, magnified by a factor $1/\theta$ and rotated by $90° + \theta/2$ [141, 175].

The extracted variation in twist angle and heterostrain for various regions of the sample, including those in Figure 6.1**f-i**, is summarized in Figure 6.3**f,g**, respectively. The twist angle variation within each domain is much smaller than the variation in twist angle between the separate, fold-bounded areas. Within domains, standard deviations range from 0.005° to 0.015°, i.e. significantly smaller (by a factor 3–10) than previously reported [141, 164, 165]. The strain observed is around a few tenths of a percent, which is considerable. In some domains, we find an average strain of the atomic lattice of up to $\epsilon = 0.4\,\%$. According to earlier theoretical work, such values are high enough to locally induce a quantum phase transition [160].

The variation of ϵ, as for θ^*, within the domains is significantly lower than in earlier studies. We do note that the use of GPA introduces a point spread function (PSF) that is broader than the PSF of the instrument, resulting in a lower displacement field frequency response at small scales and therefore a somewhat reduced variation. Nevertheless, the combined PSF of instrument and analysis is still comparable to other techniques that do not image the unit cell directly, allowing for a direct comparison.

We hypothesize that the difference in variations with literature stems from the relatively high temperature to which we heated the sample and measured at, combined with the relatively long averaging time of this measurement ($\geq 16\,$s for all data in Figure 6.3). The high temperature induces thermal fluctuations of the lattice (as demonstrated below), allowing the system to approach a lower energy, more homogeneous, state.

6.2.2 EDGE DISLOCATIONS

So far, we have discussed structural properties varying on the moiré length scale. However, the moiré magnification of deformations is general and extends to atomic edge dislocations (visualized in Figure 6.4**a**). This type of topological defect stems from a missing row of atomic unit cells and is characterized by an in-plane Burgers vector (in red) [176, 177]. The addition of a second (twisted) atomic layer magnifies (and rotates) the defect to an edge dislocation in the moiré lattice (illustrated in Figure 6.4**d,e**) [175]. In all cases, the location of the defect can be pinpointed by a singularity in the GPA phases and characterized by a Burgers vector (Figure 6.4**b,e**) [178].

The movement of edge dislocations in single-layer graphene and their interaction with both the in-plane and out-of-plane deformations of the atomic lattice have been studied extensively using TEM [178–180].

In our sample, we find a few such defects in the moiré lattice (See Appendix C.3). In Figure 6.4**f,g** we show an edge dislocation in a topographically flat region with $\theta = 0.63°$ (AFM data in Appendix C.4). The absence of any visible out-of-plane buckling in AFM suggests the dislocation, which in the freestanding case would be buckled [179], is flattened out by vdW adhesion between the layers and to the hBN substrate. Contrary to

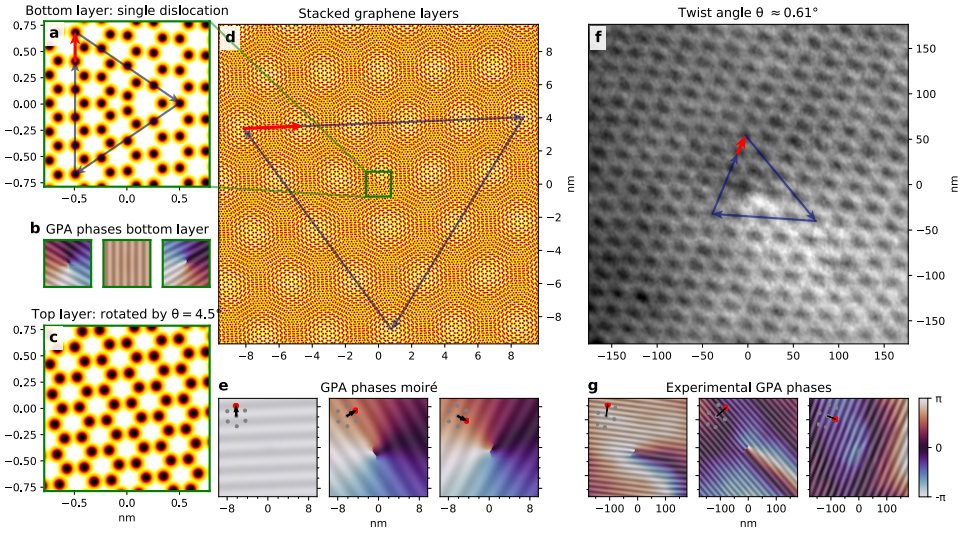

Figure 6.4: Edge dislocations in moiré systems. ***a,*** *Schematic of an edge dislocation in a single layer graphene (centered in the field-of-view), with the corresponding Burgers vector analysis (Blue arrows, Burgers vector indicated in red).* ***b,*** *GPA phases of* ***a****.* ***c,*** *Top layer without dislocation, rotated 4.5° with respect to the layer in* ***a****.* ***d,*** *Schematic of an edge dislocation of a single layer graphene in a twisted bilayer system. The green square in the center corresponds to the combination of* ***a*** *and* ***c****. The Burgers vector analysis of the moiré lattice defect is indicated by blue arrows, the resulting Burgers vector in red. Note: Both the schematics in a and d are mathematical representations of the dislocation, i.e. without taking atomic relaxation into account.* ***e,*** *GPA phases of* ***d****, exhibiting a singularity in the center. The used moiré reference vectors are indicated.* ***f,*** *LEEM image of an edge dislocation in a TBG moiré lattice with a twist angle $\theta \approx 0.63°$. The corresponding moiré Burgers vector is indicated in red.* ***g,*** *GPA phases corresponding to* ***f****.*

TEM, the low-energy electrons used for imaging here do not sputter carbon atoms, preventing creation of edge dislocations pairs and impairing movement. We do not observe creation or annihilation of edge dislocation pairs in the microscope, even at elevated measurement temperatures (500 °C) and under prolonged (i.e. hours) low-energy electron irradiation [180]. The mobility of the defects observed is low, with only one edge dislocation moving over several moiré cells between measurements, after which it remained at the same position even after a month at room temperature and reheating (See Figure C.7 in Appendix C.3). This stability suggests that the moiré lattice itself could play a role in stabilizing these defects, via a minimum of the local stacking fault energy within the moiré unit cell.

These topological dislocations break translational symmetry of the moiré lattice, which may lead to singular electronic properties on the local scale [181–183]. Specifically, a phase difference will appear between electron paths encircling the defect clockwise and counterclockwise.

6.2.3 HIGH TEMPERATURE DYNAMICS OF THE MOIRÉ LATTICE

All measurements presented so far were performed at 500 °C, to minimize hydrocarbon contamination under the electron beam.

In literature, there is concern about the graphene layers untwisting at such temperatures, due to energy differences between different rotations [112, 168]. However, no direct observation of untwisting has been presented in literature, apart from the relaxation observed above 800 °C in Ref. [106], and theoretical work indicates untwisting of large flakes would be unlikely [184]. Indeed, we see no sign of untwisting. The twist angles within the domains are stable from 100 °C up to 600 °C for all samples studied, including samples with significantly larger domains between folds, such as the one studied in Ref. [5]. However, in the current experiment a full distinction between local pinning of the moiré lattice by defects and intrinsic rotational stability of large area twisted bilayer graphene cannot be made. For that, the experiment is to be repeated on a homogeneous area, carefully isolated from the rest of the TBG sample by lithographic means.

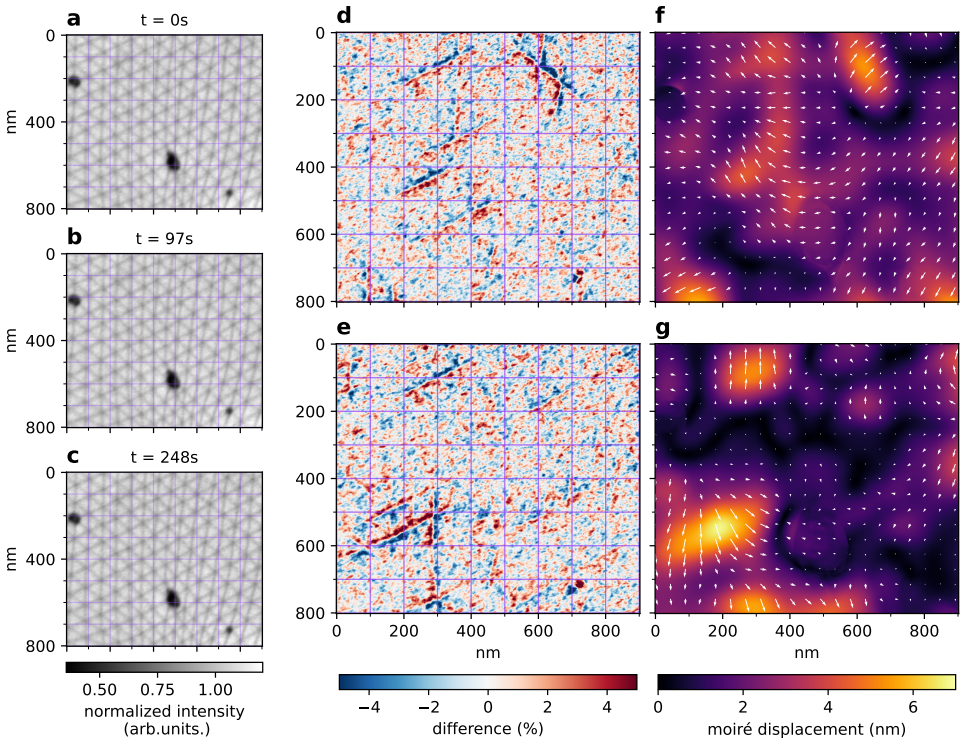

Figure 6.5: Dynamics of moiré patterns. ***a-c,*** *Three images of the same area (in the same domain as Figure 6.1* ***f****), taken minutes apart at a constant temperature of* 500 °C. *Here,* $\theta^* \approx 0.18$ *and* $\epsilon \approx 0.04\%$ *(local values as extracted by GPA can be found in Figure C.3).* ***d,e,*** *Difference of respectively* ***b*** *and* ***c*** *with* ***a****, i.e.* $t = 0$ s*, highlighting the shift of the domain boundaries.* ***f,g,*** *GPA extracted displacement of respectively* ***b,*** *and* ***c,*** *with respect to* $t = 0$ s*, with the arrows indicating the direction and amplitude magnified 8 times for visibility.*

A more subtle dynamic effect we did observe is a thermal influence on the moiré pattern. At a temperature of 500 °C, the position of the stacking domain boundaries fluctuates slightly as a function of time (see Figure 6.5**a-c**). Taking the difference of later images (Figure 6.5**b-c**) with the first image (Figure 6.5**a**), we clearly see the domain boundaries shifting (Figure 6.5**d,e**). Moreover, we can quantify these fluctuations via the difference in displacement field with respect to the image at $t = 0$ s using GPA (Figure 6.5**f,g**). Interestingly, these involve the collective movement of millions of atoms, but only over very small distances. The full dynamics are shown in Supplementary Video 1.[1]

We stress that a translation of the domain boundary by 4 nm, as observed, corresponds to a shift of less than half the width of the domain boundary itself [120, 185]. As the relative shift of the layers over the full domain boundary is a single carbon bond length, the corresponding atomic translations are less than half of that, i.e. less than 70 pm. Hence, the 'moiré magnification' makes it possible to detect these sub-Angstrom changes in TBG in real time using LEEM. Our data suggest that domain boundary displacement follows a random pattern of forward and backward steps. This indicates a possible source for the twist angle disorder observed in low(er) temperature experiments [141, 162, 164, 165]: frozen-in thermal fluctuations of the moiré lattice. The thermal fluctuations found, corresponding to ±0.005° for twist angle and ±0.02% for strain, are smaller than the extracted static deformations, though not negligible. Note that these values are damped by the intrinsic broadening of GPA and the time integration. Future experiments will focus on deducing the detailed statistics of the domain boundary dynamics versus temperature. Following these local collective excitations in time, will yield quantitative information on the energy landscape of these atomic lattice deformations within the moiré lattice. This will be important to answer the question if moiré lattices can be relaxed and homogenized using controlled annealing. If so, this would yield higher-quality magic-angle TBG devices in which charge transport is not limited by percolative effects and higher critical temperatures are reached.

6.3 CONCLUSION

This quantitative LEEM study on TBG reveals a wide variety in twist angles and strain levels in a single sample. We show that spontaneous changes in global twist angle do not occur, even at elevated temperatures, but that local collective fluctuations do take place. This suggests that high-temperature annealing causes relaxation of the local moiré lattice, reducing lattice disorder. Vice versa, this points to frozen-in thermal fluctuations as a possible source of the (significant) short-range twist angle disorder observed previously. Furthermore, this potentially offers insight into energetic aspects of the atomic lattice deformation within the moiré lattice.

We also report the observation of stable topological defects, i.e. edge dislocations, in the moiré lattice of two van der Waals layers. Combining our methods with other techniques that can access the electronic structure, such as STS, nanoARPES, and even in-situ potentiometry [6], will allow for a systematic study of the electronic properties around these defects. Finally, the methods we describe here extend beyond TBG, to any type of twisted system. Therefore, our work introduces a way of studying deformations of

[1] The supplementary video is available at https://doi.org/10.1038/s41467-021-27646-1.

moiré patterns and of connecting these to the (local) electronic properties of this exciting class of materials.

6.4 METHODS

6.4.1 SAMPLE FABRICATION

The twisted bilayer graphene sample was fabricated using the standard tear-and-stack method [4, 186]. The monolayer graphene was first exfoliated with scotch tape on to a SiO_2/Si substrate. A polycarbonate (PC)/polydimethylsiloxane (PDMS) stamp was used for the transfer process, where the PC covered only half of the PDMS surface. After the first half of the graphene flake was successfully torn and picked up, it was rotated by 1.0°. The flake was then overlapped with the bottom half and used to pick it up. The stack was then stamped on a moderately thick (~140nm) hBN flake, priorly exfoliated with PDMS on to a silicon substrate, along with the PC layer. Part of the graphene flake is deliberately put in contact with the Silicon surface for electrical contact purposes, i.e. to absorb the beam current. The whole substrate is then left in chloroform for 3 hours to dissolve the PC. All flakes were exfoliated from crystals, commercially bought from `hq graphene`[2] and the fabrication process was performed using the Manual 2D Heterostructure Transfer System sold by the same company.

6.4.2 LEEM

All LEEM measurements where performed in the ESCHER LEEM, based on the SPECS P90 [25, 27, 187]. Samples were loaded into the ultrahigh-vacuum (base pressure better than 1.0×10^{-9}mbar) LEEM main chamber and heated to 500°C at a rate not exceeding 0.45K per second (as measured by pyrometer and confirmed by IR-camera) and left at this temperature to get rid of any (polymer) residue (temperature log is shown in Figure C.10 in Appendix C). All measurements were conducted at elevated temperatures, 450°C – 500°C, unless specified otherwise. The sample was located on the substrate using photo-emission electron microscopy (PEEM) with an unfiltered mercury short-arc lamp, by comparing to optical microscopy images taken beforehand. Spectra were taken in high-dynamic-range mode and drift corrected and all images were corrected for detector artefacts, as described in Chapter 3. When needed to obtain a sufficient signal-to-noise ratio, multiple 250 ms exposures were accumulated for each image, e.g. 8 exposures (2 seconds) per landing energy in the spectra in Figure 6.1b and 16 exposures (4 seconds) at each location for the overview at 37 eV in Figure 6.1c,e.

TIME SERIES

To measure the dynamics as presented in Figure 6.5, a time series of accumulated $4 \times 250\,\text{ms} = 1\,\text{s}$ exposure images was taken back-to-back. After regular detector correction and drift correction, each image was divided by a Gaussian smoothed version of itself ($\sigma = 50$ pixels) to get rid of spatial and temporal fluctuations in electron illumination intensity. To further reduce noise, a Gaussian filter with a width of $\sigma = 1$ image ~ 1 s, was applied in the time direction before applying GPA.

[2] hq graphene, G. Meirstraat 1, 9728 TB Groningen, The Netherlands, www.hqgraphene.com

6.4.3 STITCHING

To enable high resolution, large field-of-view LEEM imaging, the LEEM sample stage [28] was scanned in a rectangular pattern over the sample, taking an image at each position, leaving sufficient overlap (2 μm steps at a 4.7 μm field-of-view). To obtain meaningful deformation information from this, care needs to be taken to use a stitching algorithm that does not introduce additional deformation, i.e. as faithfully reproducing reality as the constituting images.

To achieve this, a custom stitching algorithm tailored towards such LEEM data, was developed, as described in Appendix B and in the implementation [42].

In addition, for the composite bright field in Figure 6.1**c**, minor rotation and magnifications differences due to objective lens focus differences were compensated for. This was done by registering the stitches for different energies using a log-polar transformation based method to obtain relative rotations and magnification. Subsequently, areas where a color channel was missing, were imputed using a k-nearest neighbor lookup in a regularly sliced subset of the area with all color channels present.

6.4.4 IMAGE ANALYSIS

To quantify the large deviations in lattice shape due to the moiré magnification of small lattice distortions, we extended the GPA algorithm to use an adaptive grid of reference wave vectors, based on related to earlier work in laser fringe analysis [173].

The spatial lock-in signal is calculated for a grid of wave vectors around a base reference vector, converting the GPA phase to reference the base reference vector every time. For each pixel, the spatial lock-in signal with the highest amplitude is selected as the final signal. To avoid the problem of globally consistent phase unwrapping, the gradient of each GPA phase was directly converted to the displacement gradient tensor. More details of the used algorithm are given in Appendix A.5.

All image analysis code was written in Python, using `Numpy` [188], `Scipy` [189], `Dask` [67] and `scikit-image` [69]. The core algorithms are available as an open source Python package [88]. Throughout the development of the algorithms and writing of the paper, `matplotlib` [190, 191] was extensively used for plotting and figure creation.

6.4.5 REFLECTIVITY CALCULATIONS

The theoretical reflectivity spectra are obtained with the ab-initio Bloch-wave-based scattering method described in Ref. [117]. Details of the application of this method to stand-alone two-dimensional films of finite thickness can be found in Ref. [136]. The underlying all-electron Kohn-Sham potential was obtained with a full-potential linear augmented plane-wave method within the local density approximation, as explained in Ref. [116]. Inelastic scattering is taken into account by an absorbing imaginary potential $-iV_i$, which is taken to be spatially constant ($V_i = 0.5$ eV) over a finite slab (where the electron density is non-negligible) and to be zero in the two semi-infinite vacuum half spaces. In addition, a Gaussian broadening of 1 eV is applied to account for experimental losses.

6.4.6 DATA & CODE AVAILABILITY

The data supporting the findings of this chapter is available at 4TU.researchdata [140]. The analysis code is split in three parts: core algorithms are available at ref. [88], lattice rendering code used is available at ref. [192] and specific code to generate the figures in this paper is available at ref. [193].

REFERENCES

4. Y. Cao, V. Fatemi, S. Fang, et al. Unconventional superconductivity in magic-angle graphene superlattices. *Nature* **556,** 43–50. doi:10.1038/nature26160 (2018).
5. S. Lisi*, X. Lu*, T. Benschop*, T. A. de Jong*, et al. Observation of flat bands in twisted bilayer graphene. *Nature Physics* **17,** 189–193. doi:10.1038/s41567-020-01041-x (2021).
6. J. Kautz, J. Jobst, C. Sorger, et al. Low-Energy Electron Potentiometry: Contactless Imaging of Charge Transport on the Nanoscale. *Scientific Reports* **5,** 13604. doi:10.1038/srep13604 (2015).
25. R. Tromp, J. Hannon, A. Ellis, et al. A new aberration-corrected, energy-filtered LEEM/PEEM instrument. I. Principles and design. *Ultramicroscopy* **110,** 852–861. doi:10.1016/j.ultramic.2010.03.005 (2010).
27. R. M. Tromp, J. B. Hannon, W. Wan, A. Berghaus & O. Schaff. A new aberration-corrected, energy-filtered LEEM/PEEM instrument II. Operation and results. *Ultramicroscopy* **127,** 25–39. doi:10.1016/j.ultramic.2012.07.016 (2013).
28. A. W. Ellis & R. M. Tromp. A versatile ultra high vacuum sample stage with six degrees of freedom. *Review of Scientific Instruments* **84,** 075112. doi:10.1063/1.4813739 (2013).
29. J. I. Flege & E. E. Krasovskii. Intensity-voltage low-energy electron microscopy for functional materials characterization. *Physica Status Solidi - Rapid Research Letters* **8,** 463–477. doi:10.1002/pssr.201409102 (2014).
31. T. A. de Jong, J. Jobst, H. Yoo, et al. Measuring the Local Twist Angle and Layer Arrangement in Van der Waals Heterostructures. *physica status solidi (b)* **255,** 1800191. doi:10.1002/pssb.201800191 (2018).
34. J. Jobst, A. J. H. van der Torren, E. E. Krasovskii, et al. Quantifying electronic band interactions in van der Waals materials using angle-resolved reflected-electron spectroscopy. *Nature Communications* **7,** 13621. doi:10.1038/ncomms13621 (2016).
37. T. A. de Jong, E. E. Krasovskii, C. Ott, et al. Intrinsic stacking domains in graphene on silicon carbide: A pathway for intercalation. *Physical Review Materials* **2,** 104005. doi:10.1103/PhysRevMaterials.2.104005 (2018).
42. T. A. de Jong. *Quantitative Data Analysis for spectroscopic LEEM* version v0.2.0. 2021. doi:10.5281/zenodo.3539538.
46. R. M. Feenstra, N. Srivastava, Q. Gao, et al. Low-energy electron reflectivity from graphene. *Physical Review B* **87,** 041406. doi:10.1103/PhysRevB.87.041406 (2013).

67. Dask Development Team. *Dask: Library for dynamic task scheduling* (2016). https://dask.org.

69. S. van der Walt, J. L. Schönberger, J. Nunez-Iglesias, et al. scikit-image: image processing in Python. *PeerJ* **2,** e453. doi:10.7717/peerj.453 (2014).

88. T. A. de Jong. *pyGPA* 2021. doi:10.5281/zenodo.5589555.

106. J. S. Alden, A. W. Tsen, P. Y. Huang, et al. Strain solitons and topological defects in bilayer graphene. *Proceedings of the National Academy of Sciences* **110,** 11256–11260. doi:10.1073/pnas.1309394110 (2013).

112. Y. Cao, V. Fatemi, A. Demir, et al. Correlated insulator behaviour at half-filling in magic-angle graphene superlattices. *Nature* **556,** 80–84. doi:10.1038/nature26154 (2018).

116. E. E. Krasovskii, F. Starrost & W. Schattke. Augmented Fourier components method for constructing the crystal potential in self-consistent band-structure calculations. *Physical Review B* **59,** 10504–10511. doi:10.1103/PhysRevB.59.10504 (1999).

117. E. E. Krasovskii. Augmented-plane-wave approach to scattering of Bloch electrons by an interface. *Physical Review B* **70,** 245322. doi:10.1103/PhysRevB.70.245322 (2004).

120. H. Yoo, R. Engelke, S. Carr, et al. Atomic and electronic reconstruction at the van der Waals interface in twisted bilayer graphene. *Nature Materials* **18,** 448–453. doi:10.1038/s41563-019-0346-z (2019).

135. T. A. de Jong, T. Benschop, X. Chen, et al. Imaging moiré deformation and dynamics in twisted bilayer graphene. *Nature Communications* **13,** 70. doi:10.1038/s41467-021-27646-1 (2022).

136. E. Krasovskii. Ab Initio Theory of Photoemission from Graphene. *Nanomaterials* **11,** 1212. doi:10.3390/nano11051212 (2021).

140. T. de Jong, T. Benschop, X. Chen, et al. *Data underlying the paper: Imaging moiré deformation and dynamics in twisted bilayer graphene.* (4TU.ResearchData, 2021). doi:10.4121/16843510.

141. T. Benschop*, T. A. de Jong*, P. Stepanov*, et al. Measuring local moiré lattice heterogeneity of twisted bilayer graphene. *Physical Review Research* **3,** 013153. doi:10.1103/PhysRevResearch.3.013153 (2021).

143. M. J. Lawler, K. Fujita, J. Lee, et al. Intra-unit-cell electronic nematicity of the high-Tc copper-oxide pseudogap states. *Nature* **466,** 347–351. doi:10.1038/nature09169 (2010).

151. D. Halbertal, N. R. Finney, S. S. Sunku, et al. Moiré metrology of energy landscapes in van der Waals heterostructures. *Nature Communications* **12,** 242. doi:10.1038/s41467-020-20428-1 (2021).

155. R. Bistritzer & A. H. MacDonald. Moire bands in twisted double-layer graphene. *Proceedings of the National Academy of Sciences* **108,** 12233–12237. doi:10.1073/pnas.1108174108 (2011).

156. X. Lu, P. Stepanov, W. Yang, et al. Superconductors, orbital magnets and correlated states in magic-angle bilayer graphene. *Nature* **574,** 653–657. doi:10.1038/s41586-019-1695-0 (2019).

157. J.-B. Qiao, L.-J. Yin & L. He. Twisted graphene bilayer around the first magic angle engineered by heterostrain. *Physical Review B* **98,** 235402. doi:10.1103/PhysRevB.98.235402 (2018).

158. Z. Khatibi, A. Namiranian & F. Parhizgar. Strain impacts on commensurate bilayer graphene superlattices: Distorted trigonal warping, emergence of bandgap and direct-indirect bandgap transition. *Diamond and Related Materials* **92,** 228–234. doi:10.1016/j.diamond.2018.12.007 (2019).

159. Z. Bi, N. F. Q. Yuan & L. Fu. Designing flat bands by strain. *Physical Review B* **100,** 035448. doi:10.1103/PhysRevB.100.035448 (2019).

160. D. E. Parker, T. Soejima, J. Hauschild, M. P. Zaletel & N. Bultinck. Strain-Induced Quantum Phase Transitions in Magic-Angle Graphene. *Physical Review Letters* **127.** doi:10.1103/physrevlett.127.027601 (2021).

161. N. Tilak, X. Lai, S. Wu, et al. Flat band carrier confinement in magic-angle twisted bilayer graphene. *Nature Communications* **12.** doi:10.1038/s41467-021-24480-3 (2021).

162. E. Y. Andrei & A. H. MacDonald. Graphene bilayers with a twist. *Nature Materials* **19,** 1265–1275. doi:10.1038/s41563-020-00840-0 (2020).

163. Y. Xie, B. Lian, B. Jäck, et al. Spectroscopic signatures of many-body correlations in magic-angle twisted bilayer graphene. *Nature* **572,** 101–105. doi:10.1038/s41586-019-1422-x (2019).

164. A. Uri, S. Grover, Y. Cao, et al. Mapping the twist-angle disorder and Landau levels in magic-angle graphene. *Nature* **581,** 47–52. doi:10.1038/s41586-020-2255-3 (2020).

165. N. P. Kazmierczak, M. Van Winkle, C. Ophus, et al. Strain fields in twisted bilayer graphene. *Nature Materials,* 1–8. doi:10.1038/s41563-021-00973-w (2021).

166. T. I. Andersen, G. Scuri, A. Sushko, et al. Excitons in a reconstructed moiré potential in twisted WSe2/WSe2 homobilayers. *Nature Materials* **20,** 480–487. doi:10.1038/s41563-020-00873-5 (2021).

167. M. Koshino & Y.-W. Son. Moiré phonons in twisted bilayer graphene. *Physical Review B* **100.** doi:10.1103/physrevb.100.075416 (2019).

168. Y. Choi, J. Kemmer, Y. Peng, et al. Electronic correlations in twisted bilayer graphene near the magic angle. *Nature Physics* **15,** 1174–1180. doi:10.1038/s41567-019-0606-5 (2019).

169. H. Hibino, S. Tanabe, S. Mizuno & H. Kageshima. Growth and electronic transport properties of epitaxial graphene on SiC. *Journal of Physics D: Applied Physics* **45,** 154008. doi:10.1088/0022-3727/45/15/154008 (2012).

170. T. E. Beechem, T. Ohta, B. Diaconescu & J. T. Robinson. Rotational Disorder in Twisted Bilayer Graphene. *ACS Nano* **8,** 1655–1663. doi:10.1021/nn405999z (2014).

171. J. Mao, S. P. Milovanović, M. Anđelković, et al. Evidence of flat bands and correlated states in buckled graphene superlattices. *Nature* **584,** 215–220. doi:10.1038/s41586-020-2567-3 (2020).

172. M. J. Hÿtch, E. Snoeck & R. Kilaas. Quantitative measurement of displacement and strain fields from HREM micrographs. *Ultramicroscopy* **74,** 131–146. doi:10.1016/s0304-3991(98)00035-7 (1998).

173. Q. Kemao. Two-dimensional windowed Fourier transform for fringe pattern analysis: Principles, applications and implementations. *Optics and Lasers in Engineering* **45,** 304–317. doi:10.1016/j.optlaseng.2005.10.012 (2007).

174. A. Kerelsky, L. J. McGilly, D. M. Kennes, et al. Maximized electron interactions at the magic angle in twisted bilayer graphene. *Nature* **572,** 95–100. doi:10.1038/s41586-019-1431-9 (2019).

175. D. A. Cosma, J. R. Wallbank, V. Cheianov & V. I. Fal'ko. Moiré pattern as a magnifying glass for strain and dislocations in van der Waals heterostructures. *Faraday Discussions* **173,** 137–143. doi:10.1039/C4FD00146J (2014).

176. J. Burgers. Geometrical considerations concerning the structural irregularities to be assumed in a crystal. *Proceedings of the Physical Society (1926-1948)* **52,** 23 (1940).

177. R. Lardner. *Mathematical Theory of Dislocations and Fracture* doi:10.3138/9781487585877 (University of Toronto Press, 1971).

178. J. H. Warner, E. R. Margine, M. Mukai, et al. Dislocation-Driven Deformations in Graphene. *Science* **337,** 209–212. doi:10.1126/science.1217529 (2012).

179. O. Lehtinen, S. Kurasch, A. Krasheninnikov & U. Kaiser. Atomic scale study of the life cycle of a dislocation in graphene from birth to annihilation. *Nature Communications* **4.** doi:10.1038/ncomms3098 (2013).

180. C. Gong, A. W. Robertson, K. He, et al. Thermally Induced Dynamics of Dislocations in Graphene at Atomic Resolution. **9,** 10066–10075. doi:10.1021/acsnano.5b05355 (2015).

181. A. Mesaros, D. Sadri & J. Zaanen. Berry phase of dislocations in graphene and valley conserving decoherence. *Physical Review B* **79.** doi:10.1103/physrevb.79.155111 (2009).

182. Y.-W. Liu, Y.-N. Ren, C.-Y. Hao & L. He. Direct observation of magneto-electric Aharonov-Bohm effect in moiré-scale quantum paths of minimally twisted bilayer graphene. *Preprint at http://arxiv.org/abs/2102.00164.* http://arxiv.org/abs/2102.00164 (2021).

183. C. De Beule, F. Dominguez & P. Recher. Aharonov-Bohm Oscillations in Minimally Twisted Bilayer Graphene. *Physical Review Letters* **125,** 096402. doi:10.1103/PhysRevLett.125.096402 (2020).

184. S. Bagchi, H. T. Johnson & H. B. Chew. Rotational stability of twisted bilayer graphene. *Physical Review B* **101.** doi:10.1103/physrevb.101.054109 (2020).

185. F. Gargiulo & O. V. Yazyev. Structural and electronic transformation in low-angle twisted bilayer graphene. *2D Materials* **5,** 015019. doi:10.1088/2053-1583/aa9640 (2017).

186. K. Kim, A. DaSilva, S. Huang, et al. Tunable moiré bands and strong correlations in small-twist-angle bilayer graphene. *Proceedings of the National Academy of Sciences* **114,** 3364–3369. doi:10.1073/pnas.1620140114 (2017).

187. S. M. Schramm, J. Kautz, A. Berghaus, et al. Low-energy electron microscopy and spectroscopy with ESCHER: Status and prospects. *IBM Journal of Research and Development* **55,** 1:1–1:7. doi:10.1147/jrd.2011.2150691 (2011).

188. C. R. Harris, K. J. Millman, S. J. van der Walt, et al. Array programming with NumPy. *Nature* **585,** 357–362. doi:10.1038/s41586-020-2649-2 (2020).

189. P. Virtanen, R. Gommers, T. E. Oliphant, et al. SciPy 1.0: fundamental algorithms for scientific computing in Python. *Nature Methods* **17,** 261–272. doi:10.1038/s41592-019-0686-2 (2020).

190. J. D. Hunter. Matplotlib: A 2D Graphics Environment. *Computing in Science & Engineering* **9,** 90–95. doi:10.1109/MCSE.2007.55 (2007).

191. T. A. Caswell, M. Droettboom, A. Lee, et al. *matplotlib/matplotlib: REL: v3.3.4* 2021. doi:10.5281/zenodo.4475376.

192. T. A. de Jong. *TAdeJong/moire-lattice-generator* version 0.0.5. 2021. doi:10.5281/zenodo.5156831.

193. T. A. de Jong. *Figure generation code for "Imaging moiré deformation and dynamics in twisted bilayer graphene"* Zenodo, 2021. doi:10.5281/zenodo.5713908.

7

STACKING DOMAIN MORPHOLOGY IN EPITAXIAL GRAPHENE

Parts of this chapter are submitted as T. A. de Jong, L. Visser, J. Jobst, R. M. Tromp & S. J. van der Molen, Stacking domain morphology in epitaxial graphene on silicon carbide [194]

In this chapter we will study stacking domain boundaries in high quality epitaxial graphene from three different sources. These domains are due to the lattice mismatch between the graphene and the $\left(6\sqrt{3}\times 6\sqrt{3}\right)R30^\circ$ reconstructed buffer layer. In addition to the Dark Field LEEM observations in Chapter 4, such domains have been observed using other techniques as well, including thermoelectric imaging and STM [137, 195, 196]. Using the domain morphology, we here extract properties of the graphene itself.

We image graphene on SiC using Bright Field LEEM at a landing energy $E_0 \approx 40$ eV. By employing stitching of high resolution AC-LEEM data as described in Appendix B, we obtain a field of view exceeding 10×10 μm, while retaining a high enough resolution of at least 2.2 nm/pixel to characterize the stacking domain boundaries, enabling the gathering of statistics.

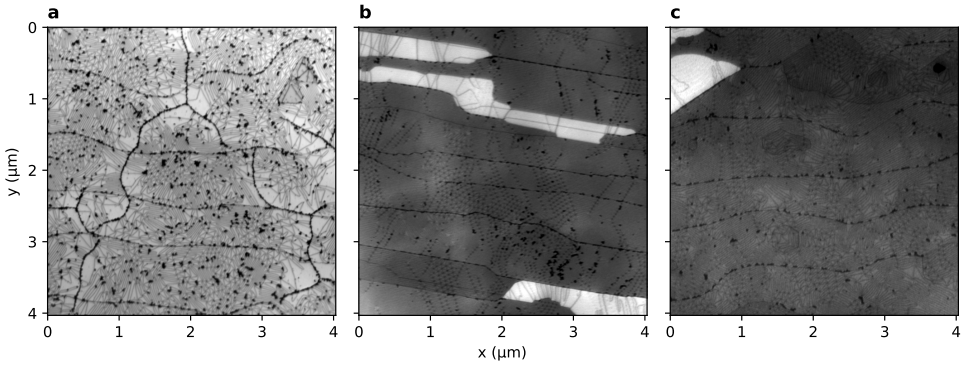

7

Figure 7.1: Sample comparison. a, *Intercalated quasi-freestanding graphene on SiC, grown using an experimental carbonated growth from Heiko Weber's group in Erlangen-Nürnberg imaged using BF-LEEM at $E_0 = 40$ eV.* ***b,*** *Commercially bought graphene on 4H-SiC from Graphensic based on the Linköping growth technique, imaged at $E_0 = 37$ eV.* ***c,*** *Polymer assisted growth on 6H-SiC sample grown at PTB Braunschweig imaged at $E_0 = 36$ eV.*

Samples from three different sources are imaged in this way. A comparison of unprocessed stitched data is shown in Figure 7.1. First, *sample A*, grown at the University of Erlangen-Nürnberg using an early prototype of a variation on polymer assisted growth, where a layer of carbon is sputtered onto the SiC before growth. This sample is grown with an argon back pressure to enable uniform growth and hydrogen intercalated to create quasi-freestanding bilayer graphene [197]. Second, *sample B*, a commercially bought sample from the company Graphensic. Finally, *sample C* grown at the PTB in Braunschweig using polymer-assisted sublimation growth in argon back pressure [10, 128].[1]

In the next section the full datasets are shown and the visible features in the images are described qualitatively. Then, we will use GPA to quantitatively analyze the domain sizes and connect this to the relative strain between the layers. In Sections 7.3 and 7.4 we will take a closer look at two peculiar features: spiral domain walls and edge dislocations,

[1] A big thanks to Christian Ott, Heiko Weber, Robbert Schoo, Cees Flipse, Anna Sinterhauf, Martin Wenderoth Davood Momeni and Klaus Pierz for sharing their samples!

before we will interpret the results and draw conclusions about strain and local variation in these materials.

The Python code used to generate the figures in this Chapter is available at Ref. [146].

7.1 QUALITATIVE DESCRIPTION OF SAMPLE FEATURES

Before analysis, the full datasets are normalized by dividing each by a smoothed version of itself with a width of $\sigma = 50$ pixels, where for samples B and C the bilayer areas are normalized separately. The resulting overviews are shown in Figure 7.2.

For sample A an area of $305\mu m^2$ is imaged at a resolution of 2.2 nm/pixel with an average total integration time of 194.7 s (per position). For sample B an area of $111\mu m^2$, of which 7.1% is bilayer, is imaged at 1.4 nm/pixel with an average total integration time of 103.8 s. For sample C an area of $112\mu m^2$, of which 3.5% is bilayer, is imaged at a resolution of 2.2 nm/pixel with an average total integration time of 16.6 s.

For all three samples, terrace step edges of the SiC substrate are visible, running roughly horizontal. On all samples, some conglomerated (carbohydrate?) adsorbates are visible as black spots, sticking to these substrate step edges and some other defects. Sample A shows a bit more adsorbates than the other samples, more likely due to sample handling and imaging conditions than due to the growth procedure. This sample also shows additional defect lines running roughly vertical. Two examples are indicated with red arrows in Figure 7.2**a**. As they terminate in points (indicated with red circles) and cross substrate steps, they seem unlikely to be terrace edges. Instead, they are probably folds or residue from excess carbon from the experimental carbonated growth process.

All three samples show some bilayer areas, occurring bright in Figure 7.2**b,c**. For sample A, they occur dark (e.g. just above and below the center, indicated with orange arrows in **a**), due to the different value of E_0 used and the hydrogen intercalation. Furthermore both the samples in Figure 7.2**b,c** show terraces with a slightly different contrast, next to the lower bilayer area in **b** (indicated with a green arrow) and in several spots in **c**, in particular in round spots in the center of terraces (some examples indicated with green arrows). This difference in intensity is due to the stacking order and termination of the underlying silicon carbide [198, 199].

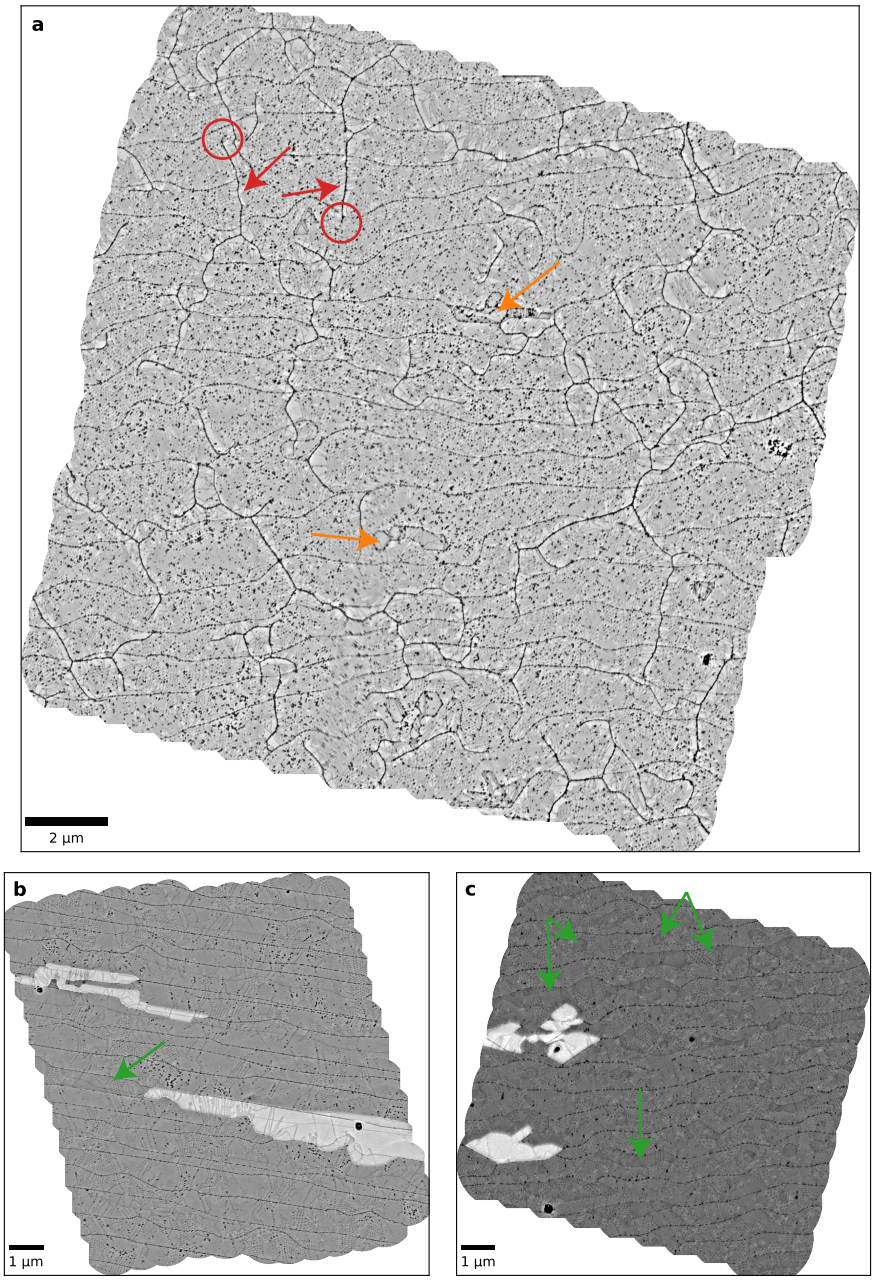

Figure 7.2: Normalized sample overviews. *Similar to Figure 7.1, but all full areas normalized by dividing by a Gaussian smoothed version of the image (with width $\sigma = 50$ pixels) to eliminate global brightness variation, treating bilayer areas separately for* ***b,c****. Details about the indicated features are given in the main text.*

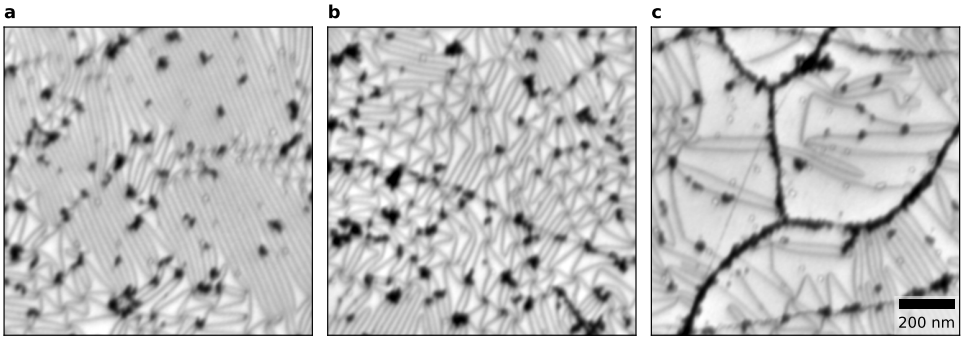

Figure 7.3: Details in sample A. a, *Striped stacking domains* ***b,*** *Chaotic triangular stacking domains. Domain boundaries cross the horizontal step edge in this field of view.* ***c,*** *Along the vertical dark features on this sample, significantly larger domains occur. All panels have the same scale.*

Of the three samples, Sample A is the most irregular. In addition to the aforementioned vertically running defect lines, the SiC substrate step edges are wavier than in the other two samples, although further apart, due to a step bunching procedure applied in the process before graphene growth as described in Section 4.2.1. In Figure 7.3, some full-resolution detail images showcase the domain boundary morphology. The domain shapes are irregular. Stripe domains (Figure 7.3**a**) occur in roughly three directions. Triangular domains occur as well, but are irregularly shaped, not forming larger regular grids (Figure 7.3**b**). Remarkably, around the defect lines, domains are significantly larger and irregular (Figure 7.3**c**), suggesting they are folds out of plane which absorb some of the lattice mismatch.

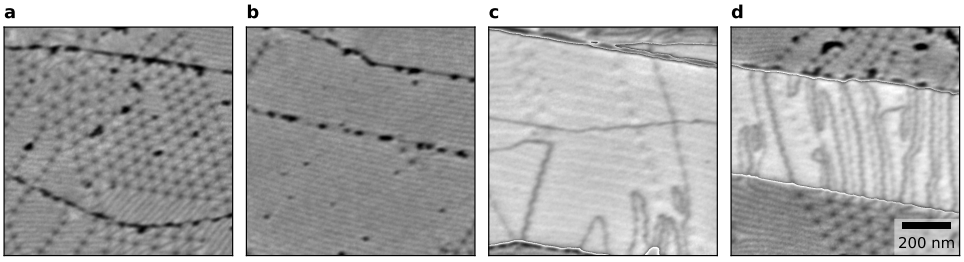

Figure 7.4: Details in sample B. a, *More regular triangular stacking domains.* ***b,*** *Very large and regular striped domains with high stripe density.* ***c,*** *Domains in the bilayer region: Twinned stripe domains between the buffer layer and the lower graphene layer (faint horizontal lines) and irregular domains between the two graphene layers.* ***d,*** *Relation between triangular domains in the monolayer and domain boundaries in the bilayer area. All panels have the same scale.*

Sample B is much more regular. In Figure 7.4**a,b**, it is visible that both relatively regular triangular domains and very dense stripe domains occur [103, 107]. Although these stripe domains again occur in three directions, they occur parallel to the substrate step edges in the very large majority of the cases. Details of the bilayer-on-buffer layer areas

are shown in Figure 7.4**c,d**. Stripe domain boundaries occur between the buffer layer and the lower graphene layer, with the domain boundaries 'twinning', i.e. forming pairs closer together, due to the energy mismatch between ABC and ABA stacked graphene, as discussed in Section 5.3. Domain boundaries between the top two graphene layers also occur, distinguishable by much higher contrast than those lower down, as expected. However, they seem largely irregular, which matches the observation in Chapter 4 that those domain boundaries are caused by nucleation instead of strain [47, 195]. However, in some areas where triangular domains border the bilayer, e.g. in Figure 7.4**d**, it seems that the domain boundaries in the monolayer on buffer layer connect to domain boundaries in the bilayer-on-buffer layer on both levels, i.e. alternating between the buffer layer and the bottom graphene layer and between the two graphene layers.

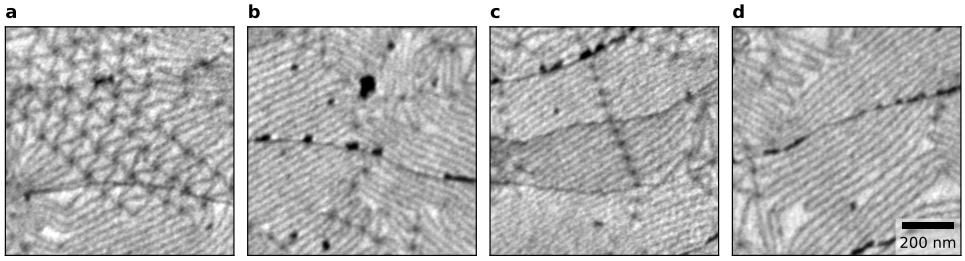

Figure 7.5: Details in sample C. a, *Large triangular domains.* ***b,*** *Stripe domains in two distinct directions.* ***c,*** *Stripe domains with a node line crossing across substrate step edges.* ***d,*** *Low density stripes and disorder. All panels have the same scale.*

For Sample C, details are shown in Figure 7.5. Some triangular domains occur, but a larger part is covered by stripe domains in three directions. Both the triangles and stripe widths vary, but generally are significantly larger than in Sample B. Domain boundaries and even AA node strings (Figure 7.5**c**, also occurring on Sample B) seem to cross substrate step edges unperturbed. Finally, like in Sample A, irregular domain shapes are quite common and will be explored in Section 7.4. But first, in the next section we will apply GPA to quantify the domain morphology and leverage the large size of the imaged areas to obtain some statistics.

7.2 STRIPE DOMAINS IN EPITAXIAL GRAPHENE

From the morphology of the domains as shown in the previous section, it was already clear that the graphene on SiC samples are less homogeneous than expected. Although strain in graphene on SiC and even non-homogeneity of the strain has been studied extensively using e.g. Raman spectroscopy [123, 200, 201], the mere existence of domain boundaries which concentrate the strain means that extra care should be taken interpreting these results, as these techniques average over relatively large areas. In this section we will extract more quantitative information from the stacking domains, and use the relation between the stacking domains and the atomic lattice to quantify strain and disorder on the atomic level.

Assuming the amount of carbon atoms in the graphene layer is fixed after the growth

stops, the average size of the domains is determined by the remaining mismatch between graphene and the $6\sqrt{3}$ reconstruction of the buffer layer on the SiC at the growth temperature. The remaining mismatch is given by:

$$\epsilon = 1 - \frac{13 a_{\mathrm{G}}}{6\sqrt{3} a_{\mathrm{SiC}}}$$

Because the mismatch is relatively small (otherwise the reconstruction would not be able to form!), accurate values of the relevant lattice parameters and their temperature dependence are needed to calculate the expected domain size. To obtain an estimate, we use the same values as used in Ref. [202]: $a_{\mathrm{SiC}} = 0.3096\,\mathrm{nm}$ and $a_{\mathrm{G}} = 0.2458\,\mathrm{nm}$ at $T \approx 1200°\mathrm{C}$. This corresponds to a remaining lattice mismatch of $\epsilon = 0.7\%$ (where graphene has the smaller lattice constant compared to the buffer layer). Note that given the thermal expansion coefficients this number is strongly dependent on the growth temperature, decreasing by about 0.05% for a 100K lower growth temperature. Finally, it is claimed that a shorter growth time can give a small carbon deficiency, effectively yielding a tensile strain in the graphene layer at the growth temperature.

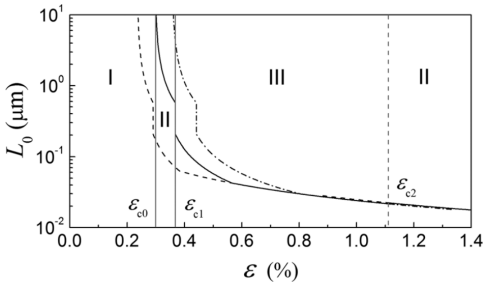

Figure 7.6: *Calculated phase diagram and period of the superstructure as a function of relative biaxial strain in bilayer graphene as computed by Lebedeva and Popov [19]. Indicated phases: I: commensurate, II: triangular incommensurate, III: striped incommensurate. The solid line indicate the periodicity of the superstructure in the respective phases. The dashed and dash-dotted lines indicate the calculated periodicities if the SP barrier height in the GSFE would be 40% different (in which case the critical values would also shift).* [2]

If domain boundary crossings, i.e. AA-sites cost extra energy compared to a domain boundary, there is an extra phase transition in the two-dimensional Frenkel-Kontorova model, even under the assumption of bilateral symmetric/isotropic strain, as described in Section 1.2. Even in this relatively simple case, if the energy cost of AA-sites is high enough, it is beneficial to form parallel domain boundaries instead of a triangular domain pattern by elongating triangular domains along one direction to essentially infinite length in one direction [19]. This is a discontinuous, symmetry-breaking transition and thus a first order phase transition. For bilayer graphene, the ratio between stacking energy costs of AA stacking and SP stacking is about 9. This corresponds to stripe domains forming if the strain is above a lower critical strain value of $\epsilon_{c1} = 0.4\%$. Therefore, stripe domains can be expected in graphene on SiC samples (assuming the graphene–buffer layer interaction is close enough to the one of bilayer graphene, or intercalated samples). For samples created with short enough growth times or at low enough temperature, a mixture of both parallel domain boundaries and triangular patterns can be expected.

[2] Figure reprinted with permission from Ref. [19]. Copyright 2022 by the American Physical Society.

Finally, note that as the sample cools after growth, the lattice mismatch between the graphene and the SiC reconstruction decreases (to 0.1% or less at room temperature), but the number of carbon atoms in the graphene layer is already roughly fixed and the graphene layer is pinned to the substrate by defects and step edges. This yields a total compressive strain on the graphene (which might be partially offset by a carbon deficiency tensile strain for short growth times), but the relative lattice mismatch is globally kept the same by defect pinning.

Indeed, this is what we observe for the graphene on SiC samples, where the periodicity of the buffer layer is forced by the underlying SiC substrate, but the behavior of the graphene layer on top of that is governed by the van der Waals interaction and graphene's properties.

Note however, that unlike on some metals [203, 204] for these boundaries all the strain compensation happens in-plane, i.e. no wrinkles form.

7.2.1 GPA ANALYSIS OF STRAIN

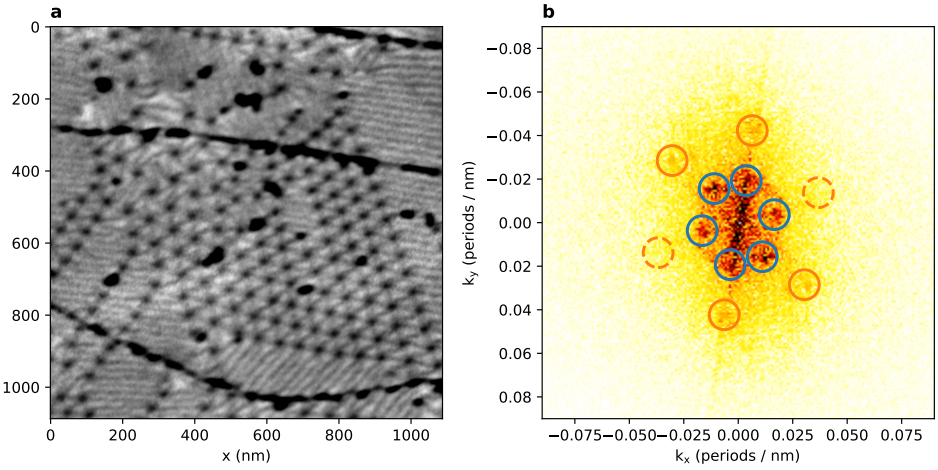

Figure 7.7: FFT of stripe and triangular phases. ***a,*** *Small crop of sample B with both triangular domains and stripe domain in two directions. A straight and a curved step edge run horizontally through the image and are decorated with adsorbates appearing in black.* ***b,*** *Center of the FFT of* ***a****. Detected triangular domain spots are circled in blue. Four detected stripe domain spots are circled orange, and their difference used as the third reference vector is circled in dashed orange.*

To characterize the stacking domains, we use (adaptive) geometric phase analysis (See Appendix A). In this way, we can extract local periodicities from the real space images and calculate back to relative strain values.

The transition from triangular to striped domains causes the length of the corresponding k-vector to double as one direction of domain boundaries aligns with a second to become parallel, thus doubling the frequency (with the third being pushed out). Therefore stripe domains yield separate peaks at roughly double the frequency in the FFT of domain images compared to triangular domains, as highlighted in orange and

blue respectively for Sample B in Figure 7.7. This relatively large separation in Fourier space between the triangular phase and the three striped phases means we can perform GPA for each separately and use this to distinguish them on a large scale and characterize each phase independently.

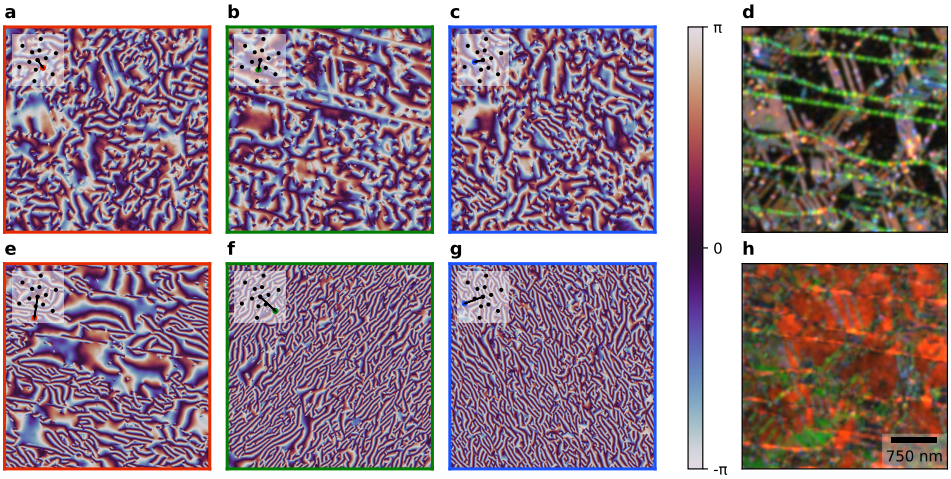

Figure 7.8: GPA phases. ***a-c,*** *GPA phases of an area of sample B corresponding to triangular domains. The k-vector used for each panel is indicated its inset.* ***d,*** *GPA amplitudes in RGB channels corresponding to the triangular domains. The substrate steps are visible as green lines.* ***e-g,*** *GPA phases of stripe domains. Red (**e**) corresponds to the dominantly present stripe phase.* ***h,*** *Similar to **d**, but for the stripe phases.*

The GPA phases for the triangular phase of Sample B are shown in Figure 7.8**a-c**, those for the stripe phase in Figure 7.8**e-g**. For both the triangular and the stripe phase, the corresponding amplitudes are shown as red, green, and blue channels in Figure 7.8**d** and **h** respectively.

The GPA phases only contain relevant information in the areas where the corresponding (stacking domain) phase occurs, as indicated by a high amplitude, and corresponding to a slowly varying GPA phase in real space.

By comparing the GPA amplitudes, we create a mask dividing the sample in stripe domains and triangular domains. For sample B, we use a threshold on the red and blue triangular domains, as the green GPA amplitude is dominated by the substrate steps, resulting in the mask shown in Figure 7.9**a**, with 45% of the characterized area triangular phase and 55% stripe phase. The stripe phase is subdivided over the directions in 48% red (parallel to the step edges), 6% green, and less than 1% blue, i.e. 88% of the stripe domains is roughly parallel to the step edges.

For both the stripe domains and the triangular domains, we compute a local periodicity from the gradient of the GPA phases. This local periodicity we then convert the local relative strain between the layers, which is shown in Figure 7.9**b,c**. Here, we have taken an average over the three directions for the triangular phase. In total, we observe strain between 0.2% and 0.7%. On average, the stripe domains exhibit higher strain val-

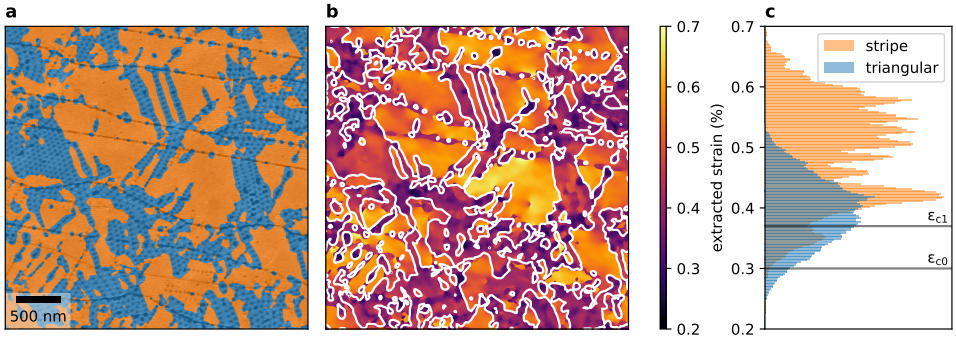

Figure 7.9: a, *Mask distinguishing stripe and triangular domains based on the triangle GPA magnitudes.* ***b,*** *Extracted strain for both types of domains in sample B for the same region. Boundary between the different domains is indicated with white lines.* ***c,*** *Histogram of extracted strain values for both phases.*

ues than the triangular domains. Nevertheless, there is a large overlap and additionally a large part of the triangular domains exhibit a strain larger than the critical value ϵ_{c1}.

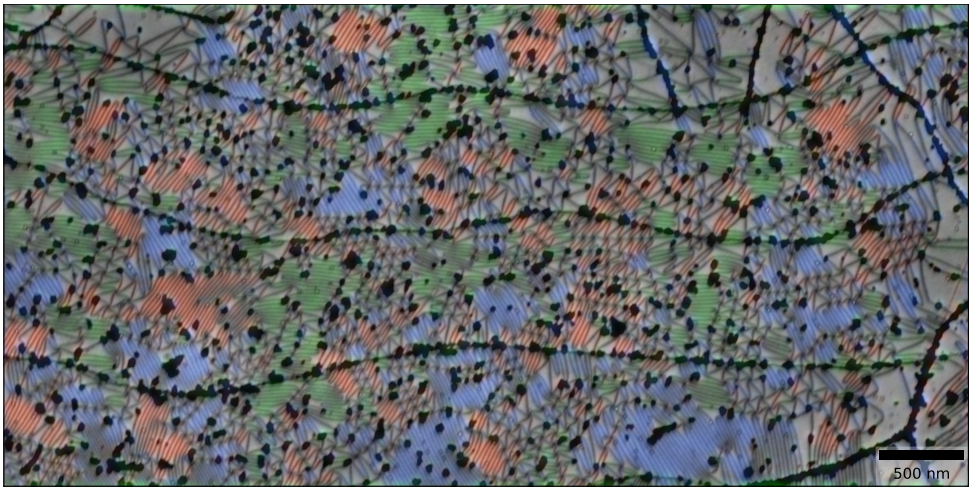

Figure 7.10: *Area in Sample A with the GPA amplitudes corresponding to the three directions of stripe domains overlayed in red, green and blue.*

For sample A and C, the triangular domains were not regular enough to obtain a GPA signal. Nevertheless, the GPA amplitudes of the stripe domains indicate the stripe domains well, as is visible in Figure 7.10. Therefore, as an alternative approach, masks are created by using a threshold value on these stripe domain amplitudes. Contrary to sample B, for sample A the three different stripe domains are almost divided equally, making up 18%, 17% and 19% of the area respectively, for a total of 53% (discrepancy due to rounding) stripe domains and 47% otherwise. Sample C is in between, with stripe

domains making up 40%, 11% , and 10% respectively for 61% stripe domains in total. Here, like in sample B, the majority stripe direction (in red) is roughly parallel to the step edges.

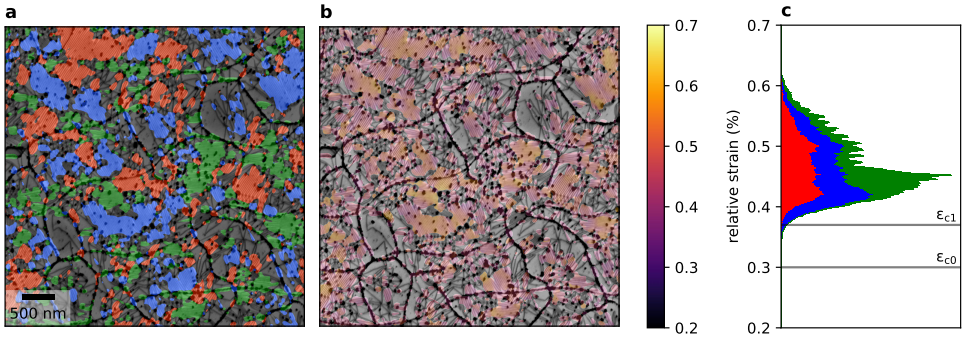

Figure 7.11: a, *Mask on sample A based on the GPA amplitudes labeling stripe domains in three directions in red, green and blue, showing stripe domains of several hundred nanometer across.* ***b,*** *Extracted strain for all three directions of stripe domains for a region in the sample A.* ***c,*** *Histogram of extracted strain values for three domain directions.*

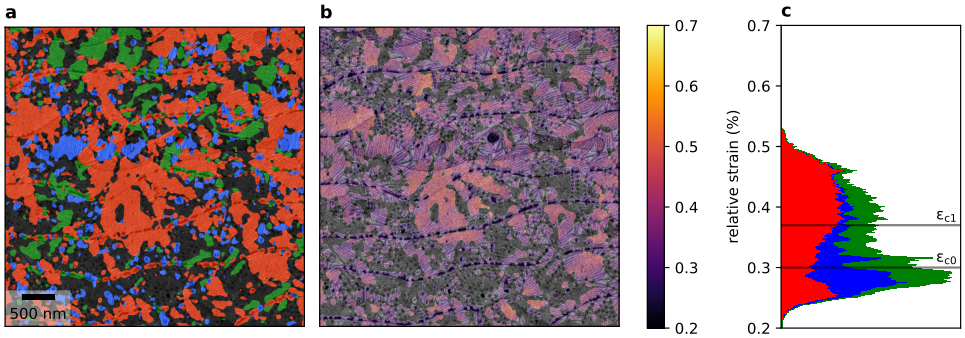

Figure 7.12: a, *Mask on sample C based on the GPA amplitudes labeling stripe domain in three directions in red, green and blue.* ***b,*** *Extracted strain for all three directions of stripe domains for a region in the sample C.* ***c,*** *Histogram of extracted strain values for three domain directions.*

In Figure 7.11 and Figure 7.12 the occurrence of the three orientation domains and the extracted relative strain for these samples is shown. Notably, the extracted strain values for the three different samples cover different ranges, with the strain in the stripe domains in sample C significantly lower than in the others.

7.2.2 DISCUSSION

The extracted strain is not without error. The equidistant peaks visible in the histograms in Figures 7.9**c**, 7.11**c** and 7.12**c** are due to the discretization of the adaptive k-vector, and the k-vector perpendicular to the substrate steps is sensitive to those substrate steps,

which is the cause of the large peak at low strain values for the green stripe domains of sample A (Figure 7.11**c**) and the stripe domains of sample B (Figure 7.9**b**).

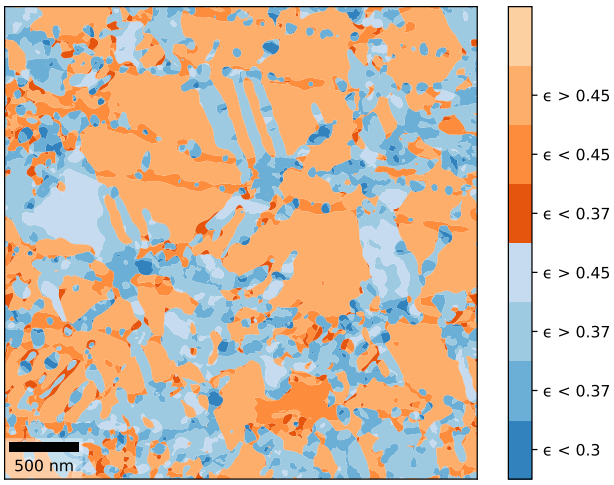

Figure 7.13: *Extracted strain of Figure 7.9 split in different ranges for each phase, based on the theoretical critical strain value $\epsilon_{c0} = 0.3$ (below which no domains are expected to form), and $\epsilon_{c1} = 0.37$ (below which no stripe domains are expected). Both for the stripe domains (orange) and for the triangular domains (blue), the values below the critical values seem to exclusively correspond to artifacts of the GPA method, e.g. step edges.*

To assess the influence of such artifacts on the histograms, we split the extracted strain values for Sample B in different groups, based on the expected phase transitions, as visualized in Figure 7.13. This shows that the large peak at low strain values is indeed almost completely due to the adsorbates on the step edges causing erroneous signal in the GPA.

Nevertheless, even discounting those artifacts, it is clear that a significant spread of the strain within a phase and a difference between the average strain value for the two phases remains, but also that triangular domains occur at higher strains than predicted by the model.

To interpret the stripe domains in terms of strain of the graphene, we need to closely consider what happens in a stripe domain. Perpendicular to the stripe, all the lattice mismatch (at growth temperature) relative to the buffer layer is released and concentrated in the domain boundaries. Parallel to the stripe, we can roughly expect the same lattice mismatch, but now the graphene in that direction is strained to be commensurate to the buffer layer. The variation in period and lattice mismatch perpendicular to the stripe is therefore also a measure of the variation and value of the strain itself parallel to the stripe.

Of course, the patches of anisotropic strain in different directions fit together, meaning that there will be local variation in the magnitude and direction of the strain, both relative to the substrate and in absolute terms.

DOMAIN WALL ORIENTATIONS

For sample B, domain walls in the stripe phases align with one of the domain wall directions in the triangular phase, i.e. the peaks in the FFT in Figure 7.8**b** for both phases are in the same direction. This is in contradiction with the theory of a strained lattice,

where the domain walls in the triangular phase run along the zigzag directions of the graphene lattice and the domain walls in the stripe phases along one of the armchair directions [19]. Although the triangular domains in sample A and sample C are not ordered enough to show up as sharp peaks in the FFT, visual inspection of the images indicates a better adherence to this theoretical prediction, but also a spread of the orientation of the triangular domains, which will be explored in more detail in the next section. This does however suggest that the step edges in sample B have a strong influence on the direction of the domain boundary, presumably by uniaxially straining the lattice.

7.3 SYMMETRY BREAKING AA-SITES (SPIRAL DOMAIN WALLS)

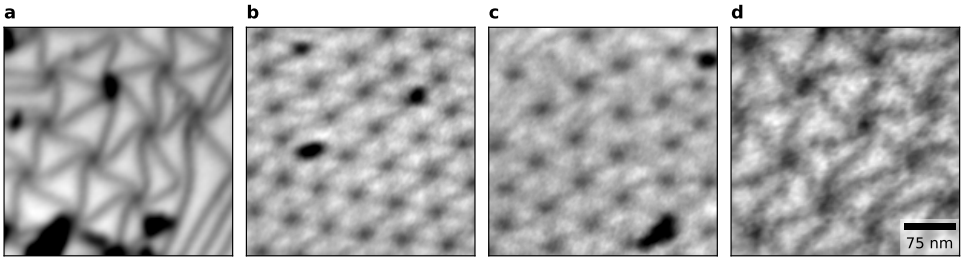

Figure 7.14: a, *Spiral domain walls around AA-sites in sample A.* ***b,*** *Very regular triangles with very little spiral rotation in Sample B.* ***c,*** *Less regular area of Sample B with more rotation in each spiral and opposing orientations.* ***d,*** *Spiral domain walls in Sample C. Contrast optimized per sample, scalebar valid for all images in this figure.*

Taking a closer look at the AA-sites in the different samples in Figure 7.14, we observe spiral domain walls. As the six domain boundaries approach a AA-site, they do not connect straight to it, but bend, either all to the left or all to the right, before connecting in a small spiral. Such spiral domain boundaries have been observed before in various systems, including epitaxial metal systems such as Cu(111)/Ni(111) and Cu/Ru(1000) interfaces, graphene grown on copper, and 2H–1T-TaS_2 polytype heterostructures (See Chapter 8) [17, 18, 196, 205–207] and have been reproduced in simulations [16, 208]. Authors seem however hesitant to give a qualitative explanation for this symmetry breaking. One tentative intuitive explanation would be that the spiral domain walls are just a result of the shear domain boundary having lower energy cost per unit length than the strain type domain boundary. Thus a deviation from straight domain boundaries is promoted in the case of strain domain boundaries, but no such deviation is forced in the case of pure twist, where the domain boundaries are already in the lowest possible energy configuration [19].

In the samples studied here, both orientations of spirals occur, even on the same SiC terrace, even as direct neighbors. According to simulations of a wide variety of twist angles, biaxial strain and combinations thereof [16], a coexistence of both spiral orientations is an indication of pure lattice mismatch, without twist angle (as we would expect for this system), as the system is mirror symmetric and only the spiral itself breaks the symmetry. A pure twist moiré pattern would be signaled by no spiraling and indeed

for the TBG sample studied in Chapter 6, no spiraling is visible. For a combination of strain and a small twist between the layers, the mirror symmetry is broken, and all spirals should align.

There is variation in how much the spirals curl near the AA sites. It seems to depend on the sample, but there is even variation on the same sample, as exemplified by the difference between Figure 7.14**b** and **c**, both on Sample B. Curiously, the moiré lattice also seems somewhat rotated between those areas, indicating that in at least one of the two cases a local twist between the graphene and buffer layer occurs in addition to the biaxial strain. A biaxial strain magnifies the relative twist of the atomic lattices, similar to how a twist angle magnifies a uniaxial strain. In this case, the atomic twist angle θ_a can be expressed as function of the biaxial strain ϵ and the apparent moiré twist angle θ as follows:[3]

$$\theta_a = \theta - \arcsin\left(\frac{\sin\theta}{1+\epsilon}\right) \approx \epsilon\theta$$

Therefore, the observed moiré angle difference of the moiré patterns in Figure 7.14**b** and **c** of $\theta \approx 15^\circ$ at a strain of $\epsilon \approx 0.45\%$ corresponds to a twist angle difference of the atomic lattices of $\theta_a \approx 0.07^\circ$. Here, the lattice in **b** should actually correspond to a larger twist than the one in **c**. Note that this twist angle is the average angle between the unrelaxed lattices, as the atomic lattices within the domain are commensurate.

To fully analyze this, an optimization approach disentangling strain and twist just like employed in Chapter 6 could be employed.

Nevertheless, this demonstrates that the triangular moiré pattern is not only a very sensitive measure of the lattice constant mismatch, but in the presence of such a lattice constant mismatch, the direction of the spiraling of the domain boundaries combined with the orientation of the moiré lattice is a very sensitive probe to the relative local orientation.

7.4 TOPOLOGICAL DEFECTS: EDGE DISLOCATIONS

The strain-caused moiré patterns observed in these systems magnify topological defects of the atomic lattice, just like in the twisted bilayer graphene case studied in Chapter 6.2.2. More precisely, in the absence of any edge dislocations in the graphene layer and the buffer layer, each domain borders on precisely 3 AA-nodes and each pair of neighboring AA-nodes has only 1 domain boundary connecting them. Any deviation from these two rules indicates an atomic edge dislocation in one of the constituting layers.

Despite the fact that we can expect the number of edge dislocations in the underlying SiC substrate, and therefore in the buffer layer, to be very low on these microscopic levels [209, 210], we observe many such defects in all three samples, although in different densities. Examples for sample A and sample C are shown in Figure 7.15. Contrary to the TBG case, domain boundaries near edge dislocations in areas with more disorder deform the surrounding lattice significantly, with a domain boundary crossing over to the next domain boundary often with a significant kink, i.e. domain boundaries running between the same nodes repel each other and form a triangle.

[3] For any realistic atomic strain, this expression is valid for $|\theta_a| \lesssim \epsilon$, but the crossover at $\theta = 30^\circ$ makes it impossible to distinguish the sign for $|\theta_a| \gtrsim \frac{\epsilon}{2}$ in BF-LEEM.

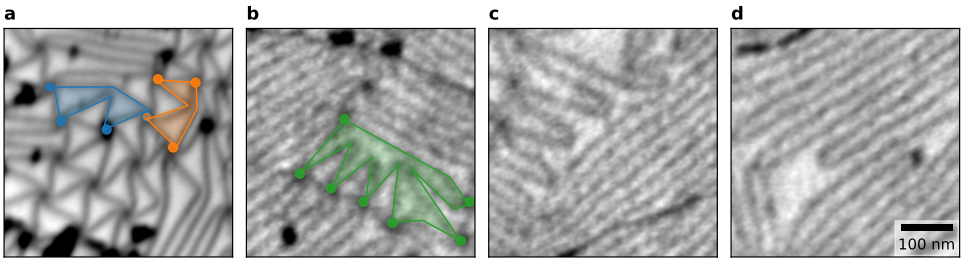

Figure 7.15: a, *Detail of Sample A. Two sets of four AA-nodes, each set bordering one domain are indicated in blue and orange. Each of these domains therefore contains one edge dislocation.* ***b,*** *Detail of Sample C. A set of seven AA-nodes bordering a single domain is indicated in green. This domain therefore contains multiple edge dislocations. Each edge dislocation also corresponds to a domain boundary with a characteristic kink in it, forming a triangle with another domain boundary connecting the same nodes.* ***c,d,*** *Details of Sample C showing more kinked domain boundaries at the edges of striped domain areas. Contrast optimized per sample, scalebar valid for all images in this figure.*

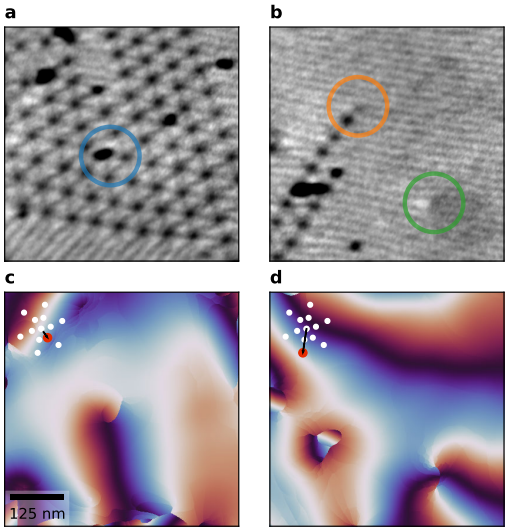

Figure 7.16: Dislocations in Sample B. a, *Dislocation in a triangular domain area at the center of the blue circle.* ***b,*** *Two dislocations in a stripe domain area, indicated by orange and green circles.* ***c,*** *GPA phases of* ***a****, where the dislocation corresponds to a singularity in the GPA phase.* ***d,*** *Similarly, GPA phase for the stripe domain in* ***b****. The singularity of the dislocation in the lower right is of order 2, as the Burgers vector is parallel to the lattice vector corresponding to the GPA phase. The singularity at the end of the AA-node chain in the upper left is not visible in the GPA phase, as the Burgers vector is perpendicular to the to the relevant lattice vector. Insets of (c,d) indicate the corresponding reciprocal vectors of the GPA phases. scalebar in* ***c*** *applies to all panels.*

Edge dislocations in highly ordered areas in sample B, both in triangular and stripe areas show minimal distortion of the surrounding lattice. Using GPA, we can highlight these atomic edge dislocations, just like in TBG, as shown in Figure 7.16, except in the case when the Burger's vector corresponding to the dislocation is parallel to the stripes.

As the density of dislocations is not dominated by edge dislocations in the buffer-layer / SiC substrate itself, this should be another indicator of the quality of the graphene layer. In particular in sample C, high numbers of dislocations within a single stacking domain are found between areas of different stripe directions. This suggest that stripe domains might already form during growth and coalesce, reconciling the lattice mismatch

due to the different strain directions with edge dislocations.

7.5 CONCLUSION

In this Chapter, we have shown that LEEM imaging of domain boundaries in epitaxial graphene on SiC enables the study of strain and atomic edge dislocations on large scales. We have shown that the growth conditions of high quality graphene on SiC cause areas of anisotropic stripes in different directions. We have shown that these stripe domains might already form during the nucleation phase of the growth (as opposed to during cooldown) and cause atomic edge dislocations when different directions grow together.

The growth temperature, growth duration and the amount of carbon pre-deposited all have significant effects on the growth, but also on the domain boundaries formed. Thus the study of these domain boundaries can aid the optimization of growth parameters. In addition to these known parameters influencing the growth, we have seen strong indications that the direction of the step edges of the substrate with respect to the atomic lattice influences the stacking domains and therefore this miscut direction also influences the quality of the resulting graphene. Finally, similar to the TBG case, we suspect that the topological defects in the domain boundary network could be interesting in itself.

7.6 OUTLOOK

We have only scratched the surface of the information available in these domain boundary datasets. Therefore we here give a few more suggestions of information that could be extracted, but are beyond the scope of this chapter. First, it would be informative to connect the images directly to the atomic lattice directions, either by connecting to LEED data, or possibly by observing the local directions of the substrate step edges. Second, for the triangular domains the local uniaxial and biaxial strain, and twist should be separated using a Kerelsky-style decomposition based on the extracted k-vectors as described for the TBG case in Appendix A.6. Third, statistics of left versus right orientation spiral domain walls as a function of the local (minimal) twist angle between the lattices could be obtained. These could be used to measure energy differences as a function of twist angle and strain. Finally, it would be worthwhile to observe dynamics of domain walls, to study the stability of the orientation of spiral domain walls in the twist-free case and potentially obtain more detailed experimental data on the energy landscape that governs these domain boundaries.

REFERENCES

10. D. Momeni Pakdehi, J. Aprojanz, A. Sinterhauf, et al. Minimum Resistance Anisotropy of Epitaxial Graphene on SiC. *ACS Applied Materials & Interfaces* **10,** 6039–6045. doi:10.1021/acsami.7b18641 (2018).

16. S. Quan, L. He & Y. Ni. Tunable mosaic structures in van der Waals layered materials. *Physical Chemistry Chemical Physics* **20,** 25428–25436. doi:10.1039/C8CP04360D (2018).

17. J. Ravnik, I. Vaskivskyi, Y. Gerasimenko, et al. Strain-Induced Metastable Topological Networks in Laser-Fabricated TaS_2 Polytype Heterostructures for Nanoscale Devices. *ACS Applied Nano Materials* **2,** 3743–3751. doi:10.1021/acsanm.9b00644 (2019).

18. C. Gutiérrez, C.-J. Kim, L. Brown, et al. Imaging chiral symmetry breaking from Kekulé bond order in graphene. *Nature Physics* **12,** 950–958. doi:10.1038/nphys3776 (2016).

19. I. V. Lebedeva & A. M. Popov. Two Phases with Different Domain Wall Networks and a Reentrant Phase Transition in Bilayer Graphene under Strain. *Physical Review Letters* **124,** 116101. doi:10.1103/PhysRevLett.124.116101 (2020).

47. H. Hibino, S. Mizuno, H. Kageshima, M. Nagase & H. Yamaguchi. Stacking domains of epitaxial few-layer graphene on SiC(0001). *Physical Review B* **80,** 085406. doi:10.1103/PhysRevB.80.085406 (2009).

103. F. Speck, M. Ostler, S. Besendörfer, et al. Growth and Intercalation of Graphene on Silicon Carbide Studied by Low-Energy Electron Microscopy. *Annalen der Physik* **529,** 1700046. doi:10.1002/andp.201700046 (2017).

107. B. Butz, C. Dolle, F. Niekiel, et al. Dislocations in bilayer graphene. *Nature* **505,** 533–537. doi:10.1038/nature12780 (2014).

123. T. Schumann, M. Dubslaff, M. H. Oliveira, et al. Effect of buffer layer coupling on the lattice parameter of epitaxial graphene on SiC(0001). *Physical Review B* **90,** 041403. doi:10.1103/PhysRevB.90.041403 (2014).

128. M. Kruskopf, D. M. Pakdehi, K. Pierz, et al. Comeback of epitaxial graphene for electronics: large-area growth of bilayer-free graphene on SiC. *2D Materials* **3,** 041002. doi:10.1088/2053-1583/3/4/041002 (2016).

137. H. Hibino, S. Mizuno, H. Kageshima, M. Nagase & H. Yamaguchi. Stacking domains of epitaxial few-layer graphene on SiC(0001). *Physical Review B* **80,** 085406. doi:10.1103/PhysRevB.80.085406 (2009).

146. T. A. de Jong. *Graphene stacking domains code* 2022. https://github.com/TAdeJong/graphene-stacking-domains-code.

194. T. A. de Jong, L. Visser, J. Jobst, R. M. Tromp & S. J. van der Molen. Stacking domain morphology in epitaxial graphene on silicon carbide. *under review.* https://arxiv.org/abs/2207.14623 (2022).

195. S. Cho, S. D. Kang, W. Kim, et al. Thermoelectric imaging of structural disorder in epitaxial graphene. *Nature Materials* **12,** 913–918. doi:10.1038/nmat3708 (2013).

196. B. Lalmi, J. C. Girard, E. Pallecchi, et al. Flower-Shaped Domains and Wrinkles in Trilayer Epitaxial Graphene on Silicon Carbide. *Scientific Reports* **4,** 4066. doi:10.1038/srep04066 (2014).

197. C. Ott. *Light and electron emission at epitaxial graphene nano-contacts* PhD thesis (Friedrich-Alexander-Universität Erlangen-Nürnberg, 2021). https://opus4.kobv.de/opus4-fau/files/16722/ChristianOttDissertation.pdf.

198. D. Momeni Pakdehi, P. Schädlich, T. T. N. Nguyen, et al. Silicon Carbide Stacking-Order-Induced Doping Variation in Epitaxial Graphene. *Advanced Functional Materials* **30,** 2004695. doi:10.1002/adfm.202004695 (2020).

199. A. Sinterhauf, G. A. Traeger, D. Momeni Pakdehi, et al. Substrate induced nanoscale resistance variation in epitaxial graphene. *Nature Communications* **11,** 555. doi:10.1038/s41467-019-14192-0 (2020).

200. D. A. Schmidt, T. Ohta & T. E. Beechem. Strain and charge carrier coupling in epitaxial graphene. *Physical Review B* **84,** 235422. doi:10.1103/PhysRevB.84.235422 (2011).

201. N. Ferralis, R. Maboudian & C. Carraro. Evidence of Structural Strain in Epitaxial Graphene Layers on 6H-SiC(0001). *Physical Review Letters* **101,** 156801. doi:10.1103/PhysRevLett.101.156801 (2008).

202. J. Bao, W. Norimatsu, H. Iwata, et al. Synthesis of Freestanding Graphene on SiC by a Rapid-Cooling Technique. *Physical Review Letters* **117,** 205501. doi:10.1103/PhysRevLett.117.205501 (2016).

203. H. Hattab, A. T. N'Diaye, D. Wall, et al. Interplay of Wrinkles, Strain, and Lattice Parameter in Graphene on Iridium. *Nano Letters* **12,** 678–682. doi:10.1021/nl203530t (2012).

204. P. Sutter, J. T. Sadowski & E. Sutter. Graphene on Pt(111): Growth and substrate interaction. *Physical Review B* **80,** 245411. doi:10.1103/PhysRevB.80.245411 (2009).

205. S. Shao, J. Wang, A. Misra & R. G. Hoagland. Spiral Patterns of Dislocations at Nodes in (111) Semi-coherent FCC Interfaces. *Scientific Reports* **3,** 2448. doi:10.1038/srep02448 (2013).

206. J. C. Hamilton & S. M. Foiles. Misfit Dislocation Structure for Close-Packed Metal-Metal Interfaces. *Physical Review Letters* **75,** 882–885. doi:10.1103/PhysRevLett.75.882 (1995).

207. C. Günther, J. Vrijmoeth, R. Q. Hwang & R. J. Behm. Strain Relaxation in Hexagonally Close-Packed Metal-Metal Interfaces. *Physical Review Letters* **74,** 754–757. doi:10.1103/PhysRevLett.74.754 (1995).

208. J. A. Snyman & H. C. Snyman. Computed epitaxial monolayer structures: III. Two-dimensional model: zero average strain monolayer structures in the case of hexagonal interfacial symmetry. *Surface Science* **105,** 357–376. doi:10.1016/0039-6028(81)90168-0 (1981).

209. T. Kimoto & H. Watanabe. Defect engineering in SiC technology for high-voltage power devices. *Applied Physics Express* **13,** 120101. doi:10.35848/1882-0786/abc787 (2020).

210. J. Łażewski, P. T. Jochym, P. Piekarz, et al. DFT modelling of the edge dislocation in 4H-SiC. *Journal of Materials Science* **54,** 10737–10745. doi:10.1007/s10853-019-03630-5 (2019).

8

CHARGE DENSITY WAVES IN MIXED POLYTYPE TaS_2

In this chapter the interaction between polytypes and charge density waves in TaS_2, a transition metal dichalcogenide, is studied. First, these concepts are each introduced. After reference experiments on pristine 1T-TaS_2, mixed polytypes are introduced and we show they can be distinguished from each other using the observed LEEM spectra. Using dark field LEEM and μLEED, charge density wave states are observed in the mixed polytypes. A mixed orientation, twinned commensurate charge density wave state consisting of in-plane orientational domains is observed. Here, a varying exact orientation of the CDW is tentatively connected to the domain size.

8.1 INTRODUCTION

8.1.1 TRANSITION METAL DICHALCOGENIDES

Transition metal dichalcogenides (TMDs) are a class of materials consisting of layers of transition metal atoms, sandwiched between two layers of chalcogen atoms (S, Se, Te), giving rise to metal dichalcogenide trilayers. The chalcogens are bonded to the metal by strong bonds, that vary in character from covalent to ionic, depending on the specific combination of the metal and chalcogen [211]. However, subsequent chalcogenide layers are only bonded by much weaker van der Waals interactions. This means that TMDs are van der Waals materials, which can be exfoliated into atomic layers, like graphene and hBN (although the thinnest possible 'atomic' layer for TMDs actually consists of three layers of atoms). It also means that these materials are intrinsically 2D-like, with the direction perpendicular to the layers (typically called the c-axis) different from the in-plane directions (a-axis, or, if needed $\mathbf{a}_0$- and $\mathbf{a}_1$-axis).

8.1.2 POLYTYPISM

Each layer of either metal or chalcogen atoms in TMDs is arranged in a trigonal lattice and occupies one of three sublattices, denoted a,b or c. In general, the atoms within a TMD layer can be arranged in one of two forms: Either the chalcogens are situated directly above each other, resulting in a prismatic (Pr) or '2H-like' layer, or the chalcogens are on two different sublattice sites, resulting in an octahedral (Oc) or '1T-like' layer, as shown in Figure 8.1.

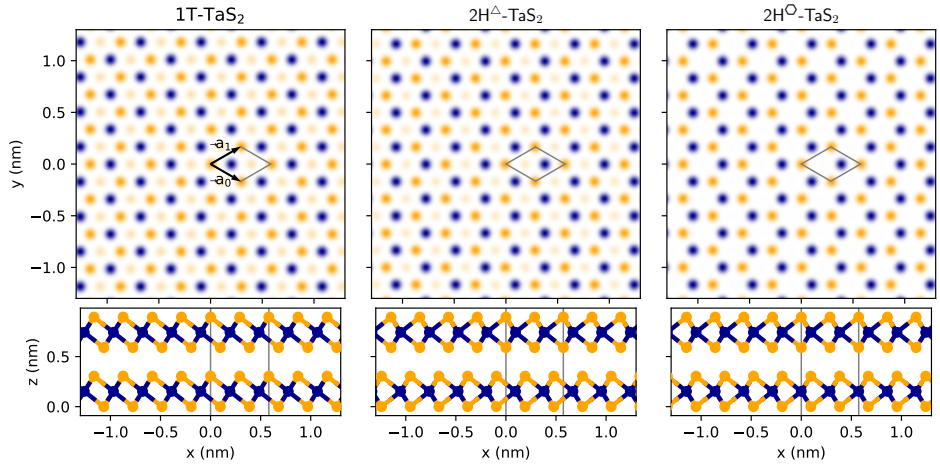

Figure 8.1: *Top and side view of the atomic structure of polytypes occurring in TaS_2. Sulfur atoms are depicted in yellow, tantalum atoms in dark blue. The 1T polytype (left) has an octahedral (Oc) arrangement of the sulfurs and a 1-layer unit cell. The 2H polytypes (center and right) have a prismatic (Pr) arrangement and a 2-layer unit cell. Unlike in MoS_2, in 2H-TaS_2, the bulk polytype is $2H^{\triangle}$ with the tantalum atoms directly on top of each other, although $2H^{\hexagon}$ might occur in mixed stackings.*

By stacking these two building blocks in different order and rotations, different bulk

polytypes are formed: lattice structures with the same atoms in it, but in different relative positions. Stacking octahedral layers results in the 1T polytype (where the "T" signifies a trigonal unit cell, and the "1" signifies a single van der Waals layer in that unit cell), stacking prismatic layers in the same orientation results in the 3R polytype (3 vdW layers in the rhombohedral unit cell), stacking prismatic layers in alternating orientations results in the 2H polytype (2 vdW layers in a hexagonal unit cell). Notably, depending on the exact TMD, two different stackings exist, both designated '2H' in literature. Both tantalum and niobium based TMDs occur in a stable bulk polytype with a (aba cbc) stacking, with the metal atoms in the same sublattice, which we will denote $2H^{\triangle}$ in this work, as all three of the trigonal sublattices are occupied. On the other hand, $Mo(S,Se,Te)_2$ and W based TMDs occur in a (aba bab) stacking, which we will here denote $2H^{\hexagon}$, as from a top-view atoms occur in hexagons [212]. For some TMDs, more complicated bulk polytypes, consisting of a mixture of layer types, are reported, e.g. $4H_a$ and $4H_b$ in $TaS(e)_2$, consisting of two 2H-like layers, separated by 1T-like layers [212, 213].

8.1.3 CHARGE DENSITY WAVES

Many TMDs, with their 2D-like nature, exhibit Charge Density Waves / Periodic Lattice Distortions behavior (CDW / PLD, the combined effects will be referred to as CDW in this work) at low temperatures, i.e. a new, larger periodicity spontaneously forms as the atomic positions over several unit cells and the associated electron density reorder to exchange electronic (band) energy with Coulomb energy of the atomic core positions. However, both the exact periodicity of the CDW with respect to the atomic lattice (some common in-plane periodicities being 3×3 and $\sqrt{13} \times \sqrt{13}$, although more complicated stripe-phases also occur) as well as the temperature dependence vary strongly between TMDs. In general, CDW behavior has a strong influence on the temperature-dependent properties of the material, making it interesting for applications. Furthermore, CDW, and its cousin spin density waves (SDW), are closely related to superconductivity in these materials, although it seems unclear if the CDW behavior competes with superconductivity or, alternatively, is a necessary component [214].

CDW behavior is the (two- or) three-dimensional equivalent of the Peierls transition, where dimerisation of a mono-atomic chain occurs at half-filling of the electron band [215]. The three-dimensional extension of the Peierls mechanism, Fermi surface nesting, suggests the need for large parallel parts of the Fermi surface to be connected by a CDW wave vector and therefore a strongly anisotropic Fermi surface, such as occurs in quasi-1D and -2D materials. In practice however, the Peierls mechanism is severely limited as a model. It suggests that in the 1D case, a CDW should always occur at low enough energy, but it was later realized the effect can already be suppressed in the presence of electron-electron interaction [216]. It turns out that more generally Fermi surface nesting has little to no predictive power for real materials, beyond materials with a strong 1D-like nature, i.e. atomic chains.

To properly model the CDW behavior in TMDs, Fermi surface nesting is therefore not sufficient. Instead, the combination of both the atomic cores and the electrons in the bands needs to be taken into account, including the electron-phonon coupling and its dependence on the relevant wave vectors [20, 217]. This does however significantly

increase the theoretical effort needed to understand the causes of CDW behavior. This is especially true in some materials, such as TaS_2, where the relative phase of the in-plane CDW in subsequent van der Waals layers is relevant [218–220].

8.1.4 TANTALUM DISULFIDE

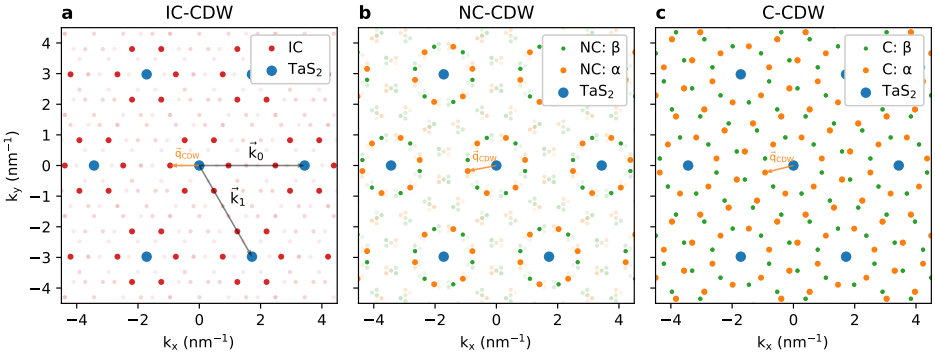

Figure 8.2: CDWs in 1T-TaS_2. *Schematic showing the different diffraction peaks for the different CDW phases occurring in TaS_2, incommensurate (IC), nearly commensurate (NC) and commensurate (C), with relevant parameters indicated. The atomic Bragg peaks of the TaS_2 are indicated in blue, the IC-CDW peaks in red. (See also Figure 1.1***c** *for a real space schematic of the CDW.) For the commensurate and nearly commensurate phase, the CDW peaks are indicted in orange and CDW peaks of the second possible orientation of the CDW (β-phase, vs α-phase) are indicated in green.*

The specific TMD studied here, TaS_2, exists in two bulk polytypes, 1T-TaS_2 and 2H-TaS_2. They have slightly different in-plane lattice constants, $a = 0.336$ nm and $a = 0.331$ nm respectively.[1] The former is meta-stable at room temperature, and can be acquired by quenching a crystal from high temperatures. Both polytypes exhibit CDW behavior. The 2H polytype only exhibits an (almost) commensurate 3×3 CDW below $T_c = 75$K in bulk [221], with the T_c rising up beyond 130K in the monolayer [222, 223]. However, the bulk 1T-TaS_2 polytype exhibits a more complicated set of CDW states. Starting from high temperatures, at $T \approx 540$K the crystal transitions into an incommensurate $\sqrt{13} \times \sqrt{13}$ CDW (IC-CDW) state, where the wave vectors of the CDW are parallel to the atomic lattice vectors (Figure 8.2**a**). At $T \approx 350$K, the material undergoes a transition to a nearly commensurate CDW state (NC-CDW, Figure 8.2**b**). In this state, the CDW vectors keep the same length as in the IC-CDW state, but rotate to $\theta_{NC} \approx 10.9°$. This is close to the commensurate angle of $\theta_C = \arccos\left(\frac{7}{2\sqrt{13}}\right) \approx 13.9°$, corresponding to a realspace CDW vector of $3\mathbf{a}_0 + \mathbf{a}_1$. However, in this state, it remains discommensurate with respect to the atomic lattice. This slight mismatch results in superdomains much larger than the $\sqrt{13} \times \sqrt{13}$ domains. At room temperature, the size of these NC-CDW superdomains can

[1] This slight difference in lattice constant can cause stacking domains just like in graphene on SiC as described in Chapter 7, see e.g. Ref. [17].

be expressed in terms of the mismatch between θ_{NC} and the commensurate angle θ_C:

$$L = \frac{a}{2\sin(\theta_C - \theta_{NC})} = \frac{0.336\text{nm}}{2\sin(13.9° - 10.9°)} \approx 7\,\text{nm} \tag{8.1}$$

This has been confirmed directly using STM [224], but also indirectly with X-ray diffraction [219]. The mismatch in k-space decreases (and therefore the real space period increases) for lower temperatures.

Below $T \approx 200$K the CDW undergoes a final transition and becomes commensurate (C-CDW) corresponding to a perfect match to the atomic lattice at $3\mathbf{a}_0 + 1\mathbf{a}_1$ and a rotation of the CDW vector of $\theta_C \approx 13.9°$ with respect to the atomic lattice vector (Figure 8.2**c**). In the atomic plane, this corresponds to 12 tantalum atoms in the unit cell moving towards the central final tantalum atom in a 'star-of-David' pattern.

The relative in-plane phase of the CDW in subsequent layers gives rise to an extra out-of-plane periodicity. While both the IC-CDW and the NC-CDW have a periodicity of 3 van der Waals layers along the c-axis (corresponding to face-centered cubic stacking of the CDW phases), literature states that the C-CDW either has a periodicity of 13 layers (iterating the center of the star-of-David over all 13 tantalum atoms in the in-plane unit cell) or is not periodic at all [218, 219].

The transition to C-CDW also incurs a transition to insulating behavior, just like in the simple Peierls model [213]. Finally, there are reports of stripe phases when warming the sample up from the C-CDW state [225] and "hidden" states accessed by laser excitation at low temperatures [226].

It is worth noting at this point that both the NC-CDW and C-CDW can exist in two equivalent mirror variants, referred to as α-phase and β-phase (green and orange in Figure 8.2). In a bulk 1T-TaS_2 sample, the whole sample exhibits a single orientation (which is then labeled α), but mixtures of both orientations can be induced by, for example, voltage pulses from an STM tip [227].

8.1.5 TOWARDS 2D

With the advent of TMDs as two-dimensional materials, CDWs in TMDs have received renewed interest. The CDWs extend out-of-plane in the TMDs. As the stacking of layers actually seems to play a role in stabilizing the CDW, let alone the fact that most CDW states have a periodicity of more than one van der Waals layer, the behavior of CDWs in the 2D limit has been an interesting open question. However, in addition to thickness, a number of other aspects seem to influence the CDW and the critical temperatures of its phase transitions, such as electrical or chemical doping, strain induced during exfoliation, increasing current densities in transport measurements, and even plain cracks in the sample and oxidation from ambient air. Unfortunately, all these factors become increasingly relevant when exfoliating a crystal to thinner layers.

These and other factors, as the following will show, complicate the study of how the CDW behavior changes for thinner samples closer to the true 2D limit using transport experiments or optical probes, as any change measured can be contributed either to (approaching) the 2D limit, or to one of these other extrinsic factors [228]. Here, we use Low-Energy Electron Microscopy (LEEM) to study local aspects of CDWs in TaS_2. Previous results using (Ultrafast) Low-Energy Electron Diffraction ((U)LEED) already showed that

low-energy electrons can be used to detect the presence of CDW, in particular in TaS_2 with CDWs above room temperature [218, 229]. Unlike these pure diffraction techniques LEEM can correlate the observation of CDWs with real space features using μLEED and dark field imaging modes, and thus help to distinguish the effect of (local) artifacts from intrinsic effects.

Beyond studying two-dimensional condensed matter physics, the second big potential of van der Waals materials is the possibility to combine different lattices and material properties by stacking layers. Arguably, the most famous example of this is superconductivity due to a flat band in 'magic' angle twisted bilayer graphene (See Chapter 6). Bottom-up combining 2D van der Waals layers does however suffer from the same complicating factors as described above. To study the layer interactions and the 2D limit of the CDW in TaS_2 and to try to avoid these issues, we will use an alternative approach here: by partially converting a single 1T crystal to 2H by annealing, we create a heterostack of 1T-like and 2H-like layers without the need to exfoliate single layers [230].

8.2 SAMPLE PREPARATION

Samples were prepared from exfoliated flakes. First, flakes were exfoliated using blue NITTO tape from a 1T-TaS_2 crystal purchased at `hq graphene`[2]. Next, these flakes were deposited directly onto silicon substrates with only a native oxide. To increase adhesion, the substrates were treated using an ozone cleaner[3] for approximately 20 minutes before flake deposition. This resulted in flakes of bulk-like thickness, i.e. in the order of 100 nm as measured by AFM (See Figure 8.3).

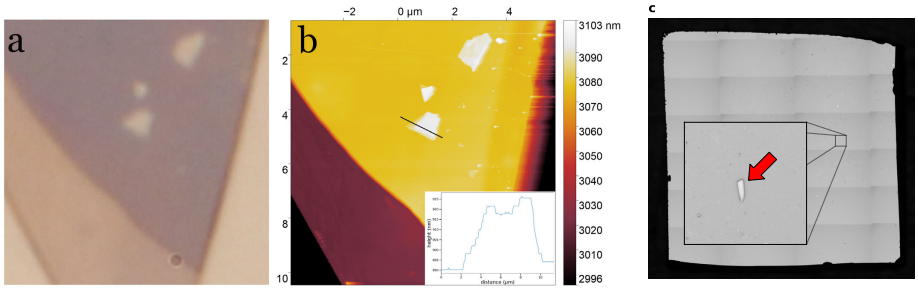

Figure 8.3: a, *Optical microscopy image of part of a TaS_2 flake.* ***b,*** *Corresponding AFM topography. Reproduced under CC-BY from [231].* ***c,*** *Optical overview of the full Si substrate. Red arrow indicates the flake in* ***a,b****. Full substrate is approximately* 5×5 *mm. Image taken by J.P. van Soest.*

Immediately after deposition from the tape onto the silicon, the substrates with flakes were mounted with a molybdenum backplate into the loadlock of the LEEM instrument and pumped down to a pressure lower than 1×10^{-6} mbar. This was achieved by exfoliating directly next to the instrument, to minimize exposure of exfoliated flakes to air, resulting in a time between deposition on the substrate and pump down of less than five minutes. For samples exposed to air for longer periods than this, no CDWs could be

[2] hq graphene, G. Meirstraat 1, 9728 TB Groningen, The Netherlands, `www.hqgraphene.com`
[3] Bioforce nanosciences UV/Ozone ProCleaner, nominal UV intensity of 19.39 mW/cm^2.

observed. After pump down, samples were transferred to the main UHV chamber (base pressure $< 1 \times 10^{-9}$ mbar) and annealed for at least an hour at a temperature of at least 200 °C (see below).

Annealing at a temperature of 200 °C is low enough to preserve the 1T polytype. A common technique in LEEM experiments to obtain a clean surface is to anneal beyond 450 °C in UHV to evaporate any surface adsorbates. Such annealing goes beyond the stability point of the 1T polytype and will convert parts of the sample to the 2H polytype.

8.3 PRISTINE 1T-TaS_2

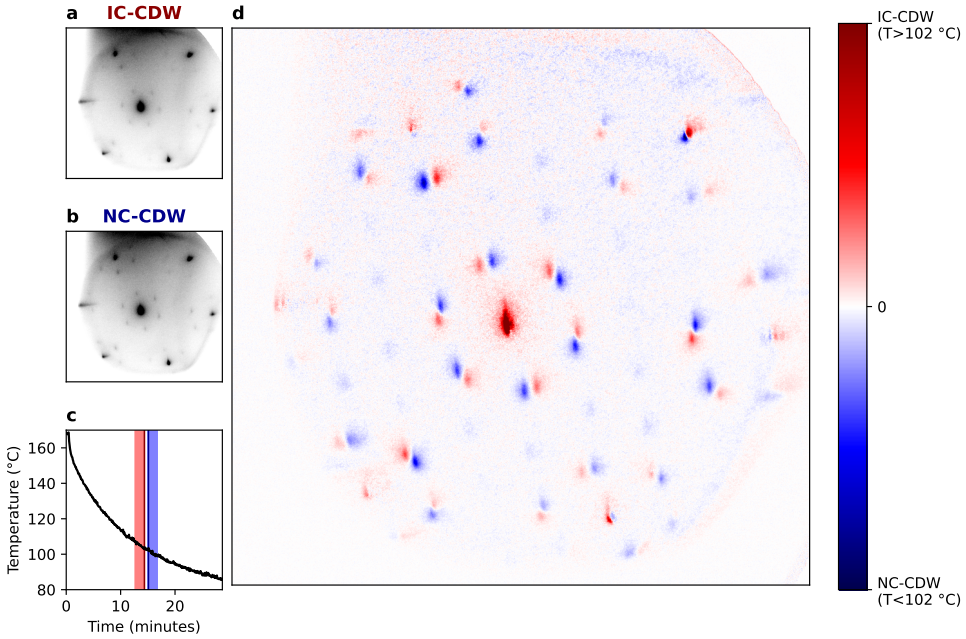

Figure 8.4: ***a,b,*** *Diffraction pattern for full beam illumination (~ 6μm across) of pristine 1T-TaS_2 respectively just above and just below the transition from incommensurate to nearly commensurate.* ***c,*** *Temperature during cooldown integration windows for* ***d*** *is indicated.* ***d,*** *Difference image of both diffraction patterns.*

For pristine 1T-TaS_2 samples prepared near-situ (as described above) and annealed at $T \approx 200$°C for several hours before cooling down again, weak CDW spots are visible. As expected for 1T-TaS_2, above $T \approx 102$°C (as measured using the IR-camera of the system)[4] an IC-CDW is present with the CDW vectors along the reciprocal atomic lattice vectors, and below $T \approx 102$°C a NC-CDW is present with the CDW vectors rotated away to almost a $\sqrt{13} \times \sqrt{13}$ grid, as shown in Figure 8.4. The measured IC–NC transition temperature is

[4] This is therefore an approximate value: all temperatures reported in this work are measured with an IR-camera without absolute calibration.

23K higher than values reported in literature, but this is well within the expected inaccuracy of the temperature measurement using the IR-camera.

However, we find surface quality to be far from optimal. This is evident by three aspects of the imaging: a high background intensity in the diffraction images obscuring the CDW spots, low contrast and smudging of features in real space images and finally contamination buildup during prolonged imaging at energies above ~ 5 eV.

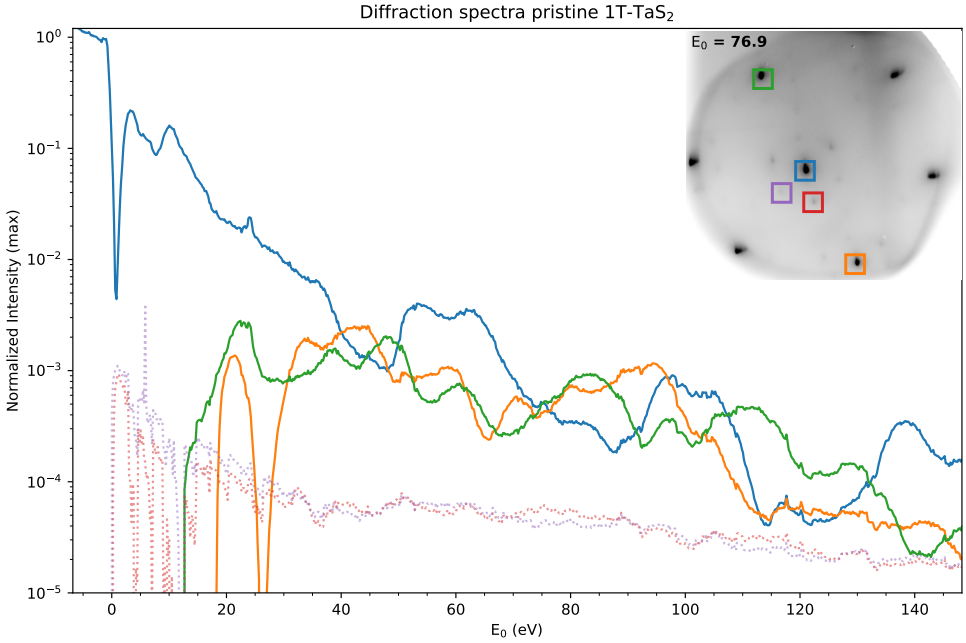

Figure 8.5: *LEED spectrum of pristine 1T-TaS_2 for the zeroth-order spot (blue) and two types of first-order diffraction spots (orange and green, as indicated in inset). The gain of the detector was actively tuned during the measurement as described in Section 3.3. Despite this, the NC-CDW spots (red and purple dashed) are very weak and hardly rise above the noise.*

Especially the contamination buildup is detrimental to any spectral imaging, with visible contamination buildup and signal deterioration during a single sweep of the landing energy. However, to serve as a reference for what is to follow, a LEED spectrum, where reflectivity for various diffraction spots is recorded as a function of landing energy E_0 [29], was measured on this surface in the NC-CDW state and is shown in Figure 8.5 [5]. In addition to the spectrum of the specular reflection, which corresponds to a bright field LEEM spectrum (as obtained for the mixed polytypes in the following), the spectra

[5] LEED-IV, LEED-I(V), LEED-IV spectrum, (for Low Energy Electron Diffraction Intensity vs Voltage) and their equivalent terms using LEEM and even LEER spectrum (Low Energy Electron Reflectivity spectrum) are used throughout literature to denote similar measurements. Here, LEED spectrum and LEEM spectrum are used to distinguish between diffraction and real space data, but the redundant 'IV' moniker is dropped, as measurements are properly normalized and therefore correspond to reflectivity as a function of landing energy and it can be easily confused with current-voltage transport measurements.

of two first order Bragg peaks are shown. Although the absolute intensity values at higher landing energies are lowered due to contamination, the relative positions of maxima and minima can still serve as a reference. A final note on these spectra: Just like in MoS_2 [31], neighboring first order peaks are inequivalent due to the 3-fold symmetry of the lattice. Similarly, although the spectra of the CDW-peaks barely rise above the background intensity, they also show signs of a 3-fold symmetry.

To reduce contamination buildup and contamination-induced beam damage, samples were annealed at temperatures beyond 450°C. Although this did reduce contamination buildup to workable levels, it has an additional effect of partially converting the 1T polytype to 2H, yielding a more complicated material system, as explained in the next section.

8.4 MIXED POLYTYPES

Before considering the results on mixed polytype samples, we consider the complexity of mixed polytypes. Due to the limited penetration depth of electrons at LEEM energies, in general the top layer contributes most to the reflectivity spectrum, with each subsequent layer contributing exponentially less. Therefore, we start out considering only two layers of TaS_2. For a bilayer of TaS_2, with each layer either 1T-like or 2H-like, several inequivalent stackings exist, even when taking into account rotation, mirror symmetry and relative in-plane position, as relevant for bright field LEEM (and without taking into account CDWs).

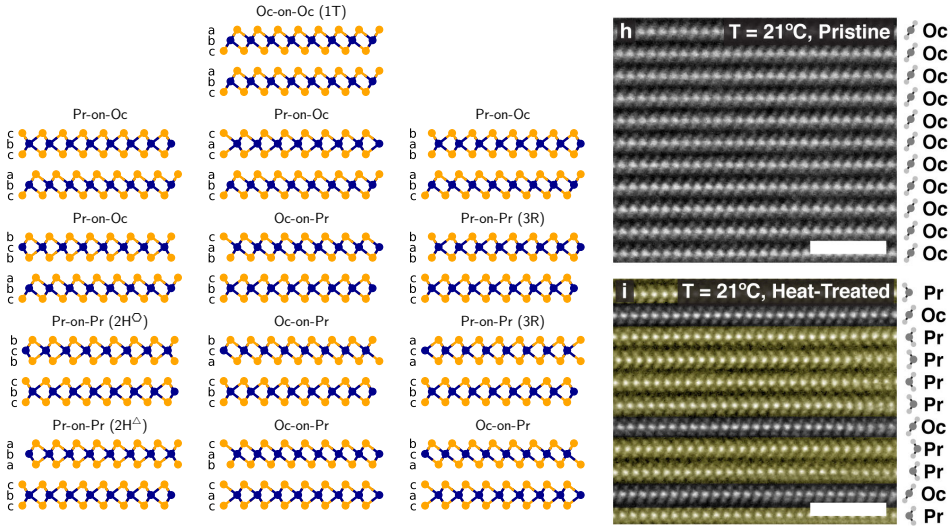

Figure 8.6: (left) *Schematic of possible stackings of two layers of TaS_2 either of the Oc or Pr type. Labels (abc) indicate the sublattice positions of the atoms in the layer.* ***(right)****: Stacking of pristine and (heat-treated) mixed state TaS_2 as measured by HR-TEM, scalebars are 2 nm. Reproduced under CC-BY from Ref. [230].*

Due to the three atomic layers in the unit cell, stacking these two layers has the same

complexity as stacking six graphene layers: subsequent layers can not occupy the same sublattice, leaving two out of three sublattices as a possibility for each added layer (in graphene, equivalently, the subsequent empty sublattices can not occupy the same position to obtain a Bernal stacking). Therefore, before taking symmetries into account, there are $2^5 = 32$ possible stackings.

However, taking into account the symmetries and the fact that all layers are formed from a pristine 1T crystal, only thirteen possible stackings remain[6], as all 1T layers must have the same orientation and sublattice (as corroborated by High resolution transmission electron microscopy (HR-TEM) data, see Figure 8.6):

- Oc-on-Oc: 1 option (bulk-like 1T)
- Oc-on-Pr: 4 options (2 for the top sulfur of the Pr layer times 2 for the Ta).
- Pr-on-Oc: 4 options (similarly).
- Pr-on-Pr: 4 options (2× 3R-like stacking (Ta on top of S or S on top of Ta), $2H^{\hexagon}$, and $2H^{\triangle}$).

Notably, using HR-TEM in Ref. [230] no 3R-like stacking was observed and all subsequent 2H-like layers were $2H^{\hexagon}$, as opposed to the supposedly $2H^{\triangle}$ in bulk.

As suggested by this number of different possibilities to stack only two layers, a wide variety of LEEM spectra could be expected if annealing results in a state of mixed polytypes.

However, if energy differences between different stackings are too large, some of these stacking options might still not occur. To compare, the authors of Ref. [17] report on STM observations of two Oc-on-Pr stackings, with the other two options not occurring, because the low temperature laser-induced polytype transformation they apply only influences the top-most sulfur layer. The fact that the parallel domain boundaries in their results are twinned, i.e. move closely together in pairs, does indicate an energy difference between the observed stackings, but at the same time show that the energy difference is small enough for both stackings to co-exist.

8.4.1 SPECTRA

Indeed, after annealing at 450°C, a cleaner surface is achieved than when annealed at lower temperatures[7], as indicated by higher contrast LEEM images and a higher intensity of the Bragg peaks compared to secondary electrons.

For almost all samples, a complex set of areas with different reflectivity appears, even after annealing overnight, suggesting indeed a state of mixed polytypes, as previously reported in TEM work [230].

[6] From (unpublished) twisted MoS_2 data, it is known that relative lattice positions are relevant to the BF LEEM spectra, as contrast is observed in ~ 0° (3R-like) stacked layers and the spectra both show differences compared to 2H-like stacking.

[7] There is one alternative explanation for the observed behavior that could be considered. By the nature of the exfoliation process, there are two types of flake surface: a surface that was in contact with the tape, and surface that was cleaved of the crystal upon transfer to the substrate, which never touched the tape. *If* a crystal still contains trace amounts of different polytypes, the internal lattice mismatch would cause it to preferentially tear in this area, especially on the last transfer, causing clean, but mixed polytype surfaces.

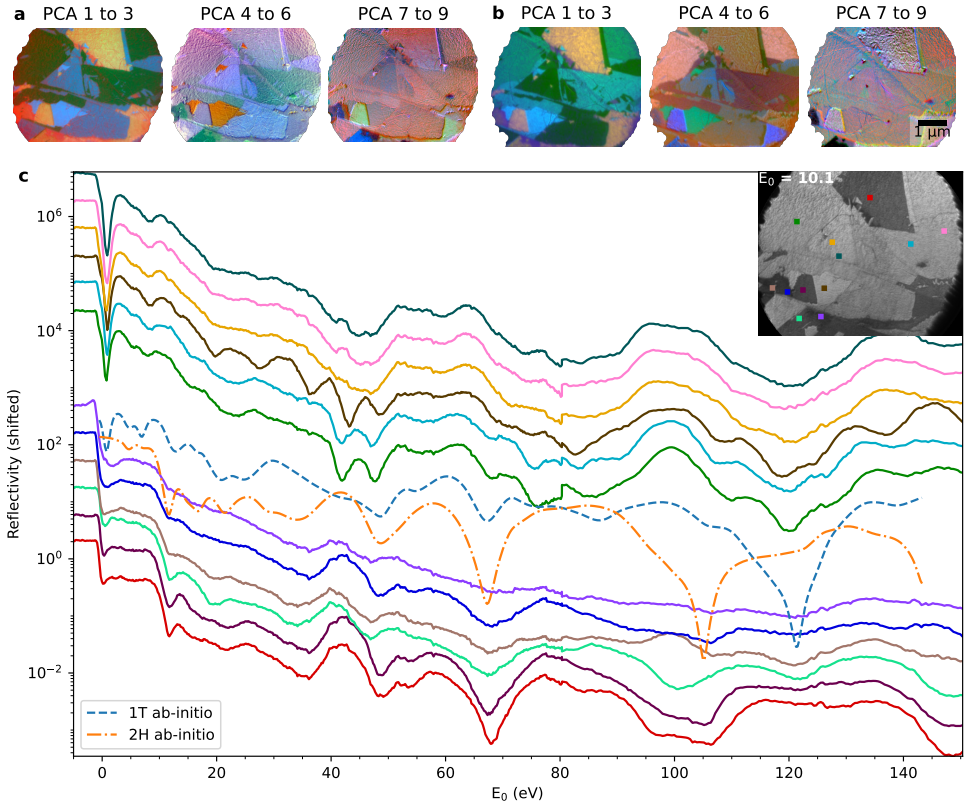

Figure 8.7: a, *PCA decomposition visualizations of BF-LEEM spectra for 0–80 eV [35]* ***b,*** *Same, but starting at 80eV up to 150 eV.* ***c,*** *LEEM spectra of different mixed polytypes. Curves are offset for clarity, with spectra resembling 1T at the top and those more similar to 2H below. The yellow curve (third from top) most closely resembles the pristine 1T curve in Figure 8.5. A slight mismatch at 80 eV is due to the changes between taking the two parts of these IV curves. (Separate datasets at same location). For comparison, ab-initio calculations of 1T-TaS_2 and 2H-TaS_2, both without any CDW taken into account, are shown as dashed and dashed-dotted respectively.*

Recording reflectivity as a function of E_0 using real space bright field (i.e. using the specular reflection), we observe at least twelve different area types, as shown in Figure 8.7**a,b**, visualized using the PCA decomposition described in Chapter 3. Some differences in the spectra themselves (Figure 8.7**c**) are very subtle, corresponding to a small shift in the energy direction, but other spectra show larger deviations.

The observed spectra split into two categories: about half of the curves are similar to the curve of pristine, low temperature annealed 1T-TaS_2 in Figure 8.5, with a steep minimum directly at 0 eV, minima around 80 and 120 eV and a maximum around 100 eV. These spectra are shown at the top of Figure 8.7**c**. The other set of curves has opposite traits, with only a very shallow minimum around 0 eV and large plateaus of high intensity around 80 and 120 eV. These are shown at the bottom of Figure 8.7**c**. Unfortu-

nately, comparison of these spectra to theory using standard calculations is complicated by the presence of CDW and the single experimental curve available per area type in bright field LEEM experiments. Ab-initio calculations (as described in Refs. [116–118]) of the bulk 1T and 2H polytypes are shown dashed and dashed-dotted in Figure 8.7**c**. A rudimentary tensorLEED approach similarly not taking into account the CDW, but simulating different stackings of Pr and Oc layers has further confirmed this and additionally suggests that the other observed differences could indeed be attributed to different stackings (See Figure D.3 in Appendix D) [232]. However, for a specific assignment of the different LEEM spectra to specific stackings, ab-initio calculations of different stackings are needed and in addition spectra of 1T-like areas above the IC-CDW onset are needed to assess the influence of the CDW on the BF-LEEM spectra.

8.5 CHARGE DENSITY WAVE STATES

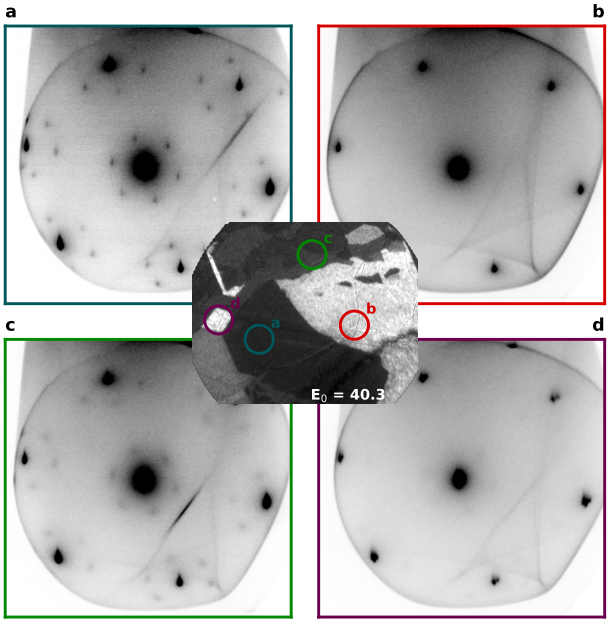

Figure 8.8: *μLEED patterns of different areas at elevated temperatures. Frame colors correspond to spectra of similar areas in Figure 8.7. The 1T-like areas (**a,c**) show ICCDW spots, the 2H-like area (**b**) does not show any CDW spots. Very low intensity IC-CDW spots are visible in 2H-like (**d**), which could be due to a CDW in a lower layer. However, it can not be excluded that these are from edges around the 2H-like area, but within the aperture. Color assignment of (c) is not 100% certain, a mix of areas might be present there as it lies outside of the area imaged in Figure 8.7. All diffraction patterns were taken at $E_0 = 56$ eV, $T \approx 233°C$.*

Upon cooling down well below the IC-CDW threshold, the assignment into two classes of 1T-like and 2H-like areas is further corroborated by the μLEED measurements in Figure 8.8: taking diffraction patterns of single areas, 1T-like areas have (varying degrees of) IC-CDW order, which is absent in 2H-like areas, as expected for the respective bulk polytypes.

A difference compared to measurements on pristine 1T samples is that upon cooling down further to below $T \approx 125°C$, a twin rotational order CDW appears, i.e. both the α and β phase coexisting, as shown in Figure 8.9**a**. Notably, this transition temperature is

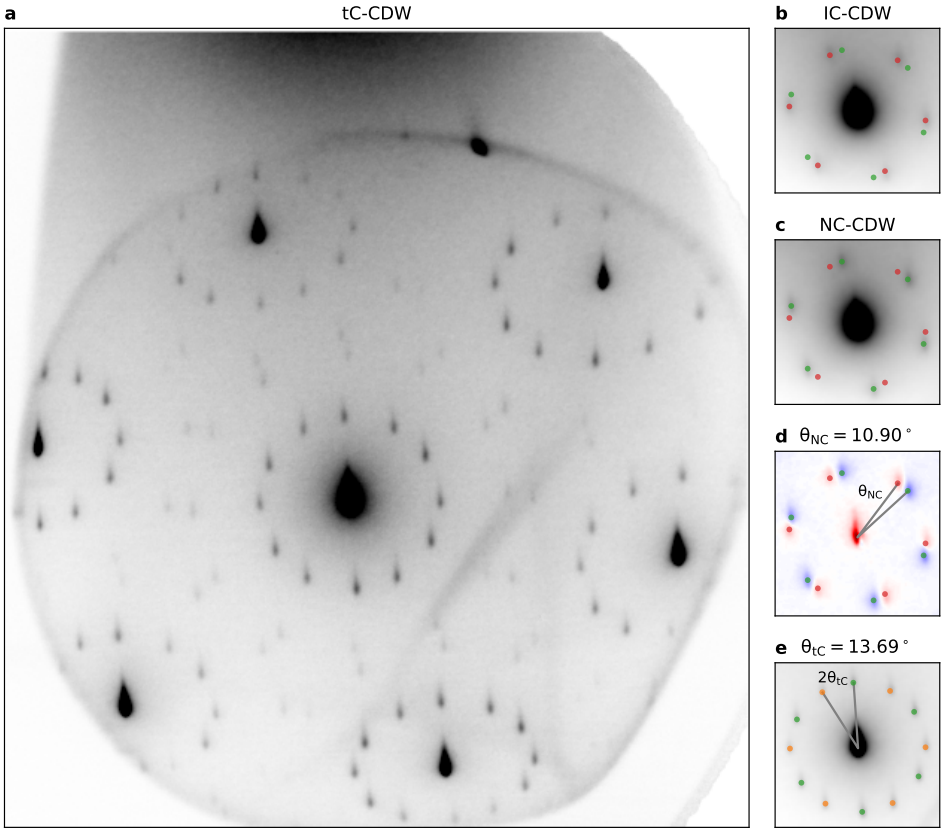

Figure 8.9: ***a,*** *Diffraction pattern of an annealed sample at 56 eV, taken after cooling, with an illumination aperture of 2 µm effective diameter. A twin pattern of CDW peaks is visible, i.e. including both α and β phase peaks.* ***b,c,*** *Detected diffraction peaks in the pristine sample. Same data as Figure 8.5.* ***d,*** *Difference image of* ***b,c*** *with the detected twist angle θ_{NC} between the NC phase and the IC phase (which is parallel to the atomic lattice). The reported angles are the average of all six angles to cancel out experimental distortions of the diffraction plane.* ***e,*** *Crop of* ***a*** *with the detected diffraction peaks and the twist angle θ_{tC} with respect to the atomic lattice.*

about 23°C higher than for the pristine IC–NC transition.[8] What is more, when heating again, the IC-CDW spots only start appearing at $T \approx 136$°C, and the diffraction spots corresponding to twinned phases remain all the way up to $T \approx 168$°C, indicating a relatively large hysteresis and coexistence of all three phases in the illuminated area.

In the twin rotational CDW order, the angle between the CDW vector and the atomic lattice is measured to be $\theta_{CDW} = 13.7°$ (Figure 8.9**e**), while for the pristine NC-CDW we measure $\theta_{NC} = 10.9°$ (Figure 8.9**d**). Furthermore, the second order CDW bragg peaks

[8] This *difference* between temperatures is significant as these were measured on the same instrument. Although the *accuracy* of the measurements using the IR-camera is relatively low, the measurements should be *precise* to within 5 K.

are as sharp as the first order peaks, i.e. no broadening due to splitting is observed (cf. Figure 8.4). As the observed CDW angle is much closer to commensurate than observed for the nearly-commensurate state and splitting is expected for the NC-CDW state, we conclude that the measured state is actually a twinned *commensurate* CDW (tC-CDW), even though the expected (and observed) CDW around room temperature in pristine 1T-TaS_2 is *nearly commensurate*.

This twinned rotational pattern has been observed before in the early days of TEM measurements [213, 233]. At the time, it was also concluded that the pattern actually corresponds to tC-CDW (as opposed to a NC variant). The pattern was attributed to a $4H_b$ polytype, with alternating layers of Oc and Pr layers of alternating rotation, as no in-plane spatial domains for these CDW orders were observed. This polytype would allow separate Oc layers on top of each other to exhibit opposing orientations, with adjacent Pr layers providing a sufficiently different environment to allow for the CDW state to be commensurate and the projection along the c-axis of the TEM measurement causing the superposition of both sets of peaks. However, as will become clear in the following, our observations do not match this attribution.

8.5.1 IN-PLANE CDW DOMAINS

In the previous section we described μLEED measurements, which already use the unique capability of a LEEM to do local LEED measurements of areas imaged. A further obvious capability of LEEM to apply to charge density wave order is Dark Field imaging to directly observe the spatial distribution of the CDWs.

Contrary to earlier TEM measurements on the twin rotational state, we *do* observe in-plane rotational domains when imaging using the tC-CDW diffraction spots, as shown in Figure 8.10. Comparing different dark field images, 1T-like areas exhibit two complementary sets of bright domains, as shown by composite images in Figure 8.10, with one corresponding to the α phase, and the other to the β phase, i.e. rotated in the opposite direction with respect to the atomic lattice directions. These domains were observed in multiple samples prepared in the way described (and confirmed semi-independently at the TU Chemnitz by P. Schädlich, see Figure D.5).

Although all 2H-like areas appear white in these images, no diffraction spots corresponding to CDWs were observed in any 2H-like area, just like in Figure 8.8**b**. However, 2H-like areas exhibited a much higher background intensity in diffraction at the imaging energy used, indicating a higher inelastic electron reflectivity of the 2H-like areas than in the 1T-like areas. (A fit of the diffraction peak profiles can be found in Appendix D, Figure D.6.) Furthermore, close inspection of the composite DF images in Figure 8.10 reveals that the domains in 1T-like areas occur in two different intensities (a boundary between a bright and dark area is indicated with a dark red line in Figure 8.7**b**). From the overlap of these DF images with the area used for spectral imaging in Figure 8.7, we conclude that the area corresponding to the dark green curve in Figure 8.7 (sixth from top) exhibits a dimmer CDW than the area corresponding to the ochre one (third from the top; this spectrum is closest to the pristine 1T spectrum). As both of these spectra are 1T-like, they are both assumed to have an Oc top layer. This indicates an influence of the layer below on the observed magnitude of the CDW. The increased contrast even suggests that no vertical mixing of the orientation domains occurs, i.e. that α-phase do-

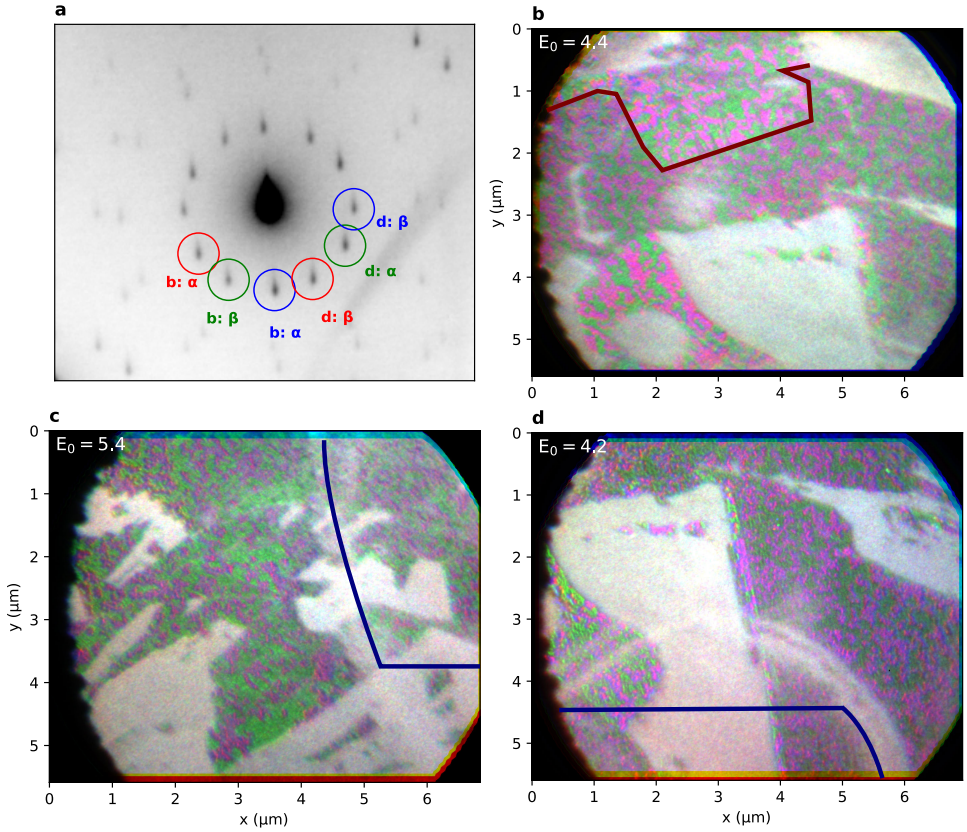

Figure 8.10: ***a,*** *Zoom of the tC-CDW diffraction pattern shown in Figure 8.9* ***a*** *indicating the aperture positions used for Dark Field LEEM.* ***b-d,*** *Composite Dark Field of CDW domains, using spots indicated in* ***a*** *of slightly different areas (c uses different but equivalent spots as d). By using three spots, of which two equivalent, the one orientation appears green, while the other appears purple, as both the red and the blue channel contribute there. Large areas of white correspond to 2H-like areas. Circular spots of white in* ***b*** *correspond to contamination due to µLEED measurements in Figure 8.8. In dark red the edge of a bright CDW domain is indicated (see main text). Half rings in* ***c,d*** *correspond to contamination at the edge of the beam during the measurement of the spectra in Figure 8.7: the boundary of the field-of-view of that measurement is indicated with dark blue lines.*

mains in the ochre areas do not lie on top of β domains in the layer below, or vice versa. Although a relative phase shift of the CDW in the underlying layer with respect to the CDW in the top layer could cause bright field and dark field contrast, the strict equivalency of the brightness of the different dark fields and the fact that the orientational (α versus β phase) domains are much smaller than these areas indicates that these differences are caused by the polytype of the underlying layer.

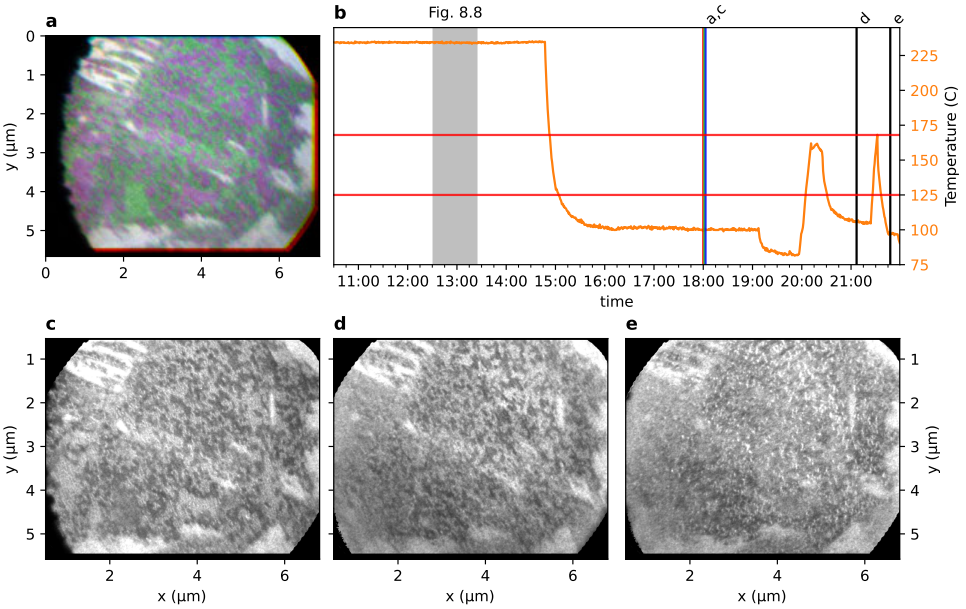

Figure 8.11: a, *Composite Dark Field image with twin rotational domains in green and purple.* ***b,*** *Temperature during temperature cycling experiment. Vertical lines indicate times of subsequent images, the time span during which the data in Figure 8.8 was taken is shaded gray.* ***c-e,*** *Dark Field LEEM images of the same area after heat cycling to IC-CDW. The domains reappear in a similar fashion, but orientation (α or β) are uncorrelated to earlier cycles.*

A question in the case of any observation of domains in a complicated system like this would be whether the observed domains are not simply a result of pinning to extrinsic defects, which could have been generated by the annealing or during exfoliation. To check this, the sample was thermally cycled into the IC-CDW state and back. As shown in Figure 8.11, similar domains reform after thermal cycling, but the shapes (i.e. what position on the sample is α or β-phase) is uncorrelated to the previous cycle, indicating the domains are no direct consequence of sample geometry or local strain.

8.6 DISCUSSION

To consider the implications of the observed tC-CDW state with in-plane domains and what it means for the NC-CDW state in pristine 1T-TaS_2, we first need to reconsider the role of the ~ 7 nm diameter superdomains in the NC-CDW caused by the near-commensurability. Although the presence of these superdomains at room temperature and the apparent suppression of the CDW amplitude at the domain boundaries in STM (See e.g. Ref. [225, 234]) are sometimes seen as an indication of a low spatial coherence, they are in fact the opposite, as the phase of the CDW shifts consistently over the length scale of multiple domains. Therefore, a high spatial coherence is needed for the NC-CDW to be energetically favorable over the C-CDW. Furthermore, the fact that meso-

scopic/macroscopic pristine bulk samples exhibit only a single orientation of the CDW (i.e. only α-phase, both at room temperature / NC-CDW as well as low temperature C-CDW) also indicates very high spatial coherence.

The hexagonal superdomains are similar to the stacking domains in twisted bilayer graphene in more than one way. Although globally the NC-CDW lattice vector is rotated away from the C-CDW lattice vector, within a domain it is actually equal to the C-CDW vector [234, 235], with all the phase shift concentrated in the domain boundaries, just like the graphene lattices are commensurate within the TBG stacking domains, but the relative (lattice-) phase shifting in the shear domain boundaries to maintain a globally consistent lattice displacement corresponding to the twist.

Second, just like in TBG for incommensurate twist angles, the hexagonal superdomains in the NC-CDW phase are irregular, with each domain slightly different than its neighbors, but this is a result of the incommensurability of the NC-CDW vectors, not to be confused with disorder, as the latter would actually cause smeared CDW diffraction spots, which are not observed in electron diffraction and X-ray diffraction [219, 228, 229].

In the mixed polytype state after annealing, however, we observe twinned commensurate CDW domains with a characteristic size of ~ 150 nm. (Details about the domain size extraction are given in Appendix D, see Figure D.4.) This means the spatial coherence of the CDW is limited by the domain boundaries between α and β domains, even though the domain size is still an order of magnitude larger than the NC-CDW superdomains in bulk 1T-TaS_2. Apparently so much so, that the NC-CDW state is no longer energetically favorable.

An alternative assumption would be that the measured value of $\theta_{tC} \approx 13.7°$ does not correspond to a commensurate angle, but to a very nearly commensurate state. In that case, by Equation 8.1, the NC-CDW superdomains would have a corresponding size $L \approx 49$ nm, much closer to the observed characteristic size of the orientation domains. In this case interaction between the CDW and the rotational domains seems inevitable.

A further question is whether the observed tC-CDW state with domains is an inherent property of specific mixed polytype stackings or is due to some other property like lattice strain or contamination. Although the influence of such extrinsic properties cannot be fully excluded, the fact that the tC-CDW state reproduces in different local orientations after thermal cycling and the fact that the same state was reproduced on other samples and with slight variations of the annealing procedure point to an inherent property.

TEM measurements on comparable tC-CDW states [230, 233], however, reported no distinguishable domains. Although at first sight those observations seem incompatible with the reported domains here, it should be noted that while LEEM measurements are inherently surface sensitive, meaning for any LEEM signal the top-layer dominates the result, TEM projects through the entire sample. It therefore seems plausible that the lack of observation of CDW domains in these TEM measurements could be caused by the averaging along the c-axis of the CDW of different orientations in various 1T-like layers isolated from each other by Pr layers.

A final question is whether the tC-CDW angle compared to the nearly-commensurate angle in pristine 1T-TaS_2 is really due to the limited size of the domains, or an inherent property of the polytype stackings.

As shown in Figure 8.12, larger domains were observed on another sample, which

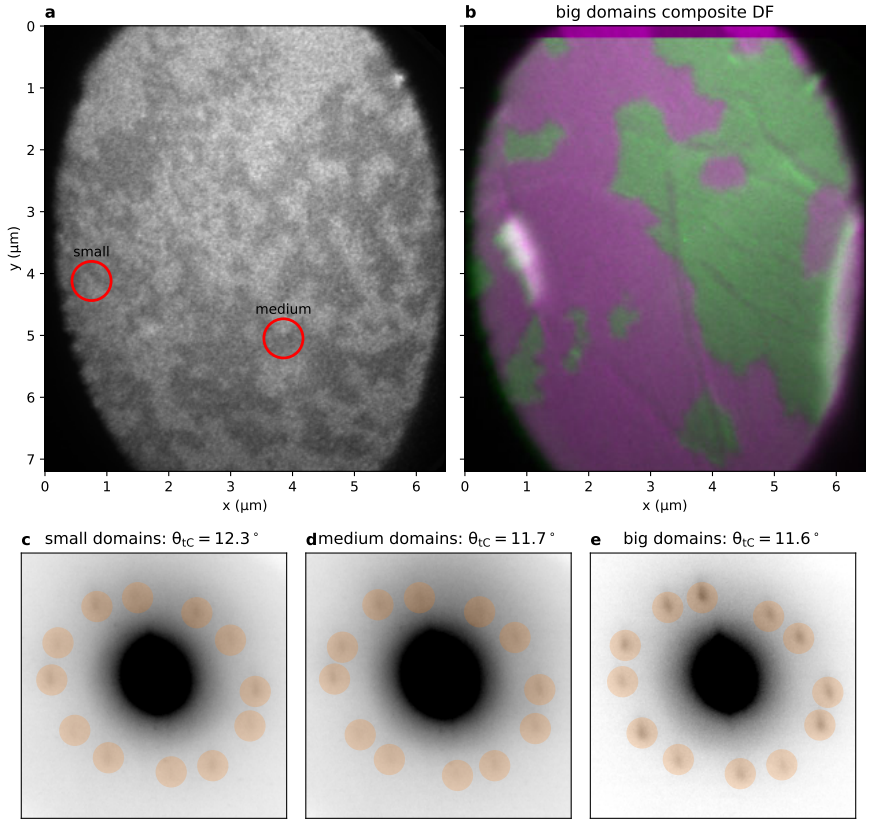

Figure 8.12: ***a,*** *Dark Field LEEM measurement on a newly annealed sample, showing various domain sizes. µLEED apertures of* ***c,d*** *are indicated with red circles. The 'small' domain areas still corresponds to somewhat larger domains than observed in the other sample.* ***b,*** *Composite dark field LEEM image of a different location on the same flake showing very large, micron-sized domains.* ***c,d,*** *Zoomed µLEED patterns with tC-CDW peaks marked, corresponding to* $\theta_{tC} \approx 12.3°$ *and* $\theta_{tC} \approx 11.7°$ *respectively.* ***e,*** *LEED pattern of the entire gun spot of the area shown in* ***b****, with* $\theta_{tC} \approx 11.6°$*. All measurements in this figure taken at* $T \approx 70°C$*.*

was annealed for a much shorter time. However, due to unrelated reasons, imaging conditions on that sample were unfortunately not good enough to obtain spectroscopic measurements or even detailed diffraction patterns to measure θ_{CDW} accurately. Nevertheless, cooling rates through the transition were similar to other cooldowns at $\sim 0.05\,\mathrm{K/s}$ as this is limited by the thermal mass and dissipation of the sample stage.

However, the limited evidence gathered from this sample does *suggest* that θ_{tC} decreases towards the 1T bulk value of $\theta_{\mathrm{NC}} = 10.9°$ for larger domains, as shown in Figure 8.12**c-e**, but strong distortion and low diffraction intensity causes a large uncertainty on these measurements (although independent reproduction of θ_{tC} for small domains, see Figure D.5 in Appendix D, seems to indicate the error is small enough for the mea-

sured difference to be significant).

8.6.1 COMPARISON TO LOW-TEMPERATURE HIDDEN STATE

A different, as-of-yet undiscussed CDW state in 1T-TaS_2 is the metallic, so-called 'hidden' (H) phase, which can be accessed at low temperatures by exposing the sample to a laser pulse or electrical excitation [227, 236, 237]. This state exhibits a irregular mosaic of shifted commensurate domains, where the changed relative stacking order of the CDW in subsequent layers seems responsible for the transition from an insulating to a metallic state [236]. This H-phase exhibits a diffraction pattern with an angle relative to the atomic lattice that is closer to the C-CDW than the NC-CDW phase, similar to the tC-CDW reported here [226, 238]. However, contrary to the tC-CDW state, the domains (almost) all remain in the α-phase in the H-phase and the H-phase reverts to the C-CDW phase upon heating before converting to the NC-CDW phase.

8.7 CONCLUSION

We have studied charge density wave states in TaS_2 using LEEM. In particular, we have studied mixed polytype states which occur after annealing a 1T-TaS_2 sample above its stability threshold of $T \approx 550$K. We have shown that a wide variety of different areas can be distinguished on such samples using spectroscopic LEEM. By comparing to ab-initio calculations, we distinguish areas with a 1T-like top layer which *do* host charge density wave states and areas with a 2H-like top layer which *do not* show any sign of charge density wave states in LEEM at room temperature and above. Many more differences in the spectra are observed, which can be due to difference in polytype order, differences in relative stacking of these layers or even different CDW states.

Interestingly, the CDW states in these mixed polytype samples show significant differences compared to the behavior in bulk 1T-TaS_2. Where in the bulk 1T material a single α-phase orientation occurs, here both possible orientations occur in a twinned orientation CDW. Using dark field LEEM, we show that the twinned orientation is due to rotational domains with a characteristic size of ~ 150 nm.

Furthermore, we have shown that the twinned CDW in these small domains is actually commensurate (tC-CDW) instead of the nearly commensurate CDW observed in the 1T bulk, and we found significantly higher transition temperatures than in bulk 1T and a large hysteresis to the IC-CDW state.

Finally, we have shown that the domain size is not always so small, and we observed indications that the domain size itself might cause the shift from NC to C, due to a lack of spatial coherence needed to realize an energy benefit for the NC state.

However, to fully confirm this influence and its potential implications for the nature of the tC-CDW in these samples and even of the NC-CDW in the pristine 1T-TaS_2 itself, two things are needed: first, confirmation of the precise stacking configurations in these samples, for example by comparing to theoretical calculations of the LEEM spectra of different stackings. Second, connecting this to more precise measurements on the relation between domain size and θ_{tC}. This way, it would be possible to infer whether the observed tC-CDW state is inherent to the 2D-limit of 1T-TaS_2, or due to some other mechanism.

REFERENCES

17. J. Ravnik, I. Vaskivskyi, Y. Gerasimenko, et al. Strain-Induced Metastable Topological Networks in Laser-Fabricated TaS_2 Polytype Heterostructures for Nanoscale Devices. *ACS Applied Nano Materials* **2,** 3743–3751. doi:10.1021/acsanm.9b00644 (2019).

20. J. Henke, F. Flicker, J. Laverock & J. van Wezel. Charge order from structured coupling in VSe_2. *SciPost Physics* **9,** 056. doi:10.21468/SciPostPhys.9.4.056 (2020).

29. J. I. Flege & E. E. Krasovskii. Intensity-voltage low-energy electron microscopy for functional materials characterization. *Physica Status Solidi - Rapid Research Letters* **8,** 463–477. doi:10.1002/pssr.201409102 (2014).

31. T. A. de Jong, J. Jobst, H. Yoo, et al. Measuring the Local Twist Angle and Layer Arrangement in Van der Waals Heterostructures. *physica status solidi (b)* **255,** 1800191. doi:10.1002/pssb.201800191 (2018).

35. T. A. de Jong, D. N. L. Kok, A. J. H. van der Torren, et al. Quantitative analysis of spectroscopic low energy electron microscopy data: High-dynamic range imaging, drift correction and cluster analysis. *Ultramicroscopy* **213,** 112913. doi:10.1016/j.ultramic.2019.112913 (2020).

116. E. E. Krasovskii, F. Starrost & W. Schattke. Augmented Fourier components method for constructing the crystal potential in self-consistent band-structure calculations. *Physical Review B* **59,** 10504–10511. doi:10.1103/PhysRevB.59.10504 (1999).

117. E. E. Krasovskii. Augmented-plane-wave approach to scattering of Bloch electrons by an interface. *Physical Review B* **70,** 245322. doi:10.1103/PhysRevB.70.245322 (2004).

118. V. U. Nazarov, E. E. Krasovskii & V. M. Silkin. Scattering resonances in two-dimensional crystals with application to graphene. *Phys. Rev. B* **87,** 041405. doi:10.1103/PhysRevB.87.041405 (4 2013).

211. D. Lin, S. Li, J. Wen, et al. Patterns and driving forces of dimension-al-i-ty-de-pendent charge density waves in 2H-type transition metal dichalcogenides. *Nature Communications* **11,** 2406. doi:10.1038/s41467-020-15715-w (2020).

212. J. Wilson & A. Yoffe. The transition metal dichalcogenides discussion and interpretation of the observed optical, electrical and structural properties. *Advances in Physics* **18,** 193–335. doi:10.1080/00018736900101307 (1969).

213. J. A. Wilson, F. J. Di Salvo & S. Mahajan. Charge-density waves and superlattices in the metallic layered transition metal dichalcogenides. *Advances in Physics* **50,** 1171–1248. doi:10.1080/00018730110102718 (2001).

214. A. H. Castro Neto. Charge Density Wave, Superconductivity, and Anomalous Metallic Behavior in 2D Transition Metal Dichalcogenides. *Physical Review Letters* **86,** 4382–4385. doi:10.1103/PhysRevLett.86.4382 (2001).

215. K. Rossnagel. On the origin of charge-density waves in select layered transition-metal dichalcogenides. *Journal of Physics: Condensed Matter* **23,** 213001. doi:10.1088/0953-8984/23/21/213001 (2011).

216. P. B. Littlewood & V. Heine. The effect of electron-electron interactions on the Peierls transition in metals with strong nesting of Fermi surfaces. *Journal of Physics C: Solid State Physics* **14,** 2943–2949. doi:10.1088/0022-3719/14/21/012 (1981).

217. M. D. Johannes & I. I. Mazin. Fermi surface nesting and the origin of Charge Density Waves in metals. *Physical Review B* **77,** 165135. doi:10.1103/PhysRevB.77.165135 (2008).

218. G. von Witte, T. Kißlinger, J. G. Horstmann, et al. Surface structure and stacking of the commensurate $(\sqrt{13}\times\sqrt{13})R13.9^\circ$ charge density wave phase of 1T–TaS_2(0001). *Physical Review B* **100,** 155407. doi:10.1103/PhysRevB.100.155407 (2019).

219. A. Spijkerman, J. L. de Boer, A. Meetsma, G. A. Wiegers & S. van Smaalen. X-ray crystal-structure refinement of the nearly commensurate phase of 1 T–TaS_2 in (3 + 2)-dimensional superspace. *Physical Review B* **56,** 13757–13767. doi:10.1103/PhysRevB.56.13757 (1997).

220. S.-H. Lee, J. S. Goh & D. Cho. Origin of the Insulating Phase and First-Order Metal-Insulator Transition in 1T-TaS_2. *Physical Review Letters* **122,** 106404. doi:10.1103/PhysRevLett.122.106404 (2019).

221. G. A. Scholz, O. Singh, R. F. Frindt & A. E. Curzon. Charge density wave commensurability in 2H-TaS_2 and Ag_xTaS_2. *Solid State Communications* **44,** 1455–1459. doi:10.1016/0038-1098(82)90030-8 (1982).

222. M. Lee, M. Šiškins, S. Mañas-Valero, et al. Study of charge density waves in suspended 2H-TaS_2 and 2H-$TaSe_2$ by nanomechanical resonance. *Applied Physics Letters* **118,** 193105. doi:10.1063/5.0051112 (2021).

223. D. Zhang, Y. Wu, Y.-H. Su, et al. Charge density waves and degenerate modes in exfoliated monolayer 2H-TaS_2. *IUCrJ* **7,** 913–919. doi:10.1107/S2052252520011021 (2020).

224. X. L. Wu & C. M. Lieber. Direct observation of growth and melting of the hexagonal-domain charge-density-wave phase in 1T-TaS_2 by scanning tunneling microscopy. *Physical Review Letters* **64,** 1150–1153. doi:10.1103/PhysRevLett.64.1150 (1990).

225. R. E. Thomson, B. Burk, A. Zettl & J. Clarke. Scanning tunneling microscopy of the charge-density-wave structure in 1T-TaS_2. *Physical Review B* **49,** 16899–16916. doi:10.1103/PhysRevB.49.16899 (1994).

226. K. Sun, S. Sun, C. Zhu, et al. Hidden CDW states and insulator-to-metal transition after a pulsed femtosecond laser excitation in layered chalcogenide 1T-$TaS_{2-x}Se_x$. *Science Advances*. doi:10.1126/sciadv.aas9660 (2018).

227. D. Cho, S. Cheon, K.-S. Kim, et al. Nanoscale manipulation of the Mott insulating state coupled to charge order in 1T-TaS_2. *Nature Communications* **7,** 10453. doi:10.1038/ncomms10453 (2016).

228. A. W. Tsen, R. Hovden, D. Wang, et al. Structure and control of charge density waves in two-dimensional 1T-TaS_2. *Proceedings of the National Academy of Sciences* **112,** 15054–15059. doi:10.1073/pnas.1512092112 (2015).

229. S. Vogelgesang, G. Storeck, J. G. Horstmann, et al. Phase ordering of charge density waves traced by ultrafast low-energy electron diffraction. *Nature Physics* **14,** 184–190. doi:10.1038/nphys4309 (2018).

230. S. H. Sung, N. Schnitzer, S. Novakov, et al. Two-dimensional charge order stabilized in clean polytype heterostructures. *Nature Communications* **13,** 413. doi:10.1038/s41467-021-27947-5 (2022).

231. J.-P. v. Soest. *Optical and Electronic Reflectivity of TaS_2* BSc thesis (Leiden University, 2018). https://hdl.handle.net/1887/64692.

232. T. Iking. *Identifying TaS_2 polytypes in LEEM images using LEED simulations* BSc thesis (Leiden University, 2019). https://hdl.handle.net/1887/75227.

233. J. v. Landuyt, G. v. Tendeloo & S. Amelincky. Electron diffraction study of inter- and intrapolytypic phase transitions in transition metal dichalcogenides. I. Electron diffraction patterns. *physica status solidi (a)* **26,** 359–376. doi:10.1002/pssa.2210260138 (1974).

234. B. Burk, R. E. Thomson, A. Zettl & J. Clarke. Charge-density-wave domains in 1T-TaS_2 observed by satellite structure in scanning-tunneling-microscopy images. *Physical Review Letters* **66,** 3040–3043. doi:10.1103/PhysRevLett.66.3040 (1991).

235. K. Nakanishi, H. Takatera, Y. Yamada & H. Shiba. The Nearly Commensurate Phase and Effect of Harmonics on the Successive Phase Transition in 1T-TaS_2. *Journal of the Physical Society of Japan* **43,** 1509–1517. doi:10.1143/JPSJ.43.1509 (1977).

236. L. Ma, C. Ye, Y. Yu, et al. A metallic mosaic phase and the origin of Mott-insulating state in 1T-TaS2. *Nature Communications* **7,** 10956. doi:10.1038/ncomms10956 (2016).

237. L. Stojchevska, I. Vaskivskyi, T. Mertelj, et al. Ultrafast Switching to a Stable Hidden Quantum State in an Electronic Crystal. *Science* **344,** 177–180. doi:10.1126/science.1241591 (2014).

238. Q. Stahl, M. Kusch, F. Heinsch, et al. Collapse of layer dimerization in the photo-induced hidden state of 1T-TaS2. *Nature Communications* **11,** 1247. doi:10.1038/s41467-020-15079-1 (2020).

9

OUTLOOK

Before I started this PhD project, the potential of studying van der Waals physics using LEEM was already clear. The high intrinsic surface sensitivity, fast imaging, with low damage, reasonable resolution, atomic information via diffraction and a large field of view (using PEEM) are all desired properties for the study of 2D materials, and the combination of all these properties in a single instrument is unique. Indeed LEEM is widely used to study material growth, including van der Waals materials, on substrates and the ability to count layers of graphene (also possible for other materials) has played a significant role in the optimization of the growth of graphene on SiC. However, further realization of the true potential for van der Waals physics was hampered by relatively simple engineering limitations, already solved in other forms of microscopy.

Adopting calibration and image analysis practices from other microscopy fields, in particular TEM, and adapting them for the specific properties of LEEM data has pushed the boundaries of the capabilities. This has opened up a wide range of new research topics, of which only a small part could be pursued within the scope of this thesis. Therefore, I will here list some possibilities for future research that I think are exciting and worthwhile to pursue.

9.1 DEVICE SCALE IMAGING

The combination of an automated sample stage and the implementation of the stitching algorithm as described in Appendix B, has enabled high resolution imaging of complete van der Waals heterostacks in device geometry. In contrast to TEM imaging, no electron-transparent substrate is needed. Therefore, electron transport devices can be imaged with little to no adaptations, and without electron-damage to the device. What is more, beyond identifying the material and number of layers, we have shown in Chapters 5 and 8 that by comparing to calculations, LEEM spectroscopy can be used to deduce the relative stacking of layers in van der Waals materials, thus enabling the identification of different polytypes and the imaging of stacking domain boundaries.

This has become especially relevant in the field now known as twistronics: when combining van der Waals materials in heterostacks, the twist angle between them is an important parameter determining the electronic properties. We have already demonstrated this relevance for twistronics in Ref. [5], where LEEM imaging of the full device enabled the first detailed ARPES measurements of a flat band in magic angle TBG. The stacking contrast and μLEED enable full characterization of the local twist angle on transport-like devices. The strong phase contrast of relatively high twist angles enables this even for deeper layers. Thus, even the imaging of encapsulated twistronics devices using LEEM has become possible, provided the encapsulating hBN layer is no more than a few atomic layers thick.

9.2 TEMPERATURE-DEPENDENT MEASUREMENTS

A significant opportunity still lies in combining dynamics and temperature dependence for domain walls in graphene on SiC as well as in TBG. Measuring the movement of domain boundaries for different temperatures can yield a variety of information on the energy differences involved and could thus be used to calibrate theoretical calculations, adding an extra dimension to the moiré metrology of Section 5.4.

In chapter 8, we for the first time distinguished different polytypes in TaS_2 and imaged Charge Density Waves using LEEM. However, this only scratched the surface of the possibilities. An immediate follow up is to study the range of tC-CDW – IC-CDW transition temperatures in the mixed polytypes. It seems that the exact transition temperature depends on the local polytype stacking. By combining dark field imaging of the transition with spectroscopy, it is possible to deduce exactly how these transition temperatures depend on the precise polytype stacking and how the CDW behaves in the 2D limit. Furthermore, an exciting prospect is to extend this research to cryogenic temperatures. LEEM below room temperature and down to cryogenic temperatures has long been in technological development [239], but is now finally possible. This opens up a much wider range of CDW states in different TMDs. In particular in the mixed polytype TaS_2 system, the study of the transition to C-CDW is a promising research goal. Furthermore, in 2H-TaS_2 a CDW appears at 75 K in bulk material and up to 122K in thin layers [222]. How it behaves in the mixed polytype studied in this thesis and whether any interaction between the CDW in the different polytypes occurs are further promising research goals.

Another interesting avenue of research is to study the influence of an additional

twisted lattice in a heterostack on the NC-CDW. In Ref. [240], it was already shown that the CDW can be observed through a capping graphene layer. However, the twist angle can be chosen specifically to influence the behavior of the NC-CDW. By selecting a twist angle such that the periodicity matches the periodicity of the NC-CDW, it might be possible to either lock it in or suppress it for a specific temperature range. Another possibility is to break the mirror symmetry to promote the formation of pure α-phase in a mixed polytype situation (the situation where in Chapter 8 a mix of α and β phases was observed).

Beyond interest in the fundamental properties of the CDW phases in such mixed states, their strong influence on the electrical conductivity, fast switching and variety in transition temperatures also make it interesting for technological applications.

9.3 TECHNIQUE COMBINATIONS

Device-scale imaging becomes even more powerful if the imaging of electron transport devices is combined with in situ transport experiments. It was already shown that in situ potentiometry is possible in the LEEM [6, 241], although at the time the benefits relative to scanning tunneling potentiometry were minor. Since then, analysis methods and calibrations were significantly improved, which should significantly increase the precision. The addition of a third prism to energy-filter the illuminating electrons would further increase the spectroscopic and spatial resolution of LEEM potentiometry. Furthermore, stitching of LEEM data can directly be applied to potentiometry, enabling potentiometry over complete transport devices, a scale infeasible using STM-based potentiometry.

However, other, potentially even more interesting, transport properties can also be measured in situ with relatively small experimental effort. In particular, gated moiré heterostacks might be an interesting subject for both moiré metrology (as described in Section 5.4) and the direct observation of dynamics of the moiré pattern as a function of carrier density. Another curious option would be to attempt to measure electro-migration of the domain boundaries by observing shifts of the domain boundaries while applying different in-plane currents.

All the ingredients, i.e. device fabrication, in situ contacts and data analysis, to perform such combined measurements in a LEEM exist. However, integrating them all will require significant effort and tight feedback between a significant sample fabrication effort and LEEM measurement efforts, but it seems the resulting measurements would be worthwhile.

9.4 COMPUTATIONAL OPPORTUNITIES

A large portion of the work that was needed for the results in this thesis did not go into sample fabrication or the experimental work to obtain the images, but into computational efforts to process the raw data and analyze the results. Just like the precise methods of sample fabrication, these efforts often remain hidden in the final scientific publication. This is unfortunate, as sharing the data analysis methods and making them usable to other does not only increase the quality and reproducibility of the science, but also enables faster scientific progress by reducing the effort needed to perform future analyses. In other words, the publication of a well-written software library enabling

analysis methods can have more impact on scientific progress than the publication of a well-written paper detailing a discovery or measurement. I therefore made an effort to publish the implementations of the procedures described in Chapter 3 and Appendices A and B and also make those implementations reusable [42, 88, 192, 193]. Towards the same goal, I will here describe some opportunities to reuse and extend those implementations.

9.4.1 APPLICATIONS OF ADAPTIVE GPA

Geometric Phase Analysis as described in A is a powerful tool and has uses in both TEM and STM (where it is often used for and known as Lawler-Fujita correction). However, no (open) standard implementation existed, despite many possible pitfalls in the implementation. I therefore created a open source implementation of (adaptive) GPA, which tests against simulated lattices with known deformations [88]. This way, the actual error in the extracted deformation field can be determined and the merit of adaptive reference vectors and deconvolution can be judged based on the parameters of the actual measurement. Although both extended GPA itself and the unit cell averaging it enables have applications to LEEM data of moiré materials, it finds application and even more merit in other techniques such as TEM, STM, AFM and even (macroscopic) deformation characterization. Especially for techniques with a much sharper instrument point spread function (PSF), such as (S)TEM and STM, unit cell averaging can combine high resolution imaging of the average unit cell with larger overviews.

9.4.2 COMPUTATIONAL DENOISING

Detector correction and drift correction enabled accurate enough images to measure dynamics of the moiré lattice in TBG. However, these measurements are currently limited by the signal-to-noise ratio. Although better detectors such as the direct fiber coupled devices that are now replacing the classical MCP+CCD detectors will help to bring down the noise level [242], an even better signal-to-noise ratio will still further increase the amount of information that can be extracted. In machine learning, recent progress has been made to suppress noise purely based on noisy images, i.e. without the need for an 'ideal' image to train the algorithm on, by the so-called `noise2noise` algorithm and its derivatives [243–245]. Adaptation of such algorithms tailored specifically for LEEM imaging can further increase the time resolution of the dynamics extracted. What is more, adaptation of such algorithms will also find application in increasing the accuracy of 'drizzle'-like integration of images, by increasing the accuracy of the determination of the relative shifts between noisy images before integration.

9.5 CONCLUDING REMARKS

The field of van der Waals materials research has exploded since its start and the advent of twistronics in van der Waals heterostacks has only accelerated this growth. LEEM as a technique can play an important role in this field, thanks to the capabilities to characterize the atomic structure of samples in detail and over large scales, as showcased in this thesis. In particular, it can play a large role in characterizing and improving sample fabrication in close feedback loops, but also in directly contributing to the understand-

ing of the physics involved. This role seems to be under-utilized, not due to a lack of capabilities, but more likely due to a lack of fame compared to regularly used techniques such as AFM and STM, and the smaller size of the community. Given its versatility and broad range of capabilities, I however look forward to seeing the use of LEEM to study van der Waals materials and moiré patterns become much more widespread in the coming years.

REFERENCES

5. S. Lisi*, X. Lu*, T. Benschop*, T. A. de Jong*, et al. Observation of flat bands in twisted bilayer graphene. *Nature Physics* **17,** 189–193. doi:10.1038/s41567-020-01041-x (2021).

6. J. Kautz, J. Jobst, C. Sorger, et al. Low-Energy Electron Potentiometry: Contactless Imaging of Charge Transport on the Nanoscale. *Scientific Reports* **5,** 13604. doi:10.1038/srep13604 (2015).

42. T. A. de Jong. *Quantitative Data Analysis for spectroscopic LEEM* version v0.2.0. 2021. doi:10.5281/zenodo.3539538.

88. T. A. de Jong. *pyGPA* 2021. doi:10.5281/zenodo.5589555.

192. T. A. de Jong. *TAdeJong/moire-lattice-generator* version 0.0.5. 2021. doi:10.5281/zenodo.5156831.

193. T. A. de Jong. *Figure generation code for "Imaging moiré deformation and dynamics in twisted bilayer graphene"* Zenodo, 2021. doi:10.5281/zenodo.5713908.

222. M. Lee, M. Šiškins, S. Mañas-Valero, et al. Study of charge density waves in suspended 2H-TaS_2 and 2H-$TaSe_2$ by nanomechanical resonance. *Applied Physics Letters* **118,** 193105. doi:10.1063/5.0051112 (2021).

239. S. M. Schramm. *Imaging with Aberration-Corrected Low Energy Electron Microscopy* PhD thesis (Leiden University, 2013). https://hdl.handle.net/1887/20843.

240. M. A. Altvater, N. Tilak, S. Rao, et al. Charge Density Wave Vortex Lattice Observed in Graphene-Passivated 1T-TaS2 by Ambient Scanning Tunneling Microscopy. *Nano Letters* **21,** 6132–6138. doi:10.1021/acs.nanolett.1c01655 (2021).

241. J. Jobst, J. Kautz, M. Mytiliniou, R. M. Tromp & S. J. van der Molen. Low-energy electron potentiometry. *Ultramicroscopy* **181,** 74–80. doi:10.1016/j.ultramic.2017.05.015 (2017).

242. D. Janoschka, P. Dreher, A. Rödl, et al. Implementation and operation of a fiber-coupled CMOS detector in a low energy electron Microscope. *Ultramicroscopy* **221,** 113180 (2021).

243. J. Lehtinen, J. Munkberg, J. Hasselgren, et al. Noise2Noise: Learning Image Restoration without Clean Data. *arXiv:1803.04189 [cs, stat]*. http://arxiv.org/abs/1803.04189 (2022) (2018).

244. J. Batson & L. Royer. Noise2Self: Blind Denoising by Self-Supervision. *arXiv:1901.11365 [cs, stat]*. http://arxiv.org/abs/1901.11365 (2022) (2019).

245. A. A. Hendriksen, D. M. Pelt & K. J. Batenburg. Noise2Inverse: Self-Supervised Deep Convolutional Denoising for Tomography. *IEEE Transactions on Computational Imaging* **6,** 1320–1335. doi:10.1109/TCI.2020.3019647 (2020).

A

GEOMETRIC PHASE ANALYSIS

This appendix provides a more elaborate description of Geometric Phase Analysis / Spatial lock-in and adaptive GPA.

A.1 DEFORMATIONS OF A LATTICE

We perform lock-in measurements on images that clearly display a periodic lattice. In STM, this implies we can use any topography of sufficient quality that displays the crystal lattice. The idea is to use a lock-in measurement in order to find a transformation of coordinates between the measured, "distorted" image and its pristine, undeformed equivalent (in this work, a perfect triangular lattice). Defining the measured and pristine image as $T_m(\mathbf{r})$, $T_r(\mathbf{r}')$ respectively, both with measurement coordinates $\mathbf{r} = (x, y) \in \mathbb{R}^2$ and lattice coordinates $\mathbf{r}' = (x', y') \in \mathbb{R}^2$, the following relation holds:

$$T_m(\mathbf{r}) = T_r\left(\mathbf{r} + \mathbf{u}(\mathbf{r})\right) = T_r\left(\mathbf{f}(\mathbf{r})\right) = T_r(\mathbf{r}') = T_m\left(\mathbf{f}^{-1}(\mathbf{r}')\right)$$

where the transformation from measurement coordinates to lattice coordinates is given by:

$$\mathbf{f}(\mathbf{r}) = \mathbf{r} + \mathbf{u}(\mathbf{r}) = \mathbf{r}' \tag{A.1}$$

Here, $\mathbf{u}(\mathbf{r})$ is called the displacement field, connecting the measurement coordinates to the lattice coordinates, as is well-established in continuum mechanics. For convenience, we also define the inverse displacement:

$$\mathbf{u}'(\mathbf{r}') := \mathbf{f}^{-1}(\mathbf{r}') - \mathbf{r}' = \mathbf{r} - \mathbf{r}'$$

Note that by substitution, we have the following relation between forward and inverse displacement:

$$\mathbf{u}'(\mathbf{r}') = \mathbf{f}^{-1}(\mathbf{f}(\mathbf{r})) - (\mathbf{r} + \mathbf{u}(\mathbf{r})) = -\mathbf{u}(\mathbf{r})$$

Parts of this appendix have been published in the Supplementary materials of Phys. Rev. Research **3**, 013153 [141] and Nat. Commun. **13**, 70 (2022) [135]. Tjerk Benschop made a significant contribution to this appendix.

With this, we can express the pristine image at lattice coordinates in terms of the measured image:

$$\begin{aligned} T_r(\mathbf{r}') &= T_m\left(\mathbf{f}^{-1}(\mathbf{r}')\right) = T_m(\mathbf{r}' + \mathbf{u}'(\mathbf{r}')) \\ &= T_m\left(\mathbf{r}' - \mathbf{u}(\mathbf{r})\right) \\ &= T_m\left(\mathbf{r}' - \mathbf{u}(\mathbf{r}' - \mathbf{u}(\mathbf{r}))\right) \\ &\approx T_m\left(\mathbf{r}' - (\mathbf{u}(\mathbf{r}') - (\nabla\mathbf{u})(\mathbf{r}' - \mathbf{r}))\right) \\ &= T_m\left(\mathbf{r}' - (\mathbf{u}(\mathbf{r}') + (\nabla\mathbf{u})\mathbf{u}(\mathbf{r}))\right) \\ &= T_m\left(\mathbf{r}' - \mathbf{u}(\mathbf{r}') + (\nabla\mathbf{u})\mathbf{u}'(\mathbf{r}'))\right) \end{aligned}$$

Therefore, if we can determine $\mathbf{u}(\mathbf{r})$, and thereby $\mathbf{u}'(\mathbf{r}')$, we can reconstruct the pristine image. This is the idea of the Lawler–Fujita reconstruction algorithm [143]. In their original paper, Lawler–Fujita uses $\mathbf{u}'(\mathbf{r}') = -\mathbf{u}(\mathbf{r}')$, which is a good approximation if $\mathbf{u}$ varies slowly.

A.2 PROPERTIES OF THE DEFORMATION

The displacement field $\mathbf{u}(\mathbf{r})$ as defined above, fully describes the deformation of the lattice, but does not directly provide insight into the relevant properties. To that end, we first define the Jacobian of the transformation $\mathbf{f}$:

$$J \equiv \nabla\mathbf{f} = \mathbb{1} + \nabla\mathbf{u}$$

, where $\nabla\mathbf{u}$ is the Jacobian of the displacement field, in continuum mechanics terminology the deformation gradient tensor, and in canonical terms defined as follows:

$$\nabla\mathbf{u} = \begin{pmatrix} \frac{du_x}{dx} & \frac{du_x}{dy} \\ \frac{du_y}{dx} & \frac{du_y}{dy} \end{pmatrix}$$

In order to fully characterise the deformation of the lattice, we decompose J in its polar form:

$$J = WP = WV^\top DV\,, \tag{A.2}$$

where W is the rotation matrix corresponding to the rotation of the full lattice and the matrix P describes the local anisotropy and scaling. P is further decomposed in the rotation matrix V indicating the orientation of the axis of anisotropy (i.e. the axis of largest scaling, with the axis of smallest scaling perpendicular to it) and the diagonal scaling matrix $D = \begin{pmatrix} d_1 & 0 \\ 0 & d_2 \end{pmatrix}$, where by convention and implementation $d_1 \geq d_2$ holds for any position $\mathbf{r}$.

The geometric mean of these directional scaling factors is equal to the square root of the determinant of D and therefore of J: $\sqrt{d_1 d_2} = \sqrt{\det(J)}$. As this corresponds to the local scaling of the wavelength of the moiré lattice, we can use this to quantify the local twist angle:

$$\lambda(\mathbf{r}) = \sqrt{d_1 d_2}\frac{4\pi}{\sqrt{3}|\mathbf{q}_j|} \tag{A.3}$$

Where $|\mathbf{q}_j|$ is the length of the chosen reference vectors. This local wavelength is then converted to a local twist angle using the well-known expression:

$$\theta(\mathbf{r}) = 2\arcsin\left(\frac{2\lambda(\mathbf{r})}{a}\right)$$

, where $a = 2.46$Å is the lattice constant of graphene and $\theta(\mathbf{r})$ the local twist angle.

A quantification of the local anisotropy is given by the ratio $\kappa = d_1/d_2$ and the angle between the anisotropy axis and the x-axis is finally calculated from V: $\psi = \arctan\left(\frac{V_{xy}}{V_{xx}}\right)$.

In our practical implementation, the singular value decomposition (SVD) is used to obtain the decomposition in equation A.2 for each point in the image, and numpy's `atan2` is used to find the right quadrant of the angles from the signs of V_{xx} and V_{xy}.

A.3 DETERMINATION OF THE DISPLACEMENT FIELD $\mathbf{u}(\mathbf{r})$

In order to determine $\mathbf{u}(\mathbf{r})$ for a certain image, we perform a lock-in measurement. To clarify, we can represent any (nearly) periodic image as:

$$T_m(\mathbf{r}) = T_0\sum_j e^{i\mathbf{q}_j\cdot(\mathbf{r}+\mathbf{u}(\mathbf{r}))} = T_0\sum_j e^{i(\mathbf{q}_j\cdot\mathbf{r}+\phi_j)} \tag{A.4}$$

where $\phi_j = \mathbf{q}_j\cdot\mathbf{u}(\mathbf{r})$ is the position-dependent phase of the lattice. The summation runs over the reciprocal lattice vectors $\mathbf{q}_j$ ($j \in \{1,2,3\}$ for a hexagonal lattice), T_0 is the constant indicating the amplitude of the modulation and $\mathbf{u}(\mathbf{r})$ is again the displacement field.

The phase is measured using standard lock-in procedure: The existing image is mixed with a reference image containing a specific plane wave. If we choose the periodicity of this reference wave sufficiently close to that of the lattice in the image itself, we can then low-pass filter the mixed image and end up with a phase map for a specific wave. For clarification:

$$\cos(\mathbf{q}_j\cdot\mathbf{r}+\phi_j)e^{-iq_j\cdot\mathbf{r}} = \frac{e^{i\phi_j}}{2}\left(1+e^{-2i(\mathbf{q}_j\cdot\mathbf{r}+\phi_j)}\right) \mapsto \frac{1}{2}e^{i\phi_j}$$

where the cosine in the first term denotes the (real-valued) measured image, whereas the complex exponential denotes the reference wave and $\mapsto$ denotes low-pass filtering in order to get rid of the last term between brackets, corresponding to a rotating wave approximation. Alternatively, for a gaussian low-pass filter, this corresponds to a real space gaussian integration window of the lock-in.

By taking the (pointwise) angle of the complex, filtered product image, we end up with the phase map. In particular, this phase map contains information about the displacements of each pixel in the measured image $T_m(\mathbf{r})$ with respect to the pristine reference lattice $T_r(\mathbf{r})$ along the wave vector $\mathbf{q}_j$ used for the lock-in procedure. This procedure is repeated for at least one additional reciprocal lattice vector. The two phase maps are then used to find the displacement field $\mathbf{u}(\mathbf{r})$. From the definition of $\mathbf{u}(\mathbf{r})$ (eq. A.1), the following holds: $\mathbf{r}' = \mathbf{r}+\mathbf{u}(\mathbf{r})$. Multiplying this equation by the reciprocal lattice

vectors, we get a system of equations expressing the projection of the distortion onto the reciprocal lattice vectors:

$$\mathbf{q}_j \cdot \mathbf{r}' = \mathbf{q}_j \cdot \mathbf{r} + \phi_j,\ j \in 1,2,3$$

Selecting only $j \in \{1,2\}$, we have in matrix notation:

$$Q = \begin{pmatrix} -\mathbf{q}_1 - \\ -\mathbf{q}_2 - \end{pmatrix} = \begin{pmatrix} q_{1x} & q_{1y} \\ q_{2x} & q_{2y} \end{pmatrix}$$

such that we can write for $\phi = \binom{\phi_1}{\phi_2}$:

$$Q\mathbf{r}' = Q\mathbf{r} + \phi\,. \tag{A.5}$$

Multiplying by Q^{-1}, we find $\mathbf{r}' = \mathbf{r} + Q^{-1}\phi$, and therefore $\mathbf{u}(\mathbf{r}) = Q^{-1}\phi(\mathbf{r})$.

A.4 ADDITIONAL NOTES ON CHOICE OF REFERENCE VECTORS

SELECTING TWO REFERENCE VECTORS

To obtain $\mathbf{u}(\mathbf{r})$ as described above, we only used the phase of the lock-in signal of two reference vectors. For a triangular/hexagonal lattice, *a priori* three possible choices of which two reference vectors to use are possible from the three linear independent references vectors as fitted to the FFT of the image. To select which two vectors to use for the reconstruction of $\mathbf{u}(\mathbf{r})$, we either selected the ones with the largest average lock-in amplitude, or by inspecting the phase-unwrapped images and selecting the ones where no remaining phase slips occurred.

USING MORE THAN TWO REFERENCE VECTORS

In principle, information is lost when only selecting the phase of the lock-in signal of two reference vectors to obtain $\mathbf{u}(\mathbf{r})$. In low signal-to-noise ratio situations, it could be beneficial to use all the information. Equation A.5 also holds for more than two phases and reference vectors. Although Q is not a square matrix in this case, a solution can be obtained for each pixel using linear least squares minimization of the following equivalent equation:

$$Q\mathbf{u}(\mathbf{r}) = \phi(\mathbf{r})$$

Where additionally the amplitude of the lock-in signals can be used as weights to the minimization problem.

ISOTROPY

Enforcing the reference lattice to be isotropic can be done either in advance, by enforcing isotropic reference wavevectors (as applied in this work) or alternatively, after the initial lock-in step, by adding an additional linear phase $\Delta\phi_j = \Delta\mathbf{q}_j \cdot \mathbf{r}$ to the obtained phase, where $\Delta\mathbf{q}_j$ is the difference between the used reference wavevector and the isotropic wavevector.

The advantage of the latter method would be a slightly improved signal-to-noise ratio, as the smoothing window can be centered around the actual average wavevector occurring in the image instead of the ideal, equal-length, 60 degree rotated ones.

A.5 ADAPTIVE GPA

Regular GPA is limited in the wave vector deviations (with respect to the reference wave vector) it can measure, due to the limitations in spectral leakage. This is no problem when applied to atomic lattices, as the expected deviations are very small there. However, due to the moiré magnification of small lattice distortions, it does become a limiting factor when applying GPA to small twist angle moiré lattices.

To overcome this limitation, we extended the GPA algorithm to use adaptive reference wave vectors, based on the combination of two ideas and related to earlier work in laser fringe analysis [173]: First, a GPA phase calculated with respect to one reference vector can always be converted to the GPA phase with respect to another reference vector by adding a phase corresponding to the phase difference between the reference vectors. Second, a larger lock-in amplitude corresponds to a better fit between the reference vector and the data.

The adaptive GPA algorithm therefore works as follows: The spatial lock-in signal is calculated for a grid of wave vectors around a base reference vector, converting the GPA phase to reference the base reference vector every time. For each pixel, the spatial lock-in signal with the highest amplitude is selected as the final signal.

It was realized that to deduce the deformation properties, reconstruction to a globally consistent phase (requiring 2D phase unwrapping), as reported previously [141], is not strictly needed, making it possible to circumvent the problems associated with 2D phase unwrapping. Instead, the gradient of each GPA phase was calculated, requiring only local 1D phase unwrapping (i.e. assuming the derivative of the phase in both the x and y direction will never be more than π per pixel, an assumption in practice always met). Subsequently, these three GPA gradients are converted to the displacement gradient tensor (in real space coordinates), estimating the transformation via weighted least squares, using the local spatial lock-in amplitudes as weights.

As an added benefit, this entire procedure is local, i.e. not depending on pixels beyond nearest neighbors in any way except for the initial Gaussian convolution in determining the GPA. This reduces the effect of artefacts in the image to a minimum local area around each artefact (where for in the 2D phase unwrapping they have a global influence on the phases).

However, when the gradient is computed based on phase values stemming from two different GPA reference vectors, i.e. at the edge of their valid/optimal regions, artefacts appear due to their relatively large absolute error. To prevent this, the local gradient of the phase with the highest lock-in magnitude is stored alongside the lock-in signal itself in the GPA algorithm. This way, the gradient is calculated based on a single reference phase, propagating only the much smaller relative/derivative error between the two signals instead of the absolute error.

As mentioned in Chapter 6, even adaptive GPA has its limits. In particular, too large deviations from the base reference vector can not be resolved correctly, causing an erroneous, lower, extracted deviation, as is visible in the lower right of Figure 6.3**e**). As the deformation becomes too large, e.g. towards the folds in the TBG, the highest lock-in amplitude will occur at a different moiré peak or at the near-zero components of the fourier transform, causing an incorrect value to be extracted.

A.6 DECOMPOSITION OF THE DISPLACEMENT FIELD.

Kerelsky et al. [174] use the following idea to extract twist angle θ_T, strain magnitude ϵ and strain direction θ_s from reciprocal moiré lattice vectors K_{is}: These difference vectors of the constituting atomic lattices are written in terms of a rotated and a strained lattice vector each:

$$K_{is} = k_{ir} - k_{is} = R(\theta_T)\,k_i - S(\theta_s,\epsilon)\,k_i$$

where k_i are the original lattice vectors. Kerelsky et al. assume k_0 to be along the x-axis, and get around this by taking amplitudes, discarding any global rotation. Here, we do however introduce that global rotation, by a multiplication with $R(\xi)$:

$$K_{is} = \left(R(\theta_T) - S(\theta_s,\epsilon)\right) R(\xi)\,k_i$$

Eihter of these expressions can, and indeed by Kerelsky et al. is, numerically fitted to the found amplitudes or k-vectors for each triangle. However, from GPA analysis we most naturally obtain a Jacobian transformation J_{ac} of the moiré k-vectors with respect to some specific set of reference vectors with predefined strain and rotations:

$$K_{is} = (J+I)K_{i0} = J_{ac}K_{i0} = J_{ac}\left(R(\theta_{T0}) - S(\theta_{s0},\epsilon_0)\right) R(\xi_0)\,k_i := J_{ac}A_0R(\xi_0)\,k_i$$

Note that we can force $\epsilon_0 = 0 \rightarrow S(\theta_{s0},\epsilon_0) = I$.
This simplifies to:

$$J_{ac}A_0R(\xi_0)\,k_i = \left(R(\theta_T) - S(\theta_s,\epsilon)\right) R(\xi)\,k_i$$

The linear transformation is uniquely described by its effect on two points in k-space, so their matrix representations should be equal:

$$\begin{aligned} J_{ac}A_0R(\xi_0) &= \left(R(\theta_T) - S(\theta_s,\epsilon)\right) R(\xi) \\ J_{ac}A_0 &= \left(R(\theta_T) - S(\theta_s,\epsilon)\right) R(\xi - \xi_0) \end{aligned}$$

The left hand side is a known quantity at each position, the right hand side remains to be numerically fitted or extracted. This is implemented in `pyGPA` using `scipy.optimize` and `numba` to just-in-time compile the fitting code [88, 246].

Alternatively, we could formulate a symmetric expression with two strains, but without allowing for further joint rotation of the lattices:

$$K_{i0} = \left(R(\theta_{T0}/2) - R(-\theta_{T0}/2)\right) R(\xi_0)\,k_i := B_0R(\xi_0)\,k_i$$

$$\begin{aligned} J_{ac}B_0R(\xi_0)\,k_i &= \left(S(\theta_b,\epsilon_b)R(\theta_T/2) - S(\theta_a,\epsilon_a)R(-\theta_T/2)\right) R(\xi_0)\,k_i \\ J_{ac}B_0 &= \left(S(\theta_b,\epsilon_b)R(\theta_T/2) - S(\theta_a,\epsilon_a)R(-\theta_T/2)\right) \end{aligned}$$

REFERENCES

88. T. A. de Jong. *pyGPA* 2021. doi:10.5281/zenodo.5589555.

135. T. A. de Jong, T. Benschop, X. Chen, et al. Imaging moiré deformation and dynamics in twisted bilayer graphene. *Nature Communications* **13,** 70. doi:10.1038/s41467-021-27646-1 (2022).

141. T. Benschop*, T. A. de Jong*, P. Stepanov*, et al. Measuring local moiré lattice heterogeneity of twisted bilayer graphene. *Physical Review Research* **3,** 013153. doi:10.1103/PhysRevResearch.3.013153 (2021).

143. M. J. Lawler, K. Fujita, J. Lee, et al. Intra-unit-cell electronic nematicity of the high-Tc copper-oxide pseudogap states. *Nature* **466,** 347–351. doi:10.1038/nature09169 (2010).

173. Q. Kemao. Two-dimensional windowed Fourier transform for fringe pattern analysis: Principles, applications and implementations. *Optics and Lasers in Engineering* **45,** 304–317. doi:10.1016/j.optlaseng.2005.10.012 (2007).

174. A. Kerelsky, L. J. McGilly, D. M. Kennes, et al. Maximized electron interactions at the magic angle in twisted bilayer graphene. *Nature* **572,** 95–100. doi:10.1038/s41586-019-1431-9 (2019).

246. S. K. Lam, A. Pitrou & S. Seibert. *Numba* in *Proceedings of the Second Workshop on the LLVM Compiler Infrastructure in HPC - LLVM '15* (ACM Press, 2015). doi:10.1145/2833157.2833162.

B

LEEM STITCHING

To achieve stitching of images without inducing any additional deformation, a custom stitching algorithm tailored towards such LEEM data, was developed, working as follows:

To compensate sample stage inaccuracy, nearest neighbor (by sample stage coordinates) images are compared, finding their relative positions by cross-correlation. Using an iterative procedure, calculating cross correlations of overlapping areas at each step, the absolute positions of all images are found. Images are then combined in a weighted fashion, with the weight sloping to zero at the edges of each image, to smooth out any mismatch due to residual image warping. The full stitching algorithm is implemented in `Python`, available as a `Jupyter Notebook`[42].

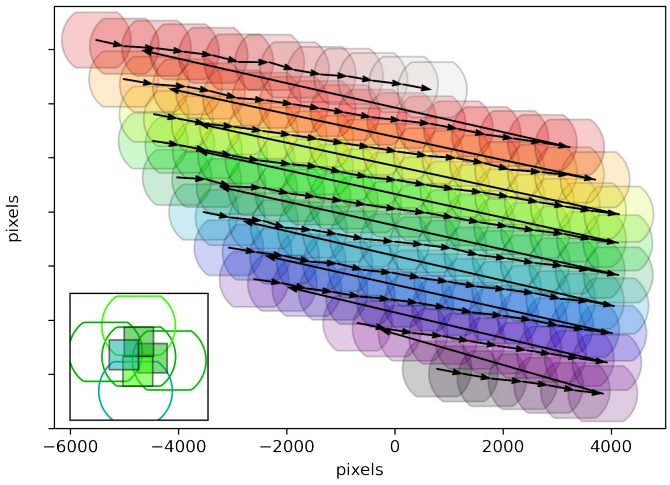

Figure B.1: *Illustration of the sample stage scanning for stitched overview images. Black arrows indicate the direction of the sample stage movement.* ***inset,*** *Illustration of the square overlapping regions of neighboring images used to determine relative positions.*

It is designed for use with ESCHER LEEM images. For those images, their positions are known approximately in terms of *stage coordinates*, i.e. the positions as reported by

This appendix has been published prior in the Supplementary material Nat. Commun. **13**, 70 (2022) [135].

the sensors in the sample stage. It should however generalize to any set of overlapping images where relative positions of the images are known in some coordinate system which can approximately be transformed to coordinates in terms of pixels by an affine transformation (rotation, translation, mirroring).

The algorithm consists of the following steps:

1. Using the stage coordinates for each image, obtain a nearest neighbour graph with the nearest `n_neighbors` neighbouring images for each image.
2. Obtain an initial guess for the transformation matrix between stage coordinates and pixel coordinates, by one of the following options:
    1. Copying a known transformation matrix from an earlier run of a comparable dataset.
    2. Manually overlaying some nearest neighbor images from the center of the dataset, either refining the estimate, or making a new estimate for an unknown dataset
3. Calculate an initial estimate of the pixel coordinates of the images by applying the corresponding transformation to the stage coordinates
4. Apply a gaussian filter with width `sigma` to the original dataset and apply a magnitude sobel filter. Optionally scale down the images by an integer factor `z` in both directions to be able to reduce `fftsize` by the same factor, without reducing the sample area compared.
5. Iterate the following steps until the calculated image positions have converged to within `sigma`:
    1. Obtain a nearest neighbour graph with per image the nearest `n_neighbors` neighbouring images from the current estimate of the pixel coordinates and calculate the difference vectors between each pair of nearest neighbours.
    2. For each pair of neighboring images:
        i. Calculate the cross-correlation between areas estimated to be in the center of the overlap of size `fftsize*fftsize` of the filtered data. If the estimated area is outside the valid area of the image defined by `mask/radius`, take an area as close to the intended area but still within the valid area as possible.
        ii. Find the location of the maximum in the cross-correlation. This corresponds to the correction to the estimate of the difference vector between the corresponding image position pair.
        iii. Calculate the weight of the match by dividing the maximum in the cross-correlation by the square root of the maximum of the auto-correlations.
    3. Compute a new estimate of the difference vectors by adding the found corrections. Reconvert to a new estimate of pixel coordinates by minimizing the squared error in the system of equations for the positions, weighing by modified weights, either:

   i. $w_{mod} = w - w_{min}$ for $w > w_{min}$, $w = 0$ else, with w_{min} the maximum lower bound such that the graph of nearest neighbours with non-zero weights is still connected
   ii. Only use the 'maximum spanning tree' of weights, i.e. minus the minimum spanning tree of minus the weights, such that only the n best matches are used.

6. (Optional) Refine the estimate of the transformation matrix, using all estimated difference vectors with a weight better than $w_{min\ est}$ and restart from step 3.

7. Repeat step 4. and 5. until `sigma` is satisfactory small. Optionally repeat a final time with the original data if the signal to noise of the original data permits.

8. Select only the images for stitching where the average of the used weights (i.e. where $w > w_{min}$) is larger than q_{thresh} for an appropriate value of q_{thresh}.

9. (Optional) For those images, match the intensities by calculating the intensity ratios between the overlap areas of size `fftsize*fftsize` and perform a global optimization.

10. Define a weighting mask, 1 in the center and sloping linearly to zero at the edges of the valid region, over a width of `bandwidth` pixels, as illustrated in Figure B.2.

11. Per block of output `blocksize*blocksize`, select all images that have overlap with the particular output block, multiply each by the weighting mask and shift each image appropriately. Divide by an equivalently shifted stack of weighting masks. As such information at the center of images gets prioritized, and transitions get smoothed.

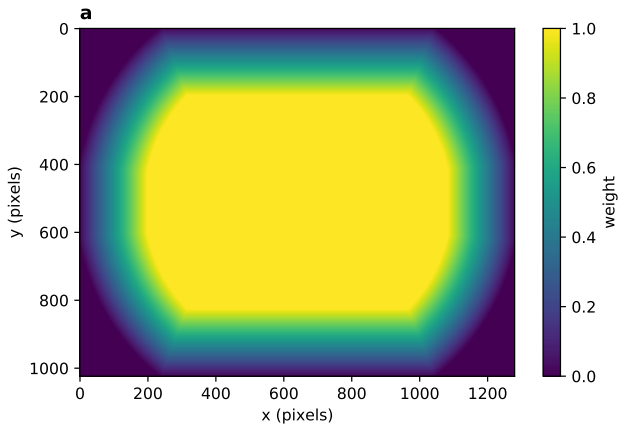

Figure B.2: a, *Weight mask used to merge images. A linear slope of the weight towards the edges of the round microchannel plate detector is used to smoothly merge images.*

B.1 CONSIDERATIONS

For square grids with a decent amount of overlap, it makes sense to put `n_neighbors` to 5 (including the image itself), however, for larger overlaps or datasets where an extra dimension is available (such as landing energy), it can be appropriate to increase the number of nearest neighbors to which each image is matched.

Parameters and intermediate results of the iteration are saved in an `xarray` and saved to disk for reproducibility.

B.2 PARALLELIZATION

Using `dask`, the following steps are parallelized:

- step 5B , where each pair of images can be treated independently. In practice parallelization is performed over blocks of subsequent images with their nearest neighbours. This could be improved upon in two ways: firstly by treating each pair only once, and secondly by making a nicer selection of blocks of images located close to each other in the nearest neighbor graph. This would most likely require another (smarter) data structure than the nearest neighbour indexing matrix used now.
- Step 6 is quite analogous to 5B and is parallelized similarly.
- Step 11 is parallelized on a per block basis. To optimize memory usage, results are directly streamed to a `zarr` array on disk.
- The minimizations are parallelized by `scipy` natively.

REFERENCES

42. T. A. de Jong. *Quantitative Data Analysis for spectroscopic LEEM* version v0.2.0. 2021. doi:10.5281/zenodo.3539538.

135. T. A. de Jong, T. Benschop, X. Chen, et al. Imaging moiré deformation and dynamics in twisted bilayer graphene. *Nature Communications* **13,** 70. doi:10.1038/s41467-021-27646-1 (2022).

C

ADDITIONAL DATA OF THE TWISTED BILAYER GRAPHENE SAMPLE

Parts of this appendix have been published in the Supplementary materials of T. A. de Jong, T. Benschop, X. Chen, E. E. Krasovskii, M. J. A. de Dood, R. M. Tromp, M. P. Allan and S. J. van der Molen, Nat. Commun. **13**, 70 (2022) [135]. Xingchen Chen performed the AFM measurements in Section C.4.

C.1 ADDITIONAL LEEM IMAGES/CROPS

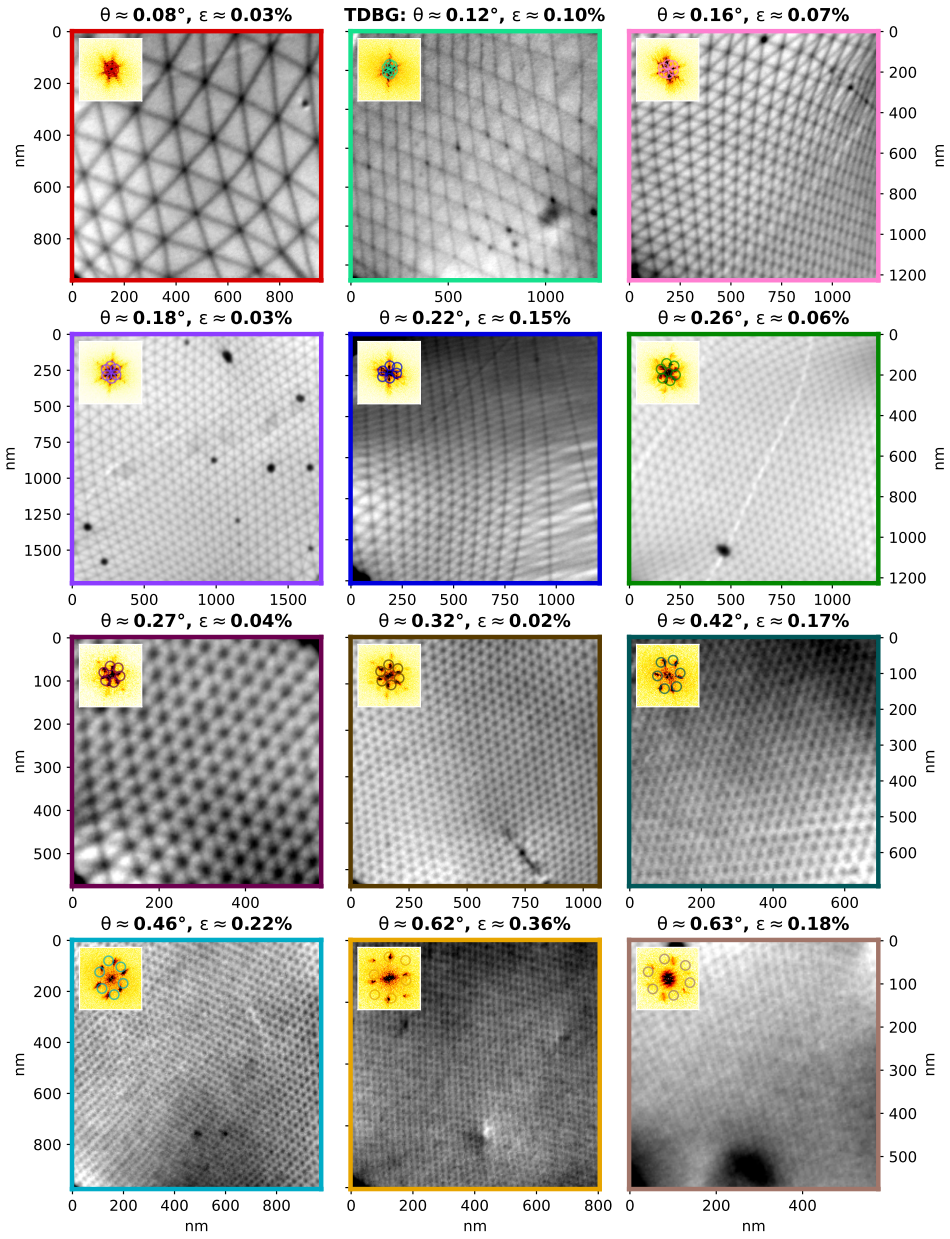

Figure C.1: *A wider range of images found in the sample from Chapter 6, as used to determine the histograms of twist angles and strain in Figure 6.3. Insets show FFT's with the detected moiré peaks*

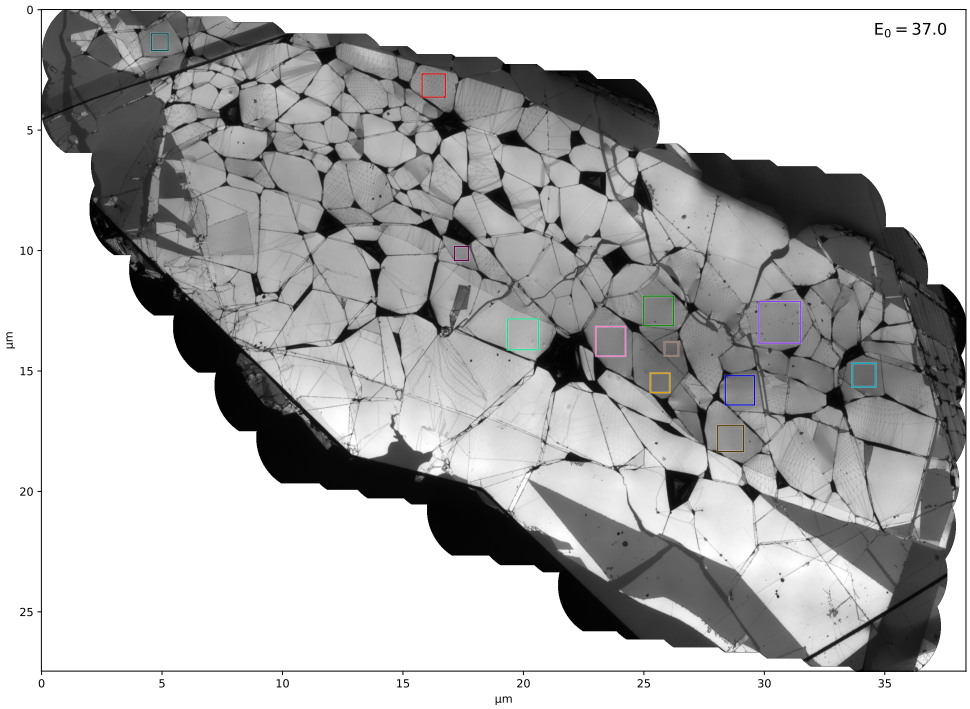

Figure C.2: *Locations of the crops in Figure C.1 indicated in the full overview (data is a super set of the data in Figure 6.1* ***e*** *in Chapter 6).*

C.2 ADDITIONAL FIGURES ON DYNAMICS

Supplementary Video 1, the full movie showing the dynamics of a larger Field of View compared to Figure 6.5 in Chapter 6, in real space LEEM data, difference data and GPA-extracted displacement field is available in the Supplementary information of the published paper, Ref. [135] at https://doi.org/10.1038/s41467-021-27646-1.

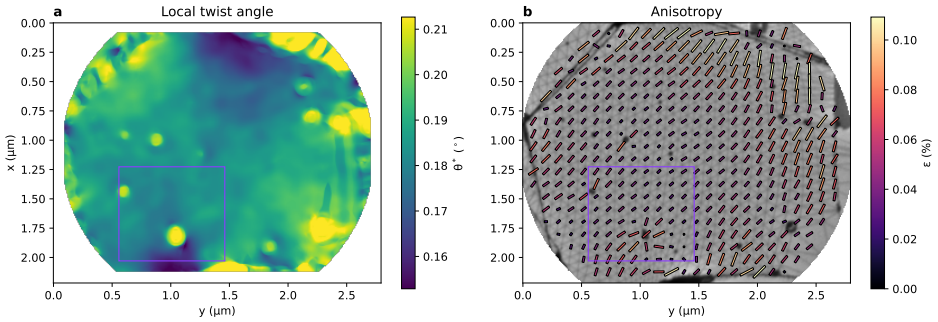

Figure C.3: a, *Local twist angle as extracted with GPA of the area imaged in Supplementary Video 1.* ***b,*** *Local strain magnitude and direction as extracted with GPA of the same area. Purple rectangles indicate the area depicted in Figure 6.5 in Chapter 6.*

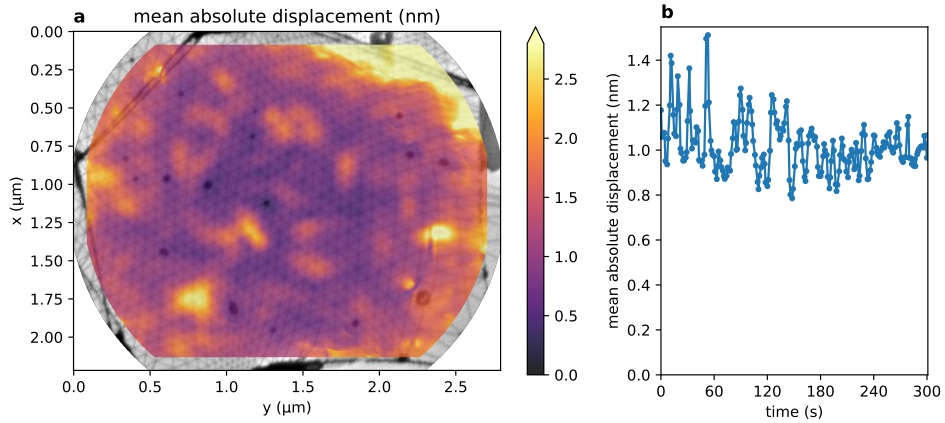

Figure C.4: a, *(Temporal) Mean absolute displacement from mean position during Supplementary Video 1.* ***b,*** *Spatial mean absolute displacement from mean position during Supplementary Video 1 as a function of time for a center area.*

C.3 ADDITIONAL DISLOCATIONS

More dislocations than single one shown in Figure 6.4 in Chapter 6 were found on the same sample. One additional dislocation in a low twist angle area is shown in Figure C.5**a** together with the GPA phases, and next to a larger area around the dislocation in Figure 6.4. More dislocations in less clean areas of the sample are shown in Figure C.6. The original dislocation had moved when re-examining the sample a few days later. The dislocation before and after movement, together with a reconstruction based on the decomposition of the displacement field as described in Appendix A.6 is shown in Figure C.7.

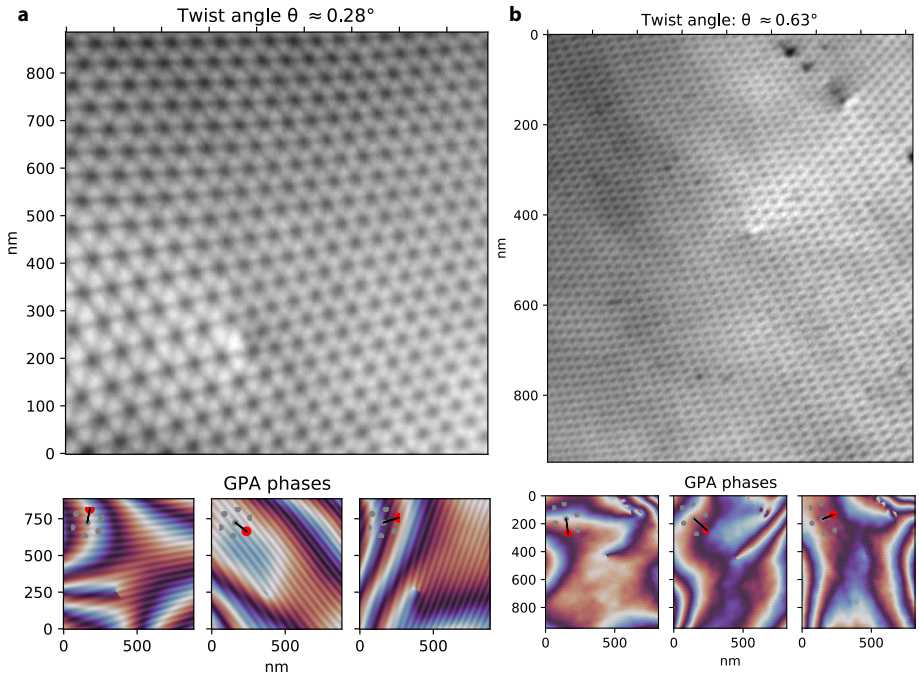

Figure C.5: a, *Additional edge dislocation found on the sample at a lower twist angle.* ***b,*** *Larger area around edge dislocation in Figure 6.4* ***f*** *in Chapter 6. In both case GPA phases are also displayed.*

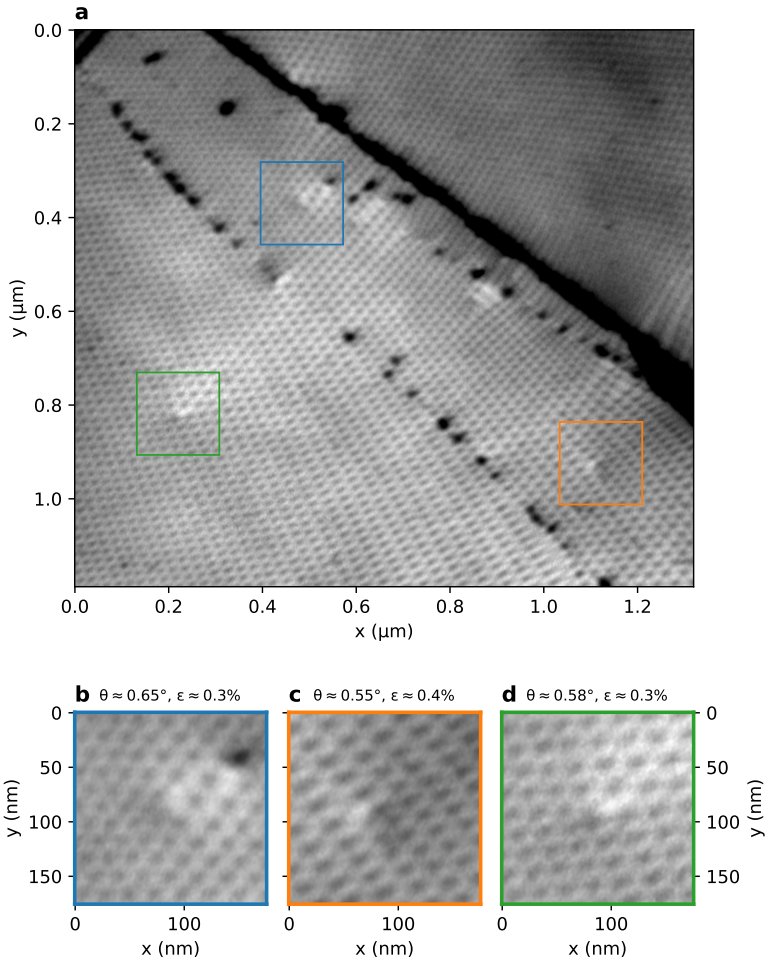

Figure C.6: *More dislocations in the vicinity of the dislocation shown in Figure C.5* ***b****.* ***d,*** *corresponds to the dislocation there. θ as extracted from the shown area here is a bit lower as unit cell area tends to be a bit larger near the dislocation.*

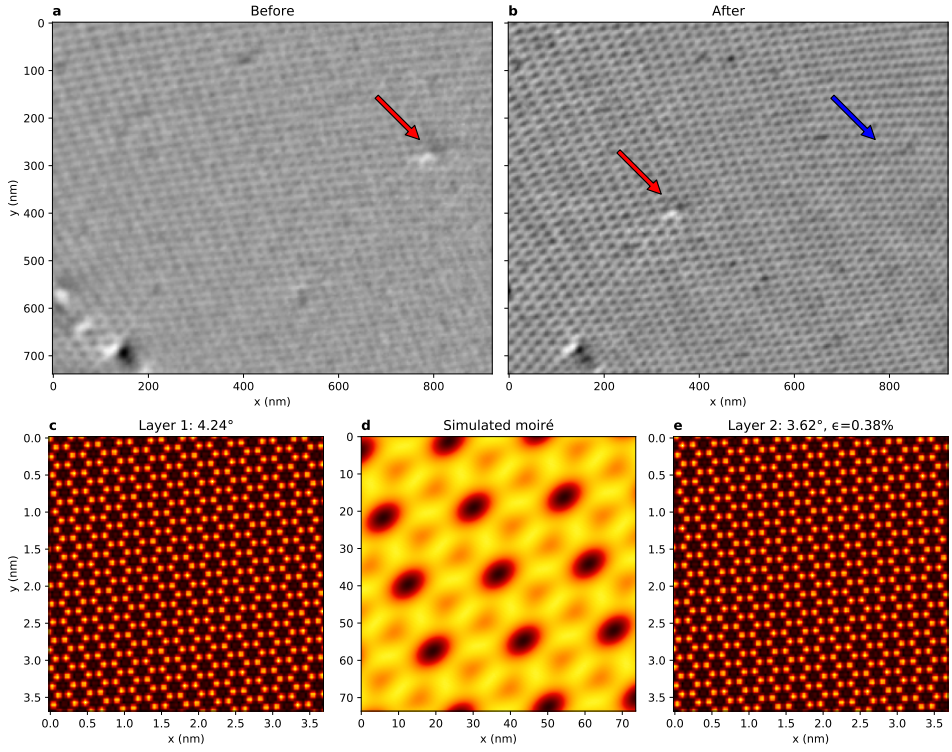

Figure C.7: Movement of dislocation. ***a,*** *Dislocation in its original location, indicated by red arrow.* ***b,*** *Image of the same area as in* ***a,****, but imaged two days later. The dislocation has moved, as indicated by the red arrow. The former location is indicated with a blue arrow.* ***c-e,*** *Rendering of the individual atomic lattices and the resulting moiré lattice from the extracted lattice parameters, showing the atomic lattice directions.*

C.4 AFM COMPARISON

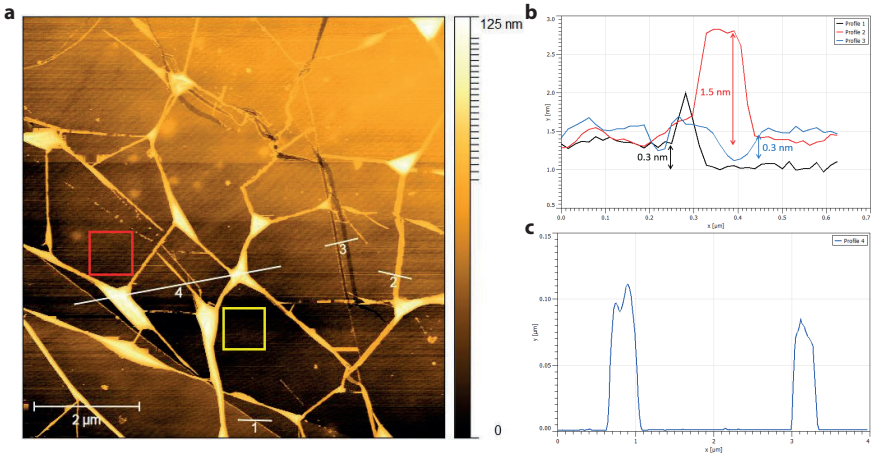

Figure C.8: ***a,*** *Atomic Force Microscopy overview of sample area. Locations of line profiles and detailed topographies in Figure C.9 are indicated.* ***b,c,*** *Line cuts along the cuts indicated in* ***a****.*

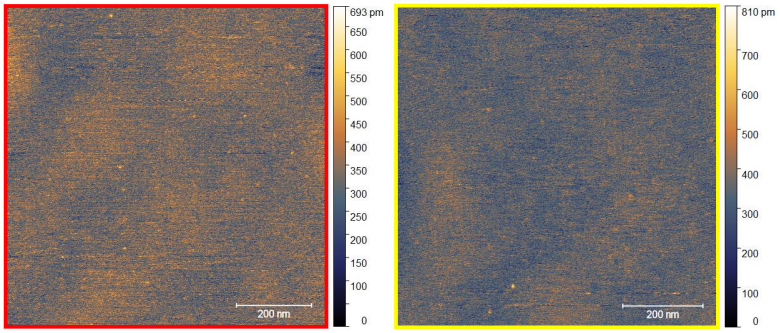

Figure C.9: ***a,*** *Atomic Force Microscopy of the dislocation area in Figure C.5****a****. Area is indicated in red in Figure C.8****a****.* ***b,*** *Atomic Force Microscopy of the dislocation area in Figure C.5****b****. Area is indicated in yellow in Figure C.8****a****.*

To further characterize the surface properties of the sample, an AFM (JPK, NanoWizard 3) measurement was performed in AC tapping mode following the LEEM measurements. Predominantly, the results show a very flat and clean graphene surface between folds, indicating annealing at 500 °C in UHV had successfully removed the polymer residue left on the surface.

In profile 1, the terrace height sees a difference of 0.3 nm, demonstrating the graphene layer count goes down by one at this location. This corresponds to the layer counts extracted from the LEEM spectra.

Profile 2 to 4 shows 3 different kinds of defects in the bilayer graphene region. The ridge at location 2 seems to be a neat folding of both the bilayer graphene flake (1.5 nm in

height, four layers of graphene), whereas profile 4 shows wrinkles that are up to 120 nm tall. This is also reflected by the distinct patterns in the LEEM bright field overview image, respectively. While the wrinkles merely appear black, the ridge resembles more like a unique layer count domain. Profile 3 shows two tears within the one layer of graphene, corresponding nicely to the defect region observed in LEEM where monolayer graphene shines through.

The zoomed-in small scale measurements marked by the red and yellow box shows the topography on top of two dislocations observed in LEEM. As shown in Figure C.9, no distinctive feature was observed at either dislocation. The topography, however, shows an exceptionally flat surface with a height variation (peak-to-peak) of less than 1 nm.

C.5 SAMPLE HEATING

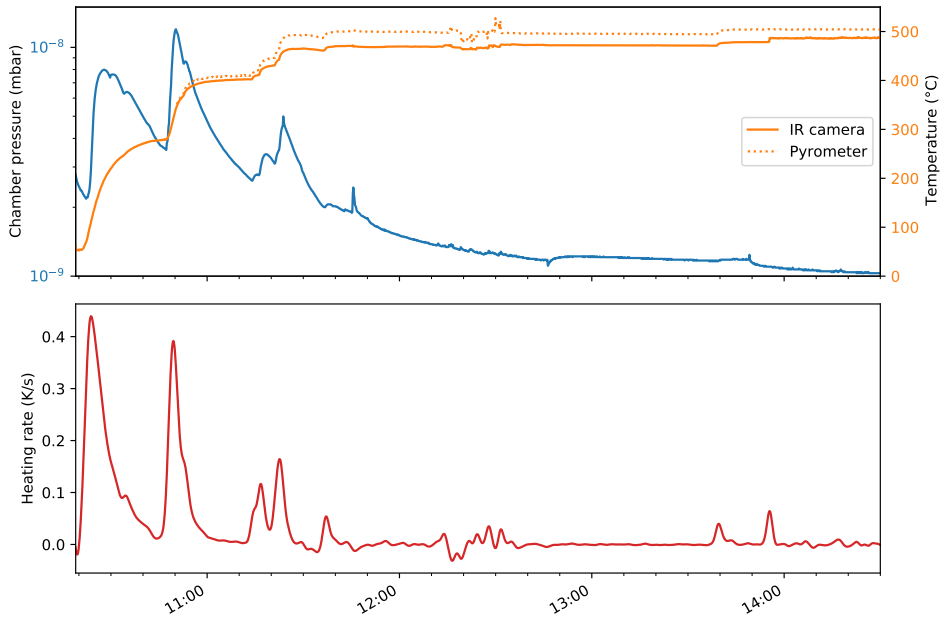

Figure C.10: *Sample temperature, heating rate and chamber pressure as measured by pyrometer and IR camera during initial heating.*

D

ADDITIONAL TaS_2 FIGURES

This appendix contains extra figures with spectra and other information supporting the work in Chapter 8.

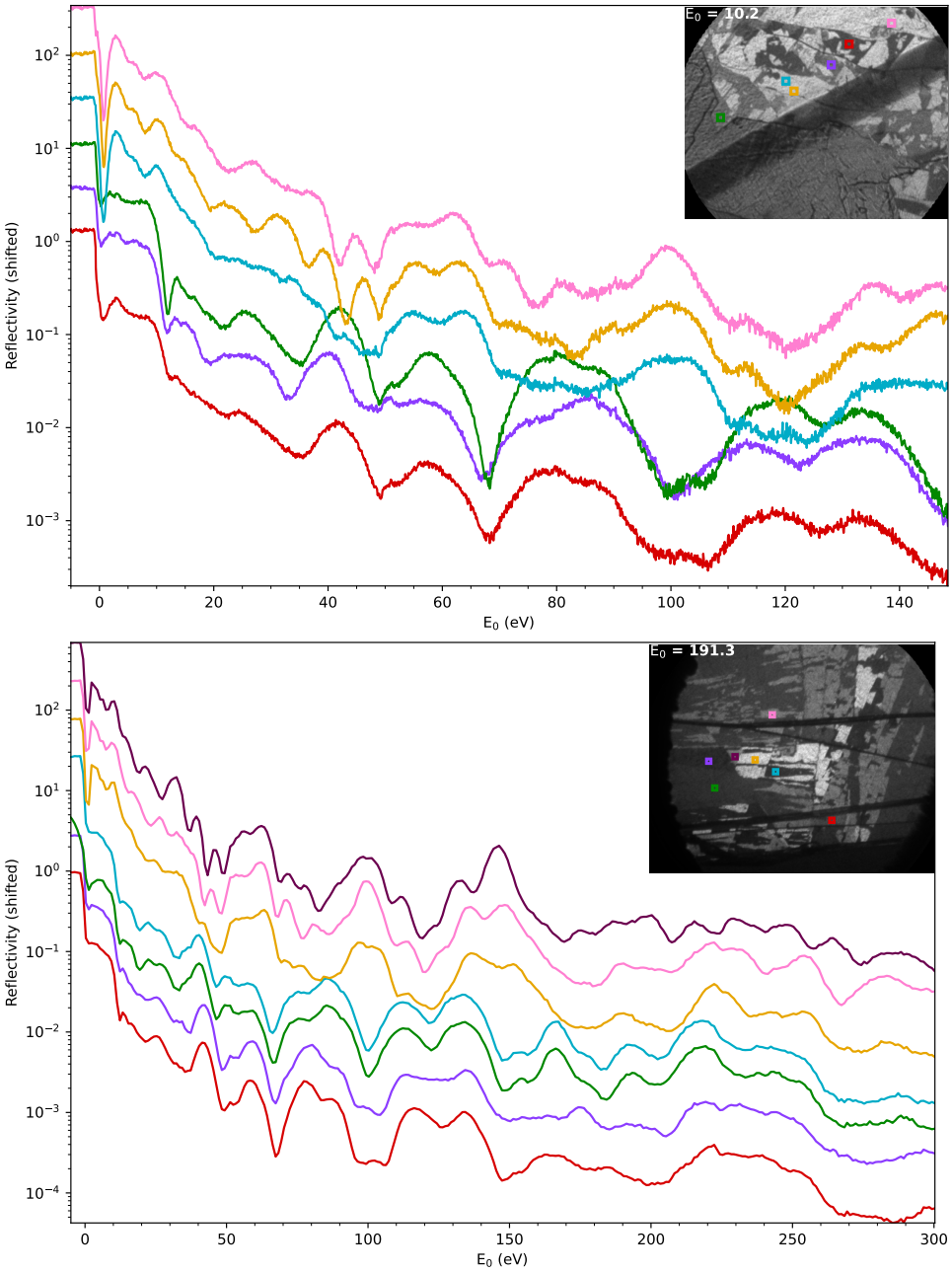

Figure D.1: More BF-LEEM spectra of mixed polytypes. *Curves are offset for clarity, with 2H-like curves below 3 1T-like curves in each panel. Data in the lower panel and in Figure D.2 was taken after the sample was kept in vacuum for 80 days.*

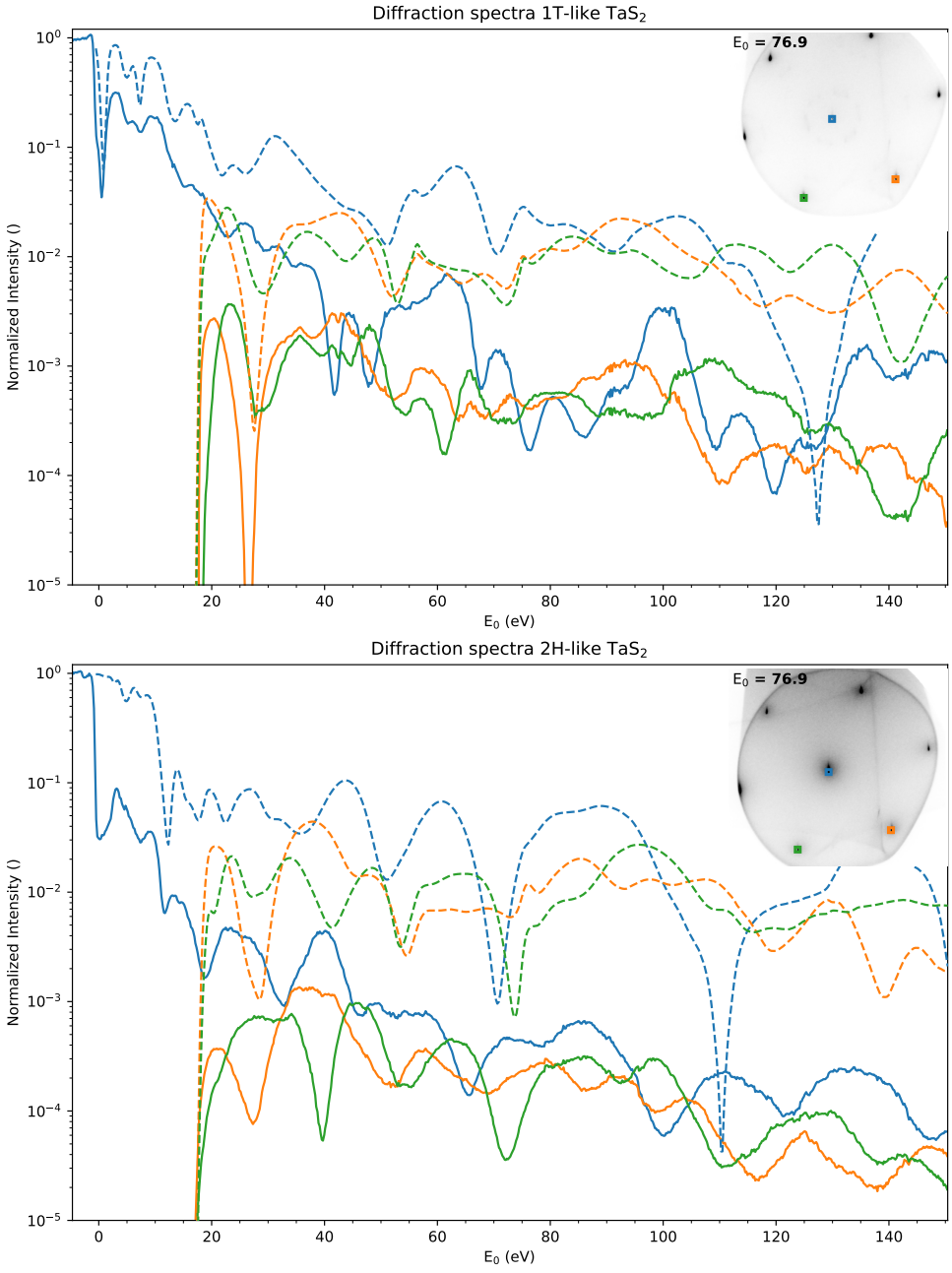

Figure D.2: ***(top),*** *Diffraction spectrum of an 1T-like polytype, most similar to the brown curve in Figure 8.7, i.e. fourth from the top in that figure and not the most similar to the pristine 1T.* ***(bottom),*** *Diffraction spectrum of 2H-like polytype, most similar to the green and turquoise curves in tyhe lower panel of Figure D.1. Dashed curves are corresponding ab-initio calculations for the bulk polytypes without taking into account the CDW.*

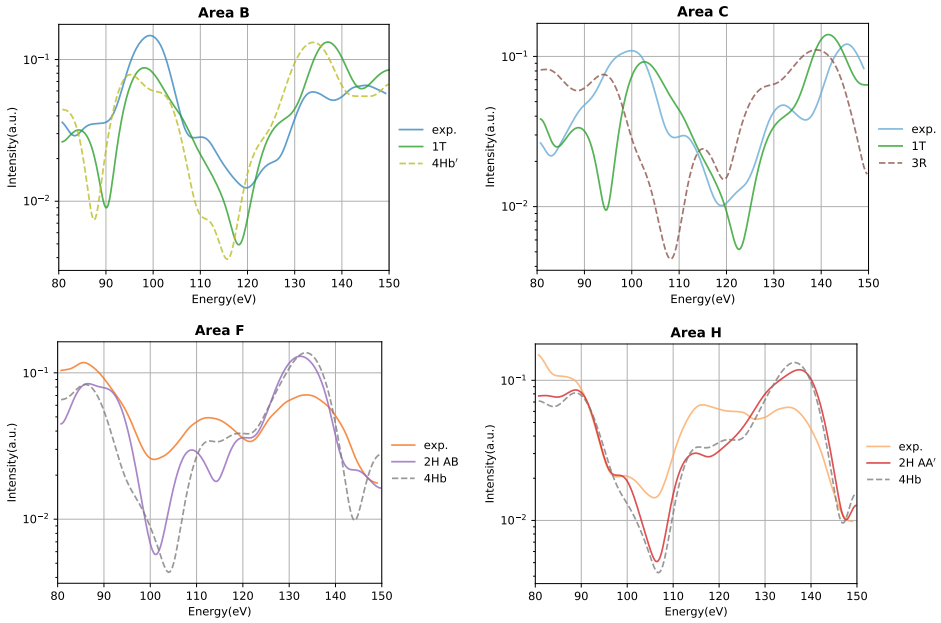

Figure D.3: TensorLEED calculations for selected data from Figure 8.7. *Taken from Ref. [232]. For each area the closest matching structure and second closest match (dashed) are shown. Here,* ***4Hb*** *denotes alternating Oc and Pr layers, terminating in a Pr layer (i.e. a 2H-like layer on top),* ***4Hb'*** *the same, but terminating in a Oc layer,* ***2H AB*** *denotes the* $2H^{\triangle}$ *polytype, and* ***2H AA'*** *corresponds to* $2H^{\hexagon}$*.*
B: *corresponds to ocre spectrum in Figure 8.7.*
C: *dark brown spectrum (fourth from top).*
F: *mint green spectrum (third from bottom).*
H: *bright red spectrum, (bottom spectrum).*
Although the match between experiment and calculations is far from perfect (best Pendry R-factor of 0.31), this comparison does support the hypothesis of 1T-like terminated and 2H-like terminated polytype structures as discussed in the main text.

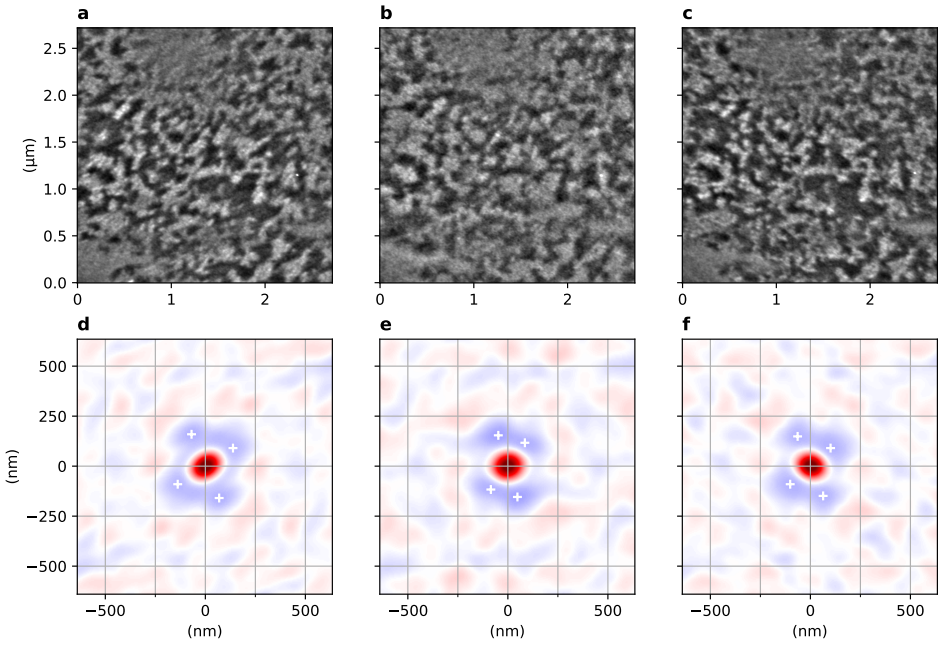

Figure D.4: Auto-correlation of DF-LEEM images of the tC-CDW. a-c, *Three DF-LEEM images of the same area using different CDW spots.* ***d-f,*** *Auto-correlations of these images. From the minima in the cross-correlations, we extract a characteristic domain size between 135 and 175 nm.*

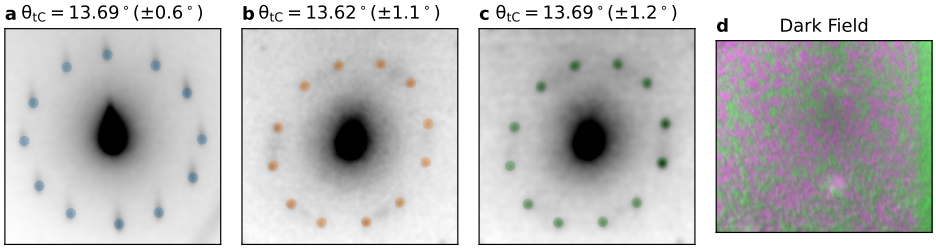

Figure D.5: Comparison with data measured by Philip Schädlich at Chemnitz. a, *Same as Figure 8.9* ***e****.* ***b,c,*** *Diffraction images taken in Chemnitz with the detected peaks indicated.* ***d,*** *Composite Dark Field image taken in the same area as* ***b,c****. The indicated margin on the angles is the standard deviation of the six angles within a single diffraction image. The fact that the data from independently prepared samples in Chemnitz give such a similar mean angle suggests the error on the mean angle is however much lower than this standard deviation, as averaging over all six cancels out most diffraction pattern distortions.*

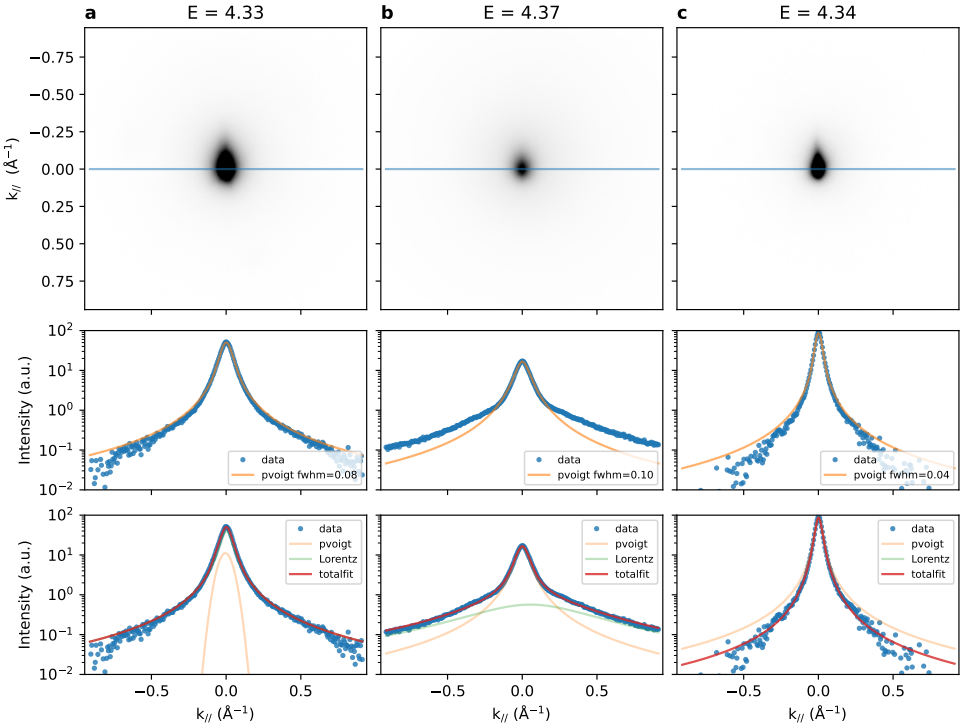

Figure D.6: 2H and 1T Diffraction profile fits. ***a-c,*** *Diffraction images, corresponding to Figure 8.8* ***a-c****, but at the landing energy of the dark field images in Figure 8.10. For the 1T-like areas in a and c, a single pseudovoigt peak is enough to fit the profile (center row). For the 2H-like area in b however, a broad background intensity is present, which can be sufficiently fit by a broad Lorentzian background (bottom row). This broad background causes 2H-like areas to appear bright in the Dark Field images, as the total intensity of this background in the aperture is larger than the total intensity of the CDW diffraction spot in the 1T-like areas.*

ACKNOWLEDGEMENTS

This thesis would not have been possible without all the amazing people around me. I would like to thank my promotores Sense Jan van der Molen and Ruud Tromp for their guidance and allowing me to put more time into projects than they at the time thought was needed. I would like to thank Johannes Jobst for stepping up when Sense Jan could not, and providing supervision long beyond what was expected of him. I want to thank my parents for always having a listening ear ready when I needed it. My students Wouter Gelling, Jean-Paul van Soest, Peter Neu, Luuk Visser, Tim Iking, Arend-Jan Quist, Lionel Kielhofer and Dianto Bosman for contributing to the group and making me feel productive when I myself wasn't and all other students in the group for putting up with my interference. I hope my net contribution to your projects was in the end positive. I want to thank Jan Aarts, Daniela Kraft, and Eric Eliel, who showed me that teaching can be fun. My direct colleagues with whom I enjoyed building, if not a better world, at least a better LEEM and better papers: Daniël Geelen, Ivan Bespalov, Vera Janssen, Peter Neu, Marcel Hesselberth, Douwe Scholma, Xingchen Chen and Guido Stam. Federica Galli, Ruud van Egmond and Peter van Veldhuizen for their technical support. Ellie van Rijsewijk and Michelle Wijfje for their indispensable support in navigating the bureaucracy of Leiden University. Milan Allan and the people from his group, Willem, Koen, Doohee, Maarten and in particular Tjerk Benschop for giving me an insight into the world of STM and for all the bakkies koffie. David Kok for all the times I needed a fellow mathematician. There is a list of people of the 'old guard' who have shown me how fun research can be, and therefore without whom I would not have started on this journey: Jelmer Wagenaar, Jelmer Renema, Christopher Smiet, Frank Buters, Hedwig Eerkens and Martin de Wit. Kier Heeck would also be in this list of 'old guard', except that he is in a class of his own. Thank you for all the interesting discussion before starting measurements and after programming data analyses. I must acknowledge that I am in debt to all the people who were willing to share samples with me, even if the collaborations did not always bring them what they had hoped: Christian Ott, Hyobin Yoo, Anna Sinterhauf, Robbert Schoo and Petr Stepanov. Finally, all those friends who provided company to go to every time I needed to get away from this journey, especially when the journey led through a pandemic: Lisette, Tom, Annette, Heleen, all three Irenes, Reiny, Sylvie, Rik and Esmee, Pieter. And outside the pandemic, all the other people from De Leidsche Flesch in the FooBar.

CURRICULUM VITÆ

Tobias Arie DE JONG

05-05-1992 Born in Leiderdorp, The Netherlands.

EDUCATION

2004–2010 Highschool VWO/Gymnasium
Bonaventuracollege, Leiden, The Netherlands

2010–2014 Bachelor of Science in Mathematics
Universiteit Leiden

2010–2014 Bachelor of Science in Physics
Universiteit Leiden

2014–2017 Master of Science in Physics
Universiteit Leiden
Completed with distinction (cum laude)

Thesis:	Stacking domains in bilayer Van der Waals materials
Supervisors:	Prof. dr. ir. S.J. van der Molen Dr. J. Jobst

2017–2022 PhD. Physics
Universiteit Leiden

Thesis:	Superlattices in van der Waals materials
Promotor:	Prof. dr. ir. S.J. van der Molen
Co-promotor:	Prof. dr. ir. R.M. Tromp

LIST OF PUBLICATIONS

13. T. A. de Jong et al. LEEM study of Charge Density Waves in mixed polytype TaS_2. *in preparation* (2022)

12. G. Gatti, J. Issing, L. Rademaker, F. Margot, T. A. de Jong, S. J. van der Molen, J. Teyssier, T. Kim, M. D. Watson, C. Cacho, K. Cordero Edwards, P. Paruch, N. Ubrig, I. Gutiérrez-Lezama, A. Morpurgo, A. Tamai & F. Baumberger. Observation of flat bands in twisted bilayer WSe_2. *in preparation* (2022)

11. J. Jobst, E. E. Krasovskii, R. Ribeiro, T. A. de Jong, C. R. Dean, R. M. Tromp & S. J. van der Molen. Evolution of the unoccupied bands in the series of MoX_2 Transition Metal Dichalcogenides ($X = S, Se, Te$). *in preparation* (2022)

10. T. A. de Jong, X. Chen, E. E. Krasovskii, R. M. Tromp, J. Jobst & S. J. van der Molen. Low-Energy Electron Microscopy contrast of stacking boundaries: comparing twisted few-layer graphene and strained epitaxial graphene on silicon carbide. *under review.* https://arxiv.org/abs/2207.14616 (2022)

9. T. A. de Jong, L. Visser, J. Jobst, R. M. Tromp & S. J. van der Molen. Stacking domain morphology in epitaxial graphene on silicon carbide. *under review.* https://arxiv.org/abs/2207.14623 (2022)

8. T. A. de Jong, T. Benschop, X. Chen, E. E. Krasovskii, M. J. A. de Dood, R. M. Tromp, M. P. Allan & S. J. van der Molen. Imaging moiré deformation and dynamics in twisted bilayer graphene. *Nature Communications* **13,** 70. doi:10.1038/s41467-021-27646-1 (2022)

7. T. Benschop*, T. A. de Jong*, P. Stepanov*, X. Lu, V. Stalman, S. J. van der Molen, D. K. Efetov & M. P. Allan. Measuring local moiré lattice heterogeneity of twisted bilayer graphene. *Physical Review Research* **3,** 013153. doi:10.1103/PhysRevResearch.3.013153 (2021)

6. S. Lisi*, X. Lu*, T. Benschop*, T. A. de Jong*, P. Stepanov, J. R. Duran, F. Margot, I. Cucchi, E. Cappelli, A. Hunter, A. Tamai, V. Kandyba, A. Giampietri, A. Barinov, J. Jobst, V. Stalman, M. Leeuwenhoek, K. Watanabe, T. Taniguchi, L. Rademaker, S. J. van der Molen, M. P. Allan, D. K. Efetov & F. Baumberger. Observation of flat bands in twisted bilayer graphene. *Nature Physics* **17,** 189–193. doi:10.1038/s41567-020-01041-x (2021)

5. T. A. de Jong, D. N. L. Kok, A. J. H. van der Torren, H. Schopmans, R. M. Tromp, S. J. van der Molen & J. Jobst. Quantitative analysis of spectroscopic low energy electron microscopy data: High-dynamic range imaging, drift correction and cluster analysis. *Ultramicroscopy* **213,** 112913. doi:10.1016/j.ultramic.2019.112913 (2020)

4. C. B. Smiet, H. J. de Blank, T. A. de Jong, D. N. L. Kok & D. Bouwmeester. Resistive evolution of toroidal field distributions and their relation to magnetic clouds. *Journal of Plasma Physics* **85.** doi:10.1017/S0022377818001290 (2019)

3. T. A. de Jong, J. Jobst, H. Yoo, E. E. Krasovskii, P. Kim & S. J. van der Molen. Measuring the Local Twist Angle and Layer Arrangement in Van der Waals Heterostructures. *physica status solidi (b)* **255,** 1800191. doi:10.1002/pssb.201800191 (2018)

*These authors contributed equally to the work

2. T. A. de Jong, E. E. Krasovskii, C. Ott, R. M. Tromp, S. J. van der Molen & J. Jobst. Intrinsic stacking domains in graphene on silicon carbide: A pathway for intercalation. *Physical Review Materials* **2,** 104005. doi:10.1103/PhysRevMaterials.2.104005 (2018)

1. J. J. T. Wagenaar, A. M. J. den Haan, J. M. de Voogd, L. Bossoni, T. A. de Jong, M. de Wit, K. M. Bastiaans, D. J. Thoen, A. Endo, T. M. Klapwijk, J. Zaanen & T. H. Oosterkamp. Probing the Nuclear Spin-Lattice Relaxation Time at the Nanoscale. *Physical Review Applied* **6,** 014007. doi:10.1103/PhysRevApplied.6.014007 (2016)